



# From charge- and spin-ordering to superconductivity in the organic charge-transfer solids

R. T. Clay<sup>a</sup>, S. Mazumdar<sup>b</sup>

<sup>a</sup>*Department of Physics and Astronomy and HPC<sup>2</sup> Center for Computational Sciences, Mississippi State University, Mississippi State, MS 39762, USA.*

<sup>b</sup>*Department of Physics, University of Arizona, Tucson, AZ 85721, USA*

## Abstract

We review recent progress in understanding the different spatial broken symmetries that occur in the normal states of the family of charge-transfer solids (CTS) that exhibit superconductivity (SC), and discuss how this knowledge gives insight to the mechanism of the unconventional SC in these systems. A great variety of spatial broken symmetries occur in the semiconducting states proximate to SC in the CTS, including charge ordering, antiferromagnetism and spin-density wave, spin-Peierls state and the quantum spin liquid. We show that a unified theory of the diverse broken symmetry states necessarily requires explicit incorporation of strong electron-electron interactions and lattice discreteness, and most importantly, the correct bandfilling of one-quarter, as opposed to the effective half-filled band picture that is often employed. Uniquely in the quarter-filled band, there is a very strong tendency to form nearest neighbor spin-singlets, in both one- and two-dimension. The spin-singlet in the quarter-filled band is necessarily charge-disproportionated, with charge-rich pairs of nearest neighbor sites separated by charge-poor pairs of sites in the insulating state. Thus the tendency to spin-singlets, a quantum effect, drives a commensurate charge-order in the correlated quarter-filled band. This charge-ordered spin-singlet, which we label as a paired-electron crystal (PEC), is different from and competes with both the antiferromagnetic (AFM) state and the Wigner crystal (WC) of single electrons. Further, unlike these classical broken symmetries, the PEC is characterized by a spin gap. The tendency to the PEC in two dimension is enhanced by lattice frustration. The concept of the PEC mirrors parallel development of the idea of a density wave of Cooper pairs in the superconducting high  $T_c$  cuprates, where also the existence of a charge-ordered state in between the antiferromagnetic and the superconducting phase has now been confirmed. Following this characterization of the spatial broken symmetries, we critically reexamine spin-fluctuation and resonating valence bond theories of frustration-driven SC within half-filled band Hubbard and Hubbard-Heisenberg Hamiltonians for the superconducting CTS. We present numerical evidence for the absence of SC within the half-filled band correlated-electron Hamiltonians for any degree of frustration. We then develop a valence-bond theory of SC within which the superconducting state is reached by the destabilization of the PEC by additional pressure-induced lattice frustration that makes the spin-singlets mobile. We present limited but accurate numerical evidence for the existence of such a charge order-SC duality. Our proposed mechanism for SC is the same for CTS in which the proximate semiconducting state is antiferromagnetic instead of charge-ordered, with the only difference that SC in the former is generated via a fluctuating spin-singlet state as opposed to static PEC. In [Appendix B](#) we point out that several classes of unconventional superconductors share the same band-filling of one-quarter with the superconducting CTS. In many of these materials there are also indications of similar intertwined charge order and SC. We discuss the transferability of our valence-bond theory of SC to these systems.

**Keywords:** unconventional superconductivity, organic superconductors, strongly correlated materials

## Contents

<b>1</b>	<b>Introduction and Scope of the Review</b>	<b>4</b>
<b>2</b>	<b>Electron-electron interaction effects - survey of early work</b>	<b>6</b>
2.1	Classification: cationic, anionic and two-chain conductors . . . . .	6
2.2	Charge-spin decoupling . . . . .	7
2.3	The $4k_F$ instability, Peierls CDW versus Wigner crystallization . . . . .	7
2.4	Intermolecular versus intramolecular electron-phonon interactions . . . . .	9
2.5	$\rho$ -dependent correlation effects . . . . .	10
2.6	Summary . . . . .	11
<b>3</b>	<b>Broken symmetries in quasi-one dimensional CTS, Theory</b>	<b>11</b>
3.1	Theoretical model and parameters . . . . .	12
3.2	Spatial broken symmetries - configuration space based physical ideas . . . . .	14
3.2.1	The one dimensional limit . . . . .	14
3.2.2	Weak two dimensional interactions . . . . .	18
3.3	Numerical Results . . . . .	18
3.3.1	One dimensional extended Hubbard model . . . . .	18
3.3.2	One dimensional Peierls-extended Hubbard model . . . . .	19
3.3.3	Weakly two dimensional results . . . . .	21
3.4	Summary . . . . .	22
<b>4</b>	<b>Broken symmetries in quasi-one-dimensional CTS, Experiments</b>	<b>22</b>
4.1	Traditional Fabre salts . . . . .	23
4.1.1	The FCO phase . . . . .	24
4.1.2	The AFM-I phase . . . . .	25
4.1.3	The SP phase in $X = PF_6$ and $AsF_6$ . . . . .	25
4.2	(TMTTF) <sub>2</sub> Br and (TMTSF) <sub>2</sub> PF <sub>6</sub> , the AFM-II region . . . . .	27
4.2.1	(TMTTF) <sub>2</sub> Br . . . . .	27
4.2.2	(TMTSF) <sub>2</sub> PF <sub>6</sub> . . . . .	27
4.3	Non-traditional 2:1 cationic salts . . . . .	28
4.3.1	(TMTTF) <sub>2</sub> I . . . . .	28
4.3.2	(BCPTTF) <sub>2</sub> X . . . . .	28
4.3.3	( <i>o</i> -DMTTF) <sub>2</sub> X . . . . .	28
4.3.4	$\delta$ -(EDT-TTF-CONMe <sub>2</sub> ) <sub>2</sub> X . . . . .	30
4.3.5	(EDO-TTF) <sub>2</sub> X and BCDW-II . . . . .	31
4.4	Summary . . . . .	32
<b>5</b>	<b>Broken symmetries in quasi-two dimensional CTS, Experiments</b>	<b>32</b>
5.1	Quasi-two dimensional cationic CTS . . . . .	32
5.1.1	$\kappa$ CTS . . . . .	32
5.1.2	$\beta$ , $\beta'$ , and $\beta''$ type CTS . . . . .	40
5.1.3	$\theta$ CTS . . . . .	46
5.1.4	$\alpha$ CTS . . . . .	48
5.2	Quasi-two dimensional anionic CTS . . . . .	50
5.2.1	AFM, CO, and SC in M(dmit) <sub>2</sub> . . . . .	52
5.2.2	EtMe <sub>3</sub> P[Pd(dmit) <sub>2</sub> ] <sub>2</sub> . . . . .	53
5.2.3	$\beta'$ -EtMe <sub>3</sub> Sb[Pd(dmit) <sub>2</sub> ] <sub>2</sub> . . . . .	55
5.3	Summary . . . . .	56

<b>6</b>	<b>Broken symmetries in quasi-two dimensional CTS, Theory</b>	<b>56</b>
6.1	Half-filled band	58
6.1.1	Magnetic Phases	58
6.1.2	Superconductivity: suppression of superconducting pair-pair correlations	58
6.1.3	$\rho = 1$ $U$ - $t$ - $J$ models	60
6.2	Quarter-filled band	61
6.2.1	Coupled spin-singlet and charge order at $\rho = \frac{1}{2}$	61
6.2.2	Paired Electron Crystal in two dimensions	63
6.2.3	Paired Electron Crystal in quasi-two dimensional CTS	66
6.2.4	Selective enhancement of superconducting pair-pair correlations at $\rho = \frac{1}{2}$	69
6.2.5	Superconducting pair-pair correlations in the $\kappa$ -(ET) <sub>2</sub> X lattice	70
6.3	Summary	74
6.3.1	Application of theory to CO-to-SC transitions.	74
6.3.2	Where is the PEC in the $\kappa$ -(ET) <sub>2</sub> X?	74
6.3.3	Application to the quasi-1D superconductors.	75
6.3.4	Similarities with high- $T_c$ cuprates	75
<b>7</b>	<b>Conclusions</b>	<b>76</b>
	<b>Acknowledgments</b>	<b>77</b>
	<b>Appendix A Molecule abbreviations</b>	<b>78</b>
	<b>Appendix B Other <math>\rho = \frac{1}{2}</math> superconductors</b>	<b>79</b>
	Appendix B.1 Superconducting layered cobalt oxide hydrate	79
	Appendix B.2 Spinel superconductors	80
	Appendix B.3 Superconducting vanadium bronzes	81
	Appendix B.4 Superconducting fullerides	82
	Appendix B.5 Li <sub>0.9</sub> Mo <sub>6</sub> O <sub>17</sub>	83
	Appendix B.6 Intercalated and doped IrTe <sub>2</sub>	84
	Appendix B.7 Superconducting hole- and electron-doped cuprates	84
	<b>References</b>	<b>86</b>

## 1. Introduction and Scope of the Review

Superconductivity (SC) is only one of many mysterious features of the high critical temperature (high  $T_c$ ) superconductors. More enigmatic is perhaps the violation of the Landau Fermi liquid theory in the normal state, which had been a cornerstone of traditional condensed matter theory until thirty years ago, when high  $T_c$  in the cuprate materials was first discovered [1]. The list of experiments that demonstrate the unusual characteristics in the so-called normal state of the cuprates, especially in the under-doped region, is now very long [2–4]. Similar unusual behavior have now been observed in the iron-based superconductors [5–7]. It is widely recognized that these peculiarities, including in particular the proximity of SC to multiple competing or coexisting broken symmetries separated by quantum criticalities, are the common features of systems with strongly correlated charge carriers [8]. Furthermore, there is now widely-shared agreement that there exist many other correlated-electron superconductors, albeit with relatively lower  $T_c$  (due to perhaps smaller one-electron bandwidths) [9–17]. The present review is largely about one such family of materials with strong electron-electron (e-e) interaction, low-dimensional organic charge-transfer solids (CTS). Even as we restrict our discussions to this one family of materials, we believe that the key concept, viz., SC in the CTS evolves from a Wigner crystal of nearest neighbor spin-singlet electron pairs that we term the Paired Electron Crystal, may be widely transferable. In order to avoid confusion, henceforth we will use the term “Wigner crystal” (WC) to refer to the Wigner crystal of single electrons only; the ordered state of spin pairs will be referred to as the “Paired Electron Crystal” (PEC). We show in our work that the tendency to form such a charge-ordered spin-singlet state, a quantum effect, is particularly strong in the correlated-electron quarter-filled band, where this broken symmetry competes with other more thoroughly researched broken symmetries such as antiferromagnetism, quantum spin liquid and the WC of single electrons. A generalization of our theory is that there must exist other unconventional correlated-electron superconductors that share the same bandfilling of one-quarter with the CTS, and that exhibit some of the same peculiar features. In particular, there should exist evidence for the occurrence of the same PEC. We discuss several such materials (families of materials) in [Appendix B](#). While clearly further research on these other materials are warranted before firm conclusions can be arrived at, the identification of any common theme between these diverse families is encouraging.

SC in the CTS has been known since 1980 [18, 19]. While the first organic superconductors were “low  $T_c$ ” and belonged to the weakly two-dimensional (2D) (and are hence often referred to as “quasi-one-dimensional”, quasi-1D) TMTSF family (see [Appendix A](#) for a compendium of the full names of organic molecules referred to by their acronyms in the review), within a few years the more strongly 2D “high  $T_c$ ” superconducting compounds belonging to the BEDT-TTF (hereafter ET) family were discovered [20]. The chemical formulas of the two series of compounds are similar [(TMTSF)<sub>2</sub>X versus (ET)<sub>2</sub>X, where X is a closed-shell inorganic anion.] While (TMTSF)<sub>2</sub>X exhibit the same basic crystal structure independent of X, (ET)<sub>2</sub>X are obtained with many different crystal structures, which are labeled  $\alpha$ ,  $\beta$ ,  $\theta$ ,  $\kappa$ , ... etc., with no particular significance attached to these Greek prefixes. The original anions X in the family (ET)<sub>2</sub>X were the same as in the (TMTSF)<sub>2</sub>X. Subsequently, however, compounds with more complicated polymeric anions such as Cu(NCS)<sub>2</sub>, Cu[N(CN)<sub>2</sub>]Cl, Cu[N(CN)<sub>2</sub>]Br etc. became more popular because of the higher  $T_c$ ’s reached with these compounds. The compound  $\kappa$ -(ET)<sub>2</sub>Cu[N(CN)<sub>2</sub>]Br is an ambient pressure superconductor below 11.6 K [21], in contrast to the others in which SC is reached only under pressure. Several other families of superconducting CTS, including compounds of BEDT-TSF (hereafter BETS) as well as compounds with asymmetric cations such as DMET are known. We point the reader to several excellent resources on the chemistry and physics of these materials [22–25]. While the charge carriers in the above materials are holes, CTS superconductors with electrons as charge carriers are also known [26]. These last compounds have the general chemical formula X[M(dmit)<sub>2</sub>]<sub>2</sub>, where M = Ni, Pd or Pt, and X<sup>+</sup> is a closed-shell monovalent cation, such as EtMe<sub>3</sub>P<sup>+</sup>, EtMe<sub>3</sub>Sb<sup>+</sup> etc.

Two characteristic features are common to nearly all known superconducting CTS. First, with very few exceptions [27–29], all hole carriers have 2:1 cation:anion stoichiometry, implying a hole concentration of  $\frac{1}{2}$  per cationic molecule [22–24] (the stoichiometry of CTS superconductors with large unit cells is sometimes written as 4:2; the carrier concentration per cationic molecule is the same in these.) We will refer to the carrier concentration per molecule as  $\rho$ , which we believe is a more fundamental quantity than apparent bandfillings in these strongly correlated systems [30–32]. The exceptions mentioned above actually prove the “ $\rho = \frac{1}{2}$  rule”, in that these systems are complex structures in which the deviation of  $\rho$  from  $\frac{1}{2}$  is very small. Similarly, the electron carriers have 1:2 cation:anion stoichiometry [26]. With the anions forming the active layer now, the electron concentration  $\rho$  is  $\frac{1}{2}$  per anionic molecule.

The second characteristic common to superconducting CTS is that in nearly every case, the ambient pressure

state at low temperature  $T$  is an unconventional semiconductor with spatial broken symmetry, and SC is obtained by application of pressure at constant carrier concentration. These two features, SC being limited to a very narrow carrier concentration range or even fixed concentration, as well as an apparent *semiconductor-superconductor transition*, are common to many known correlated-electron superconductors beyond the CTS [16]. We discuss several such families of materials in [Appendix B](#). Interestingly, the electron-doped cuprate superconductors share these characteristics [33].

We report a two-pronged effort to understanding the mechanism of SC in the CTS. On the one hand, we report recent experimental and theoretical studies that have attempted to understand the spatial broken symmetries in the semiconducting states proximate to SC. We will be interested in the detailed *patterns of charge, bond and spin distortions in the insulating phases, beyond merely their periodicities*. We will attempt to show that the patterns of distortions, as well as the *phase relationships between any coexisting broken symmetries* are both relevant when trying to arrive at a clear understanding of the complex phenomenon of correlated-electron SC. (We will, for instance, show that the bond-charge distortion pattern in the charge-ordered phase proximate to SC is universal, while other patterns that are also observed do not lead to SC [34].) Hence our discussions of SC will be limited strictly to theoretical approaches that are based on *discrete lattice Hamiltonians*. We refer the reader to recent reviews for discussions of competing theories that start from continuum electron-gas models [35, 36]. Following the discussions of spatial broken symmetries, we discuss various proposed theoretical mechanisms of SC in the CTS, focusing on theories that emphasize the correlated-electron nature of the CTS. We show that spin-fluctuation and resonating valence-bond (RVB) theories of SC that are based on mean-field theories of e-e interaction or approximate approaches such as the random phase approximation (RPA), fluctuation-exchange (FLEX) or the dynamic mean-field theory (DMFT) fail to explain the SC in the CTS, even as they might successfully explain select non-superconducting spatial broken symmetry phases [37, 38]. Our principal goal is to report the collected theoretical and experimental results which indicate that quantum fluctuations in systems with the specific carrier concentration of  $\frac{1}{2}$  per unit drive a strong tendency to form charge-ordered local singlets. The strong quantum effects are not limited to 1D, but will also occur in 2D and perhaps even 3D in the presence of strong geometric lattice frustration (see [Appendix B.2](#) and [Appendix B.4](#)). We discuss experiments that reveal these local singlets in the dominant spatial broken symmetry states in the CTS at the lowest  $T$ . A new viewpoint about correlated-electron SC, that has conceptual overlaps with both the RVB theory [39, 40] and bipolaron theories of SC [41], and is yet distinct, is shown to emerge. The proposed mechanism of SC, while still incomplete, also has strong overlaps with the emergent ideas of intertwined charge order-superconductivity in the cuprates [42] as well as the proposition that the charge-ordered phase there is a density wave of Cooper pairs [43, 44].

This review is broken into the following parts. In [Section 2](#) we introduce our theoretical model and describe early applications of the theory to the family of CTS as a whole, both non-superconducting and superconducting. The purpose of this section is to show that many of the later developments, in particular, the conclusion that the specific carrier density per molecule  $\rho = \frac{1}{2}$  is special, emerges already from the early literature. In [Section 3](#) we develop a comprehensive theory of broken symmetries specifically for  $\rho = \frac{1}{2}$ , in quasi-one dimension. This is where we first encounter the concepts of Bond-Charge-Density Wave (BCDW) and Bond-Charge-Spin-Density Wave (BCSDW), which are simply PECs in one dimension, or on weakly coupled 1D chains. The two most notable conclusions of the theoretical work here are, (a) even within the extended Hubbard model with nonzero nearest neighbor repulsion, the WC is not the obvious ground state; rather, for a wide range of realistic parameters, the ground states are the BCDW and BCSDW; (v) there exists a broad range of realistic Coulomb parameters where even as the high temperature phase is the WC, at the lowest temperatures the BCDW dominates. In [Section 4](#) we discuss experimental observations in the Fabre (TMTTF) and Bechgaard (TMTSF) salts, along with non-traditional  $\rho = \frac{1}{2}$  cationic CTS. The wide applicability of the PEC concept in these quasi-one-dimensional materials is pointed out. In [Sections 5](#) and [6](#) we discuss experiments and theory in quasi-two-dimension. From explicit calculations we develop the PEC concept in two dimensions. Manifestations of the PEC in both cationic and anionic quasi-two-dimensional CTS are the occurrence of insulating stripes, and nonzero spin gap. In [Section 6.2.3](#) we present detailed evidence that in every case where there occurs transition to SC from a charge-ordered state, and the pattern of the charge-order is known, this pattern corresponds to that of the PEC. Following this we present detailed numerical calculations of superconducting pair-pair calculations and present our conclusions. We then point out in [Appendix B](#) that there exist many other unconventional semiconductors characterized by strong electron-electron interactions, frustrated lattice and  $\rho = \frac{1}{2}$ .

“Generic” unconventional behavior is observed in these cases, as we point out in [Appendix B](#), where we discuss briefly the experimental observations in the individual systems.

*Guide to the reader:* Because of the lengths of the individual sections and subsections that follow, and the seemingly diverse topics that are discussed, we present a summary paragraph at the end of each of Sections 2–6. Sections 4 and 5 review in detail the experimental work on the quasi-one and quasi-dimensional materials and are by necessity quite dense; we have therefore presented summary paragraphs here after each subsection. Readers who are short of time are encouraged to read just the introduction and summary paragraphs of these sections, and refer back to subsections on specific materials as needed in the following sections.

## 2. Electron-electron interaction effects - survey of early work

Many of the concepts related to e-e interaction effects in CTS have their roots in early work done through the 1960s to the 1980s. We report on these studies here, not merely for the sake of completeness. The justification of many of the claims made in the present review come from comparisons of early and recent theories against experiments from this period as well as later work. It is also conceivable that the astute reader may still find new directions of research from this report on early work.

### 2.1. Classification: cationic, anionic and two-chain conductors

Several early reviews on CTS emphasize the role of e-e interactions [45–47]. The earliest CTS were mostly *mixed stack* systems in which planar aromatic  $\pi$ -electron donors  $D$  and acceptors  $A$  alternated along quasi-1D stacks, with intermolecular distances slightly smaller than the sum of the van der Waals’ radii of the  $D$  and  $A$  molecules. Predominantly neutral  $\cdots DADA \cdots$  as well as predominantly ionic  $\cdots D^+A^-D^+A^- \cdots$  were both known. Later demonstrations of pressure [48], temperature [49] and light [50] induced neutral-ionic transitions in the CTS have led to a wide field of research, but mixed stack CTS are outside the scope of this review, as they are necessarily  $\frac{1}{2}$ -filled band semiconductors.

Prototype one-chain *segregated stack* CTS are the anionic M-TCNQ, in which the M are alkali metals that donate one complete electron to the acceptor TCNQ molecules, and in which the TCNQ form acceptor-only  $\cdots AAAA \cdots$  segregated stacks. The semiconducting behavior of M-TCNQ, along with their unusual optical and magnetic behavior led to the Hubbard model description of these systems,

$$H = - \sum_{\langle ij \rangle \sigma} t_{ij} c_{i\sigma}^\dagger c_{j\sigma} + U \sum_i n_{i\uparrow} n_{i\downarrow} \quad (1)$$

where  $c_{i\sigma}^\dagger$  creates an electron or a hole with spin  $\sigma$  ( $\uparrow$  or  $\downarrow$ ) on the frontier orbital of molecular site  $i$ ,  $\langle \dots \rangle$  implies nearest neighbors (NN), and all other terms have their usual meanings. The TCNQ $^-$  stacks with one electron per anion are 1D Mott-Hubbard semiconductors with  $U \geq 4|t|$  [51] [Very recently, Soos *et al.* have suggested that Na-TCNQ and K-TCNQ are charge-ordered,  $\cdots \text{TCNQ}^{2-}\text{TCNQ}^0\text{TCNQ}^{2-}\text{TCNQ}^0 \cdots$  [52]. We believe that additional theoretical and experimental work are needed before this issue could be considered as settled.]

Many different groups pointed out that 1D chains with  $\rho \neq 1$  are expected to be conductors in spite of large  $U$  [45–47, 51]. Research on conducting CTS began in earnest with the discovery of the peculiar T-dependent transport in NMP-TCNQ, a two-chain segregated stack CTS. Initial work had assumed that the degree of charge-transfer  $\rho$  from NMP to TCNQ was 1 [53], but later more precise measurements [54] indicated this to be  $\frac{2}{3}$ . Two-chain conductors TTF-TCNQ [55, 56], TSF-TCNQ, HMTTF-TCNQ and HMTSF-TCNQ [57] with high conductivities and with  $\rho = 0.59, 0.63, 0.74$  and  $0.74$ , respectively, were discovered around the same period, establishing firmly the concept of conductors with incomplete charge-transfer ( $\rho \neq 1$ ). Two-chain  $\rho = 1$  systems, such as HMTTF-TCNQF $_4$  and HMTSF-TCNQF $_4$ , are also Mott-Hubbard semiconductors [58, 59]. The one-chain cationic systems of interest in the present Review were discovered subsequently. We refer the readers to several conference and workshop proceedings from this period that give excellent discussions of the work done during this period [57, 60, 61].

## 2.2. Charge-spin decoupling

Early theoretical works that introduced the concept of charge-spin decoupling in the context of the quasi-1D CTS were by Bernasconi *et al.* [62] and Klein and Seitz [63]. Bernasconi *et al.* showed that the Peierls instability, which in noninteracting 1D chains opens a gap at the Fermi wavenumbers  $\pm k_F$ , will for large  $U$  occur in a band of *spinless* Fermions at new wavenumbers  $\pm 2k_F$ , leading to a so-called  $4k_F$  instability. This was one of the earliest discussions of metal-insulator transitions leading to Bond Order Wave (BOW) and periodic lattice distortion with wavevector other than the conventional Peierls'  $2k_F$ . In this review we will use BOW to describe a periodic lattice distortion that leaves the site charge densities homogeneous; in general however for  $\rho \neq 1$  a BOW must coexist with a simultaneous periodic distortion of the charge density on each site (see Section 3.2.1). Specifically for  $\rho = \frac{1}{2}$ , the ordinary  $2k_F$  BOW instability would correspond to bond tetramerization ( $2k_F = \pi/2a$ , where  $a$  is the lattice constant of the undistorted lattice) while the  $4k_F$  BOW instability implies bond dimerization ( $4k_F = \pi/a$ ).

Klein and Seitz showed that the lowest excitations of the large  $U$  1D Hubbard model with nearest neighbor-only hoppings ( $t_{ij} = t$ ) reduces in the  $U \gg |t|$  limit to

$$H = N_2 U - t \sum_{i=1}^N (a_i^\dagger a_{i+1} + H.c.) + H_{\text{spin}} \quad (2)$$

$$H_{\text{spin}} = \sum_{\theta, i=1}^{N_1} J_\theta \vec{S}_i \cdot \vec{S}_{i+1} \quad (3)$$

where  $N$  is the total number of sites,  $N_1$  and  $N_2$  are the number of single and double occupancies, respectively ( $N_2 = 0$  for  $\rho \leq 1$ ),  $a_i^\dagger$  creates a spinless Fermion, and  $H_{\text{spin}}$  is the Heisenberg spin Hamiltonian describing spin excitations corresponding to each different occupancy  $\theta$  of the spinless Fermion band. The authors gave a closed form expression for the exchange integral within  $H_{\text{spin}}$  for the ground state occupancy ( $\theta = 0$ ) of the spinless Fermions [63],

$$J_0 = \frac{2t^2}{U} \rho \left[ 1 - \frac{\sin(2\pi\rho)}{2\pi\rho} \right] \quad (4)$$

This work formed the basis for comparing the temperature-dependence of the static magnetic susceptibilities  $\chi(T)$  of 1D CTS with arbitrary  $\rho$  below the metal-insulator transition temperature to the Bonner-Fisher  $\chi(T)$  of the 1D Heisenberg chain [30]. Coupling of the spins to the lattice can therefore lead to the spin-Peierls transition even for  $\rho \neq 1$ . Interestingly, the spin-Peierls (SP) transition was observed in the  $\rho = 1$  CTS [64, 65] considerably before it would be seen in inorganic systems, and the experimental observations led to sophisticated theoretical developments of this phenomenon [66]. Much of our current understanding of the SP transitions in the  $\rho = \frac{1}{2}$  cationic CTS (see next section) come from these early papers.

## 2.3. The $4k_F$ instability, Peierls CDW versus Wigner crystallization

Diffuse X-ray scattering [67–69] and inelastic neutron scattering [70, 71] of TTF-TCNQ gave the first experimental detection of the  $4k_F$  instability in the donor stack of TTF-TCNQ. Subsequent measurements detected the  $4k_F$  instability in the one-chain compounds MEM(TCNQ)<sub>2</sub> [72–74] and (NMP)<sub>x</sub>(phen)<sub>1-x</sub>TCNQ for  $0.5 \leq x \leq 0.54$  [54]. MEM(TCNQ)<sub>2</sub> continues to enjoy the status of being one of the most well-characterized materials, in that both the  $4k_F$  and the  $2k_F$  phases here were clearly identified as bond dimerized and tetramerized, respectively [73]. The systems (NMP)<sub>x</sub>(phen)<sub>1-x</sub>TCNQ were interesting as the carrier concentration in the TCNQ acceptor stack could be varied almost continuously by changing the ratio between the electron donor NMP and the neutral phenazine molecule. Strong diffuse X-ray scattering at  $4k_F = \pi/a$ , where  $a$  is the lattice constant was found at  $x$  exactly equal to 0.5, where there occurs complete charge-transfer from each NMP molecule. As  $x$  is increased from 0.5, there is a concomitant but nonlinear increase in  $\rho$ , with  $\rho$  reaching the value  $\frac{2}{3}$  at  $x = 1$ . Interestingly, while for low electron densities both  $4k_F$  and  $2k_F$  instabilities on the TCNQ stack are observed, for  $x > \frac{2}{3}$  there is no  $4k_F$  scattering at all and only  $2k_F$  scattering is observed. This specific observation was the first experimental demonstration of the systematic carrier concentration dependent behavior of correlated one-dimensional bands (see Section 2.5), and is summarized in Fig. 1. Very interestingly, the  $4k_F$  scattering vector is unshifted between  $x = 0.5$  and  $x = 0.54$  [54]. This was interpreted

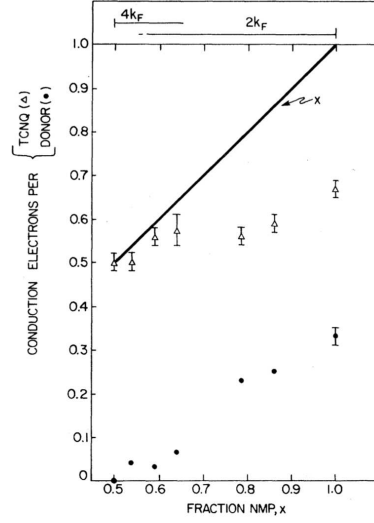


Figure 1. Number of conduction electrons per TCNQ (triangles) and per donor molecule (dots) in  $(\text{NMP})_x(\text{phen})_{1-x}\text{TCNQ}$ . The solid line is equal to  $x$ . Reprinted with permission from Ref. [54], © 1981 The American Physical Society.

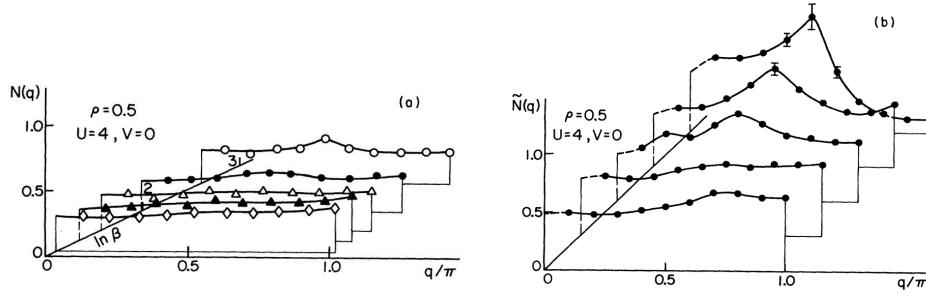


Figure 2. (a) Charge susceptibility of the 1D Hubbard model as a function of wavevector and inverse temperature  $\beta$  for a 20-site lattice with  $U = 4$  and  $V = 0$  at  $\rho = \frac{1}{2}$ . Here  $q = \pi (\frac{\pi}{2})$  corresponds to  $4k_F$  ( $2k_F$ ). (b) bond-order susceptibility for the same parameters. Reprinted with permission from Ref. [78], © 1984 The American Physical Society.

as evidence for the formation of fractionally charged  $e/2$  solitons [75, 76], which had been theoretically suggested earlier by Rice and Mele within the  $U \rightarrow \infty$  Peierls-Hubbard model [77].

Identification of the ground state as a manifestation of the  $4k_F$  Peierls charge-density wave (CDW) (see above) appeared reasonable, but it was suggested by Torrance [31] that the mechanism of the instability was in fact different. Torrance was of the opinion that the  $4k_F$  instability was driven by intersite Coulomb interactions and resulted in a gain in *potential energy*, as opposed to the gain in kinetic energy that drives the Peierls instability. This was the first foray into the concept of *charge ordering* (CO). Very soon after this Hubbard in a seminal paper developed the concept of Wigner crystallization driven by long range intersite Coulomb interaction  $V_{ij}$ , within the extended Hubbard Hamiltonian (EHM),

$$H = - \sum_{\langle ij \rangle \sigma} t_{ij} c_{i\sigma}^\dagger c_{j\sigma} + U \sum_i n_{i,\uparrow} n_{i,\downarrow} + \frac{1}{2} \sum_{i,j} V_{ij} n_i n_j \quad (5)$$

where  $n_i = \sum_{\sigma} n_{i,\sigma}$  is the total number of electrons on site  $i$ . Note that the intersite interaction in the last term is not limited to NN. Hubbard's actual work was for the limits of  $U = \infty$  and  $t_{ij} = 0$ , in which case Eq. 5 reduces to a classical Ising-like Hamiltonian  $H_{\text{red}} = \frac{1}{2} \sum_{i,j} V_{ij} n_i n_j$ , with  $n_i = 0, 1$ . Hubbard was able to derive the WC site occupancies by electrons in 1D for all  $\rho$  for arbitrary but downward convex  $V_{ij}$ . Interestingly, for the special case of  $\rho = \frac{1}{2}$ , Hubbard found two competing Wigner crystals, denoted by  $\dots 1010 \dots$  and  $\dots 1100 \dots$ , where 1 and 0 refer

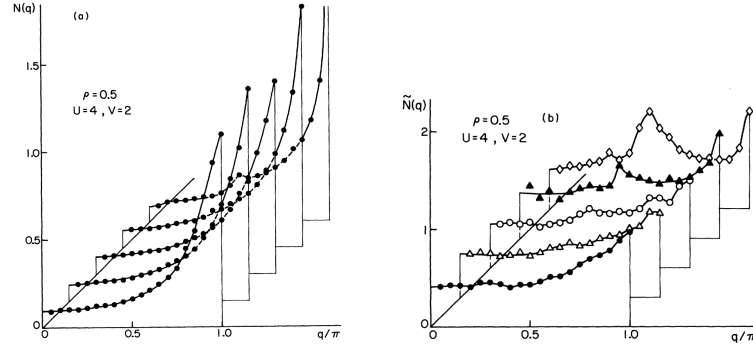


Figure 3. (a) Charge susceptibility of the 1D extended Hubbard model as a function of wavevector and inverse temperature  $\beta$  for a 40-site lattice with  $U = 4$  and  $V = 2$  at  $\rho = \frac{1}{2}$ . Here  $q = \pi (\frac{q}{\pi})$  corresponds to  $4k_F$  ( $2k_F$ ). (b) bond-order susceptibility for the same parameters. Reprinted with permission from Ref. [78], © 1984 The American Physical Society.

to sites occupied and unoccupied by charge carriers, respectively. Subsequent theoretical work showed that intersite Coulomb interactions beyond NN play insignificant role in the CTS [79]. We shall hereafter retain only the NN intersite Coulomb interaction and refer to this as  $V$ . We will refer to the Hamiltonian with  $U$ ,  $V$  and  $|t|$  as the extended Hubbard Hamiltonian. The configuration  $\dots 1100 \dots$  plays no important role in the absence of long range interaction, within this *classical picture* of lattice instability. We will refer to the configuration  $\dots 1010 \dots$  only as the WC for  $\rho = \frac{1}{2}$ .

The EHM with NN intersite interaction was investigated numerically for moderate  $U$  and  $V$  using quantum Monte Carlo (QMC) by Hirsch and Scalapino [78], for  $\rho = \frac{1}{2}$  and then for  $\rho = 0.6$ . The authors initially probed wavevector dependent charge-charge correlations only, which gives the tendency to CO [78, 80], and concluded that the  $\dots 1010 \dots 4k_F$  CO is obtained at  $\rho = \frac{1}{2}$  only for nonzero  $V$  when  $U$  is finite (see Fig. 2). In later work [78] the authors also investigated wavevector-dependent bond order-bond order correlations, and for a limited set of  $U$ ,  $V$  parameters found signatures of both  $2k_F$  and  $4k_F$  BOW instabilities (see Fig. 3). These results played a very significant role in later developments of theories of spatial broken symmetry in the correlated 1D, especially for  $\rho = \frac{1}{2}$ . They showed that information about the *tendency to CO or BOW* can be obtained even without explicit inclusion of electron-phonon interactions in the Hamiltonian, as this information is built into the purely electronic wavefunction itself. Second, the demonstration of the BOW instability, even for nonzero  $V$ , indicated that CO is obtained only for the NN interaction larger than a threshold value, a result that would be demonstrated explicitly many years later [81–83]. On the other hand, the pattern of the  $2k_F$  BOW, or the issues of coexistence versus competition between CO and BOW were, however, not understood at this point. One important experimental development was the identification of the phase below  $T_{4k_F}$  in MEM(TCNQ)<sub>2</sub> as the dimerized BOW phase [73]. We show in Fig. 4 schematics of the structure of the TCNQ stack above and below  $T_{4k_F}$ . T-dependent magnetic susceptibility  $\chi(T)$  showed Bonner-Fisher behavior in the region  $T_{2k_F} < T < T_{4k_F}$ , with an SP gap below  $T_{2k_F}$ , identifying the latter temperature as the SP temperature  $T_{SP}$ . Neutron diffraction studies showed that the SP transition led to dimerization of the bond-dimerization [84].

#### 2.4. Intermolecular versus intramolecular electron-phonon interactions

Two different kinds of electron-phonon (e-p) interactions have been discussed in the literature. The so-called Su-Schrieffer-Heeger (SSH) coupling [85] between electrons and stretching vibrations of the 1D lattice modulates the intermolecular hopping. Because of the massive molecular natures of the sites in the CTS, displacements orthogonal to the stacking axis (see Fig. 4(b)) as well as librational motion can make significant contributions to the SSH coupling. The Holstein electron-molecular vibration (EMV) coupling [86] also plays a significant role in CO instabilities as well as optical excitations [87–89]. Strictly in  $\rho = 1$  these two couplings give rise to competing BOW and site-CDW instabilities, for  $U = 0$  [90, 91] as well as nonzero  $U$  [92]. Coexistence is the norm at all other  $\rho$  [93]. The EMV coupling dictates that specific molecular frequencies vary with the charge density on the molecule, and at the onset of charge disproportionation at low T there occurs a splitting of infrared vibrational modes that are coupled strongly to the electrons [94, 95].

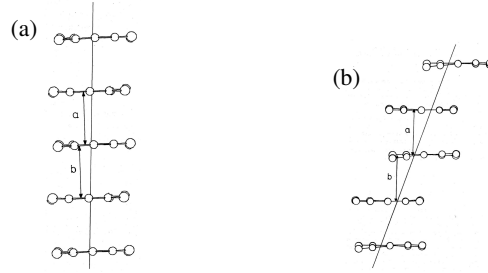


Figure 4. (a) TCNQ molecules of MEM(TCNQ)<sub>2</sub> as seen along their longest axis in the metallic state. The drawn line indicates the chain direction. Nearest neighbor intermolecular hoppings are uniform in this case. (b) Same below  $T_{4k_F}$ . The stack is now strongly dimerized. Reprinted with permission from Ref. [73], © 1979 The American Physical Society.

### 2.5. $\rho$ -dependent correlation effects

The  $4k_F$  instability, independent of its CDW or BOW nature, is clearly a signature of large Hubbard  $U$ . Yet another signature of strong correlation effects is the static magnetic susceptibility  $\chi(T)$ :  $U$  enhances the susceptibility strongly over what is expected in the noninteracting  $U = 0$  limit for the same hopping integral [30]. A mystery in this early phase was the *absence* of enhanced magnetic susceptibility and the  $4k_F$  instability in many CTS. Systems with nearly identical molecular components and very similar crystal structures behave very differently. Thus while the susceptibility of TTF-TCNQ at room temperature was enhanced by a factor of 3 over the expected Pauli value [30], the corresponding enhancement factor for HMTTF-TCNQ was only 1.15 [96]. The same enhancement factor for MEM(TCNQ)<sub>2</sub> was 20! It also appeared that enhanced (unenhanced) susceptibility and occurrence (non-occurrence) of the  $4k_F$  instability went together. This had led to considerable argument about the magnitude of  $U$  in the CTS.

The solution to this problem came from the recognition that neither the  $U \gg |t|$  nor the  $V = 0$  approximations that are often adopted for simplicity are justified. With realistic  $U$  ( $4|t| \leq U \leq 8|t|$ ) and  $V$  ( $|t| \leq V \leq 3|t|$ ), correlation effects are strongly, and *non-monotonically* dependent on  $\rho$  [32, 97]. At or near  $\rho = \frac{1}{2}$ ,  $V$  and  $U$  act in concert to reduce double occupancies of sites by charge carriers; however, over the broad region  $\frac{2}{3} \leq \rho \leq 0.8$   $V$  increases double occupancy. One measure of the  $\rho$ -dependent correlations is the normalized probability of double occupancy of sites by carriers  $g(\rho)$ , defined as,

$$g(\rho) = \frac{\langle n_{i,\uparrow} n_{i,\downarrow} \rangle}{\langle n_{i,\uparrow} \rangle \langle n_{i,\downarrow} \rangle} \quad (6)$$

The plot in Fig. 5 shows  $g(\rho)$  versus  $\rho$  for several different  $V$  ( $V = 0, 1, \text{ and } 2$  in units of  $|t|$ ) for  $U = 6|t|$  calculated using the Stochastic Series Expansion (SSE) QMC method [98, 99]. Behavior for other  $U$  is the same. For nonzero  $V$  strongly correlated behavior (small  $g$ ) is found for  $\rho$  at or near  $\frac{1}{2}$ , while relatively weakly correlated behavior (moderate to large  $g$ ) occurs for  $\frac{2}{3} \leq \rho \leq 0.8$ . A turnaround in  $g(\rho)$  is again observed as the Mott-Hubbard region of  $\rho = 1$  is approached.

Table 1 lists the known behavior of a large number of CTS with  $\rho$  spanning from 0.5 to 1. The results agree fully with the predictions of Fig 5. Enhanced susceptibilities and  $4k_F$  scattering always appear in the range  $0.5 < \rho < 0.55$  and never appear in the range  $0.63 < \rho < 0.8$ . The intervening range  $0.55 < \rho < 0.63$  forms a transition region: the symptoms appear at  $\rho = 0.59$  in TTF-TCNQ, but do not appear at  $\rho = 0.57$  in TMTSF-TCNQ with its considerably larger cation bandwidth. Compounds in the range  $0.83 < \rho < 1.0$  are unknown, and compounds with  $\rho = 1$  are universally Mott-Hubbard semiconductors.

The demonstration of  $\rho$ -dependent correlation effects is a significant result, since SC in the CTS is restricted precisely to the carrier concentration where correlation effects are the strongest! This makes it unlikely that the SC mechanism can be understood within a noninteracting electron picture. In Appendix B we will point out that many of the perplexing features that are seen in the the  $\rho = \frac{1}{2}$  CTS, including SC, are also shared by other  $\rho = \frac{1}{2}$  systems, including inorganic materials.

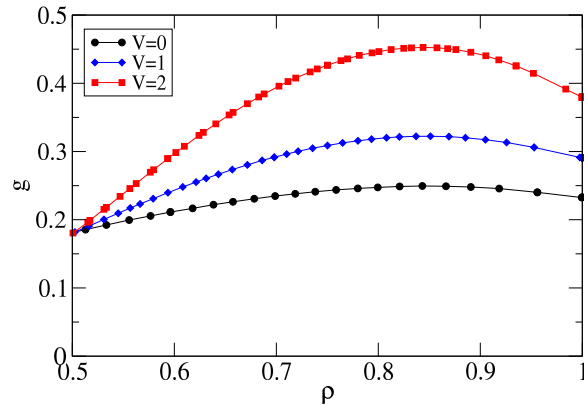


Figure 5. (Color online) Normalized double occupancy  $g(\rho)$  versus  $\rho$  for the 1D EHM of Eq 5 for  $U = 6$ , and  $V = 0$  (circles), 1 (diamonds) and 2 (squares), for a 64 site system. Lines are guides to the eye.

## 2.6. Summary

The normal state of the entire family of CTS, whether one-chain or two-chain, can be understood within the extended Hubbard model (EHM) with nonzero moderate nearest-neighbor Coulomb interaction  $V$ . The  $V$  interaction enhances single occupancy of sites by electrons near  $\rho = \frac{1}{2}$ , and double occupancy in the range  $0.67 < \rho < 0.8$ , thus explaining both the observed “strongly correlated” and “weakly correlated behavior”. Lattice instabilities can be driven by both intermolecular electron-phonon coupling and electron-molecular vibration (EMV) coupling. The periodicities of the density waves however are determined by Coulomb interactions. Correlation effects are strongest at  $\rho = \frac{1}{2}$ , which is the carrier density in the superconductors (see following sections), making it unlikely that superconductivity in the CTS can be explained within BCS theory.

## 3. Broken symmetries in quasi-one dimensional CTS, Theory

While the earliest work described in the previous section was largely on the two-chain conductors, interest over the past two decades have been focused on the 2:1 cationic materials (and more recently, on the 1:2 anionic materials), as these are the only ones that exhibit SC. The Fabre and Bechgaard salts  $(\text{TMTCF})_2\text{X}$ ,  $\text{C} = \text{S}, \text{Se}$ , have been intensively studied. A generic phase diagram (see Fig. 6) for these systems has been proposed [100]. The proposed phase diagram has received ample experimental support. It is generally agreed that the pressure axis is a measure of the interchain coupling at ambient pressure. Different materials shown along this axis indicate the role interchain interactions play in specific materials. The different transition temperatures in the phase diagram that are of interest are (i)  $T_{\text{MI}}$ , the metal-insulator (MI) transition temperature, which at the very extreme left occurs at a high temperature of 200 K or so, and is driven by charge localization, induced perhaps by counter anion-driven dimerization along the stacking axis; (ii)  $T_{\text{CO}}$ , the temperature at which charge-ordering occurs (usually 60 – 100K), and (iii)  $T_{\text{AFM}}$  and  $T_{\text{SP}}$ , temperatures at which transitions to the antiferromagnetic and SP states occur (we refer to the AFM/SDW phase of Fig. 6 as simply AFM-II, and the antiferromagnetic phase at the low pressure region as AFM-I).  $T_{\text{AFM}}$  and  $T_{\text{SP}}$  are nearly an order of magnitude lower than  $T_{\text{CO}}$  near the low pressure region of the phase diagram. On the other hand, a single transition from the metallic state to the AFM-II state occurs at the high pressure region.

One goal of the present work is to review theoretical works that have attempted to explain the phase diagram, including the temperature dependence and the evolution from the left to the right along the pressure (interchain interaction) axis. As of now though the evolution to the superconducting state still remains a mystery, and much of the theoretical work on the superconducting phase is independent of other works on the spatial broken symmetry states. We believe, however, that a correct theoretical approach should be able to explain the evolution of the SC state from the semiconducting states. Since the SC state is largely believed to be spin singlet, a strong emphasis is placed in this review to understand the transitions between the two AFM states and the singlet SP state, as the mechanisms of these AFM–spin singlet transitions may hold the key understanding the mechanism of the transition to SC. A recent

Material	$\rho$	$\chi$ enhanced?	$4k_F?$
MEM(TCNQ) <sub>2</sub>	0.5	yes <sup>a</sup>	yes <sup>a</sup>
DEM(TCNQ) <sub>2</sub>	0.5	yes <sup>b</sup>	yes <sup>b</sup>
Qn(TCNQ) <sub>2</sub>	0.5	yes <sup>c</sup>	yes <sup>d</sup>
TMTSeF-DMTCNQ	0.5	?	yes <sup>d</sup>
TMTTF-bromanil	0.5	yes <sup>e</sup>	?
TMTTF-chloranil	~0.54	yes <sup>e</sup>	?
TMTTF-TCNQ	~0.55	yes <sup>f</sup>	yes <sup>e</sup>
TMTSeF-TCNQ	0.57	yes <sup>f</sup>	no <sup>d</sup>
TTF-TCNQ	0.59	yes <sup>f</sup>	yes <sup>g</sup>
NMP <sub>x</sub> (Phen) <sub>1-x</sub> TCNQ			
0.5 ≤ x ≤ 0.57	0.5 – 0.57	yes <sup>h</sup>	yes <sup>h</sup>
0.67 ≤ x ≤ 1	0.57 – 0.67	no <sup>h</sup>	no <sup>h</sup>
TSeF-TCNQ	0.63	no <sup>f</sup>	no <sup>g</sup>
HMTTF-TCNQ	0.72	no <sup>i</sup>	no <sup>g</sup>
HMTSeF-TCNQ	0.74	no <sup>f</sup>	no <sup>g</sup>
TTF-Br <sub>0.79</sub>	~0.79	no <sup>j</sup>	no <sup>j</sup>
HMTSeF-TCNQF <sub>4</sub>	1.0	yes <sup>k</sup>	...
HMTTF-TCNQF <sub>4</sub>	1.0	yes <sup>l</sup>	...

Table 1. Summary of the properties of several quasi-1D CTS in the density range  $0.5 \leq \rho \leq 1$  [32].

suggestion that like the AFM phases there also exist two different SP states with different charge occupancies and bond distortions that are separated by a phase boundary, has however been shown to be incorrect [102–104].

Recent experimental works have shown that the phase diagram in Fig. 6 is less universal than it was originally believed to be. There exist several quasi-1D 2:1 cationic materials that actually *do not* lie in any of the regions of the phase diagram Fig. 6. Summaries of experimental results on several of these “non-traditional” quasi-1D systems are presented in Section 4.3. In the (TMTCF)<sub>2</sub>X series charge and spin transitions are separated in high and low temperature scales, with spin order (either AFM or SP) only occurring at low (<20 K) temperature. In the materials discussed in Section 4.3, there are in contrast examples of high temperature spin gap transitions, and others where the charge and spin gaps occur *simultaneously* at high temperatures. (BCPTTF)<sub>2</sub>X, X = PF<sub>6</sub> and AsF<sub>6</sub>, exhibits a magnetic transition at a temperature (30 K) significantly higher than T<sub>SP</sub> in the Fabre salts, without going through a CO phase. In (EDO-TTF)<sub>2</sub>X T<sub>MI</sub> coincides with the spin gap transition at approximately 270 K; rather than a traditional second-order SP transition, the transition in (EDO-TTF)<sub>2</sub>X is strongly first order.

While some of these unusual characteristics and details of the thermodynamics may require the inclusion of 3D interactions and anion coupling, we argue below that much *can* be understood from the underlying 1D strongly-correlated electron model. In particular, in Section 3.2.1 we show that the ...1100... CO can coexist with two *different* bond distortion patterns, BCDW-I and BCDW-II. Numerical calculations (Section 3.3) show that depending on the strength of e-e and e-p interactions, the magnitude of the CO varies by an order of magnitude, which greatly changes the magnitude of co-operative effects like anion coupling. In Section 3.3.2 we discuss the reason different thermodynamics are expected for BCDW-I and BCDW-II.

### 3.1. Theoretical model and parameters

The theoretical model appropriate for the complete families of the above materials incorporates single chain and interchain interactions, as well as interaction with the counterions. As we are not interested in material-specific behavior we ignore the interaction with counterions and write the Hamiltonian as

$$\begin{aligned}
 H = & - \sum_{v,(ij)_v} t_v (1 + \alpha_v \Delta_{ij}) B_{ij} + \frac{1}{2} \sum_{v,(ij)_v} K_\alpha^v \Delta_{ij}^2 \\
 & + g \sum_i v_i n_i + \frac{K_g}{2} \sum_i v_i^2 + U \sum_i n_{i\uparrow} n_{i\downarrow} + \frac{1}{2} \sum_{\langle ij \rangle} V_{ij} n_i n_j.
 \end{aligned} \tag{7}$$

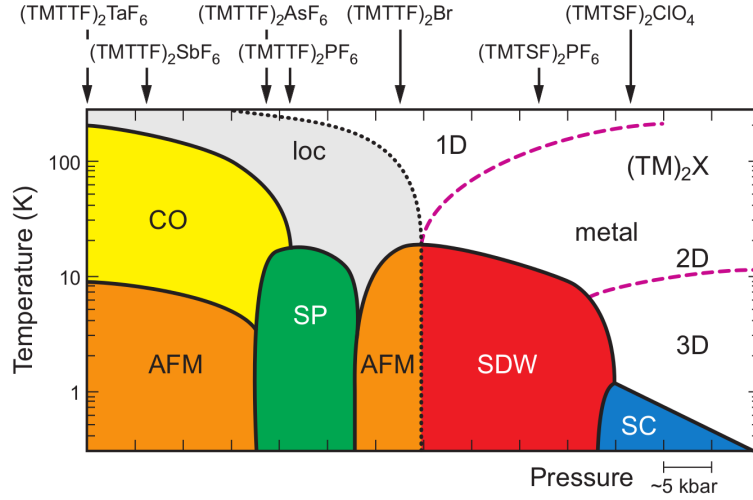


Figure 6. Phase diagram proposed by Jerome for the TMTTF<sub>2</sub>X and TMTSF<sub>2</sub>X. Arrows indicate the ambient pressure position of several materials. Reprinted with permission from Ref. [101], © 2011 The American Physical Society.

In Eq. 7,  $\nu$  runs over multiple lattice directions  $a$ ,  $b$  and  $c$  (with the stacking axis along the  $a$  direction in most of the quasi-1D materials).  $B_{ij} = \sum_{\sigma} (c_{i\sigma}^{\dagger} c_{j\sigma} + H.c.)$ ,  $\alpha_{\nu}$  is the intersite e-p coupling,  $K_{\alpha}^{\nu}$  is the corresponding spring constant, and  $\Delta_{ij}$  is the distortion of the  $i$ - $j$  bond, to be determined self-consistently;  $v_i$  is the intrasite phonon coordinate and  $g$  is the intrasite e-p coupling with the corresponding spring constant  $K_g$ . For the Fabre salts it is generally accepted that  $t_a \approx 0.1 - 0.2$  eV  $\gg t_b \gg t_c$  [22], while in the TMTSF  $t_a$  is larger and  $t_b \sim 0.1t_a$ . We will henceforth write  $t_a$  and  $t_b$  as  $t$  and  $t_{\perp}$ , respectively. Additional interesting roles played by frustration may be relevant [102]; we postpone discussions of these until later. Because of the strong anisotropies, we will consider only unidirectional SSH electron-phonon coupling ( $\alpha_{\nu}, K_{\nu} = 0$  for  $\nu \neq a$ ). Based on the strong  $\rho$ -dependent experimental behavior in the family of CTS overall (see Section 2.5) we retain only the NN intersite Coulomb interactions, which we will write as  $V$  and  $V_{\perp}$ , respectively (note that longer range interactions wipe out the  $\rho$ -dependence of correlation effects [105]). The onsite Hubbard repulsion  $U$  ranges from 0.6 - 1.0 eV. This implies  $U/t \sim 6 - 10$  in the TMTTF, with the ratio about half in TMTSF. The magnitude of  $V$  is less certain, but based on the fact that  $\frac{1}{2}$ -filled band materials are Mott-Hubbard semiconductors,  $V < \frac{1}{2}U$  (since otherwise  $\frac{1}{2}$ -filled systems would have been charge-ordered.) Based on other experiments (see Section 4) we believe that  $\frac{U}{4} \leq V \leq \frac{U}{3}$ .

The Hamiltonian in Eq. 7, especially the 1D version of it, has been investigated at  $\rho = \frac{1}{2}$  using a variety of approaches including mean-field [106–110], bosonization [111–116], exact diagonalization [81, 82, 102, 117–125], quantum Monte Carlo (QMC) [34, 78, 80, 83, 126–130] and the Density Matrix Renormalization Group (DMRG) [131–136]. Mean-field approaches ignore quantum fluctuations and in general overemphasize the AFM and the WC broken symmetries, thereby missing the subtleties associated with the transition to spin singlet states, which is a quantum effect. We will not discuss the mean-field and related approaches. Bosonization ignores the discrete nature of the lattice and thus in most cases miss the coexistences of various broken symmetries; it is also a weak coupling approach, while the strong e-e interactions in the CTS demand a strong coupling approach. The two separate requirements of retaining the lattice discreteness and the strong coupling are met only by numerical approaches, and we will largely limit ourselves to discussions of these.

Numerical approaches suffer from one serious disadvantage, in that they are often for relatively small systems (especially those results that are obtained through exact diagonalizations). Proper finite size scaling of numerical results is then crucial for obtaining the extrapolated behavior of the physical system in the thermodynamic limit. This is, however, often very difficult or even impossible, as strong e-e interactions can preclude calculations for several different system sizes, which is essential for finite size scaling. QMC and DMRG have their own difficulties (for example, self-consistent solutions to the e-p interactions can be a problem using these approaches) and are even less useful when lattice frustration plays a strong role. These limitations can make it difficult to determine whether a

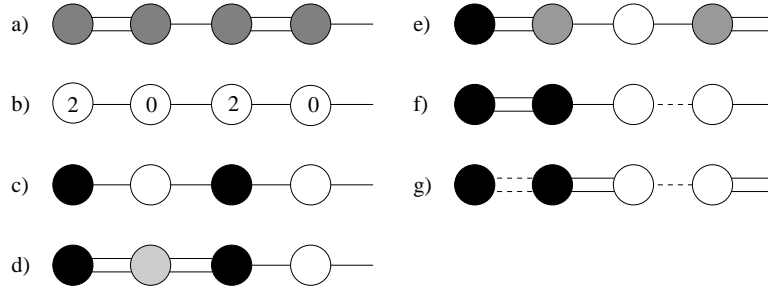


Figure 7. Broken symmetry states in 1D. (a)  $\rho = 1$   $2k_F$  BOW and  $\rho = 1$   $4k_F$  BOW, both with uniform charge. (b)  $\rho = 1$   $2k_F$  CDW. Numbers here indicate site charge occupancy. (c)  $\rho = \frac{1}{2}$   $4k_F$  CDW (d)  $\rho = \frac{1}{2}$   $4k_F$  CDW-SP (e)  $\rho = \frac{1}{2}$   $2k_F$  CDW (f)  $\rho = \frac{1}{2}$  BCDW-II (g)  $\rho = \frac{1}{2}$  BCDW-I. Lines indicate bond strength with double lines stronger than single and dashed bonds, respectively. In (c)-(g) black (white) circles indicate sites with charge density  $0.5 + \frac{1}{2}\Delta n$  ( $0.5 - \frac{1}{2}\Delta n$ ).

given broken symmetry that is found from numerical calculations is unconditional or not (an unconditional transition is one which occurs for infinitesimally small values of the coupling constants  $\alpha$  and  $g$  in the thermodynamic limit; finite systems with discrete energy gaps between states give broken symmetries only for nonzero coupling constants.) In general only unconditional transitions are expected in the physical systems. While conditional transitions that occur only for couplings above specific threshold values may also occur in a real system, it is necessary to prove in such cases that the couplings in the real system do exceed the required threshold values. This is also a difficult task within correlated-electron models. In view of the above, prior to presenting the numerical data we develop physical heuristic ideas of the unconditional broken symmetries that might be expected within Eq. 7 for  $\rho = \frac{1}{2}$  in the thermodynamic limit. Agreement between the heuristic ideas and numerical results may be considered a criterion for essential correctness of both.

### 3.2. Spatial broken symmetries - configuration space based physical ideas

There are reasons beyond justifying numerical results to develop physical ideas concerning spatial broken symmetries in correlated-electron materials. First, the alternative physical explanations are usually couched in the language of Peierls instability, with nesting as the condition for lattice or magnetic instability. This is a strictly one-electron theory and does not apply to the many-electron Hamiltonian of Eq. 7. The effect of e-e interactions are understood best in configuration space. Second, as we show below, coexisting, or even co-operative interactions between broken symmetries are most easily understood within the configuration space picture (by co-operative we refer to the situation where a given interaction enhances two or more coexisting broken symmetries simultaneously). Below we first discuss the 1D limit. The AFM phases are not obtained in this limit even at  $T=0$ . Transitions to spin-singlet states are possible, although 2D interactions are necessary to get the same transitions at finite temperature. Our discussions of the 1D limit will therefore be limited to charge- and bond-order only (see Fig.7). Following this we will discuss the 2D case, where the AFM phases are considered.

#### 3.2.1. The one dimensional limit

Our configuration space arguments are based on the observation that the ground state wavefunction of a broken symmetry state has unequal contributions from equivalent configurations that are related by the symmetry operator that is lost when symmetry is broken. For the sake of illustrating the usefulness of the arguments we first discuss the instabilities in  $\rho = 1$ , which is simpler to understand than any other  $\rho$ , because  $\rho = 1$  is an insulator for nonzero  $U$  and because there is minimal coexistence between the BOW and the CDW. We begin with the CO in the 2-site 2-electron molecule. The three configurations that describe the many-electron ground state wavefunction here are written as 20, 11 and 02, where the numbers correspond to site occupancies by electrons (for SU(2) symmetry the 11 is the spin-singlet combination of site occupancies). The symmetric wavefunction has equal relative weights of 20 and 02, but in the presence of broken symmetry (either because of different site energies or for very large EMV coupling  $g$ ) the relative weights will be different. This concept can be easily extended to the 4-site system, where the equivalent “extreme” configurations that are now related by symmetry but make unequal contributions to the wavefunction are 2020 and 0202. Configurations 2011 (or 1120) are closer to 2020, from which they are obtained by

a single one-electron hop, while three such hops will be necessary to reach them from 0202. One can then construct “paths” between the extreme configurations 2020 and 0202, such as:

$$2020 \rightarrow 2011 \rightarrow 1111 \rightarrow 0211 \rightarrow 0202$$

where each arrow denotes a single one-electron hop. There exist many such paths, as branching can occur at any intervening point:

$$2020 \rightarrow 2011 \rightarrow 2002 \rightarrow 1102 \rightarrow 0202$$

Due to the very short path lengths between the “extreme” configurations, configuration mixing is very efficient in finite molecules which do not exhibit unconditional broken symmetry. As the system size  $N \rightarrow \infty$ , however, the path lengths approach infinity, and in spite of the very large number of paths, the system may be “stuck” on one or other side of the symmetric configurations, thus undergoing broken symmetry. In the infinite system,  $g \rightarrow 0^+$  may therefore be sufficient to give the  $2k_F$  CDW (Fig. 7(b)) here in the limit of  $U = 0$ . The consequences of e-e interactions can now be determined from inspection of the paths alone.  $U$  diminishes double occupancies, thus making the paths “downhill” to the symmetric configurations, and therefore strongly reduces the amplitude of the CDW.

The  $2k_F$  BOW in  $\rho = 1$  (Fig. 7(a)) has in the past been of enormous interest because of its applicability to polyacetylene [137]. The extreme configurations that favor one or other bond alternation phase are now the valence bond (VB) diagrams 1–2 3–4 5–6 .... and 2–3 4–5 6–7....., in which nearest neighbors are linked by spin-singlet bonds. Charge-transfer between bonded sites which are spin-paired is necessarily stronger than that between non-bonded sites, and thus the bond-alternated wavefunction has inequivalent contributions from the above two VB diagrams. Unlike the case of the  $2k_F$  CDW, we now see that to reach one extreme VB diagram from the other, creation (as opposed to destruction) of double occupancies now becomes necessary. This creates an energy barrier along the path connecting the two extreme VB diagrams, and hence we expect the Hubbard  $U$  to enhance the bond alternation [92]. The predicted enhancement of the strength of the  $2k_F$  BOW by  $U$  has been confirmed by numerical calculations by many authors [138–141].

Other conclusions that can be drawn from the nature of these diagrams include the absence of coexistence between the BOW and the CDW in  $\rho = 1$ , since each of these broken symmetries is “favored” by extreme configurations that are different, and that are non-overlapping in the thermodynamic limit. Although we have limited ourselves to 1D in the above, in the special case of  $\rho = 1$  Coulomb effects on broken symmetries can be understood even in 2D (where AFM becomes relevant) using similar arguments [142]. The idea that the pattern of broken symmetry and that the effects of e-e interactions can be predicted from configuration space based physical ideas has a firm basis.

The situation is much more complicated for  $\rho \neq 1$ , which can be conductors even for nonzero  $U$  in the absence of spatial broken symmetry. Further, unlike in  $\rho = 1$ , we will see that coexistence of BOW and CDW is now the norm.

$\rho = \frac{1}{2}$ ,  $U = 0$ . There are three classes of configurations that constitute the wavefunction of the  $\rho = \frac{1}{2}$  unit cell: 2000 (class I), 1100 (class II) and 1010 (class III). There are four each of the first two (related to one another by  $C_4$  symmetry) but only two of the last (related by  $C_2$ ). At  $U = 0$  all individual configurations are equally preferred, which means that classes I and II with larger multiplicities each make larger contributions to the wavefunction than the class III configurations. Breaking of spatial symmetry at  $U = 0$  then involves either class I or II configurations. Loss of  $C_4$  symmetry, which generates  $2k_F$  periodicity, implies that the four configurations  $\dots 2000 \dots$ ,  $\dots 0200 \dots$ ,  $\dots 0020 \dots$  and  $\dots 0002 \dots$  within class I make unequal contributions to the ground state wavefunction. The  $2k_F$  broken symmetry can also involve the class II configurations, and the two competing broken symmetries are described by different phase angles (see below).

There are two inequivalent charge-poor sites labeled ‘0’ in  $\dots 2000 \dots$  distinguished by their distances from sites labeled ‘2’. For nonzero  $t$  there is significant charge-transfer across the 2-0 bonds and very little across the 0-0 bonds. Thus if  $2k_F$  instability involving class I configurations dominates we expect strong co-operative coexistence between the  $2k_F$  CDW (with charge modulations of charge-rich, intermediate charge, charge poor, intermediate charge) and  $2k_F$  BOW with bond strength modulations SSWW (S =strong, W = weak), as shown in Fig. 7(e). The charge-rich (and charge-poor) sites in  $\dots 1100 \dots$  are completely equivalent. The bond strengths will be modulated within this CDW also: at  $U = 0$  charge-transfer across the 1–1 bond occurs in both directions, while in the 1–0 bond this is in one direction only. Thus type II  $2k_F$  instability will give  $2k_F$  CDW with charge modulation charge-rich, charge-rich, charge-poor, charge-poor and bond strength modulations SMWM (S =strong, M= medium, W = weak) as shown in

Fig. 7(f). The two broken symmetries are mutually exclusive, and both correspond to Peierls  $2k_F$  CDWs, with charge densities on sites  $n$  given by  $\rho_n = \bar{\rho} + \rho_0(\cos 2k_F n + \theta)$ , where  $\bar{\rho} = \frac{1}{2}$  and  $\theta = \pi/2$  and  $\pi/4$ , respectively. From the physical arguments alone there is no way to predict which of the two CDWs wins at  $U = 0$ . Actual calculations indicate that 2000 dominates over 1100 at  $U = 0$ , but barely [93].

*Weak to intermediate U, weak V.* We imagine increasing  $U$  slowly from zero, in the  $V = 0$  limit initially. The near degeneracy between  $\dots 2000 \dots$  and  $\dots 1100 \dots$  that exists at  $U = 0$  is quickly destroyed by  $U$  and  $\dots 1100 \dots$  begins to dominate. We will refer to the coexisting BOW and CDW – a Bond-Charge Density wave (BCDW) – as the  $2k_F$  BCDW-II (Fig. 7(f)) [34, 118, 130], to distinguish it from a second BCDW that appears at stronger correlations (see below). As the above arguments indicate, the appearance of the BCDW-II phase *does not* need non-convex intersite Coulomb interaction ( $V_1 < 2V_2$ , where  $V_1$  and  $V_2$  are NN and NNN interactions, respectively), as has sometimes been claimed [143]. Non-convex Coulomb potentials are unrealistic, as they require screening at short range to be larger than that at long range. Our arguments above show that the BCDW-II can be driven by a *quantum effect*, the tendency to form nearest neighbor spin-singlets.

As  $U$  is increased further, charge-transfer across the 1-1 bond, which creates a double occupancy, will gradually get weaker, while the 1-0 bond gets relatively stronger at the expense of the 1-1 bond strength. There will thus be a gradual cross-over where at the end point is the  $2k_F$  BCDW-I, with the bond strengths now SW'SW ( $S = \text{strong}$ ,  $W = \text{weak}$ ,  $W' = \text{weak bond stronger than } W$ ), where the  $S$ ,  $W'$  and  $W$  bonds corresponding to 1–0, 1–1 and 0–0 bonds, respectively (see Fig. 7(g)). The longer bond length between the charge-rich sites implies that the crossover from the BCDW-II to the BCDW-I is facilitated by nonzero  $V$  for each  $U$ . Note that the BCDW-II and I are the two extreme distortion patterns, with the BCDW-II dominating at small  $U$  and BCDW-I at large  $U$ .

*Large U, moderate V.* This parameter region has been investigated much more widely. As already pointed out in Section 2.2, in the  $U \rightarrow \infty$  limit the system effectively mimics a band of 1D spinless Fermions. In the limit of  $\alpha$ ,  $g \rightarrow 0$ , but nonzero  $V$ , the Hamiltonian of Eq. 7 reduces to the effective Hamiltonian,

$$H_{\text{eff}} = V \sum_i n_i n_{i+1} - t \sum_i (a_i^\dagger a_{i+1} + a_{i+1}^\dagger a_i) \quad (8)$$

where as in Eq. 3 the  $a_i^\dagger$  create spinless Fermions and  $n_i = 0, 1$  only. For large  $V$ , the ground state now is the  $4k_F$  CO  $\dots 1010 \dots$ . Jordan-Wigner transformation converts the effective Hamiltonian Eq. 8 to the XXZ spin Hamiltonian with  $J_z = V$  and  $J = 2|t|$ . The AFM solution to the spin Hamiltonian corresponds to the  $4k_F$  CO in the particle language, and from exact Bethe ansatz solution of the spin Hamiltonian it is ascertained that the CO ground state is obtained only for  $V > V_c = 2|t|$ . For  $V < V_c$  the system is a Luttinger liquid (LL) [144, 145] (see [146] for a review of Luttinger liquids).

The exact result in the particle language is an entropy effect that can also be understood physically, from the perspective of the extreme configurations  $\dots 1010 \dots$  and  $\dots 0101 \dots$  and the paths connecting them. The first few steps of one such path are given below. The very first step creates a pair of nearest neighbor occupancies “11” (and a pair of vacancies “00”) and costs an initial energy  $V$ , but further electronic motion is barrierless:

$$\dots 1010101010 \dots \rightarrow \dots 1010011010 \dots \rightarrow \dots 1010010110 \dots \rightarrow \dots 1001010110 \dots$$

Band-like motion of the occupied pair “11” and the unoccupied pair “00” occurs after the first step, where each pair moves over two lattice sites, giving an approximate energy dispersion  $E_k = V - 2|t| \cos(2k_1 a) - 2|t| \cos(2k_2 a)$ ,  $k_1 + k_2 = k$ . The schematic energies of the CO state and of the excited band shown in Fig. 8(a), where a charge gap appears only for  $V \geq 2|t|$ .

The point of constructing the above argument for a case where the exact solution is available is to extend it to the *finite U* case. In addition to the paths between the two extreme CO configurations that are of the type indicated above, involving only single occupancies and vacancies, for finite  $U$  there will occur additional paths in which the intermediate configurations also possess double occupancies. The large number of such configurations increases the bandwidth due to the “excited” configurations rapidly, and we expect  $V_c(U)$  to increase as  $U$  decreases from infinity (see Fig. 8(b)).

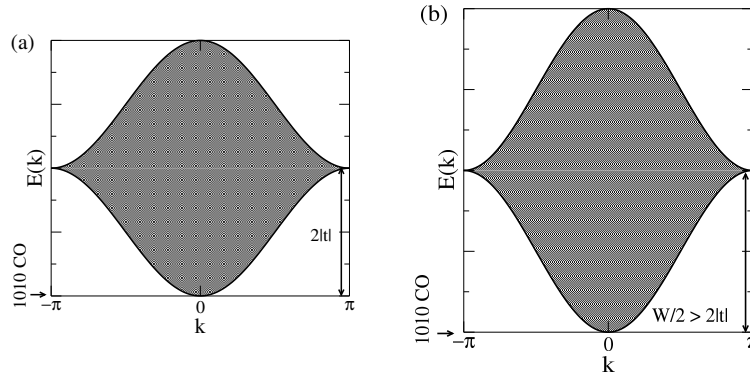


Figure 8. (a) Schematic of the energy spectrum of the spinless Fermion Hamiltonian at  $V = 2|t|$  (Eq.8). The band center is at  $E = V$ , the energy required to create one dimer. Above the  $\cdots 1010 \cdots$  CO, there is a continuum due to the band motion of the 1-1 and 0-0 dimers (see text). The width of this band is half that of a free electron band since each hop of the dimer takes it through two lattice sites. The width of the energy spectrum is fixed by  $|t|$  alone and hence an energy gap develops for  $V > W/2$ . (b) Schematic of the energy spectrum for finite  $U$ . Now the CO configuration is the same as before but the width of the total energy dispersion is larger due to the much larger number of additional configurations with double occupancies excluded in the spinless Hamiltonian.

*Spin dependence of  $V_c(U)$  and implication.* Within the 1D EHM,  $E(S) < E(S + 1)$ , where  $E(S)$  is the lowest energy in the spin subspace  $S$ . Fig. 8(b) in the above then corresponds to the case of total spin  $S = 0$ . One can visualize solving the Hamiltonian separately for each different spin subspace, and determining numerically  $V_c(U)$  for each  $S$ .  $V_c$  is clearly spin dependent, as Fig. 8(a) continues to be valid for the ferromagnetic subspace  $S = S_{max}$  even for finite  $U$ , since double occupancies are not possible in this subspace. We therefore conclude that  $V_c(U, S_{max}) < V_c(U, S = 0)$ . Our discussion of the entropy effect for finite  $U$  shows that the entropy effect increases with the probability of double occupancy, which decreases monotonically with increasing  $S$ . The total number of configurations in any spin subspace decreases with increasing  $S$  which implies that the width of the continuum in Fig. 8(b) decreases with increasing  $S$ . It is then possible to interpolate between the two extreme cases of  $S = 0$  and  $S = S_{max}$  and to conclude that  $V_c(U, S) > V_c(U, S + 1)$ . This spin-dependence implies a *temperature dependence*, since in the temperature regime  $T_{2k_F} < T < T_{4k_F}$  the excitations of the EHM are predominantly spin excitations, and hence the partition function and free energy are dominated more and more by high spin states as the temperature increases from  $T_{2k_F}$ . The consequences for the transitions in the real materials are then as follows.

The charge-gapped state below  $T_{4k_F}$  in  $\rho = \frac{1}{2}$  systems with moderate to large  $U$ ,  $V$  is understood within the spinless Hamiltonian of Eq. 8, in the presence of nonzero  $\alpha$  and  $g$ . The effective  $\frac{1}{2}$ -filled band, depending upon the value of  $V$  in the real system, will undergo transition to the site-diagonal CO  $\cdots 1010 \cdots$  (Fig. 7(c), for  $V > 2|t|$ ) or to the state with  $4k_F$  BOW (Fig. 7(a) with  $\rho = \frac{1}{2}$ , for  $V < 2|t|$ ), with alternating short and long bonds (the  $4k_F$  BOW is sometimes referred to as the Dimer Mott insulator [132, 147]). The evolution from the charge- or bond-alternated phase to the SP phase is, however, nontrivial. The straightforward scenario is that the nature of the SP phase below  $T_{2k_F}$  is predetermined already at  $T_{4k_F}$  by the nature of the high temperature phase. Within this scenario the  $4k_F$  CO phase upon cooling undergoes SP transition to a state in which the overall charge distribution remains nearly the same, and the bonds between the charge-rich sites alternate (hereafter  $4k_F$  CO-SP state, Fig. 7(d)) [132]. Similarly, the dimer units within the  $4k_F$  BOW phase move closer or further apart from one another below the SP transition. In this case the larger spin exchange between NN sites on dimers that are closer to one another leads to larger charge densities, as is shown in Fig. 7(g). In addition to these straightforward evolutions the spin dependence of  $V_c(U)$  requires that there exists a third possibility, wherein the  $4k_F$  CO upon cooling evolves into the  $2k_F$  BCDW-I instead of the  $4k_F$  CO-SP state. This will occur in experimental systems in which the material parameter  $V$  is greater than  $2|t|$  but less than  $V_c(U, S = 0)$ . We will discuss all possible cases in Section 4.

*BCDW-II.* While the CO in BCDW-I and BCDW-II is identical, their bond patterns are different [130]. Importantly, the location of the singlet bond is different, being intra-dimer in BCDW-II (Fig. 7(f)) and inter-dimer in BCDW-I (Fig. 7(g)) [34, 130]. As discussed above, in systems where the ground state is BCDW-I, a high temperature transition

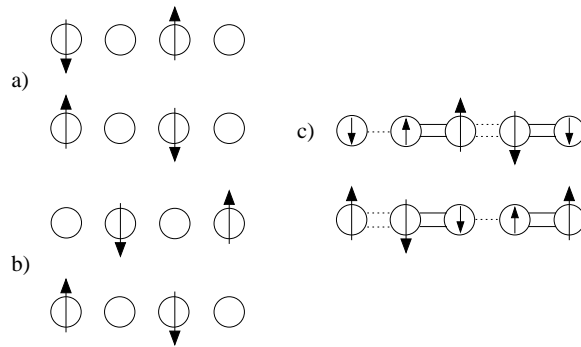


Figure 9. (a)-(b) AFM configurations possible between weakly coupled 1D chains with  $\dots 1010\dots$  CO (c) AFM coexisting with  $\dots 1100\dots$  BCDW.

to either  $4k_F$  BOW or  $4k_F$  CO is expected above the SP transition. When the high temperature state is the  $4k_F$  BOW, the low temperature  $2k_F$  BCDW-I can be intuitively understood as a “second dimerization” of a dimer lattice, with inter-dimer bonds alternating between W and W' [128]. However, the bond distortion of BCDW-II *cannot* be visualized in this manner. Instead, if an effective  $\frac{1}{2}$ -filled band dimer model is constructed for BCDW-II, the dimer occupations follow the  $\rho = 1$  CDW pattern  $\dots 2-0-2-0\dots$ . Within such an effective model there would be a single transition from uniform charge to this CO state.

Other key differences between BCDW-I and BCDW-II can be seen in results of numerical calculations that include both e-e and e-p interactions (see Section 3.3.2). In BCDW-I the amplitude of the CO is always small. However, in BCDW-II, depending on the e-e and e-p parameters, the CO amplitude can become very large. With the singlet forming at the strongest (intra-dimer) bond in the chain, larger spin gaps are expected in BCDW-II. When the CO and BOW amplitude becomes very large, the separation of the energy scales of  $4k_F$  and  $2k_F$  distortions that give low and high temperature transitions can then possibly break down in the BCDW-II case [130]. As we discuss in Section 4.3, for several 1D  $\rho = \frac{1}{2}$  CTS such as (EDO-TTF) $_2$ X, a *single* coupled MI and spin-gap (SG) transition is found at remarkably high temperatures. The measured bond distortion pattern in several of these materials follows that of BCDW-II, and large CO amplitudes are also found.

### 3.2.2. Weak two dimensional interactions

AFM becomes relevant for nonzero interchain Coulomb interactions and carrier hopping. The crystal structure of (TMTCF) $_2$ X is such that frustration also plays a role. The AFM configurations can be derived from both the charge occupancies  $\dots 1010\dots$  and  $\dots 1100\dots$ . Even with the single chain site charge occupancies  $\dots 1010\dots$  there are two distinct possibilities, as shown in Fig. 9(a) and (b), respectively. As we will see in the next subsection, charge occupancy  $\dots 1010\dots$  is most relevant at the left end of the phase diagram in Fig. 6. The correct 2D site occupancy for the AFM configurations in Figs. 9(a) and (b) is therefore the one which evolves naturally to the spin singlet SP state as interchain interactions are increased. Fig. 9(c) shows the AFM configuration with site charges  $\dots 1100\dots$ . In this AFM configuration the total charge within each dimer (sites connect by double lines in Fig. 9(c)) is one, which is however distributed unequally between the two sites comprising the dimer. Note that in this case AFM is expected to coexist with lattice distortion, as indicated in the Figure. We have termed the combined BCDW and AFM state of Fig. 9(c) a Bond-Charge Spin Density Wave (BCSDW) [128].

### 3.3. Numerical Results

In this section we review numerical results in one dimension for  $\rho = \frac{1}{2}$  and for weakly coupled  $\rho = \frac{1}{2}$  chains.

#### 3.3.1. One dimensional extended Hubbard model

In the absence of e-p interactions, the zero temperature phase diagram of Eq. 5 in one dimension in the range of parameters appropriate for quasi-1D CTS is by now well characterized. The onsite Coulomb interaction  $U/|t|$  is expected to be in the range of 6–8 [129]. Based on comparison with quasi-1D  $\rho = 1$  CTS, where a CDW driven by V with pattern  $\dots 2020\dots$  (Fig. 7(b)) does *not* occur, it is expected that  $V < U/2$  [129].

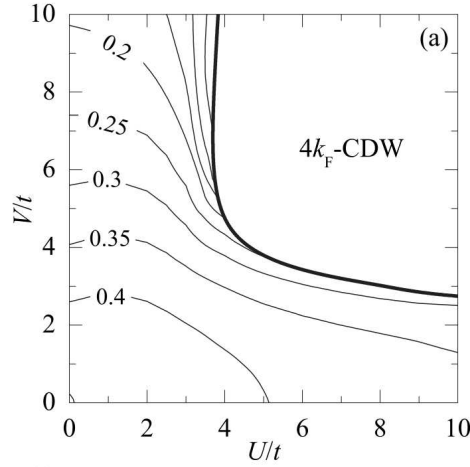


Figure 10. (color online) Zero temperature phase diagram of the 1D extended Hubbard model Eq. 5 in one dimension at  $\rho = \frac{1}{2}$ , as determined from DMRG calculations of up to 60 sites. Contours show the values of the LL exponent  $K_\rho$ . Reprinted with permission from Ref. [136], © 2009 The American Physical Society.

Except in the  $\cdots 1010 \cdots$  WC phase when  $V > V_c$ , the low energy properties of Eq. 5 are those of a LL [144–146]. The phase diagram may then be mapped out by calculating the LL correlation exponent  $K_\rho$ , which determines the asymptotic form of the charge and spin correlations [146]. For  $K_\rho < \frac{1}{3}$ ,  $4k_F$  charge correlations are more divergent than  $2k_F$  charge correlations, and for  $K_\rho = \frac{1}{4}$  the insulating  $\cdots 1010 \cdots$  phase is reached [146]. This phase boundary has been mapped out using exact diagonalization [81, 82, 120, 123], QMC [83], and DMRG [133, 136] methods. Fig. 10 shows the phase diagram as obtained from finite-size scaled DMRG calculations [136]. Two important limiting cases for the boundary to the  $\cdots 1010 \cdots$  phase are the large  $U$  limit, where as described above  $V_c = 2t$ , and in the limit of large  $V$ , where  $U_c = 4t$  [81].

### 3.3.2. One dimensional Peierls-extended Hubbard model

*4k<sub>F</sub> phases.* The competition of the  $\cdots 1010 \cdots$  CO with and without an accompanying bond distortion (Fig. 7(c) and (d)) with BCDW-I and BCDW-II has also been studied [83, 132]. Fig. 11 shows the ground-state phase diagram of Eq. 7 calculated with self-consistent exact diagonalization for 16 sites with  $U/t = 8$  [83]. As  $V/t$  increases, the amount of phase space with the  $4k_F$  CDW and  $4k_F$  CDW-SP phases compared to the BCDW increases (see Fig. 7). For smaller values of  $V/t$  a finite intrasite e-p coupling is required for the  $4k_F$  CDW-SP phase (see Fig. 11(a) and (b)), suggesting that the  $4k_F$  CDW-SP may not occur unconditionally (i.e. in the limit of  $0^+$  e-p interactions). Resolving this issue will require finite-size scaled numerical calculations, which to our knowledge have not been performed in this region of parameter space.

*Temperature-dependent WC-to-BCDW-I transition.* In a 1D electron system no phase transitions are expected except at zero temperature. However, once 2D and 3D interactions and coupling to the anions are included, finite-temperature phase transitions must result, as demonstrated by Fig. 6. To include these additional interactions is simply not feasible without making uncontrolled assumptions as in mean-field approximations. However, information as to the relative order in temperature of different transitions can still be determined by examining the excited states of the purely 1D system, as well as the temperature dependence of the charge and bond susceptibilities [129].

The spin dependence of  $V_c$  (see Section 3.2.1) has been verified by explicit calculations on the EHM [129]. Fig. 12(a)-(b) show calculations of  $V_c$  for a 32 site periodic ring for different  $S_z$  values. The QMC calculation method used here conserves  $S_z$  but not total  $S$ . However, the Lieb-Mattis theorem [148],  $E(S) < E(S + 1)$ , where  $E(S)$  is the energy of the lowest state in the spin subspace  $S$ , applies to the 1D EHM. Because of the absence of a magnetic field, all  $S_z$  states for a given  $S$  are degenerate, and results for the lowest state within each  $S_z$  must pertain to  $S = S_z$  [129]. The apparently larger  $V_c = 2.3t > 2t$  in Fig. 12(b) for the fully polarized  $S_z=8$  is the result of finite-size effects, which does not however change the ordering of critical  $V$ 's with  $S_z$ .

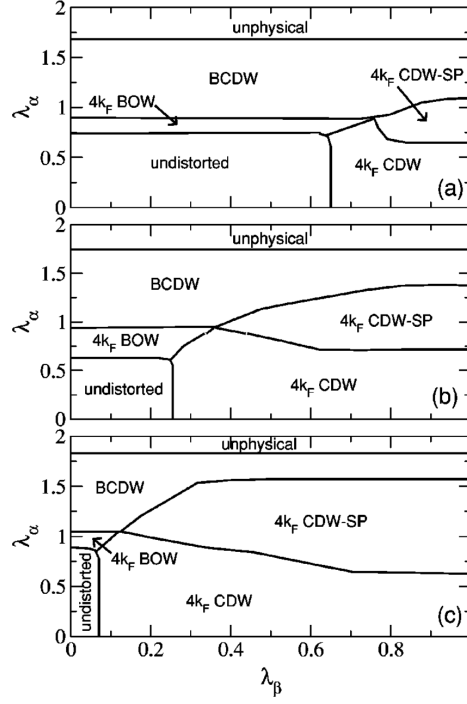


Figure 11. Phase diagram of Eq. 7 in one dimension at  $\rho = \frac{1}{2}$  from 16-site exact diagonalization calculations [83]. Here  $\lambda_\alpha = \alpha^2/(K_\alpha t)$  and  $\lambda_\beta = g^2/(K_\beta t)$  are the dimensionless inter- and intra-site e-p couplings, respectively. Parameters are  $U/t=8$  and (a)  $V/t=2$ ; (b)  $V/t=3$ ; and (c)  $V/t=4$ .

In Reference [129] temperature dependent QMC calculations were also performed for Eq. 7 with dynamic e-p interactions within the following Hamiltonian :

$$H = H_{\text{SSH}} + H_{\text{Hol}} + H_{\text{ee}} \quad (9a)$$

$$H_{\text{SSH}} = t \sum_i [1 + \alpha(a_i^\dagger + a_i)] B_{i,i+1} + \hbar\omega_S \sum_i a_i^\dagger a_i \quad (9b)$$

$$H_{\text{Hol}} = g \sum_i (b_i^\dagger + b_i) n_i + \hbar\omega_H \sum_i b_i^\dagger b_i \quad (9c)$$

$$H_{\text{ee}} = U \sum_i n_{i,\uparrow} n_{i,\downarrow} + V \sum_i n_i n_{i+1}. \quad (9d)$$

In the above,  $a_i^\dagger$  and  $b_i^\dagger$  create dispersionless SSH and Holstein phonons on the  $i$ th bond and site, respectively, with corresponding phonon frequencies  $\omega_S$  and  $\omega_H$ . The electron hopping and interaction terms are otherwise identical to Eq. 7. Figs. 12(c) and (d) show the charge and bond susceptibilities at  $2k_F$  and  $4k_F$  as a function of temperature for  $V = 2.75t$ . This value of  $V$  is between  $V(S_z = S_z^{\text{max}}) = 2t$  and  $V_c(U) \approx 3.0t$ . At high temperature,  $\chi_\rho(4k_F) > \chi_\rho(2k_F)$ , indicating that  $\cdots 1010 \cdots$  CO is favored. However, at low temperature  $\chi_\rho(2k_F) > \chi_\rho(4k_F)$ , with  $\chi_\rho(2k_F)$  and  $\chi_B(2k_F)$  becoming divergent as  $T \rightarrow 0$ , indicating that the  $\cdots 1100 \cdots$  BCDW is the ground state. This has important experimental implications, see Section 4.1.3.

*BCDW-I versus BCDW-II.* Within the semi-classical limit of Eq. 9a, the displacement of the  $i$ th site from equilibrium,  $\Delta_i$ , can be written as a superposition of  $2k_F$  (period 4) and  $4k_F$  (period 2) terms [118, 130],

$$\Delta_j = \Delta_0 [a_2 \cos(2k_F j - \phi_2) + a_4 \cos(4k_F j - \phi_4)]. \quad (10)$$

In Eq. 10,  $\Delta_0$  is the overall amplitude and the normalization condition  $a_2 + a_4 = 1$  is assumed. The phase angles are ( $\phi_2 = \frac{\pi}{2}, \phi_4 = 0$ ) for BCDW-I and BCDW-II [118, 130]. Provided ( $U, V$ ) are not close to the  $\cdots 1010 \cdots$  region of the

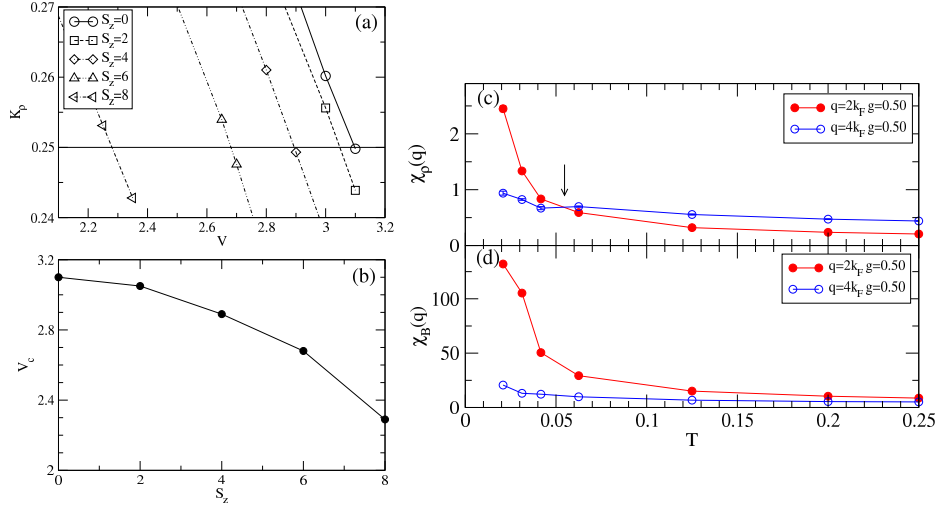


Figure 12. (a) The Luttinger liquid exponent  $K_\rho$  calculated for the EHM for  $U = 8t$  as a function of  $V$  and  $S_z$ . Results are for a 32-site periodic ring [129]. (b)  $V_c$  as determined from (a) where  $K_\rho = \frac{1}{4}$  (c)-(d) Finite-temperature QMC calculation of the charge (c) and bond (d) susceptibilities for a 64-site periodic ring as a function of temperature. Phonons are treated dynamically, with parameters  $U = 8t$ ,  $V = 2.75t$ ,  $\alpha = 0.27$ ,  $\omega_S = 0.1$ ,  $g = 0.5$ , and  $\omega_H = 0.5$  (see text). The arrow indicates where  $\chi_\rho(2k_F) = \chi_\rho(4k_F)$  [129].

electronic model, the ground state of Eq. 7 is either BCDW-II Fig. 7(f) or BCDW-I Fig. 7(g) [118, 130]. In the limit of weak e-p interactions,  $a_2/a_4$  in Eq. 10 is controlled by  $U$  and  $V$ , with stronger e-e interactions giving BCDW-I (see Section 3.2.1). In the 1D model a crossover occurs between BCDW-I and BCDW-II, shown in Fig. 13 [130].

The principal difference between BCDW-I and BCDW-II is the location of the strongest bond, which is intra-dimer in BCDW-II and inter-dimer in BCDW-I [34, 118, 130]. The amplitude of the CO coexisting with BCDW-I is of small amplitude for all choices of e-e and e-p interactions, with  $\Delta n \sim 0.1$  (we define  $\Delta n = n_{\text{large}} - n_{\text{small}}$  as the difference between the large and small charge densities) [130]. On the other hand, the CO coexisting with BCDW-II can be of very large amplitude depending on the value of the intra-site e-p coupling  $g$ , with  $\Delta n \sim 0.9$  possible for large  $g$ . Fig. 13(b)-(c) shows finite-size scaled results for  $\Delta n$  and the lattice distortion magnitude  $\Delta_0$  as a function of  $U$  and the intra-site e-p coupling [130]. Strong intra-site e-p interactions in particular can greatly enlarge the region of parameters giving BCDW-II [130].

### 3.3.3. Weakly two dimensional results

The emergence of AFM in 2D depends critically on the amount of frustration in the lattice. Numerical work shows that when 1D chains with the BCDW distortion and e-e interactions are coupled by *unfrustrated* inter-chain bonds  $t_\perp$  (see Fig. 14(a)), the result is a 2D state combining charge distortion, bond distortion, and AFM order, the BCSDW [128, 149]. The experimental relevance of this novel result is discussed in Section 4.2.

Reference [128] considered a series of rectangular lattices of coupled dimers. In Fig. 14(b)  $\Delta E$  is defined as the energy gain upon formation of the BCDW-I state from this dimer lattice, i.e. the difference in the energies of the uniformly dimerized system and the system with the BCDW-I distortion along the chains. As shown in Fig. 14(b),  $\Delta E$  per site is *greater* for the 2D system of coupled chains than for a 1D chain with the same bond distortion, *provided* e-e interactions are included. The ratio  $\Delta E/\Delta E(t_\perp = 0)$  increases rapidly above unity from  $t_\perp = 0$  through intermediate  $t_\perp$ , suggesting that the BCSDW state is favored for weak interchain interactions. In the BCSDW state the spin pattern in terms of dimers (see dotted box in Fig. 14(b)) follows the usual Néel pattern. The gain in energy over the 1D chain in the presence of interactions comes from antiferromagnetic exchange between the anti-parallel spins along the perpendicular bonds.

On a frustrated lattice, which is present in nearly all of the 2D CTS (see Section 5) and is also relevant for TMTSF under pressure, the BCSDW may no longer be the ground state. Instead, a state composed of interchain local NN singlets can become favored. We return to this possibility in Section 6.2.

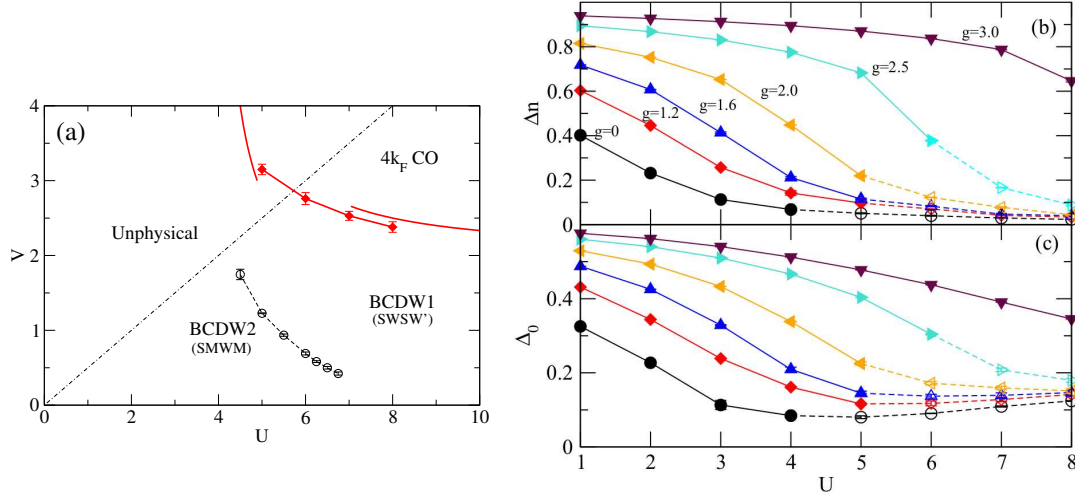


Figure 13. (color online) Left: Phase diagram of Eq. 7, for  $\rho = \frac{1}{2}$  in the limit of weak ( $\alpha = g = 0^+$ ) e-p interactions [130]. Solid lines are strong-coupling expansion results; solid symbols are QMC points where  $K_\rho = \frac{1}{3}$  (see text). Open points mark the crossover between BCDW-I and BCDW-II bond patterns. Right: Charge order amplitude  $\Delta n$  and distortion amplitude  $\Delta_0$  (see text) for the Hamiltonian of Eq. 7 at  $\rho = \frac{1}{2}$  versus  $U$ , for  $\alpha = 1.2$ ,  $K_\alpha = K_g = 2.0$ , and  $V = U/4$  [130]. Solid (dashed) lines denote parameters giving the BCDW-II (BCDW-I) bond distortion.

### 3.4. Summary

(i) Within the quarter-filled one dimensional extended Hubbard model (Eq. 5) the  $\cdots 1010 \cdots$  Wigner crystal (WC) of single electrons occurs only for the nearest-neighbor Coulomb interaction  $V > V_c(U) > 2|t|$ , and  $V_c(U)$  increases with decreasing  $U$ . (ii) The critical  $V$ ,  $V_c(U)$ , is spin-dependent with  $V_c(U, S) > V_c(U, S + 1)$ . (iii) This implies there is a range of  $V$ ,  $2|t| < V < V_c(U)$ , where at high temperature  $\cdots 1010 \cdots$   $4k_F$  charge order is accompanied at low temperature by a spin-Peierls phase that is  $\cdots 1100 \cdots$ . (iv) For weak  $t_\perp$  there exists a bond-charge-spin density wave.

## 4. Broken symmetries in quasi-one-dimensional CTS, Experiments

In spite of the significant theoretical progress achieved over the previous two decades completely consistent understanding of the spatial broken symmetries in the quasi-1D 2:1 cationic CTS has still not been reached. There are many reasons for this, the most important of which, in decreasing order of importance according to us, are given below.

(i) Not all cationic 2:1 1D materials are described by Fig. 6. The material (EDO-TTF)<sub>2</sub>X (X=PF<sub>6</sub>, AsF<sub>6</sub>), in which  $T_{MI} = T_{CO} = T_{SG}$  [150] is in a class of its own. There exist other materials in which there occurs the SP transition, but either the CO transition at a higher temperature is absent completely, or the SP transition occurs at a pressure where the CO has vanished. In all such cases  $T_{MI}$  is much larger than  $T_{SP}$ . The list here includes (TMTTF)<sub>2</sub>I [151], (BCPTTF)<sub>2</sub>X (X=PF<sub>6</sub> and AsF<sub>6</sub>) [152, 153], (*o*-DMTTF)<sub>2</sub>X (X=Cl, Br, I) [154] and (EDT-TTF-CONMe<sub>2</sub>)<sub>2</sub>X (X = AsF<sub>6</sub>, Br) [155]. In spite of their differences from the “standard” 2:1 CTS which do belong to one or more regions of the phase diagram in Fig. 6, we believe these “nonstandard” materials should also be described within a single “umbrella” theoretical viewpoint. This is attempted below within the context of the theoretical work described in the previous section, along with explicit discussions of issues that remain to be understood.

(ii) The charge difference  $\Delta n$  between charge-rich and charge-poor sites has been obtained mostly from measurements of spin-lattice relaxation time  $T_1$  and from infrared spectroscopy. Optical spectroscopy in such cases gives  $\Delta n$  that is far smaller than that obtained from  $T_1$  measurements [94, 156]. There is also disagreement between different experimental groups over whether or not  $\Delta n$  shows a significant decrease upon entering the SP phase from the CO phase [94, 156–159].

(iv) The same disagreement exists also between theoretical groups, which follows from a related but different disagreement over whether or not the SP phase can have the  $\cdots 1010 \cdots$  order [102, 103, 129].

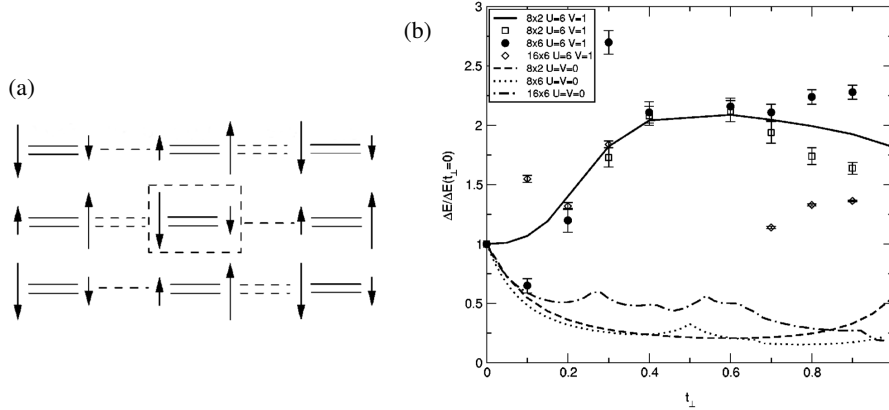


Figure 14. (a) The Bond-Charge-Spin Density wave (BCSDW) state [128]. (b) The per-site energy gained upon inter-dimer bond distortion,  $\Delta E$ , normalized to its value in 1D. The lattice is a rectangular dimer lattice with intra-dimer (inter-dimer) hopping of 1.2 (0.8) along the chains, and variable inter-chain hopping  $t_{\perp}$ . Solid lines are exact results, points are calculations using Constrained Path Monte Carlo (CPMC) [128].  $\Delta E/\Delta E(t_{\perp}=0) > 1$  over a wide range of  $t_{\perp}$  indicates that the BCSDW state of (a) is stabilized by e-e interactions.

X	$T_{\rho}$	$T_{AO}$	$T_{CO}$	$T_{SP}$	$T_N$
TaF <sub>6</sub>	?	—	175 <sup>(a)</sup>	—	9 <sup>(a)</sup>
SbF <sub>6</sub>	$\approx 240$ <sup>(b),(c),(d)</sup>	—	154–157 <sup>(e),(f)</sup>	—	8 <sup>(c),(g)</sup>
AsF <sub>6</sub>	230–250 <sup>(d),(f)</sup>	—	102 <sup>(h),(f)</sup>	13 <sup>(e),(i)</sup>	—
PF <sub>6</sub>	250 <sup>(d),(f)</sup>	—	67 <sup>(d),(f),(h)</sup>	19 <sup>(d),(e)</sup>	—
Br	$\approx 200$ <sup>(f)</sup>	—	28 <sup>(f)</sup>	—	13 <sup>(j),(k)</sup>
I	?	—	—	21 <sup>(g)</sup>	—
SCN	265 <sup>(b)</sup>	160–170 <sup>(e),(f)</sup>	—	—	7–9 <sup>(m),(n)</sup>
ReO <sub>4</sub>	290 <sup>(e),(f)</sup>	154 <sup>(e),(f)</sup>	227.5 <sup>(f)</sup>	—	—
BF <sub>4</sub>	220 <sup>(e),(f)</sup>	40 <sup>(e),(f)</sup>	83 <sup>(f)</sup>	—	—

Table 2.  $T_{\rho}$ ,  $T_{CO}$ ,  $T_{AO}$ ,  $T_{SP}$ , and  $T_N$  for different X in the series (TMTTF)<sub>2</sub>X. All temperatures are in Kelvin. (a) Reference [160], (b) Reference [161], (c) Reference [162], (d) Reference [94], (e) Reference [163], (f) Reference [164], (g) Reference [165], (h) Reference [166], (i) Reference [167], (j) Reference [168], (k) Reference [169], (l) Reference [151], (m) Reference [170], and (n) Reference [171].

In the following we discuss all of the above issues, first for the more traditional Fabre salts, then for the Bechgaard salts, and finally for the nonstandard materials mentioned in (i). Fig. 15 shows our proposed interpretation of the insulating phases in Fig. 6 [103, 129]. We discuss our interpretation of these phases in Sections 4.1–4.3 below.

#### 4.1. Traditional Fabre salts

In Table 2 we have listed the Fabre salts which are most relevant in the context of the present review. In all cases we have given the different temperatures at which the various transitions are observed.  $T_{\rho}$  is the temperature at which charge-localization, as measured from transport studies, is observed. Blanks imply that the particular state is absent in the material under consideration (AO transitions are absent in the salts with centrosymmetric anions; similarly, the CO transition does not occur in X = I, see below). Before we discuss individual materials, we point out some general trends and their implications. First, “CO” in Fig. 15 and in Table 2 refers to the  $\cdots 1010 \cdots 4k_F$  CDW. This has been confirmed from measurements of dielectric permittivity, which show giant responses at  $T_{CO}$ , indicating ferroelectricity and loss of inversion symmetry [164, 172]. We shall henceforth refer to the CO phase in Fig. 15 and in Table 2 as the ferroelectric CO (FCO), to distinguish it from the  $\cdots 0110 \cdots$  BCDW. The latter is relevant only in the case of SP and the AFM-II states (see below).

Second, given the charge carrier density of 0.5 per TMTTF, and  $T_{CO} < T_{\rho}$ , there can be only one interpretation of  $T_{\rho}$ , viz., it corresponds to the transition to the dimerized  $4k_F$  BOW state which has lost its sharpness because of the

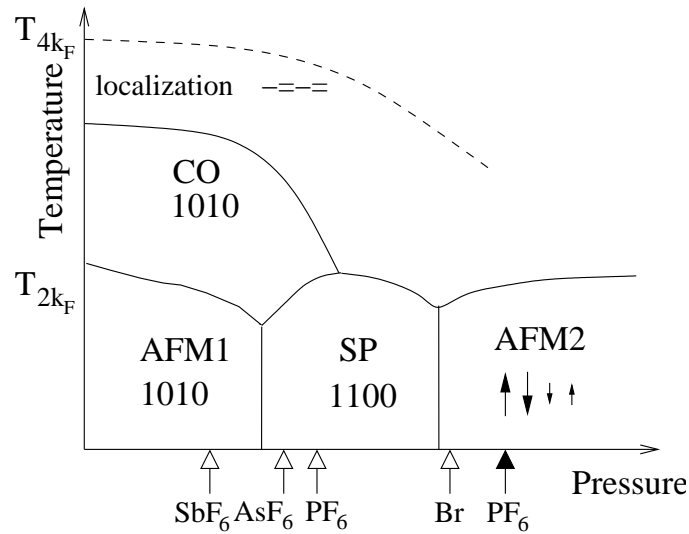


Figure 15. Schematic  $(\text{TMTSF})_2\text{X}$  and  $(\text{TMTTF})_2\text{X}$  phase diagram with proposed charge occupancies. Open (filled) arrows indicate the ambient pressure locations of TMTTF (TMTSF) salts [129].

influence of the anions. Structural data from experiments such as diffuse X-ray scattering are obscured by the intrinsic dimerization along the TMTTF stack axis that may or may not be driven by cation-anion interaction. The observed dimerizations even decrease below  $T_\rho$  in some cases, but this need not mean that the difference in the *bond orders* ( $B_{ij}$  in Eq. 7) also decreases [169]. In cases where metallic transport behavior is seen at high  $T$  in spite of crystal structure-driven dimerized structure, the bond orders of consecutive bonds must necessarily be almost equal for the charge-gap to be absent.  $T_{\text{CO}} < T_\rho$  then demonstrates that  $V$  in the real materials is less than  $V_c(U, S = 0)$ , and that the FCO transition does not result from a natural instability of the 1D chain, but from other influences.

Third, among the salts with anions of octahedral symmetry ( $\text{TaF}_6$ ,  $\text{SbF}_6$ ,  $\text{AsF}_6$  and  $\text{PF}_6$ ),  $T_{\text{CO}}$  decreases with decreasing anion size. This can be a consequence of reduced chemical pressure with large anions, which tend to give larger interstack separations. It can also indicate larger electrostatic interaction between the TMTTF molecules and larger anions, implying that the electrostatic interaction is the driving force behind the FCO transition. The strong influence of the anions on the FCO is seen most clearly from the nearly linear decrease of  $T_{\text{CO}}$  with increasing distance between the ligands of the anions (O or F) and the sulfur atom in TMTTF [94, 173]. There is then an apparent contradiction in the absence of the any kind of CO in  $X = \text{I}$ , and the observation of charge-induced instability in  $X = \text{Br}$  [169], which is smaller. As we explain below, this is due to  $(\text{TMTTF})_2\text{Br}$  belonging to the AFM-II region of the phase diagram, where the CO pattern is different from the FCO that characterizes AFM-I.

Fourth, there appears to be no correlation between  $T_{\text{CO}}$  and  $T_{\text{N}}$ . However, for the two systems where both FCO and SP transitions occur ( $X = \text{AsF}_6$  and  $\text{PF}_6$ ),  $T_{\text{SP}}$  is smaller in  $\text{AsF}_6$  with the larger  $T_{\text{CO}}$ .  $T_{\text{CO}}$  is even larger in  $X = \text{SbF}_6$ , which lies in the AFM-I region and exhibits the SP state only under pressure. In all cases therefore there is a competition between the FCO and SP phases. In the remainder of the discussions below, we will try to understand the pattern of the CO (if any) within each of the phases in Fig. 15.

#### 4.1.1. The FCO phase

Although the FCO transition was referred to as “structureless” in the earliest days [163], recent uniaxial thermal expansivity measurements in  $(\text{TMTTF})_2\text{AsF}_6$  and  $(\text{TMTTF})_2\text{PF}_6$  have found distinct lattice effects at  $T_{\text{CO}}$  [174]. The lattice effects are most dramatic along the  $c^*$ -direction, which is perpendicular to the plane containing the TMTTF molecular planes, and along which direction the TMTTF planes and the anions planes alternate. The effects are weakest along the stacking axis ( $a$ -direction) in  $X = \text{PF}_6$  and could not be measured in  $X = \text{AsF}_6$  samples, which could not sustain the strain along this direction. A peak in  $\alpha_c^*$ , the thermal expansivity along the  $c^*$ -axis is seen at  $T$  slightly above  $T_{\text{CO}}$ , with negative  $d\alpha_c^*/dT$  at higher temperatures. The anomaly in the  $c^*$ -axis thermal expansivity and the accompanying loss of inversion symmetry are believed to be due to the uniform displacement of the anions

towards the charge-rich TMTTF sites (see Fig. 4 in reference [174]). Coupling between electrons and the anion displacement field has been suggested as the driving force behind the FCO transition [121]. Bond alternation ( $4k_F$  BOW instability) within the  $4k_F$  CO phase has been suggested as an additional mechanism for ferroelectricity, as this will remove inversion symmetry too [175] (note however that if  $T_\rho$  is considered to be  $T_{MI}$  then actually the  $4k_F$  CDW is occurring here within the BOW phase and not the other way around; the symmetry-related arguments remain valid nevertheless).

#### 4.1.2. The AFM-I phase

Among the existing TMTTF salts only two materials belong in the AFM-I phase:  $X = \text{TaF}_6$  and  $\text{SbF}_6$ . Of these, the first was obtained as a consequence of a deliberate search, based on the anticipation that an octahedral anion that is even larger than  $\text{SbF}_6$  should give a complex in the AFM-I region of the phase diagram [160].  $T_{CO}$  larger than in  $\text{SbF}_6$  confirms the role of the anion in the CO formation. No pressure-dependent study of  $(\text{TMTTF})_2\text{TaF}_6$  has been carried out yet. We shall therefore focus on  $(\text{TMTTF})_2\text{SbF}_6$ , which has been taken across all the regions of the phase diagram in Fig. 15 by application of pressure (SC appears at pressure  $> 5.4$  GPa [162], which is the highest among Fabre salts with octahedral anions.)

Dielectric permittivity measurements have indicated appearance of the FCO at 157 K in  $X = \text{SbF}_6$  [164, 172]. For a long time it was assumed that  $T_{CO}$  coincides with  $T_\rho$  here [165], but the actual  $T_\rho$  is higher [173] (see also phase diagram in Fig. 9 of reference [159].) This distinction is important, as it indicates that the metal-insulator transition is likely due to bond strength alternation (as measured by actual differences in bond orders, see above), and the FCO phase occurs within the dimerized state, leaving open the mechanism of the SP transition (BCDW-I versus  $4k_F$  CDW-SP). The charge disproportionation at ambient pressure, as detected from  $^{13}\text{C}$ -NMR [159, 165], is  $\Delta n \approx 0.5$ . A significantly smaller value, 0.25 - 0.30 is obtained from infrared spectroscopy [94]. Pressure decreases  $T_{CO}$  monotonically, with  $T_{CO} \sim 110$  K at  $P = 0.5$  GPa [159] (90 K and 0.5 GPa [165]). The lowest temperature phase at ambient and low pressures is the AFM-I phase [159, 165], and  $T_N$ , like  $T_{CO}$ , decreases monotonically with pressure. Above 0.8 GPa no evidence for CO could be detected from  $^{13}\text{C}$ -NMR [159, 165]. NMR measurements indicate that the low temperature phase is the SP phase for pressure greater than 0.5 GPa [159, 165]. Taken together, all of the above suggest co-operative coexistence between the FCO and AFM-I, but competition between FCO and the SP. We believe that the lack of evidence for the FCO in the region where the SP state occurs is a signature of the  $\cdots 1100 \cdots$  BCDW nature of the SP phase, as is the observation that  $\Delta n$  decreases severely in the SP phases of  $X = \text{AsF}_6$  and  $\text{PF}_6$  (see below). Deuteration of the protons of the methyl groups in TMTTF gives  $(\text{TMTTF-d}_{12})_2\text{SbF}_6$ , in which  $T_{CO}$  is enhanced by  $\sim 20$  K [176, 177]. No simple explanation based on crystallographic structure analysis [159] seems to suffice, and an alternate explanation for this involves the Holstein e-p coupling. Specifically, the larger mass of the deuterium reduces the phonon frequency taking the system closer to the static limit.

Pressure-induced transition from the SP to the AFM-II phase in  $X = \text{SbF}_6$  at the lowest temperatures is achieved for pressure greater than 2.0 GPa [159]. We believe that the AFM-II phase is the  $\cdots 1100 \cdots$  BCSDW of Sections 3.2.2 and 3.3.3 (see Fig. 15). This is discussed further below.

#### 4.1.3. The SP phase in $X = \text{PF}_6$ and $\text{AsF}_6$

The spin-gapped states in the Fabre salts occur in the higher chemical pressure region of the phase diagram in Fig. 15, relative to the AFM-I phase. This suggests greater 2D character in the spin-gapped systems than in the AFM systems, which appears to contradict the conventional wisdom that the SP transition is associated with one-dimensionality and antiferromagnetism with two dimensionality. This has led Nakamura *et al.* to argue that the spin-gapped states here are not true SP states [151, 159]. It is our belief that this discussion is largely semantic: while it is true that weak 2D interactions stabilize the SP state against the AFM-I in the Fabre salts, *the singlet spin-bonded sites lie on the same stack in these systems*, as has been confirmed from elastic neutron-scattering studies in  $(\text{TMTTF})_2\text{PF}_6$  [178]. While frustration-induced interchain interactions, over and above the 1D e-p interactions, may indeed contribute to the driving of the transition from the AFM to the spin-gapped state, the occurrence of the spin-paired sites on the same chain ensures that the dominant spin excitations are also 1D. The overall physical behavior should therefore resemble that of the standard SP systems. The intensity of the neutron scattering from  $(\text{TMTTF})_2\text{PF}_6$ , compared to that in  $(\text{BCPTTF})_2\text{PF}_6$  is, however, very weak, indicating small amplitude of the SP stack distortion [178]. This may indeed be a consequence of 2D interactions, although other possibilities exist, as discussed below.

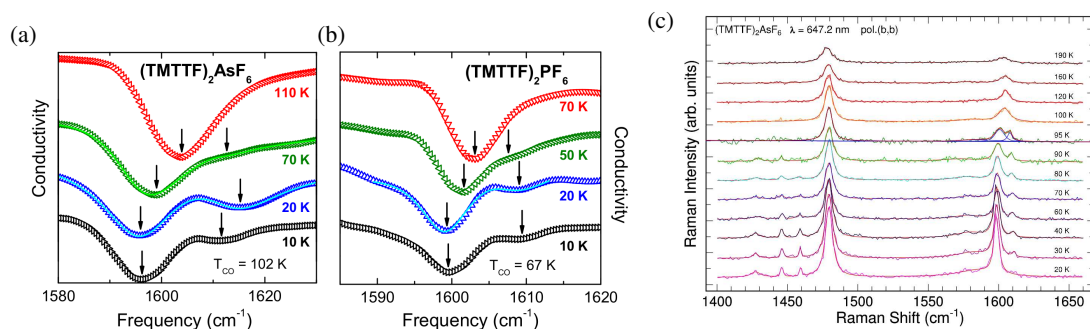


Figure 16. (color online) Mid-infrared conductivity of (a)  $(\text{TMTTF})_2\text{AsF}_6$  and (b)  $(\text{TMTTF})_2\text{PF}_6$  for light polarized parallel to the molecular stacks. The arrows indicate the positions of the anti-resonance dips.  $T_{\text{SP}} = 19$  K for  $\text{PF}_6$  and 13 K for  $\text{AsF}_6$ . (c) Raman spectra of  $(\text{TMTTF})_2\text{AsF}_6$  as a function of temperature. The  $\nu_3(\text{ag})$  mode splits below  $T_{\text{CO}} = 102$  K. Reprinted with permission from Ref. [94] under CC BY.

The patterns of the CO in the SP phases  $X = \text{PF}_6$  and  $\text{AsF}_6$  have been the most contentious [102, 129]. The high temperature broken symmetry is certainly the FCO state [164, 172]. As with  $X = \text{SbF}_6$  there is disagreement over the amplitude of the CO.  $\Delta n$ , as obtained from  $T_1$  studies in  $^{13}\text{C}$  NMR (0.30 - 0.50 in  $X = \text{AsF}_6$  [157, 167] and 0.28 in  $\text{PF}_6$  [158]) are considerably larger than those obtained from infrared spectroscopy, 0.20 - 0.25 and 0.10 - 0.15, respectively [94]. Even smaller  $\Delta n$  in  $X = \text{AsF}_6$  ( $\sim 0.11 - 0.16$ ) has been claimed from measurements of Knight shift and chemical shift [156]. A straightforward extrapolation, based on the FCO above  $T_{\text{SP}}$  predicts the SP state to also have the  $\cdots 1010 \cdots$  pattern [102]. This might even explain the weak amplitude of the SP bond distortion [178]: the extent of the SP bond distortion is indeed smaller in the  $4k_{\text{F}}$  CDW-SP state than in the BCDW-I for the same SSH e-p coupling (and  $\Delta n$  is larger) [83].

There are, however, strong reasons to believe that the SP state is BCDW-I, even with the FCO as the high temperature state. First, as pointed out in the above, the charge localization below  $T_{\rho}$  can result from a crossover into a (disordered)  $4k_{\text{F}}$  BOW, in which case it is likely that the SP transition is a dimerization of the dimerization. This could be particularly likely given that the FCO transition is driven by interaction with anions, while the bond-dimerization as well as the SP transition are both intrinsic instabilities of the quasi-1D chains. As shown in 3.3.2, a temperature-dependent transition from the WC to the BCDW-I is *expected* for e-e interactions with intermediate strength ( $6 \leq U \leq 10$ ,  $2 \leq V \leq 3$ ). Such a transition would explain the experimentally noted competition between FCO and SP [167, 179].

Theoretical work in this case predicts charge distribution leading to much smaller  $\Delta n$  in the SP state than in the FCO state [83, 129]. Charge redistribution with observable decrease in  $\Delta n$  upon entering the SP state has been claimed in both  $X = \text{AsF}_6$  [157] and  $\text{PF}_6$  [158] from  $^{13}\text{C}$  NMR studies. Optical spectroscopy in this context appear to give ambiguous results. Optical conductivity obtained from reflection studies, in the spectral region of the EMV coupled  $\nu_3$  mode, shows no charge redistribution (see Fig. 16(a) and (b)). Raman measurement of the same mode shows a splitting of the vibrational frequency below  $T_{\text{CO}}$  but apparent vanishing of the splitting below  $T_{\text{SP}}$  (see Fig. 16(c)). We note however that later Raman data continues to show a splitting of the  $\nu_3(\text{ag})$  mode at 10 K, although unexplained differences were noted with the data of Reference [94] in the low temperature region [180]. Recall also the pressure dependent measurement in  $X = \text{SbF}_6$  (see above), which finds that the CO amplitude decreases strongly and is nearly unobservable in the pressure region where the SP phase appears [159, 165], again indicating charge redistribution in the SP state. Thermal expansivity measurements have found, in addition to the FCO and SP transitions, a third likely transition at temperature  $T_{\text{int}}$  intermediate between  $T_{\text{CO}}$  and  $T_{\text{SP}}$ . A possible intermediate transition is seen also in dielectric permittivity study of  $X = \text{PF}_6$ . No explanation exists in the literature currently of this intermediate temperature transition. It is conceivable that the transition at  $T_{\text{int}}$  is the WC-to-BCDW transition discussed in Section 3.3.2 (theory does not require the transition to occur *at*  $T_{\text{SP}}$  but merely requires the charge occupancies in the SP and FCO phases to be different) and this possibility merits further experimental investigation. Finally, there exists a whole slew of systems that exhibit the SP transition within the insulating phase below  $T_{\rho}$  without going through the intermediate FCO state. These materials are discussed below.

## 4.2. (TMTTF)<sub>2</sub>Br and (TMTSF)<sub>2</sub>PF<sub>6</sub>, the AFM-II region

### 4.2.1. (TMTTF)<sub>2</sub>Br

(TMTTF)<sub>2</sub>Br lies very close to the boundary between the SP and AFM-II phases in the phase diagram of Fig 15.  $T_p$  in this case is lower than in the other TMTTF salts ( $\sim 100$  K), although some samples exhibit  $T_p$  as high as 200 K [181]. The antiferromagnetism has been determined to be commensurate under ambient pressure from both <sup>13</sup>C NMR [182] and <sup>1</sup>H NMR [168] studies, with  $\mathbf{q}_{\text{AFM}} = (\frac{1}{2}, \frac{1}{4}, 0)$ , and the low T AFM amplitude of  $0.14 \mu_B$ . Coupling of the spin fluctuations with the lattice and charge degrees of freedom was first found from diffuse X-ray scattering [169], which indicated the signature of a  $2k_F$  quasi-1D lattice instability below 70 K. This behavior is similar to the SP materials, which also show 1D SP fluctuations at a temperature considerably higher than the 3D  $T_{\text{SP}}$ . In contrast to the SP systems, the  $2k_F$  scattering here vanished abruptly at 17 K and long range SP order is not observed. This, however, does not imply complete loss of structural distortion. Instead of  $2k_F$  scatterings,  $4k_F$  scatterings are observed below  $T_N$  [169, 183].

Tendency to coupled bond-charge-spin instability (BCSDW) in the paramagnetic phase above  $T_N$ , beginning from  $\sim 50$  K, has been confirmed from a number of other experimental studies [181, 184, 185]. Nad *et al.* concluded from dielectric permittivity studies that the growth of  $\epsilon'$  in the paramagnetic phase is due to fluctuations of a  $2k_F$  displacive lattice instability of “SP type”. These fluctuations seem to persist below  $T_N$  but vanish at  $\sim 10$  K. Suppression of  $2k_F$  fluctuations, as observed in the X-ray measurements, and decrease of  $\epsilon'$  begin at the same temperature range above  $T_N$ . Relaxation via acoustic phonons and 1D lattice fluctuations were also seen in ESR studies in the temperature range between approximately  $T_N$  and 50 K [184, 185].

The above studies confirm the short-range BCSDW nature of the broken symmetry in (TMTTF)<sub>2</sub>Br in the  $T_N < T < 50$  K region. While this apparent agreement with theory might appear to be satisfying, the vanishing of the  $2k_F$  instability at  $T_N$  is not predicted within the existing theories [143, 149]. The solution to this puzzle may however be straightforward, given that the  $2k_F$  charge fluctuations can exist only in the presence of the  $2k_F$  BOW [149]. As the temperature is lowered and the 2D hoppings between chains become more relevant, it is very likely that the  $2k_F$  BOW gets weaker. While this has not been proved in the specific case of  $\rho = \frac{1}{2}$ , the weakening of the  $2k_F$  BOW in correlated 2D structures is not unanticipated [142]. We speculate that the  $4k_F$  bond dimerization, with zero phase difference between chains, continues to persist within the EHM of Eq. 5 even when weak interchain hoppings are included. This will be in agreement with the X-ray scattering data [169] and will also give the observed  $\mathbf{q}_{\text{AFM}}$ , with equal charge densities on each site. This is a topic of future research.

### 4.2.2. (TMTSF)<sub>2</sub>PF<sub>6</sub>

The compound (TMTSF)<sub>2</sub>PF<sub>6</sub> has been scrutinized perhaps the most as this was chronologically the first organic superconductor [18, 186]. An incommensurate SDW appears here at 12.5 K under ambient pressure, with the SDW moment of  $0.03 - 0.08 \mu_B/\text{molecule}$  [182, 187]. The SDW wavevector, though incommensurate, is close to commensurability with  $\mathbf{q}_{\text{SDW}} = (0.50, 0.20 \pm 0.05, 0.06 \pm 0.20)$ . The incommensurate SDW has often been thought to result from nesting of the Fermi surface [22], as in the Peierls CDW mechanism, especially in the context of the magnetic field induced SDW [25]. Of greater relevance to the present review are however indications for the coupling between the lattice, charge and spin degrees of freedom that is not expected within a simple nesting mechanism for the SDW instability, but that were indicated over the years by a variety of experiments [188–192]. Convincing proof of this coupling was obtained from direct X-ray measurements by Pouget and Ravy [169, 183] and Kagoshima *et al.* [193, 194], which we briefly discuss below. Yet another subject of interest is the nature of the very low temperature phase below 4 K [187, 193–198], which has only recently shown from <sup>13</sup>C-NMR to be commensurate SDW [199]. *The pressure-induced transition to SC is therefore a commensurate BCSDW-SC transition, making it even more likely that the mechanisms of the superconducting transition in the so-called quasi-1D compounds and the strongly 2D ET and [Pd(dmit)<sub>2</sub>]<sub>2</sub> compounds (see Section 5) are related.* X-ray scattering experiments have directly demonstrated the mixed CDW-SDW nature of the broken symmetry below  $T_{\text{SDW}}$  in (TMTSF)<sub>2</sub>PF<sub>6</sub> [169, 183, 193, 194]. Pouget and Ravy observed satellites with wave vector components  $a^*/2$  ( $2k_F$ ) as well as  $a^*$  ( $4k_F$ ), thus confirming that the CDW and SDW periodicities were identical. The identical periodicity excludes a simple classical explanation of the mixed CDW-SDW as a  $4k_F$  CO accompanied by  $2k_F$  SDW, which merely requires the  $\dots 1010 \dots$  charge periodicity driven by the intersite Coulomb interaction. The common  $2k_F$  periodicity requires that the mixed CDW-SDW is the BCSDW of Section 3.2.2. Note that this precludes a simple nesting mechanism for the instability, since strong e-e interactions is a necessary requirement for the BCSDW.

The lowest temperature at which Pouget and Ravy saw the  $2k_F$  and  $4k_F$  scatterings was 10.7 K. The intensities of the satellite reflections were weaker than the usual  $2k_F$  and  $4k_F$  reflections by 2 to 3 orders of magnitude. Kagoshima *et al.* observed that below 4 K, there was remarkable decrease in the intensities with decreasing temperature, and the satellites were completely absent at 1.6 K [193, 194]. Kagoshima *et al.*'s experiment gave strong evidence for the existence of a SDW subphase below 4 K that was presumably different from the high temperature phase, as had been conjectured already from other experiments [187, 195–198]. While the recent demonstration of the commensurate character of the low T SDW [199] has solved the mystery of the nature of the SDW subphase, it has introduced two new questions, which are (i) What is the mechanism of the T-dependent incommensurate-commensurate transition? (ii) What does this imply for the SDW-SC transition?

We believe that the answer to the first question involves again interchain interaction. As in  $(TMTTF)_2Br$ , the vanishing of the mixed CDW-SDW below 4 K is related to increased two dimensionality, which destroys the  $2k_F$  BOW. Unlike  $(TMTTF)_2Br$ , the BCSDW survives here below  $T_{SDW}$  because of the larger bandwidth of  $(TMTSF)_2PF_6$ , which makes  $U/|t|$  and  $V/|t|$  smaller. Below 4 K, the SDW then has the structure  $\uparrow, \uparrow, \downarrow, \downarrow$ . As already mentioned above, this reasoning, while highly plausible, needs confirmation from future theoretical work.

The commensurate nature of the ground state of  $(TMTSF)_2PF_6$  strongly suggests that the mechanisms of the superconducting transition here and in  $\kappa-(ET)_2Cu[N(CN)_2]Cl$  are related. We speculate that the effect of pressure on  $(TMTSF)_2PF_6$  is to create *interchain* spin singlets. Interchain singlets are discussed in Section 6.2.1 in the context of CTS ladder materials.

### 4.3. Non-traditional 2:1 cationic salts

#### 4.3.1. $(TMTTF)_2I$

We classify  $(TMTTF)_2I$  among the nontraditional materials, in spite of having the same cation as the systems discussed above, as it exhibits the SP state without going through the FCO phase. The crystal structure of this material is similar to the other Fabre salts [200].  $^{13}C$ -NMR measurements indicate completely equivalent TMTTF molecules throughout the paramagnetic phase [151]. Transition to the SP state at  $T_{SP} = 21$  K was detected from both T-dependent ESR susceptibility and  $^{13}C$ -NMR measurements [151]. Line broadening at  $T_{SP}$ , as found in  $(TMTTF)_2PF_6$ , and ascribed to charge redistribution [158] was absent in this case. The temperature at which charge localization occurs here is not known. Presumably this is greater than 300 K. In spite of the larger chemical pressure due to the smaller bromide counterion,  $(TMTTF)_2Br$  is antiferromagnetic and lies to the right of  $(TMTTF)_2I$  on the higher pressure side of the phase diagram in Fig. 15. This is a clear indication both of two different kinds of AFM states and of  $(TMTTF)_2Br$  belonging to the AFM-II region.

#### 4.3.2. $(BCPTTF)_2X$

These materials exhibit semiconducting charge-gap already at room temperature, and undergo SP transitions at  $T_{SP} = 36$  K ( $X = PF_6$ ) and 32.5 K ( $A = AsF_6$ ) [152, 153]. The molecule BCPTTF is asymmetric, but the crystal structures of  $(BCPTTF)_2X$  are close to that of  $(TMTTF)_2X$ . The calculated intrachain NN hopping integrals are smaller than those calculated for TMTTF, using the same computational technique [152]. The FCO is nevertheless absent in  $(BCPTTF)_2X$ , while the effective dimerization is larger [152]. The larger effective dimerization explains both larger  $T_\rho$  and  $T_{SP}$ . Clearly the charge localization, the transition to the FCO phase (or its absence, as in the present case) and the nature of the low temperature state (AFM versus SP) are all strongly linked and they cannot be discussed in isolation.

#### 4.3.3. $(o-DMTTF)_2X$

The DMTTF molecule is a hybrid of TTF and TMTTF, with two methyl groups attached to one side of the TTF moiety. The crystal structure of  $(o-DMTTF)_2Cl$  is shown in Fig. 17(a). The space group symmetry is  $I4_2d$ , and it is generally believed that the central locations of the halogen atoms give the uniform stacking and weak coupling between the chains.

The T vs P phase diagram for  $X = Cl$  and  $Br$  is shown in Fig. 17(b), where the  $Br$ -compound is shifted in pressure by 0.35 GPa. At the low pressure end, the system is a highly anisotropic 1D metal, as deduced from longitudinal and transverse resistivity. It is believed that a smooth charge localization at  $T_\rho$  here is associated with  $4k_F$  fluctuations driven by e-e interactions [154]. Pretransitional diffuse  $4k_F$  lines are seen below  $T_\rho$  in X-ray measurements. Additional

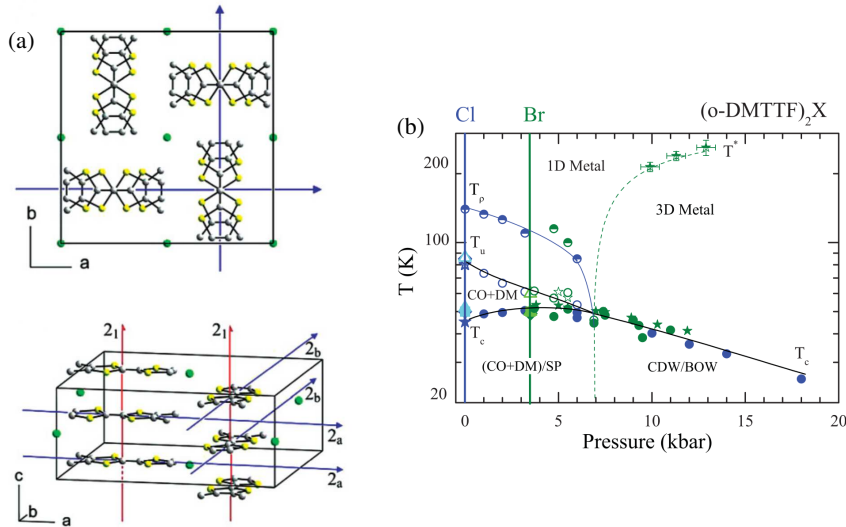


Figure 17. (color online) (a) Crystal structure and (b) phase diagram of  $(o\text{-DMTTF})_2\text{X}$ . Blue (green) symbols are data for  $\text{X}=\text{Cl}$  ( $\text{Br}$ ). The data for the  $\text{Br}$  salt is shifted by 0.35 GPa. Circles (stars) are determined from the longitudinal (transverse) resistivity. A ambient (zero) pressure, diamonds, triangles, and squares are from thermopower, ESR, and X-ray measurements, respectively. Reprinted with permission from Ref. [154], © 2011 The American Physical Society.

increase in resistivity is observed as the temperature is lowered to below  $T_u$ . This transition is considered to be the usual  $4k_F$  transition, although no significant structural modulation has been observed in X-ray diffuse scattering measurements. Absence of any change in the T-dependent magnetic susceptibility at  $T_p$  or  $T_u$  indicates charge-spin decoupling. It has been argued that the transition at  $T_u$  is a combination of  $4k_F$  FCO and BOW, with the FCO and the BOW on separate stacks, or perhaps a combined FCO-BOW on the same stack. Vibrational spectroscopy, however, has failed to detect CO [201], indicating either pure BOW nature of the  $4k_F$  phase, or at the very least, small amplitude of the FCO.

The phase transition at the lowest temperature  $T_c \approx 50$  K occurs in both  $\text{X} = \text{Cl}$  and  $\text{Br}$  and is easily observed in magnetic susceptibility measurements and diffuse X-ray scattering. Magnetic measurements indicate the state below to be nonmagnetic, while X-ray measurements find tetramerization of the stacks. Both of these suggest that the state below  $T_c$  is the SP phase expected within the  $4k_F$  BOW ( $2k_F$  BCDW-I). While this would agree qualitatively with the theory presented in Sections 2.2 and 2.3, this interpretation may be overly simplistic from a quantitative perspective. The difference between the charge- and spin-gap in  $(o\text{-DMTTF})_2\text{X}$  are much smaller than what is seen in either  $\text{MEM}(\text{TCNQ})_2$  or the Fabre salts, as evidenced from the relatively small difference between  $T_u$  and  $T_c$  in Fig. 17(b) (particularly in the  $\text{Br}$ ). The most likely reason for the relatively strong coupling between charge- and spin-degrees of freedom in  $(o\text{-DMTTF})_2\text{X}$  are that  $U/|t|$  and  $V/|t|$  here are smaller than in  $(\text{TMTTF})_2\text{X}$ . The actual charge and bond distortion patterns in the spin-gapped state are currently unknown. We believe that the charge pattern here will be found to be  $\dots 0110\dots$ , but the bond distortion pattern may be complicated and a superposition of SMWM and SWSW'.

The high pressure region in Fig. 17(b) is very different from the phase diagram of Fig. 6, in that the low temperature phase in this region is *not* AFM or SDW. Furthermore, the temperatures  $T_u$  and  $T_c$  have merged here.  $T^*$  here is obtained from the maxima in plots of transverse resistivity against temperature. Whether or not the state below  $T^*$  is a true metal is arguable (“bad metal” could be one classification). Neither is it clear whether or not there is true boundary or a crossover from the spin-gapped phase to this state. X-ray diffraction and magnetic measurements have not been performed under pressure. The low T phase in this high pressure region has been thought to be the “usual Peierls phase”. We believe that future experiments will find this state to be the  $\dots 0110\dots$  BCDW.

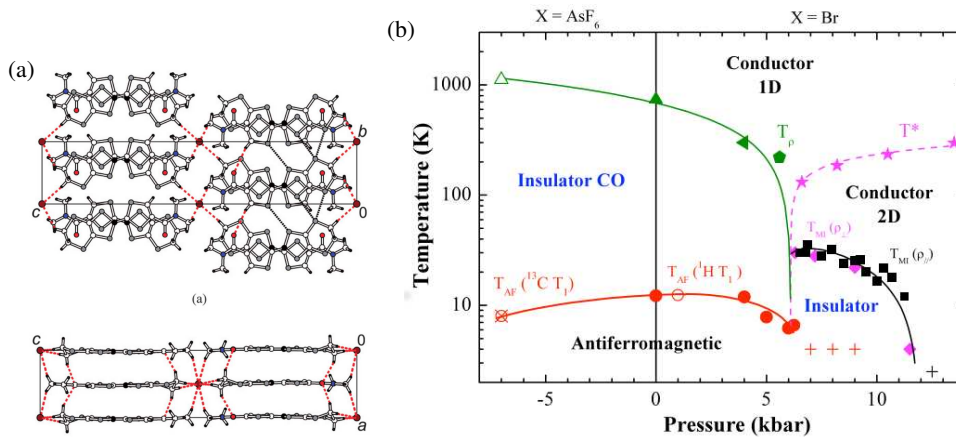


Figure 18. (color online) (a) structure of  $\delta$ -(EDT-TTF-CONMe<sub>2</sub>)<sub>2</sub>X. Reprinted with permission from Ref. [202], © 2009 The Royal Society of Chemistry. (b) phase diagram determined from resistivity and <sup>1</sup>H NMR measurements. Reprinted with permission from Ref. [155], © 2009 The American Physical Society.

#### 4.3.4. $\delta$ -(EDT-TTF-CONMe<sub>2</sub>)<sub>2</sub>X

This material is of interest for being perhaps the only one where the MI transition at ambient pressure is due to transition to the purely CO state. The crystal structure of the cation is shown in Fig. 18(a). The compounds are hereafter referred to as EDT<sub>2</sub>X (X = AsF<sub>6</sub>, Br). The T vs P phase diagram, determined from transport and NMR studies [155] is shown in Fig. 18(b). As seen in the Fig. 18, substitution of AsF<sub>6</sub> with Br is equivalent to applying hydrostatic pressure of nearly 0.7 GPa. There is no crystal-structure driven dimerization here and  $T_{MI} = T_{CO}$  in the low pressure region. Furthermore,  $T_{CO}$  are extraordinarily high here (compare against Fig. 6). The high  $T_{CO}$  suggests the WC as the charge-ordered phases. This is supported by structural analysis in the insulating phase that finds uniform intrastack intermolecular distances [202]. The stability of the WC here is a signature of very large  $V/|t|$ , with likely  $V > V_c(U)$ , as opposed to (TMTTF)<sub>2</sub>X, where additional contribution to the stabilization of the WC CO must come from cation-anion interaction or the Holstein e-mv interaction. This latter conclusion is in agreement with calculations that find rather small hopping integrals  $t_{||} = 71$  meV,  $t_{\perp} = -25$  meV for EDT<sub>2</sub>AsF<sub>6</sub> at 300 K [203] and  $t_{||} = 87$  meV,  $t_{\perp} = -32$  meV for EDT<sub>2</sub>Br at 150 K [202] (the calculated hopping integrals suggest greater two dimensionality, which reduces  $V_c$  and hence may also be responsible for stabilizing the WC [204].)

The phase diagram of Fig. 18 exhibits several interesting features, which are, (i) the occurrence of CO and AFM in the same pressure region, (ii) the steep pressure-dependence of  $T_{CO}$ , (iii) an apparent boundary between 1D and 2D conducting regions, and (iv) the low T high P insulating region that is distinct from the AFM phase, and that may be separated from the AFM phase by a real phase boundary. Of these, (i) is to be expected from our discussions in Section 2.2 and 4, identifying the CO phase at low pressure as the WC and the AFM phase at low T as AFM-I. The rapid drop in  $T_{CO}$  with pressure is unique with these compounds, suggesting a stronger role of frustration than usual. Whether or not the curve labeled  $T^*$  in the Fig. represents a true boundary or even crossover is debatable:  $T^*$  are temperatures at which broad maxima are seen in plots of transverse resistivity. The boundary between the high pressure conducting and insulating phases, on the other hand, represents the true  $T_{MI}$  as found from measurements of longitudinal and transverse resistivities. The insulating phase has been found to be nonmagnetic from NMR measurements [155].

The absence of a SP phase *within* the CO phase, while it has received relatively less attention so far, is of strong interest in view of the theoretical discussions of Sections 3.2 and 3.3. *This result is in apparent agreement with the theoretical idea that the WC CO and the SP phase are mutually exclusive in the real materials (Section 3.3.2).* The high pressure nonmagnetic insulating phase has not been completely characterized yet. We believe that this phase is a  $2k_F$  BCDW, as in the high pressure region of *o*-(DMTTF)<sub>2</sub>X.

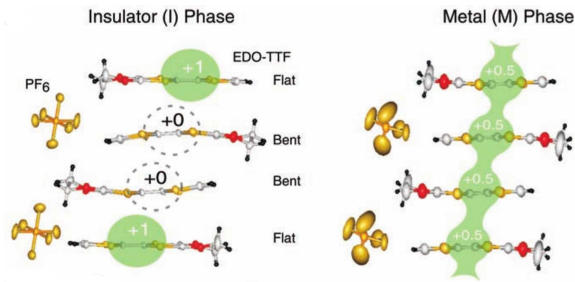


Figure 19. (color online) Crystal structures of EDO-TTF in the low temperature insulating and high-temperature metallic phases. Reprinted with permission from Ref. [206], © 2005 AAAS.

#### 4.3.5. $(\text{EDO-TTF})_2\text{X}$ and BCDW-II

The crystal structure of EDO-TTF is shown in Fig. 19(a).  $(\text{EDO-TTF})_2\text{X}$  are strongly 1D with weak interstack interaction. These compounds undergo first-order metal-insulator transitions at a very high  $T_{\text{MI}} = 280$  K and 265 K for  $\text{X} = \text{PF}_6$  and  $\text{AsF}_6$ , respectively [150, 205]. Magnetic susceptibility measurements indicate transition to a spin-gapped nonmagnetic state at the *same* temperature  $T_{\text{MI}}$ , a behavior completely different from that observed in any other 2:1 cationic material at ambient pressure (we note, however, that the high pressure phases in  $o$ -(DMTTF) $_2\text{X}$  and  $(\text{EDT-TTF-CONMe}_2)_2\text{X}$  do show single transitions involving both charge and spin). The transition to the nonmagnetic insulating state is accompanied by period 4 distortions of both the intermolecular bonds and of the cationic molecules themselves, as is shown in the Fig. 19.

The molecules are equivalent and weakly non-planar above  $T_{\text{MI}}$ , where the charges on the cations are 0.5. For  $T < T_{\text{MI}}$  there occurs tetramerized molecular distortions  $BFFB$  ( $B = \text{bent}$  and  $F = \text{flat}$ ), where the bent molecules are nearly completely neutral (charge  $\sim 0$ ), and the flat molecules are nearly completely ionic (charge  $\sim +1.0$ ). These assignments are obtained from vibrational spectroscopy [207], which gives charges of +0.96 and +0.04 for the charge-rich and charge-poor cations, and crystal structure analysis [208], which gives a smaller charge disproportionation with charges of +0.8 and +0.2, respectively. Strong role of the Holstein e-mv coupling in driving the transition is indicated by these experiments. These studies have also established that the intermolecular bond strengths are of the form SMWM, with the strongest ‘S’ bond between the charge-rich sites [207]. Thus the SSH e-p coupling also plays a strong role.

Drozдова *et al.* [207] recognized that  $(\text{EDO-TTF})_2\text{X}$  can be very clearly understood as a prototype example of  $2k_{\text{F}}$  BCDW-II, with small to moderate  $U$  and  $V$  (see Sections 3.2.1 and 3.3.2). These authors measured the charge-transfer absorption spectrum of the compound as a function of temperature, and noted that the strength of the high energy absorption band (labeled  $\text{CT}_2$  by the authors) with peak energy at  $\sim 1.38$  eV, relative to the lower energy band with peak energy  $\sim 0.52$  eV, was significantly higher than in most other CTS. The authors calculated the charge-transfer spectrum within a modified Hubbard model with modulated hopping integrals and site energies for a tetramer consisting of only four molecules (with charge arrangement 0110), and justified this boundary condition based on the weakness of the  $0 \cdots 0$  bonds, which would make each tetramer nearly decoupled from the chain. In order to obtain the  $\text{CT}_1$  and  $\text{CT}_2$  energies and the site charge densities of 0.96 and 0.04 obtained from the Raman spectrum the authors needed hopping integrals 0.15 and 0.28 eV (corresponding to the 0–1 and 1–1 bonds, respectively), site energies  $\pm 0.24$  eV and  $U = 0.93$  eV. Although the  $0 \cdots 0$  bond was excluded entirely from the calculations, and the site energies should have been in principle obtained self-consistently, the values of the Hubbard  $U$  and the hopping integrals required in this calculation were quite reasonable. The authors assigned the  $\text{CT}_1$  and  $\text{CT}_2$  transitions to predominantly  $0110 \rightarrow 0101$  and  $0110 \rightarrow 0200$  charge-transfers respectively, and ascribed the unusually large intensity of  $\text{CT}_2$  (compared to the charge-transfer absorptions in this region in the “standard” 2:1 materials) to the strength of the “isolated” 1=1 bond.

A more recent Density Functional Theory (DFT)-based modeling of  $(\text{EDO-TTF})_2\text{X}$  treats e-e interactions at the mean-field level, and ascribes the tetramerization at the MI transition to an “electric potential bias within a tetramer of EDO-TTF molecules” as opposed to SSH and Holstein e-p interactions [209]. This latter work is more difficult to understand; also, as already pointed out, if the charge distribution of  $\cdots 0110 \cdots$  has to originate entirely from

built in electric potential, the latter has to be non-convex, which is unrealistic. The authors obtained a one-electron tight-binding Hamiltonian with modulated hopping integrals and site energies from fitting to the DFT calculations. The largest tight binding integral from the fitting was 0.70 eV, which is unusually large for CTS, in which the hopping integrals range from 0.10 - 0.25 eV. This discrepancy is likely due to the neglect of e-e and e-p interactions.

(EDO-TTF)<sub>2</sub>X has also attracted recent attention as a material in which a photoinduced transition occurs from the insulating state to a metallic state that is very close to the high temperature state [206]. The transition to the metallic state takes nearly 100 picoseconds and has been thought to proceed via a metastable charge-ordered state  $\cdots 1010 \cdots$  [210, 211], with coherent phonon interactions playing a strong role. A DFT-based theory has attempted to explain why excitation at the CT<sub>2</sub> transition energy is more efficient in driving the transition than the excitation at other energies [212]. Photoinduced phase transitions are a subject of considerably broader interest [213], but are outside the scope of this review.

#### 4.4. Summary

Wigner crystal (WC) and bond-charge density waves (BCDWs) of two different types (BCDW-I and BCDW-II) are all observed experimentally in quasi-one-dimensional  $\rho = \frac{1}{2}$  CTS. The WC state in general is found in the most quasi-one dimensional of these materials, which then exhibit an antiferromagnetic phase at still lower temperatures. In the (TMTCF)<sub>2</sub>X series, the spin-Peierls (SP) phase is BCDW-I and the low temperature phase adjacent to superconductivity (SC) is BCDW-I or the bond-charge-spin density wave (BCSDW). The WC and SP phases are mutually exclusive. In (TMTTF)<sub>2</sub>PF<sub>6</sub> and AsF<sub>6</sub> there occurs a WC-to-BCDW-I transition as the temperature is lowered. Spin gap is thus a signature of BCDW-I or II. The spin-density wave state found in (TMTSF)<sub>2</sub>PF<sub>6</sub> under ambient pressure is commensurate at the lowest temperatures, and the transition to SC is a commensurate BCSDW to SC transition. The properties of materials exhibiting the alternate bond-distortion pattern BCDW-II are quite different; in (EDO-TTF)<sub>2</sub>X the transition to BCDW-II coincides with a first-order metal-insulator transition at a relatively high temperature.

## 5. Broken symmetries in quasi-two dimensional CTS, Experiments

The 2D CTS feature a much greater variety of materials than the quasi-1D CTS. We will therefore first review experimental results, and follow with a summary of theory in Section 6. Due to the expansive experimental literature, we must focus on a narrower range of materials rather than all 2D molecular charge-transfer salts. Specifically, we review the classes of 2D materials that are superconductors or exhibit charge and spin ordered states proximate to superconductivity. Some topics of current interest, for example the very large literature on magnetic field effects, are outside the scope of this review.

### 5.1. Quasi-two dimensional cationic CTS

Details of the crystal structure of 2D CTS strongly influence their electronic properties. Different CTS structural types are denoted by a Greek letter prefix ( $\alpha$ ,  $\beta$ ,  $\theta$ , etc). Below we organize the discussion according to these different crystal structures.

#### 5.1.1. $\kappa$ CTS

The  $\kappa$ -(ET)<sub>2</sub>X salts are perhaps the most studied family of organic superconductors after the quasi-1D TMTSF and TMTTF materials. The great interest in  $\kappa$ -(ET)<sub>2</sub> stems from both their relatively high  $T_c$ 's of up to 12.8 K (see Table 3; a  $T_c$  of 14.2 K is however found in the  $\beta'$  CTS [214], see Section 5.1.2), as well as their apparent similarity to the cuprate high- $T_c$  materials. As in the cuprates, the presence of AFM near to the SC phase has led to widespread belief that Mott physics is central to understanding the SC [215]. This belief has led many to suggest that the electronic properties and SC in  $\kappa$ -(ET)<sub>2</sub> can be described by an effectively  $\frac{1}{2}$ -filled band model. In this section we point out however, that many experimental observations cannot be explained within such a model.

The schematic crystal structure of the conducting layers in  $\kappa$ -(ET)<sub>2</sub>X is shown in Fig. 20(a). In the  $\kappa$  structure, dimers of BEDT-TTF molecules are arranged in an anisotropic triangular lattice. In terms of single molecules, as with other ET salts, the conducting layer is  $\frac{3}{4}$ -filled with electrons. Fig. 20(b) shows the effective dimer model commonly used to describe  $\kappa$ -(ET)<sub>2</sub>X; here each dimer is replaced by a single site, leading to an effective  $\frac{1}{2}$ -filled band model, with an average density of one hole per dimer. We discuss this model further in Section 6, but introduce it here, as the

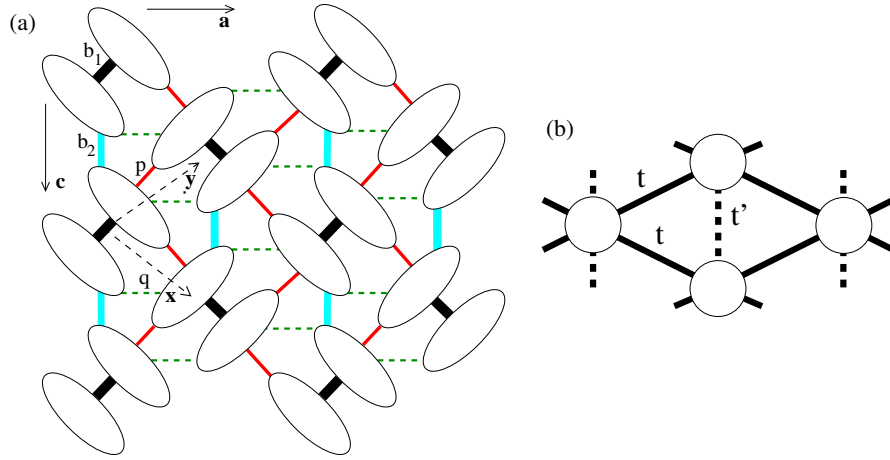


Figure 20. (color online) (a) Lattice structure of  $\kappa$ -(ET) $_2$ X showing individual BEDT-TTF molecules. In order of decreasing magnitude,  $b_1$ ,  $b_2$ ,  $p$ , and  $q$  label the intermolecular hopping integrals. The  $\mathbf{a}$  and  $\mathbf{c}$  crystal axes for  $\kappa$ -(ET) $_2$ Cu[N(CN) $_2$ ]X are indicated; for  $\kappa$ -(ET) $_2$ Cu $_2$ (CN) $_3$  the corresponding axes are conventionally labeled  $\mathbf{b}$  and  $\mathbf{c}$ . (b) effective  $\frac{1}{2}$ -filled dimer model. Here each site corresponds to a dimer in (a).  $t$  is the effective hopping in the  $\hat{x}$  and  $\hat{y}$  directions and  $t'$  the effective hopping in the  $-\hat{x} + \hat{y}$  direction.

X	$t'/t$ (EH)	$t'/t$ (DFT)	$T_c$ (K)	$P_c$ (GPa)	Notes	references
I $_3$	0.54	0.35	3.6	0	—	[218–220]
Cu[N(CN) $_2$ ]Cl	0.71	0.44-0.53	12.8	0.03	$T_N=26$ K	[216, 221, 222]
d8-Cu[N(CN) $_2$ ]Br	0.67	0.45-0.53	11	0	$T_N=15$ K	[221–223]
Cu[N(CN) $_2$ ]Br	0.67	0.46	11.6	0	—	[21, 218, 220]
Cu[N(CN) $_2$ ]I	—	—	8.0	0.1	—	[224, 225]
Ag(CN) $_2$ ·H $_2$ O	0.61	0.47	5.0	0	—	[218, 220, 226]
Cu(NCS) $_2$	0.81	0.50-0.67	10.4	0	—	[216, 217, 221, 222, 227]
Cu(CN)[N(CN) $_2$ ]	0.64	0.67	11.2	0	—	[218, 220, 228]
Hg(SCN) $_2$ Cl	—	0.80	—	—	$T_{CO}=30$ K	[229–231]
Ag $_2$ (CN) $_3$	0.97	—	5.2	0.9	—	[232]
Cu $_2$ (CN) $_3$	1.07	0.80-0.99	3.9(7)	0.6	—	[216, 217, 221, 222, 233]
CF $_3$ SO $_3$	1.79	1.30	4.8	1.1	$T_N = 2.5$ K	[234, 235]
B(CN) $_4$	—	1.80	—	—	$T_{SG}=5$ K	[222]

Table 3. Summary of the properties of  $\kappa$ -(ET) $_2$ X for different X discussed in this review. The second and third columns are the calculated  $t'/t$  using extended Hückel (EH) and density-functional theory (DFT) methods, respectively. In general, values calculated for low temperature (100 K) crystal structures are listed; the range of values listed are accounted for by slightly different temperatures and theoretical methods of fitting the calculated bandstructure. For X=Cu $_2$ (CN) $_3$ , a higher  $T_c$  (7 K) has been found under conditions of uniaxial strain [233].  $t'/t$  within the EH method for X=Cu[N(CN) $_2$ ]I is slightly smaller than for X=Cu[N(CN) $_2$ ]Br [227].

anisotropy  $t'/t$  is commonly used as a parameter to characterize  $\kappa$ -(ET) $_2$ X. Table 3 lists the most commonly studied  $\kappa$ -(ET) $_2$ X, sorted by their effective  $t'/t$  as calculated by DFT [216, 217]. A recent DFT calculation of the hopping parameters for eight different  $\kappa$ -(ET) $_2$ X found no apparent correlation between  $T_c$  and any of the four  $t_{ij}$ , or any of their ratios [218]. For example, X=Ag(CN) $_2$ ·H $_2$ O and X=Cu[N(CN) $_2$ ]Br in Table 3 have nearly the same  $t'/t$ , but have  $T_c$ 's differing by more than a factor of two.

**AFM versus SC in  $\kappa$  phase salts.** The occurrence of AFM and the proposal that it can mediate SC has played a central role in the study of  $\kappa$ -(ET) $_2$ X. The occurrence of AFM order can be simply understood within the  $\frac{1}{2}$ -filled effective model of Fig. 20(b). For sufficiently large dimer  $U$  and sufficiently small frustration ( $t'$ ) between dimers, the ground state of the  $\frac{1}{2}$ -filled Hubbard model on the anisotropic triangular lattice is  $\mathbf{Q}=(\pi,\pi)$  Néel AFM (see Section 6.1). This Néel arrangement of dimer spins has been confirmed experimentally [223, 236]. AFM with other ordering wavevectors are found theoretically in the  $\frac{1}{2}$ -filled band Hubbard model on the anisotropic triangular lattice for larger  $t'$  (for example the 120° state found on the isotropic triangular lattice [237–241]). While materials in this region of the parameter space are known (X=CF $_3$ SO $_3$ ) there is no information as of writing on the ordering wavevector here.

Despite the emphasis on AFM, experimentally antiferromagnetic ground state is only found for a few  $\kappa$  phase materials, X=Cu[N(CN) $_2$ ]Cl ( $\kappa$ -Cl), X=Cu[N(CN) $_2$ ]Br ( $\kappa$ -Br) with deuterated BEDT-TTF molecules (d8- $\kappa$ -Br) and

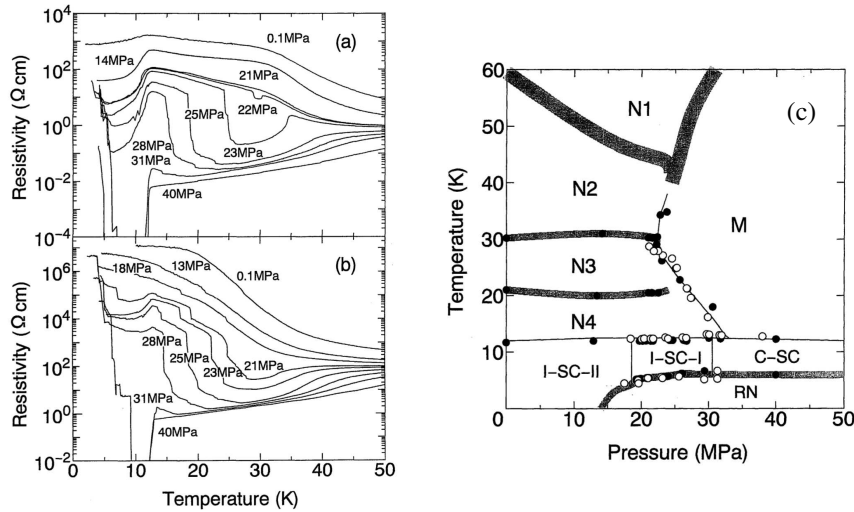


Figure 21. Pressure dependence of (a) intralayer ( $\rho_{\parallel}$ ) and (b) interlayer ( $\rho_{\perp}$ ) resistivity of  $\kappa$ -(ET) $_2$ Cu[N(CN) $_2$ ]Cl. (c) Phase diagram determined via resistivity. N1...N4 refer to nonmetallic phases, separated by anomalies in  $\rho_{\parallel}$  and  $\rho_{\perp}$ ; M is the metallic phase; I-SC-II is incomplete superconductivity with no decreases in  $\rho_{\perp}$ ; I-SC-I incomplete superconductivity with decreases in both  $\rho_{\parallel}$  and  $\rho_{\perp}$ ; C-SC complete superconductivity; RN recurrent nonmetallic phase. Reprinted with permission from Ref. [242], © 1996 The Physical Society of Japan.

$X = \text{CF}_3\text{SO}_3$ . The most well known is  $X = \kappa\text{-Cl}$  with  $T_N = 26$  K [236, 243, 244]. The AFM state is commensurate with the lattice, with a relatively large moment of 0.4–1.0  $\mu_B$  per dimer [236]. Under a small pressure (even that provided by a grease coating) of 0.03 GPa  $\kappa\text{-Cl}$  is superconducting at 12.5 K [244, 245]. At ambient pressure, the resistivity of  $\kappa\text{-Cl}$  gradually increases below 300 K, with a sharper increase below around 40 K [242, 244, 246]. The temperature and pressure dependence of the resistivity  $\kappa\text{-Cl}$ , shown in Fig. 21, is complex [242, 247]. A low pressures, an “incomplete” SC is seen below  $\sim 13$  K, where the in-plane resistivity ( $\rho_{\parallel}$ ) decreases but does not reach zero, and the inter-plane resistivity ( $\rho_{\perp}$ ) remains high [242]. The decrease in  $\rho_{\parallel}$  at low temperatures is suppressed by a magnetic field exceeding 5 T [242]. A second incomplete SC region at higher pressure has a decrease in both  $\rho_{\parallel}$  and  $\rho_{\perp}$ . These incomplete SC phases were interpreted as Cooper pair localization [242]. Several insulating phases (see Fig. 21) were identified as paramagnetic (N $_1$ ), fluctuating AFM (N $_2$ ), AFM order (N $_3$ ), and AFM with weak ferromagnetic canting (N $_4$ ). A reentrant insulating phase (RN in Fig. 21) was also identified at low temperatures under pressure, which exhibited hysteresis under thermal cycling [242, 247]. The P-T phase diagram of  $\kappa\text{-Cl}$  has been confirmed with other experimental probes, for example using  $^1\text{H}$  NMR and AC susceptibility measurements as shown in Fig. 22(a) [248]. These results confirmed that a first order transition occurs between the insulating AFM state and the metallic or superconducting states [248]. An S-shaped first order transition line separates the insulating semiconducting (and AFM) states on at low pressure from the metallic (and superconducting) states at high pressure (see Fig. 22). This line ends in at a critical point at approximately  $T_c \sim 40$  K. At low temperature near the transition line, AFM and SC are found to coexist (see further discussion below), giving way to pure SC under increasing pressure [248].  $X = \text{Cu}[\text{N}(\text{CN})_2]\text{I}$  ( $\kappa\text{-I}$ ) has a pressure-temperature phase diagram similar to  $\kappa\text{-Cl}$  but shifted slightly towards the insulating phase [225, 249, 250]. Fewer experimental results are available for this salt due to sample preparation difficulties. At ambient pressure  $\kappa\text{-I}$  is insulating at low temperature; however, to our knowledge AFM order has not yet been confirmed in this salt.

The isostructural  $\kappa\text{-Br}$  is superconducting at ambient pressure with  $T_c = 11.6$  K with no AFM phase [21], and this salt is therefore placed in the U-SC region in Fig. 22(a). It is believed that the larger Br ion, relative to Cl, induces “chemical pressure” on the BEDT-TTF layer.  $X = \text{d}8\text{-}\kappa\text{-Br}$  is located in the same phase diagram at lower pressure than  $\kappa\text{-Br}$  and has phase segregated regions of AFM and SC at low temperature [223, 251].  $\text{d}8\text{-}\kappa\text{-Br}$  has a somewhat lower  $T_N = 15$  K than  $\kappa\text{-Cl}$  and  $T_c = 11.5$  K [223, 251]. Below about 20K, the  $\text{d}8\text{-}\kappa\text{-Br}$  NMR spectra splits into two components demonstrating the phase segregation between AFM and metallic/SC phases [223]. This indicates that  $\text{d}8\text{-}\kappa\text{-Br}$  should be placed at roughly  $P \sim 250$  bar in Fig. 22(a), nearly exactly in between the AFM and SC phases. Partially deuterated [252, 253] and mixed samples of the form  $\kappa\text{-}[(\text{h-BEDT-TTF})_{1-x}(\text{d-BEDT-TTF})_x]\text{Cu}[\text{N}(\text{CN})_2]\text{Br}$  [254, 255] have also

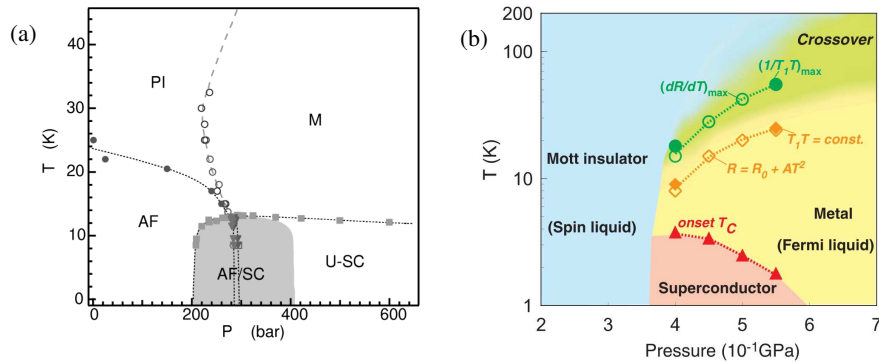


Figure 22. (a) Temperature-pressure phase diagram of  $\kappa$ -(ET)<sub>2</sub>Cu[N(CN)<sub>2</sub>]Cl determined by <sup>1</sup>H NMR and AC susceptibility measurements. Reprinted with permission from Ref. [248], © 2000 The American Physical Society. AF, PI, and M are antiferromagnetic, paramagnetic insulating, and metallic phases, respectively. Phase segregation between AF and SC takes place in the AF-SC region, while U-SC denotes a uniform SC state. (b) Phase diagram for  $\kappa$ -(ET)<sub>2</sub>Cu<sub>2</sub>(CN)<sub>3</sub>. Reprinted with permission from Ref. [256], © 2005 The American Physical Society

been studied, which show a range of superconducting  $T_c$ 's.

An important consideration for interpreting experimental data on  $\kappa$ -(ET)<sub>2</sub>X is the presence of phase segregation below 35–40 K between the AFM and metallic or superconducting phases [223]. This suggests that AFM and SC are competing phases. Phase segregation is indicated for example by the cooling rate dependence of  $T_c$  in  $\kappa$ -Cl and deuterated  $\kappa$ -Br [257]. NMR results [223] do not distinguish between phase segregation on a macroscopic or nanometer length scale. While nanometer-scale phase segregation cannot be fully ruled out, real space optical imaging on  $\kappa$ -[(h-BEDT-TTF)<sub>1-x</sub>(d-BEDT-TTF)<sub>x</sub>]Cu[N(CN)<sub>2</sub>]Br found macroscopic (micron size) AFM and metallic domains [255, 258]. Non-deuterated  $\kappa$ -Br is further from the AFM phase, but the presence of stretched exponential spin-relaxation below  $T \approx 25$  K also suggests some degree of phase segregation [259]. In comparison, the ambient pressure superconductor  $\kappa$ -(ET)<sub>2</sub>Cu(NCS)<sub>2</sub> shows a single exponential decay of spin-relaxation, suggesting phase segregation is not present [259].

**Spin liquid phase.**  $\kappa$ -(ET)<sub>2</sub>Cu<sub>2</sub>(CN)<sub>3</sub> ( $\kappa$ -CN) is considered as one of the best candidates for a quantum spin liquid (QSL) [215, 260]. As shown in Fig. 22(b), in the phase diagram for  $\kappa$ -CN, the candidate QSL state is adjacent to SC [256]. The <sup>1</sup>H NMR signal remarkably does not change down to 32 mK (except for a small broadening below about 4 K [261]), which is an energy scale several orders of magnitude smaller than the estimated inter-dimer exchange coupling,  $J \sim 250$  K [262].  $\kappa$ -CN is however a superconductor under pressure with  $T_c = 3.9$  K [263, 264]. A higher  $T_c \sim 7$  K has been found under conditions of uniaxial strain [233]. As in other  $\kappa$ -phase salts, the magnetic susceptibility begins to decrease at about 50 K, although the material remains paramagnetic at low temperature [262, 264]. The disadvantage of <sup>1</sup>H NMR studies is however the small hyperfine coupling between protons at the ends of the BEDT-TTF molecules and conduction electrons. <sup>13</sup>C NMR is much more sensitive because the central C atoms of the ET molecule are much more strongly coupled to conduction electrons [265]. In  $\kappa$ -CN, the <sup>13</sup>C NMR signal begins to broaden below around 70 K, suggesting the development of inhomogeneity [266, 267]. This broadening however disappears under pressure [268]. The Knight shift, which measures the intrinsic spin susceptibility without impurities, decreases slowly below 50 K and then sharply below 10 K [266]. As in other  $\kappa$  salts the NMR relaxation rate  $1/(T_1 T)$  increases as temperature decreases, but turns around and decreases below 10 K [266].

Many experiments have noted a transition or crossover at around 6 K, as well as a second change at lower temperature ( $\sim 1$  K). At 6 K, the <sup>13</sup>C  $1/T_1$  changes from being proportional to  $T^{1/2}$  to being temperature-independent [267]. Below about 1 K the temperature dependence of  $1/T_1$  changes again, becoming proportional to  $T^{3/2}$  [267].  $\mu$ SR in zero or weak magnetic fields confirms these three distinct temperature regions in  $\kappa$ -CN [269–271]. Importantly, a widened distribution of internal fields was not observed at zero field, meaning that the broadening and inhomogeneity observed by <sup>13</sup>C NMR are caused by the magnetic field. The effect of the field at low temperature is to create a “weak-moment antiferromagnet” state, which phase separates with the zero field state [270, 271]. At the 6 K transition the formation of bosonic pairs was suggested, with a second transition to a condensed phase at lower temperature to a spin-gapped

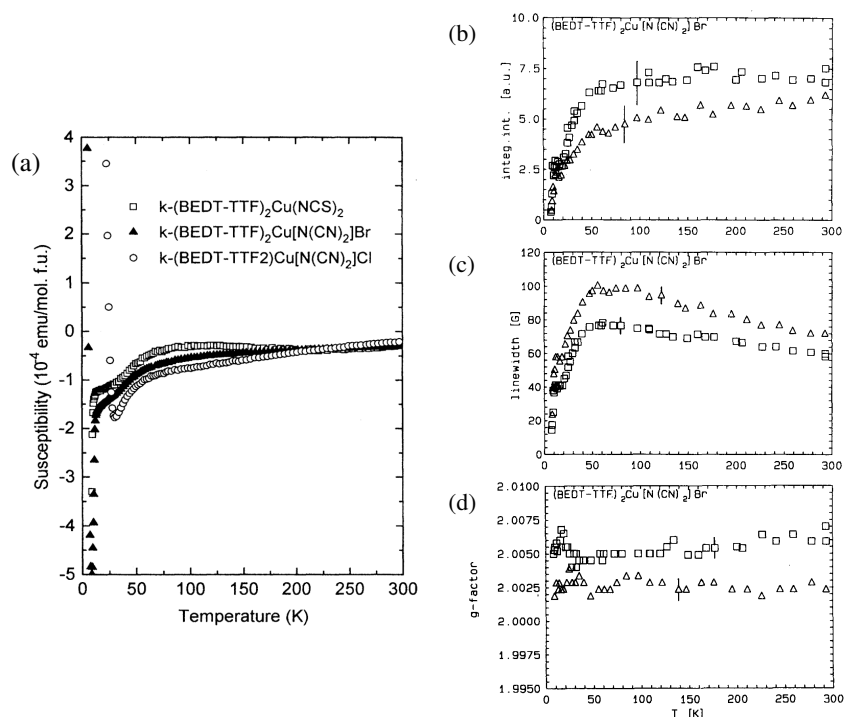


Figure 23. (a) Static susceptibility of  $\kappa$ -Cl,  $\kappa$ -Br, and  $\kappa$ -NCS. Reprinted with permission from Ref. [274], © 1995 The American Physical Society. (b)-(d) ESR parameters of  $\kappa$ -Br versus temperature. Squares and triangles correspond to the field perpendicular and parallel to the conducting plane, respectively. Reprinted with permission from Ref. [275], © 1992 Elsevier.

phase with  $\Delta \approx 3.5$  mK [270].

Under pressure, the resistivity of  $\kappa$ -CN drops suddenly below about 10 K for  $P \sim 0.4$  GPa [256]. This was interpreted as a first-order transition from Mott to a metallic state, which under lower temperature becomes superconducting [256]. Near the transition to the metallic state, two separate components are observed in the NMR signal, at first suggesting the presence of phase segregation into metallic and insulating domains [256]. However, the absence of hysteresis in measurements of the resistivity and lack of two distinct signals in  $^{13}\text{C}$  NMR suggest that the transition is not first order [268].  $^{13}\text{C}$  NMR measurements under pressure found a similar pressure dependence of  $1/(T_1T)$  to  $\kappa$ -Br under pressure, with a peak in  $1/(T_1T)$  at around 10 K that moves to higher temperatures under pressure [268].

One of the unresolved puzzles concerning  $\kappa$ -CN is the apparent disagreement between low temperature specific heat and thermal conductivity measurements. The specific heat  $C_p$  of  $\kappa$ -CN is linear in  $T$  at low temperature (0.75 to 2.5 K), characteristic of a gapless energy spectrum [272].  $C_p$  is also independent of magnetic field up to 8 T [272]. Thermal conductivity measurements (as well as  $\mu\text{SR}$ ) indicate the presence of a small spin gap [273].

*Pseudogap.* A number of experiments indicate some kind of phase transition or crossover occurring at around 50 K within the metallic state of  $\kappa$ -(ET)<sub>2</sub>X. In both  $\kappa$ -Br and  $\kappa$ -NCS an anomaly in the derivative of the resistivity is seen at around 50 K [277, 278]. Anomalies in the lattice expansivity reminiscent of second-order phase transitions are seen in the same temperature region in both of these salts [279]. In particular, NMR experiments (see reference [265] for a review) give strong evidence that this transition is to a pseudogapped state. As shown in Fig. 23(a), the static magnetic susceptibility begins to gradually decrease below around 100 K, decreasing more steeply below around 50 K [274]. Similarly, the ESR integrated intensity (see Fig. 23(b)) remains constant from 300 K down to about 50 K, below which it drops indicating a nonmagnetic ground state [275]. Similar behavior is seen in the  $^{13}\text{C}$  NMR  $1/(T_1T)$  [274, 280].  $1/(T_1T)$  is nearly identical for  $\kappa$ -Cl and  $\kappa$ -Br (see Fig. 24(a)) from 300 K down to 50 K ( $\kappa$ -NCS is similar) [274, 280]. Below 50 K  $1/(T_1T)$  diverges as  $T$  approaches  $T_N$  for  $\kappa$ -Cl, while  $1/(T_1T)$  decreases for  $\kappa$ -Br and  $\kappa$ -NCS [274, 280]. Closer to  $T_c$  some differences are however observed between different superconducting  $\kappa$  salts. In  $\kappa$ -

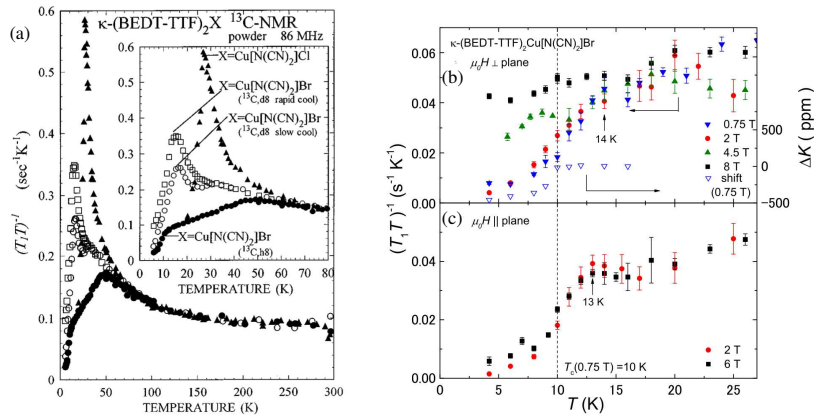


Figure 24. (a)  $1/(T_1T)$  versus temperature for  $\kappa$ -Cl and  $\kappa$ -Br. The inset expands the low temperature region. Reprinted with permission from Ref. [251], © 1997 The American Physical Society. (b)-(c)  $1/(T_1T)$  for  $\kappa$ -Br at low temperature. For  $\kappa$ -Br (but not  $\kappa$ -NCS), a depression of  $1/(T_1T)$  is observed in the temperature range immediately above  $T_c$ . Reprinted with permission from Ref. [276], © 2014 The American Physical Society.

NCS ( $T_c=9.3$  K), the  $^{13}\text{C}$  NMR  $1/(T_1T)$  is nearly constant in the region approximately 5 K above  $T_c$ , with nearly the same value as the low-temperature normal state, which was determined by suppressing SC with a magnetic field (see Fig. 24) [251, 276].  $\kappa$ -CN behaves similarly, with a nearly constant  $1/T_1T$  just above  $T_c$  [281]. In contrast, in  $\kappa$ -Br ( $T_c=11.4$  K),  $1/(T_1T)$  decreases in the region approximately 5 K above  $T_c$  before reaching  $T_c$  (Figs. 24(b) and (c)) [276]. A similar reduction of  $1/(T_1T)$  occurs just above  $T_c$  in d8- $\kappa$ -Br, where the effect appears to start at even higher temperature ( $\sim 30$  K) [223]. It has been suggested that the apparent higher pseudogap temperature in d8- $\kappa$ -Br is due to it being closer to the AFM phase in the phase diagram [223]. However, it is also possible that the apparent stronger temperature dependence of  $1/(T_1T)$  in the 10–30 K region is due to AFM domains in the phase segregated state [276].

The Nernst effect is another experimental probe that has been used to detect the presence of a pseudogap in the high- $T_c$  cuprates above  $T_c$  [282, 283]. In the Nernst effect, a transverse electric field is generated from a temperature gradient and a perpendicular magnetic field. Normally a weak effect, the transverse field is strongly enhanced in a superconductor due to superconducting vortices. In the cuprates, the large Nernst signal within the pseudogap region but well above  $T_c$  has been interpreted by some authors as evidence for a fluctuating superconducting state [282]. This conclusion, has however, been contradicted by others who believe that large Nernst signal accompanies stripe formation [284]. Measurements of the Nernst effect in  $\kappa$ -NCS and  $\kappa$ -Br both show a clear Nernst signal below  $T_c$  [285]. For  $\kappa$ -Br the Nernst coefficient is positive slightly above  $T_c$  suggesting a pseudogap, while for  $\kappa$ -NCS there is no signal above  $T_c$  [285]. It has been suggested that the presence of the Nernst effect above  $T_c$  in  $\kappa$ -Br but not in  $\kappa$ -NCS is again due to  $\kappa$ -Br being closer to the AFM state in the phase diagram [285]. Experiments on  $X=\text{Cu}[\text{N}(\text{CN})_2]\text{Cl}_{1-x}\text{Br}_x$  found a positive Nernst signal at an even higher temperature ( $\approx 5T_c$ ) for  $x = 0.73$ , which was interpreted as an increase in SC fluctuations due to closer proximity to the Mott transition [286]. Another possible reason for the difference is the different amount of disorder in these two salts [259]; in the context of cuprates it was suggested that the positive Nernst signal tracks the disorder that accompanies stripe formation in the La-based cuprates [284]. Magnetic torque measurements on  $\kappa$ -NCS did however give evidence for fluctuating SC above  $T_c$  [287].

**Symmetry of Superconducting order parameter.** Experiments using a wide range of probes suggest that the SC pairing throughout the  $\kappa$ -(ET) $_2$ X family is singlet with nodes in the order parameter. Experimental techniques that have been employed include site-selective  $^{13}\text{C}$  NMR [265, 288], specific heat measurements [289], penetration depth measurements [290–292], as well as STM tunneling experiments [293–295]. The temperature dependence of the NMR relaxation rate  $1/T_1$  in the superconducting state goes as  $T^3$  at low temperatures, consistent with an order parameter with nodes. This  $T^3$  dependence has been verified in  $\kappa$ -Br [288],  $\kappa$ -NCS [265], and  $\kappa$ -CN [281].

Experiments are generally in agreement that the SC is singlet rather than triplet, and that the order parameter has nodes. However, there is less agreement on the location of nodes in the conducting plane. The order parameter symmetries  $d_{x^2-y^2}$  and  $d_{xy}$  have nodes in different locations, rotated by  $45^\circ$ . An additional complication is that the axes in the effective dimer lattice ( $\hat{x}$  and  $\hat{y}$  in Fig. 20) are rotated at  $45^\circ$  from the crystal axes ( $\hat{a}$  and  $\hat{c}$  in Fig. 20). In

the experimental literature  $d_{x^2-y^2}$  symmetry is usually assumed to have nodes at  $45^\circ$  to the crystal axes, while  $d_{xy}$  has nodes along the crystal axes. In theory based on the effective half-filled model these two symmetries are interchanged. Magneto-optical [296] and specific heat measurements in a magnetic field find the nodes aligned with the crystal axes [297]. Thermal conductivity [298] and STM measurements [293, 294] however find the nodes between the crystal axes. STM measurements on partially deuterated  $\kappa$ -Br found two possible  $d$ -wave order parameters, probably due to phase segregation [295]. Recent STM measurements on  $\kappa$ -Br suggest a mixed order parameter of  $s + d_{x^2-y^2}$  form [299]. Such a symmetry is predicted by numerical calculations within a  $\frac{3}{4}$ -filled model (see Section 6.2.5) as well by RPA spin-fluctuation calculations [218, 299]. Disagreement in the location of the nodes is probably due to experimental factors; determining the symmetry of the order parameter from thermodynamic measurements is difficult because one must separate the small electronic contribution to the specific heat from the much larger phonon background [289, 300]. For example, earlier specific heat measurements had suggested  $s$ -wave pairing [301, 302], but more recent work is consistent with nodes in the gap function [289, 300]. In summary, experiments now agree that nodes *are* present in the superconducting order parameter, but more work appears to be needed to precisely define the functional form and determine to what degree it varies for different members of the  $\kappa$ -(ET)<sub>2</sub>X family. In relation to this point, experiments under pressure that are sensitive to the position of the nodes have yet to be performed on  $\kappa$ -CN.

*Charge and lattice effects.* Within the effective  $\frac{1}{2}$ -filled band picture at large Hubbard  $U$  there is minimal charge fluctuation and lattice effects are also expected to be weak. Nevertheless, a wide range of experiments indicate that charge and lattice degrees of freedom play important roles in the low-temperature physics  $\kappa$ -(ET)<sub>2</sub>X. Most features in the phase diagram of  $\kappa$ -Cl (the superconducting transition, MI transitions both as a function of temperature and pressure, and the critical point) were observed as anomalies in the propagation speed of ultrasound [303]. The AFM transition at  $T_N \sim 27$  K however could not be identified [303]. Precision lattice expansivity measurements have also been performed on several  $\kappa$ -(ET)<sub>2</sub>X [279, 304]. As mentioned above, anomalies are seen in the lattice expansivity in the  $\sim 50$  K region where the pseudogap opens. At lower temperatures, in  $\kappa$ -CN a large anomaly is seen in the in-plane lattice expansivity at 6 K, along with a smaller feature at 2.8 K [305]. The sharpness of the 6 K feature suggests a real phase transition rather than a crossover, and the shape of the feature is similar to the anomaly seen at the SP transition in (TMTTF)<sub>2</sub>X [174]. These features were unaltered by magnetic fields up to 8 T [305].

Measurements of the frequency-dependent dielectric constant for  $\kappa$ -CN found that the dielectric constant goes through a broad maximum at temperature  $T_{\max}$  for  $T \lesssim 50$  K [306]. The peak strengthens with decreasing frequency, with  $T_{\max}$  shifting to lower temperature [306]. The response was interpreted as being similar to relaxor ferroelectrics, with anti-ferroelectric ordering in the case of  $\kappa$ -CN. Because of the low frequencies involved, random domains of short-range charge order (with unequal charges on the two BEDT-TTF molecules in a dimer) are presumed to be fluctuating rather than the charges on individual ET molecules. The extrapolated temperature for antiferroelectric ordering is approximately 6 K [306]. While the first measurements were performed with the electric field perpendicular to the BEDT-TTF layers [306], the effect was confirmed for fields parallel to the layers [307]. A similar dielectric response is seen in  $\kappa$ -Cl [308, 309] (see [310] for a review). In the case of  $\kappa$ -Cl, the ferroelectric ordering coexists with the AFM state, giving rise to the suggestion that  $\kappa$ -Cl is an example of a multiferroic [308]. Microwave measurement of the in-plane dielectric constant of  $\kappa$ -CN also confirms the activity of charge degrees of freedom [311]. Below 6 K a peak in the microwave dielectric function is seen, which is suppressed by a magnetic field [311]. Significant sample preparation, strain, and thermal effects were noted however.

The suggestion that fluctuating charge order is present in  $\kappa$ -(ET)<sub>2</sub>X has led to a renewed interest in examining signatures of CO in these materials. No signatures of static CO are seen by NMR [215, 265]. Optical spectroscopy with light polarized perpendicular to the BEDT-TTF layers has a much smaller background from the conduction electrons in the planes and is therefore particularly sensitive to charge disproportionation on the molecules. No indications of CO to within  $\Delta n = 0.01e$  were seen in the optical spectra down to 12 K for  $\kappa$ -Br,  $\kappa$ -Cl, and  $\kappa$ -NCS [312]. Fluctuating CO with a timescale slower than  $10^{-11}$ s was excluded by [312]. Other optical measurements do give evidence for a fluctuating CO in  $\kappa$ -CN. Raman scattering found line broadening of the charge-sensitive  $\nu_2$  mode below 50 K in  $\kappa$ -CN [313]. This broadening was only seen in samples cooled slowly enough, and also disappeared under the effect of pressure once the material entered the metallic phase [313]. In pump-probe experiments on  $\kappa$ -CN, a response at  $30 \text{ cm}^{-1}$  was interpreted as evidence for fluctuating charge order within each dimer [314]. This mode begins to increase in amplitude at approximately the same temperature as the relaxor dielectric response begins ( $\sim 40$  K), and steeply increases and saturates at 6 K [314]. The fast recovery time from the photoexcitation (2.6 ps) rules out

a structural transformation or formation of domains as seen in  $\alpha$ -(ET)<sub>2</sub>I<sub>3</sub>, where the timescale is orders of magnitude slower [315, 316]. This is also much faster than the timescale of the measurements of [306].

The possibility of static CO of very small amplitude in  $\kappa$ -(ET)<sub>2</sub>X also remains. In the (TMTTF)<sub>2</sub>X salts a peak in the dielectric constant at the charge ordering temperature is seen, which is of much larger relative magnitude than in  $\kappa$ -(ET)<sub>2</sub>X [172]. Based on the known magnitude of CO in (TMTTF)<sub>2</sub>X,  $\Delta n=0.26e$  for X=AsF<sub>6</sub> and  $\Delta n=0.12e$  X=PF<sub>6</sub> [94], and the smaller relative dielectric anomaly in  $\kappa$ -(ET)<sub>2</sub>X, a charge disproportionation smaller than  $\Delta n\sim 0.01e$  is expected [309].

A second explanation for the unusual dielectric response is that it is coming not from charge disproportionation within the  $\kappa$ -(ET)<sub>2</sub>X dimers, but from the domain walls between microscopic insulating and metallic domains [317]. This picture is supported by the general tendency towards phase segregation below  $\sim 50$  K seen in many  $\kappa$ -phase materials noted above. The slower time scale seen in dielectric constant experiments (of order kHz and lower frequencies) also supports the existence of larger domains. Various explanations have been given for the source of disorder. One intrinsic source of disorder in many  $\kappa$ -(ET)<sub>2</sub>X is the Cu atom valence in the anion layer, which can also lead to a mixture of Cu<sub>2</sub>(CN)<sub>3</sub> and Cu(CN)[N(CN)<sub>2</sub>] anions [264, 318]. However, similar relaxor dielectric response is seen in both X=Cu<sub>2</sub>(CN)<sub>3</sub> and X=Ag<sub>2</sub>(CN)<sub>3</sub> [232, 319]. Another suggestion is that the anion layer, and in particular the CN groups for X=Cu<sub>2</sub>(CN)<sub>3</sub> are a source of disorder [307, 319]. Regarding the influence of the anion layer, it is important to note that relaxor dielectric response very similar to that found in  $\kappa$ -CN is also observed in other dimerized CTS, for example  $\beta'$ -(ET)<sub>2</sub>ICl<sub>2</sub> [320] and  $\beta$ -(*meso*-DMBEDT-TTF)<sub>2</sub>PF<sub>6</sub> [321]. Like  $\kappa$ -(ET)<sub>2</sub>X,  $\beta'$ -(ET)<sub>2</sub>ICl<sub>2</sub> is strongly dimerized and also has AFM order. However, the lack of a complex anion layer in  $\beta'$ -(ET)<sub>2</sub>ICl<sub>2</sub> shows that anion layer disorder is not an essential component to the relaxor dielectric response seen in many CTS.

*Charge ordered  $\kappa$  phase salts.* A family of  $\kappa$ -phase CTS that shows a variety of CO transitions are the  $\kappa$ -(ET)<sub>2</sub>Hg(SCN)<sub>3-n</sub>X<sub>n</sub>, with  $n = 1, 2$  and X a variety of anions (F, Cl, Br, I) [322]. MI transitions involving lattice and likely CO are found over a range of temperatures from 30 to 140 K within this series [229–231, 322–324]. The lower transition temperatures suggest the possibility that the CO pattern has unequal charges *within* each ET dimer. In  $\kappa$ -(ET)<sub>2</sub>Hg(SCN)<sub>2</sub>Br, the MI transition occurs at 100 K; for a deuterated analog (D<sub>8</sub>-ET)<sub>2</sub>Hg(SCN)<sub>2</sub>Br the transition temperature is lower (60 K) [323]. Below the transition the susceptibility in both materials decreases regardless of the crystal orientation indicating a spin-gapped ground state. The susceptibility can be fitted by the form usually assumed for a SP gap,  $\chi = C/T \exp(\Delta/T)$ , with  $\Delta \approx 496$  and 340 K for the protonated and deuterated Br salts, respectively [323]. We argue in Section 6.2.3 that spin gap accompanying CO is a signature that the charge-ordering does not correspond to a simple WC. In  $\kappa$ -(ET)<sub>2</sub>Hg(SCN)<sub>2</sub>I the resistivity decreases rapidly below 50 K [324]; the properties of this salt may be complicated however by the presence of two crystallographically distinct ET layers.

A number of experimental probes, as well as the effect of hydrostatic pressure have been used to investigate the Hg(SCN)<sub>2</sub>Cl salt, where  $T_{MI} \sim 30$  K [229–231]. Optical measurements find CO with  $\Delta n=0.2e$  below the transition [230]. No obvious change of the crystal structure is visible in X-ray analysis, further suggesting that the MI transition corresponds to pure charge ordering with unequal charges within each BEDT-TTF dimer [230]. While the MI transition and presence of CO is now well-confirmed in this material, the properties at lower temperatures are less certain. Slightly below  $T_{MI}$  a kink was observed in the resistivity at 27–28 K, together with a small decrease in the susceptibility which might indicate tendency towards a spin-gapped ground state [229]. However, at lower temperatures an increase in the susceptibility, as well as ESR measurements suggested that the ground state has AFM order [229]. While many samples have displayed similar anomalies in  $\rho(T)$  below  $T_{MI}$  which are reproducible under repeated heating and cooling, details of the properties are sample dependent [231]. This possibly suggests that there are several competing magnetic states. Under pressure, CO is suppressed, but to date no SC has been detected down to 1.5 K [231].

In some families of  $\kappa$ -(ET)<sub>2</sub>X CO occurs at relatively high temperatures, with the CO pattern consisting of dimers of neutral BEDT-TTF<sup>0</sup> and dimers of BEDT-TTF<sup>+1</sup> [325, 326], analogous to the CO pattern BCDW-II in 1D (see Fig. 7(f)). Such a CO state with two holes on a *single* dimer has a large charge gap and would be expected to remain an insulator at low temperatures, as is also found for quasi-1D BCDW-II CTS [34]. Materials with this CO state include  $\kappa$ -[Et<sub>4</sub>N](ET)<sub>4</sub>M(CN)<sub>6</sub>·3 H<sub>2</sub>O with M=Co<sup>III</sup>, Fe<sup>III</sup>, and Cr<sup>III</sup> [327–331], and  $\kappa$ -(ET)<sub>4</sub>- [M(CN)<sub>6</sub>][N(C<sub>2</sub>H<sub>5</sub>)<sub>4</sub>]<sub>2</sub>·2H<sub>2</sub>O with M=Co<sup>III</sup> and Fe<sup>III</sup> [325, 326, 332]. To our knowledge SC has not been observed in any of these  $\kappa$ -(ET)<sub>2</sub>X.

*Recent developments.* Here we highlight several  $\kappa$ -(ET)<sub>2</sub>X CTS that have been of interest recently, X=Ag<sub>2</sub>(CN)<sub>3</sub>, B(CN)<sub>4</sub>, and CF<sub>3</sub>SO<sub>3</sub>.

The properties of  $\kappa$ -(ET)<sub>2</sub>Ag<sub>2</sub>(CN)<sub>3</sub> are quite similar to  $\kappa$ -(ET)<sub>2</sub>Cu<sub>2</sub>(CN)<sub>3</sub>: at ambient pressure Ag<sub>2</sub>(CN)<sub>3</sub> displays QSL-like properties with no apparent magnetic order to low temperatures [232, 319]. Compared to Cu<sub>2</sub>(CN)<sub>3</sub>, Ag<sub>2</sub>(CN)<sub>3</sub> is believed to be slightly closer to an isotropic triangular dimer lattice [232, 319]. One experimental advantage of Ag<sub>2</sub>(CN)<sub>3</sub> over Cu<sub>2</sub>(CN)<sub>3</sub> is the absence of Cu valence impurity difficulties as Ag<sup>2+</sup> is unknown. Under pressure Ag<sub>2</sub>(CN)<sub>3</sub> is also superconducting with T<sub>c</sub>=5.2 K, with a slightly higher pressure required compared to Cu<sub>2</sub>(CN)<sub>3</sub> [232].

X=B(CN)<sub>4</sub> and CF<sub>3</sub>SO<sub>3</sub> are unique compared to most previously studied  $\kappa$  CTS because their effective dimer frustration  $t'/t$  is significantly larger than 1 [222, 234, 235]. For B(CN)<sub>4</sub>  $t'/t \sim 1.44$  at room temperature [222]. B(CN)<sub>4</sub> undergoes a second-order transition to a spin-gapped state at 5 K; the large ratio of  $2\Delta/T_c = 10.6$  is inconsistent with a weak-coupling mechanism for the gap [222]. While pressure does reduce the gap, this material remains semiconducting with no SC up to 2.5 GPa [222]. It is unknown whether any CO coexists with the SG at low temperatures as Raman measurements have been performed only for T>T<sub>SG</sub>.

For CF<sub>3</sub>SO<sub>3</sub>  $t'/t$  is even larger, about 1.8 at room temperature [235]. At ambient pressure AFM order is found with T<sub>N</sub> = 2.5 K [234, 235]. The much lower Néel temperature (and  $t'/t > 1$ ) may indicate this AFM state has a different spin pattern than the dimer Néel state found in  $\kappa$ -Cl [234, 235]. SC is found with T<sub>c</sub> =4.8 K at a pressure of 2.2 GPa [235]. This the only known CTS superconductor with T<sub>N</sub> <T<sub>c</sub>.

*Summary.* The cation layer in  $\kappa$ -(ET)<sub>2</sub>X is characterized by strongly dimerized anisotropic triangular lattices with one hole per dimer. Relatively few have antiferromagnetic ( $\kappa$ -(ET)<sub>2</sub>Cu[N(CN)<sub>2</sub>]Cl,  $\kappa$ -d8-(ET)<sub>2</sub>Cu[N(CN)<sub>2</sub>]Br, and  $\kappa$ -(ET)<sub>2</sub>CF<sub>3</sub>SO<sub>3</sub>) or spin liquid ( $\kappa$ -(ET)<sub>2</sub>Cu<sub>2</sub>(CN)<sub>3</sub> and  $\kappa$ -(ET)<sub>2</sub>Ag<sub>2</sub>(CN)<sub>3</sub>) ground states while the others exhibit ambient pressure superconductivity (SC), charge order, or spin gap. SC is spin-singlet and the order parameter has nodes. There is evidence for pseudogap in  $\kappa$ -(ET)<sub>2</sub>Cu[N(CN)<sub>2</sub>]Br and  $\kappa$ -(ET)<sub>2</sub>Cu(NCS)<sub>2</sub> at temperatures higher than T<sub>c</sub>. In  $\kappa$ -(ET)<sub>2</sub>Cu<sub>2</sub>(CN)<sub>3</sub> there occurs a transition or crossover at 6 K whose nature is not understood. There is evidence for intra-dimer charge-fluctuation, relatively strong lattice effects, and a small spin gap. A spin gap has been observed in some charge-ordered  $\kappa$ -(ET)<sub>2</sub>X. The Néel temperature T<sub>N</sub> is lower than the superconducting critical temperature T<sub>c</sub> in  $\kappa$ -(ET)<sub>2</sub>CF<sub>3</sub>SO<sub>3</sub>, which would seem to argue against spin-fluctuation driven SC. Taken together, the observations overall also do not support an effective  $\frac{1}{2}$ -filled band model.

### 5.1.2. $\beta$ , $\beta'$ , and $\beta''$ type CTS

The  $\alpha$ ,  $\beta$ ,  $\beta'$ ,  $\beta''$ , and  $\theta$  type CTS all have structures composed of stacks of BEDT-TTF molecules forming 2D layers (see Fig. 25). In the  $\beta$ ,  $\beta'$ , and  $\beta''$  structures, the molecules are all parallel to each other, while in  $\theta$  and  $\alpha$  (see Sections 5.1.3 and 5.1.4), molecules in adjacent stacks are inclined at an angle to each other (see Fig. 25) [364]. The differences between the  $\beta$ ,  $\beta'$ , and  $\beta''$  structures arise from different relative orientations and regularity of the molecules in the stacks. The appropriate tight-binding lattice for all of these structures is rectangular with some amount of frustration (hopping in the diagonal directions). Because of the angle as well as the relative position between two neighboring molecules strongly influences the inter-molecular transfer integrals between them, the  $t_{ij}$  for these families can be significantly different from each other.

A large number of  $\beta$ -type CTS are superconducting (see Table 4). Many undergo a MI transition at ambient pressure to a charge- and/or bond-ordered insulating state and are superconducting under the application of pressure. There are also many ambient-pressure superconductors. Antiferromagnetic ground states are found in the  $\beta'$  structure, as well as in some  $\beta$  structure CTS containing magnetic ions such as Fe (see below). Besides BEDT-TTF, superconductors in these structures have been synthesized with BEDO-TTF, DMET, *meso*-DMBEDT-TTF, BDA-TTF, and other related molecules [365].

In the  $\beta$  structures the molecular stacks are dimerized with varying degrees of dimerization. In the  $\beta'$  structure the stacks are slightly staggered (see Fig. 25), which leads to a larger intra- than inter-stack hopping. Because of this, the  $\beta'$ -structure CTS are considered more one-dimensional than the  $\beta$ -structure CTS [364]. On the other hand, in the  $\beta''$  structure [351, 366], the inter-stack overlaps are larger than the intra-stack overlaps. For this reason,  $\beta''$  materials are usually considered more 2D than  $\beta$  or  $\beta'$ .

formula	$T_c$ (K)	$P_c$ (GPa)	Notes	references
$\beta$ -(ET) $_2$ I $_3$	1.4 (8.1)	0 (0.1)	$\beta_L$ ( $\beta_H$ )	[333, 334]
$\beta$ -(ET) $_2$ IBr $_2$	2.7	0		[335]
$\beta$ -(ET) $_2$ I $_2$ Br	—	—	no SC to 0.5 K	[336]
$\beta$ -(ET) $_2$ AuI $_2$	5	0		[337]
$\beta$ -(ET) $_2$ ReO $_4$	2	0.4	$T_{MI}=81$ K	[20]
$\beta$ -(BDA-TTP) $_2$ SbF $_6$	7.5	0		[338]
$\beta$ -(BDA-TTP) $_2$ AsF $_6$	5.8	0		[338]
$\beta$ -(BDA-TTP) $_2$ PF $_6$	5.9	0		[338]
$\beta$ -(BDA-TTP) $_2$ FeCl $_4$	3.0	0.4	$T_{MI}=118$ K, $T_N=8.2$ K	[339, 340]
$\beta$ -(BDA-TTP) $_2$ GaCl $_4$	3.1	0.4	$T_{MI}=113$ K	[341]
$\beta$ -(BDA-TTP) $_2$ I $_3$	~10	1.0		[342]
$\beta$ -( <i>meso</i> -DMBEDT-TTF) $_2$ PF $_6$	4.3	0.1	$T_{MI}=91$ K, $T_{CO}=70$ K	[343, 344]
$\beta$ -( <i>meso</i> -DMBEDT-TTF) $_2$ AsF $_6$	4.2	0.4	$T_{MI}=90$ K, $T_{CO}=70$ K	[345]
$\beta'$ -(ET) $_2$ ICl $_2$	14.2	8.2	$T_N=22$ K	[214, 346]
$\beta'$ -(ET) $_2$ AuCl $_2$	—	—	$T_N=28$ K	[347, 348]
$\beta'$ -(ET) $_2$ SF $_3$ CF $_2$ SO $_3$	—	—	$T_{SG}=T_{MI}=45$ K	[349]
$\beta'$ -(ET) $_2$ CF $_3$ CF $_2$ SO $_3$	—	—	$T_{SG}=T_{MI}=30$ K	[350]
$\beta''$ -(ET) $_2$ AuBr $_2$	1.1	1.0*	$T_{CO} \sim 8$ K, *uniaxial	[351, 352]
$\beta''$ -(ET) $_2$ SF $_3$ CH $_2$ CF $_2$ SO $_3$	5.2	0	$T_{CO}=200$ K, fluct. CO	[353]
$\beta''$ -(ET) $_2$ SF $_3$ CHFCF $_2$ SO $_3$	—	—	$T_{MI}=190$ K	[354]
$\beta''$ -(ET) $_2$ SF $_3$ CH $_2$ SO $_3$	—	—	semiconductor 300 K	[349]
$\beta''$ -(ET) $_2$ SF $_3$ CHFSO $_3$	—	—	metallic, fluct. CO	[349]
$\beta''$ -(ET) $_2$ CF $_3$ CH $_2$ SO $_3$	—	—	CO semiconductor 300K	[355, 356]
$\beta''$ -(DODHT) $_2$ AsF $_6$	~3	1.5		[357]
$\beta''$ -(DODHT) $_2$ PF $_6$	2.3	1.3	$T_{MI}=255$ K	[357, 358]
$\beta''$ -(DODHT) $_2$ BF $_4$ ·H $_2$ O	~3	1.5		[358]
$\beta''$ -(ET) $_4$ [(H $_3$ O)Ga(C $_2$ O $_4$ ) $_3$ ](C $_5$ H $_5$ N)	~2	0	incomplete SC	[359]
$\beta''$ -(ET) $_4$ [(H $_3$ O)Ga(C $_2$ O $_4$ ) $_3$ ](C $_6$ H $_5$ NO $_2$ )	7.5	0		[359]
$\beta''$ -(ET) $_4$ Pt(CN) $_4$ H $_2$ O	2.0	0.65		[360]
$\beta''$ -(ET) $_4$ Pd(CN) $_4$ H $_2$ O	1.2	0.70		[361]
$\beta''$ -(ET) $_3$ Cl $_2$ ·2H $_2$ O	2-3	1.1	$T_{MI} \sim 130$ K	[362, 363]

Table 4. Summary of the properties of  $\beta$ ,  $\beta'$ , and  $\beta''$  salts discussed in this section.

$\beta$  CTS. The  $\beta$  structure CTS were the first class of organic superconductors discovered after the TMTSF/TMTTF group of materials [20]. Among  $\beta$ -(ET) $_2$ X several ambient-pressure superconductors are found, including X=I $_3$  [333], IBr $_2$  [335], and AuI $_2$  [337]. X=I $_2$ Br is not superconducting however, due to disorder in the anions [336, 367]. X=I $_3$  is superconducting at ambient pressure with a relatively low  $T_c$  of about 2 K [333], but a higher  $T_c$  phase ( $T_c=8.1$  K) appears under pressure [334]. X=ReO $_4$  at ambient pressure undergoes a first-order MI transition at  $T_{MI} = 81$  K [20]. The insulating state is accompanied with a period-4 lattice distortion along the stack [368], and is non-magnetic with a large drop in the ESR spin susceptibility accompanying the transition [369]. Optical studies estimated the gap at  $2\Delta \approx 480$  cm $^{-1}$  and confirmed that the low-temperature state is not a result of anion ordering [370]. Under a pressure of 0.4 GPa X=ReO $_4$  becomes superconducting with  $T_c \sim 2$  K [20].

Several superconductors as well as non-magnetic insulating states are found in the series  $\beta$ -(BDA-TTP) $_2$ X [372, 373]. While these have the same  $\beta$  structure as  $\beta$ -(ET) $_2$ I $_3$ , the inter-molecular overlap is weaker, with overlap integrals roughly half those of  $\beta$ -(ET) $_2$ I $_3$  [338]. Here X=SbF $_6$ , AsF $_6$ , and PF $_6$  are ambient pressure superconductors with  $T_c$ 's in the 6-7 K range [338]. X=GaCl $_4$ , FeCl $_4$ , and I $_3$  are superconducting under pressure with  $T_c \approx 3$  K, with I $_3$  having a higher  $T_c \approx 8$  K [339, 341, 342].

At ambient pressure, X=GaCl $_4$  and FeCl $_4$  undergo MI transitions at 118 K and 113 K respectively [339, 341]. FeCl $_4$  undergoes an AFM transition at 8.5 K which is absent in the isostructural GaCl $_4$ , suggesting that the transition involves the Fe spins [339, 341]. In GaCl $_4$  the ambient-pressure state at low temperatures is a nonmagnetic insulator: the ESR magnetic susceptibility drops sharply by almost two orders of magnitude at  $T_{MI}$ , indicating a first-order transition [374]. Raman measurements are consistent with a lowered lattice symmetry at the transition, likely involving bond and/or charge order [374]. X-ray structural analysis found superlattice reflections below  $T_{MI}$  similar to those found in  $\alpha$ -(ET) $_2$ I $_3$  indicating a doubling of the periodicity of the BDA-TTP stacks (to period 4) [374, 375].

$\beta$ -(*meso*-DMBEDT-TTF) $_2$ X (X=AsF $_6$  and PF $_6$ ) is another  $\beta$ -phase CTS with CO adjacent to SC (see Fig. 27) where the CO state has been studied in detail [345]. The properties of AsF $_6$  and PF $_6$  are very similar [345]. PF $_6$  undergoes a MI transition at about 90 K, and SC appears under pressure with a  $T_c=4.3$  K [343]. CO has been confirmed via optical methods, with an estimated charge disproportionation of  $\Delta n \sim 0.5$  for X=PF $_6$  under ambient pressure [376]. While the pattern of CO has been described as a ‘‘checkerboard’’, this would be true only if *pairs*

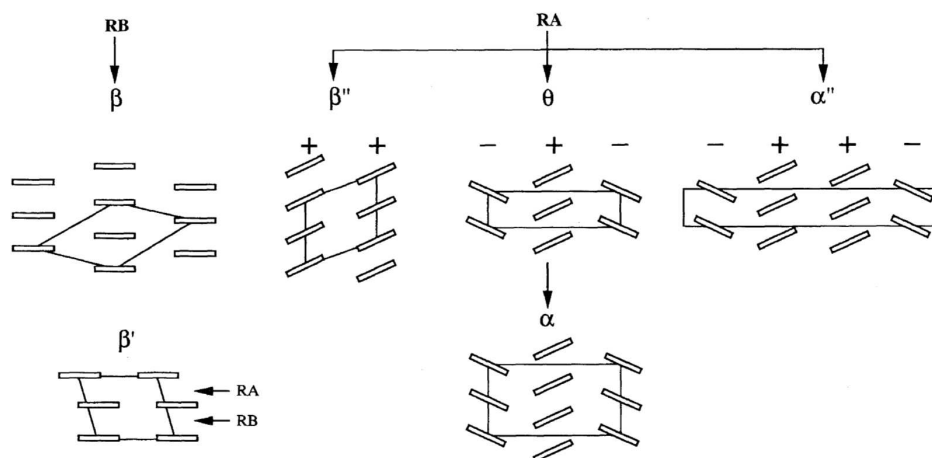


Figure 25. Comparison of  $\alpha$ ,  $\beta$ , and  $\theta$  structures. Ring-over-atom (RA) and ring-over-bond (RB) denote two different kinds of inter-molecular overlaps. Reprinted with permission from Ref. [364], © 1998 The Chemical Society of Japan.

of charge-rich and charge-poor molecules are considered as individual sites; considering the individual *molecules* as sites, the CO follows a clear  $\cdots 1100 \cdots$  pattern along the DMBEDT-TTF stacks as shown in Fig. 27(a) [371]. In infrared reflectivity and Raman measurements on  $\text{PF}_6$ , CO was found in the insulating state below 70 K at ambient pressure [344, 376, 377]. Under pressure, experiments noted the formation of metallic regions of short-range CO (see Fig. 27). The sequence of MI and CO transitions appears similar to  $\theta$ -( $\text{ET}$ ) $_2\text{RbZn}(\text{SCN})_4$  (see Section 5.1.3). First, in the 70–100 K region X-ray superlattice reflections appear, along with weak diffuse scattering above 100 K [344]. This state was interpreted as a dimer-Mott insulator (without CO) [344, 377]. Following the lattice distortion and MI transition, CO appears at a lower temperature, approximately 70 K. At the same time as CO appears the susceptibility drops, indicating a non-magnetic state [345]. In spatially resolved optical measurements, phase segregation in micron-sized domains was seen between the CO state and the dimer-Mott state, with the volume fraction of CO increasing below 70 K as the temperature was lowered [377].

$\beta'$  CTS. Among the  $\beta'$  CTS no ambient pressure superconductors are known, consistent with their more quasi-1D structures. However, under pressure  $\beta'$ -( $\text{ET}$ ) $_2\text{ICl}_2$  [346] currently has the highest  $T_c=14.2$  K of all CTS superconductors but is only superconducting under very high pressures (8.2 GPa) requiring a diamond anvil pressure cell (see Fig. 28) [214]. At ambient pressure  $\beta'$ -( $\text{ET}$ ) $_2\text{ICl}_2$  is a semiconductor at room temperature. The ground state at ambient pressure is AFM with  $T_N=22$  K [378]. The related salt  $\beta'$ -( $\text{ET}$ ) $_2\text{AuCl}_2$  has a slightly higher  $T_N=28$  K with however no SC reported in pressures up to 9.9 GPa [347, 348]. The AFM moment in the AFM state of  $\text{ICl}_2$  is large, approximately  $1.0 \mu_B$  per dimer [379]. Under a pressure of approximately 0.6 GPa the magnetic state however changes [379–381], both in moment (which decreases above 0.6 GPa), and Néel temperature (which increases above 0.6 GPa) [379, 381]. At the same time the spin susceptibility decreases with pressure [379]. These changes likely imply a change in the magnetic AFM ordering pattern. Like the insulating  $\kappa$ -phase CTS,  $\beta'$ -( $\text{ET}$ ) $_2\text{ICl}_2$  displays a very similar frequency-dependent relaxor dielectric response [320]. Under the application of a static electric field at 15 K, two additional peaks on both sides of the charge-sensitive  $\nu_2$  Raman mode were observed, indicating field-induced CO within each dimer [383].

Due to the very high pressure required, few experimental results are available in the pressure region approaching superconductivity. In optical measurements, under pressure, intra-dimer charge transfer features shift to much lower energy [382]. This was interpreted as a change of the effective electronic state of the material from an effectively  $\frac{1}{2}$ -filled dimer-Mott state at ambient pressure to a  $\frac{3}{4}$ -filled correlated insulator with a tendency to CO (see Fig. 28) [382].

While  $\beta'$ -( $\text{ET}$ ) $_2\text{ICl}_2$  is AFM at ambient pressure, some  $\beta'$  are nonmagnetic insulators under ambient pressure.  $\beta'$ -( $\text{ET}$ ) $_2\text{SF}_5\text{CF}_2\text{SO}_3$  (not to be confused with the  $\beta''$  salts with similar anions—see below) enters a spin-gapped state below 45 K [349]. In this salt the susceptibility increases slightly with decreasing temperature, with a broad peak at

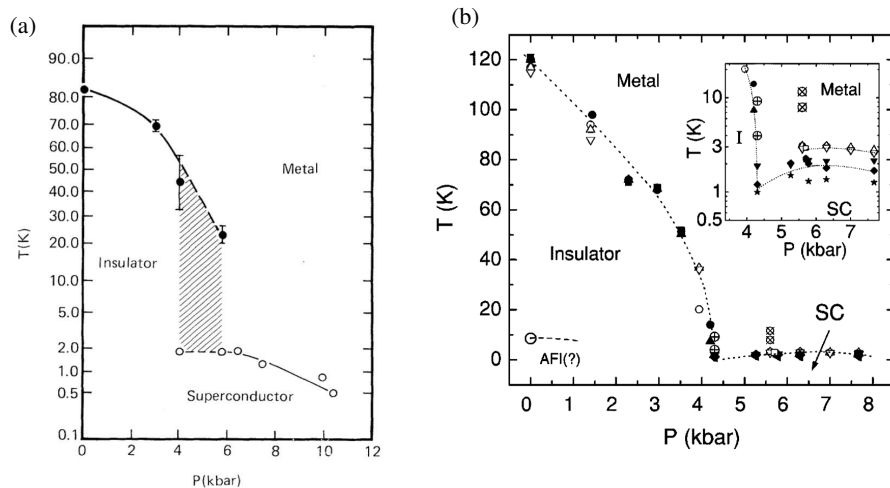


Figure 26. (a) Phase diagram of  $\beta$ -(ET) $_2$ ReO $_4$ . Thermal hysteresis was observed in the hatched area. Reprinted with permission from Ref. [20], © 1983 The American Physical Society. (b) Phase diagram of  $\beta$ -(BDA-TTP) $_2$ MCl $_4$ ,  $M$ =Fe, Ga. Solid symbols are for  $M$ =Fe and open symbols for  $M$ =Ga Reprinted with permission from Ref. [340], © 2004 The American Physical Society.

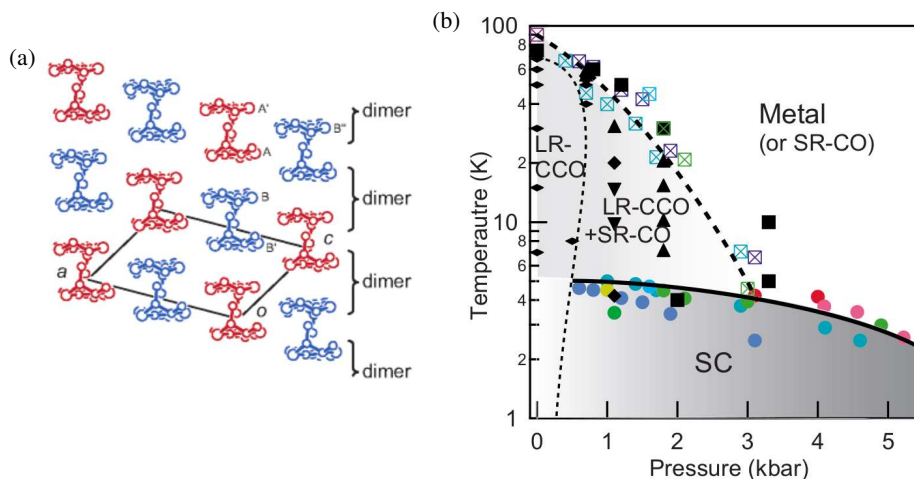


Figure 27. (a) Charge order state found in  $\beta$ -(*meso*-DMBEDT-TTF) $_2$ PF $_6$ . Reprinted with permission from Ref. [371], © 2006 The American Chemical Society. (b) Phase diagram. Long-range charge order (LR-CCO) evolves into short range order charge order (SR-CO) and SC under pressure. Reprinted with permission from Ref. [344], © 2009 The American Physical Society.

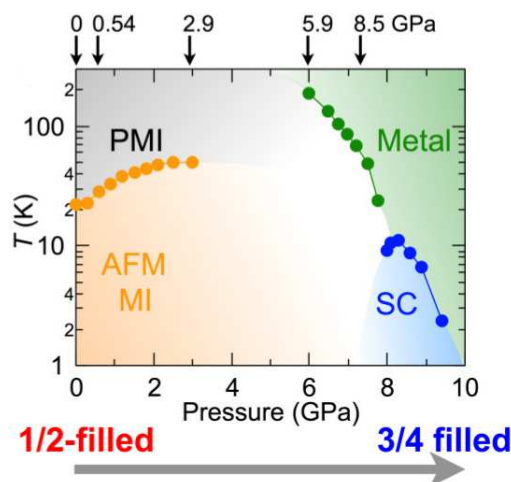


Figure 28. Phase diagram of the  $\beta'$ -(ET)<sub>2</sub>ICl<sub>2</sub>. Reprinted with permission from Ref. [382]. © 2015 The American Physical Society.

around 150 K [349]. A steep drop in the susceptibility for all orientations of the applied magnetic field indicates an SP-like spin-gapped state [349]. The similar  $\beta'$ -(ET)<sub>2</sub>CF<sub>3</sub>CF<sub>2</sub>SO<sub>3</sub> also has a spin-gap transition at 30 K [350]. For this salt Raman investigation did find evidence for symmetry breaking caused by lattice distortion in the SP phase [350]. CO however was not detected in  $\beta'$ -(ET)<sub>2</sub>CF<sub>3</sub>CF<sub>2</sub>SO<sub>3</sub>, although CO with molecular charges of 0.6 and 0.4 was found in a different structural variant ( $\delta'$  structure) of the same salt [350].

**$\beta''$  CTS.** The first  $\beta''$  salt discovered was  $\beta''$ -(ET)<sub>2</sub>AuBr<sub>2</sub> [351].  $\beta''$ -(ET)<sub>2</sub>AuBr<sub>2</sub> stays metallic until low temperatures. SC has not been found under isotropic pressure, but a  $T_c$  of approximately 1 K was found under conditions of uniaxial strain [352, 384]. AuBr<sub>2</sub> has some unusual properties at low temperatures that could indicate a weak CO state: At ambient pressure there is a kink in the resistivity at 110 K followed by a slight upturn at around 8 K that is suppressed by pressure [384]. X-ray superlattice reflections are observed at low temperatures, indicating bond ordering below 6.5 K [352]; optical studies are consistent with a gapped state coexisting with free carriers [385]. There is also a steep decrease in the susceptibility at low temperatures indicating a non-magnetic ground state [384].

$\beta''$ -(ET)<sub>2</sub>SF<sub>5</sub>R were the first CTS superconductors discovered with both cations and anions organic [349, 353, 354]. A summary of the different known R and structures is given in reference [387] (note that some also crystallize in structures different from  $\beta''$ ). Recent investigations into this series have noted the presence of SC, CO, as well as CO fluctuations.

In this series of salts  $R$ =CH<sub>2</sub>CF<sub>2</sub>SO<sub>3</sub> ( $\beta''$ -SC) is the only known superconductor, with  $T_c$  = 5.2 K under ambient pressure [353]. In this series the cation layer is composed of two inequivalent dimerized stacks of BEDT-TTF molecules along the  $a$  axis. Differences in the relative distance of these two BEDT-TTF stacks to SO<sub>3</sub><sup>-</sup> and SF<sub>5</sub> groups in the anion layer lead to a slight charge imbalance between the two stacks even at 300 K, with a charge density of  $0.5+\Delta n/2$  on one stack and  $0.5-\Delta n/2$  on the other [349, 354]. In the superconducting material the inequivalence between the two stacks decreases at lower temperatures [354].

Other members of the family include  $R$ =CHF<sub>2</sub>CF<sub>2</sub>SO<sub>3</sub> ( $\beta''$ -MI), which undergoes a first-order MI transition at 190 K, below which the stack dimerization increases greatly [354].  $R$ =CH<sub>2</sub>SO<sub>3</sub> ( $\beta''$ -I) is a charge-ordered semiconductor already at room temperature [349], with the degree of CO estimated as  $\Delta n \sim 0.4$  from optical measurements [356]. The  $R$ =CHF<sub>2</sub>SO<sub>3</sub> ( $\beta''$ -M) remains metallic to low temperature [349].  $\beta''$ -(ET)<sub>2</sub>CF<sub>3</sub>CH<sub>2</sub>SO<sub>3</sub> is another salt that is semiconducting and charge ordered at 300 K, with the CO amplitude estimated as  $\Delta n \sim 0.6$  [355, 356].

Optical investigations have provided evidence for CO and charge fluctuations in this series of salts [356, 386, 388]. In  $\beta''$ -SC the  $\nu_{27}$  IR mode splits below 200 K without any structural change [388]. Compared to  $\beta''$ -M, in  $\beta''$ -SC at low temperatures a pronounced optical conductivity in the mid-IR (300 ~ 1000 cm<sup>-1</sup>) develops [388] (see Fig. 29). A strong signal at ~40 cm<sup>-1</sup>, related to an inter-site phonon mode, also develops at low temperature in the superconducting salt [388]. These features were interpreted as the formation of a pseudogap, and evidence for the

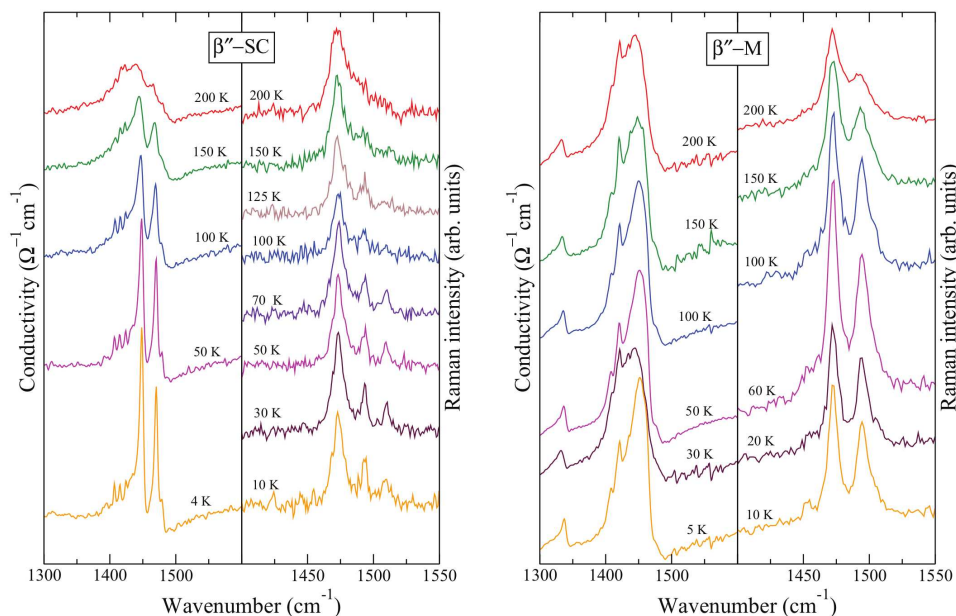


Figure 29. Optical conductivity and Raman spectra as a function of temperature for the  $\beta''$ -( $\text{ET}$ ) $_2\text{SF}_5\text{R}$  family,  $\text{R}=\text{CH}_2\text{CF}_2\text{SO}_3$  ( $\beta''$ -SC) and  $\text{R}=\text{CHF}_2\text{SO}_3$  ( $\beta''$ -M). The emergence of the doublet in the optical conductivity below about 150 K indicates the presence of charge order in  $\beta''$ -SC but not in  $\beta''$ -M. Reprinted with permission from Ref. [386]. © 2014 The American Physical Society.

importance of lattice coupling in the low-temperature electronic state [388]. Raman experiments have given more details (see Fig. 29) [386]. In Raman experiments on  $\beta''$ -SC, the totally-symmetric charge coupled mode splits at low temperature [386]. This response was well fit by a two-state “jump” model of charge fluctuations within a dimer [389, 390]. The authors concluded that (i) charge fluctuations are present in both  $\beta''$ -SC and  $\beta''$ -M which are related to the fluctuation of charge between the two inequivalent BEDT-TTF stacks; (ii) in  $\beta''$ -SC (but not  $\beta''$ -M), a second static coexisting CO develops at low temperature, which is instead characterized by an additional charge disproportionation *within* each of the BEDT-TTF stacks (see Fig. 29).

$\beta''$ -(DODHT) $_2\text{X}$  has smaller intermolecular interactions along the stacks compared to  $\beta''$ -( $\text{ET}$ ) $_2\text{AuBr}_2$  [357]. At ambient pressure and room temperature  $\text{X}=\text{AsF}_6$ ,  $\text{PF}_6$ ,  $\text{TaF}_6$ , and  $\text{BF}_4\cdot\text{H}_2\text{O}$  are semiconductors, and  $\text{X}=\text{AsF}_6$ ,  $\text{PF}_6$ , and  $\text{BF}_4\cdot\text{H}_2\text{O}$  become superconducting with  $T_c \approx 3$  K under  $\sim 1.5$  GPa pressure [357, 358, 391–393]. At ambient pressure in  $\text{X}=\text{PF}_6$ , the resistivity starts to increase steeply below 255 K indicating a transition to an insulating state [358]. The low temperature state is a non-magnetic insulator. X-ray satellite reflections indicate structural changes at low temperature and a charge-ordered ground state has been suggested [358, 394]; however to our knowledge direct charge-sensitive measurements have not yet been performed on this series of CTS.

Some other superconducting  $\beta''$  CTS include  $\beta''$ -( $\text{ET}$ ) $_4$ [( $\text{H}_3\text{O}$ ) $M$ ( $\text{C}_2\text{O}_4$ ) $_3$ ]Y, where  $M=\text{Ga}$ ,  $\text{Cr}$ , or  $\text{Fe}$ , and  $Y=\text{pyridine}$  ( $\text{C}_2\text{H}_5\text{N}$ ) or nitrobenzene ( $\text{C}_6\text{H}_5\text{NO}_2$ ) [359, 397, 398]. Of these,  $M=\text{Ga}$  and  $\text{Cr}$  with  $Y=\text{C}_6\text{H}_5\text{NO}_2$  and  $M=\text{Fe}$  with  $Y=\text{C}_6\text{H}_5\text{CN}$  are superconductors (see Fig. 30) [359, 395–397]. In this group of CTS, the resistivity decreases from room temperature until around 100 K, below which it rises to a peak at about 10 K before SC [395].  $T_c$ 's up to about 8 K are reported [395]. As in  $\kappa$ -( $\text{ET}$ ) $_2\text{X}$ , the low temperature state of this series appears to have a disordered mixture of insulating and metallic phases [395, 396]. A very low carrier density was also noted [395]. For  $M=\text{Ga}$  and  $Y=\text{C}_6\text{H}_5\text{NO}_2$ , Raman scattering spectra split below 100 K indicating charge ordering (see Fig. 30(a)); the splitting is more pronounced in the non-superconducting salts [395]. Further Raman measurements found charge disproportionation of amplitude  $0.5 \sim \Delta n \sim 0.13$  [399]. Based on the pattern of bonds lengths, the CO pattern along the stacking direction was inferred to be  $\cdots 1100 \cdots$  [399].

$\beta''$ -( $\text{ET}$ ) $_3\text{Cl}_2\cdot\text{H}_2\text{O}$  is an interesting CTS superconductor, as by stoichiometry it appears to be  $\frac{2}{3}$ - rather than  $\frac{3}{4}$ -filled [362, 400]. This salt has a wide MI transition at around 100-160 K, and is superconducting with a  $T_c$  of 2-3 K at  $\sim 1.6$  GPa [362, 363, 400, 401]. Optics and  $^{13}\text{C}$  NMR measurements indicate CO below 100 K, and a decrease in

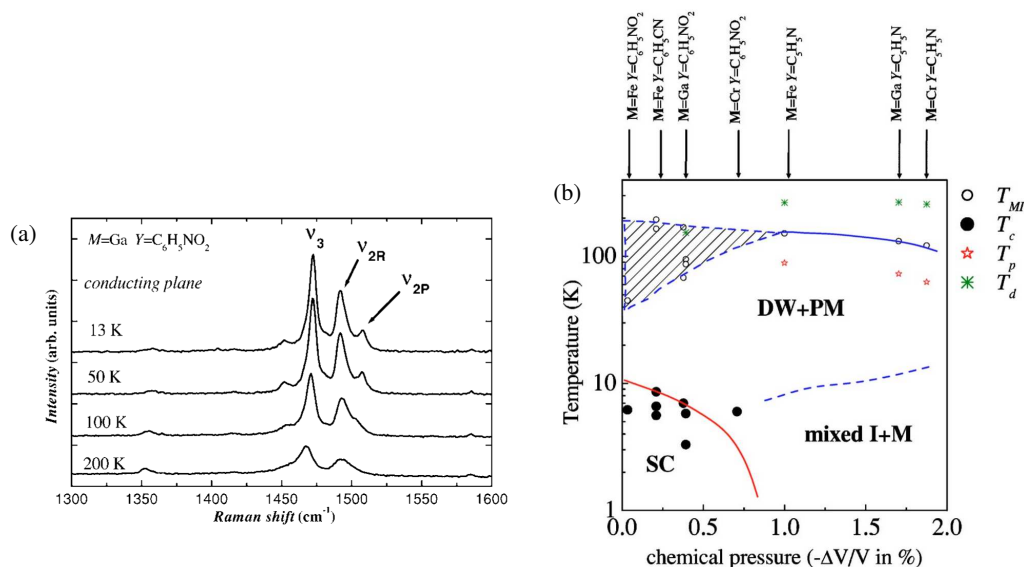


Figure 30. (a) Raman spectra of  $\beta''$ -(ET) $_4$ [(H $_3$ O) $_4$ M(C $_2$ O $_4$ ) $_3$ ]·Y,  $M$ =Ga,  $Y$ =C $_6$ H $_5$ NO $_2$ . The splitting of the  $\nu_2$  mode below  $\sim$ 100 K indicates charge ordering. Reprinted with permission from Ref. [395]. © 2005 The American Physical Society. (b) Phase diagram of this family of CTS. Here  $\Delta V/V$  is the fractional change of the unit cell volume compared to  $M$ =Fe.  $T_p$  and  $T_d$  are features observed in resistivity measurements. I, M, DW, and PM are insulating, metallic, density wave, and paramagnetic metallic phases, respectively. Reprinted with permission from Ref. [396]. © 2004 The American Physical Society.

the susceptibility shows that the low-temperature state is a non-magnetic singlet [399, 402]. The unit cell contains three independent molecules. The charges on these three sites in the CO state was estimated as  $0.4e$ ,  $0.6e$ , and  $1.0e$  [402]. This corresponds to a single  $\rho = 1$  stack of BEDT-TTF molecules, and two stacks with  $\rho = \frac{1}{2} \pm \Delta n/2$ . X-ray structural results at low temperature are consistent with one stack having  $\rho \sim 1.0e$  charge [401]. NMR measurements under pressure indicate that the spin-singlet state remains under pressure until the SC phase is reached [402].

**Summary.** A charge-order-to-superconductivity transition is common in the  $\beta$ ,  $\beta'$  and  $\beta''$  materials. In all cases where the pattern of the charge order or bond distortion is known, it appears to be different from that of the simple Wigner crystal (WC), in that in more than one direction the charge order pattern is  $\cdots 1100 \cdots$ . Spin gap (SG) often accompanies the charge order or occurs as a separate lower temperature phase. A SG is not expected within the WC (see Section 6.2.2, in particular Fig. 51).

### 5.1.3. $\theta$ CTS

In the  $\theta$  structure (see Fig. 25), molecules in neighboring stacks are tilted with respect to each other by a dihedral angle of  $100$ – $140^\circ$  (see Fig. 31) [403]. Among the  $\theta$ -(ET) $_2$ X,  $X$ =I $_3$  is superconducting at ambient pressure with  $T_c$ = $3.6$  K [403]. I $_3$  is metallic at  $300$  K. The resistivity drops with decreasing temperature, with a more rapid decrease below around  $75$  K [403]. At low temperatures the optical conductivity displays a Drude peak at low frequencies [404, 405]. Unlike conventional metals however, the Drude response has a long tail extending to higher frequencies [405]. As temperature increases, the Drude peak is replaced by a far-IR peak, which shifts to higher energy and loses spectral weight with increasing temperature [405]. These features were suggested as indicating that I $_3$  is a strongly correlated system showing “bad metal” characteristics [405].

Besides  $X$ =I $_3$ , a variety of  $\theta$  salts with  $X$ = $MM'$ (SCN) $_4$  are known, which in general undergo MI transitions between  $20$  and  $250$  K (see Fig. 31) [406–408]. The  $\theta$  CTS have been grouped into a phase diagram shown in Fig. 31(b). A convenient parameter is the dihedral angle  $\theta$  between neighboring molecules (see Fig. 31) [408]. The hopping integral  $t_p$  (see Fig. 32(a)) between stacks depends sensitively on  $\theta$ , with  $t_p$  increasing with decreasing  $\theta$  [408]. The smaller bandwidth for larger  $\theta$  was assumed to increase  $T_{MI}$  [408], although a simultaneous decrease in  $c$  (see Fig. 32(b)) increasing  $V_c$  also favors an insulating state [409]. Unlike most other insulating CTS, in  $\theta$ -(ET) $_2$ X  $T_{MI}$  increases with

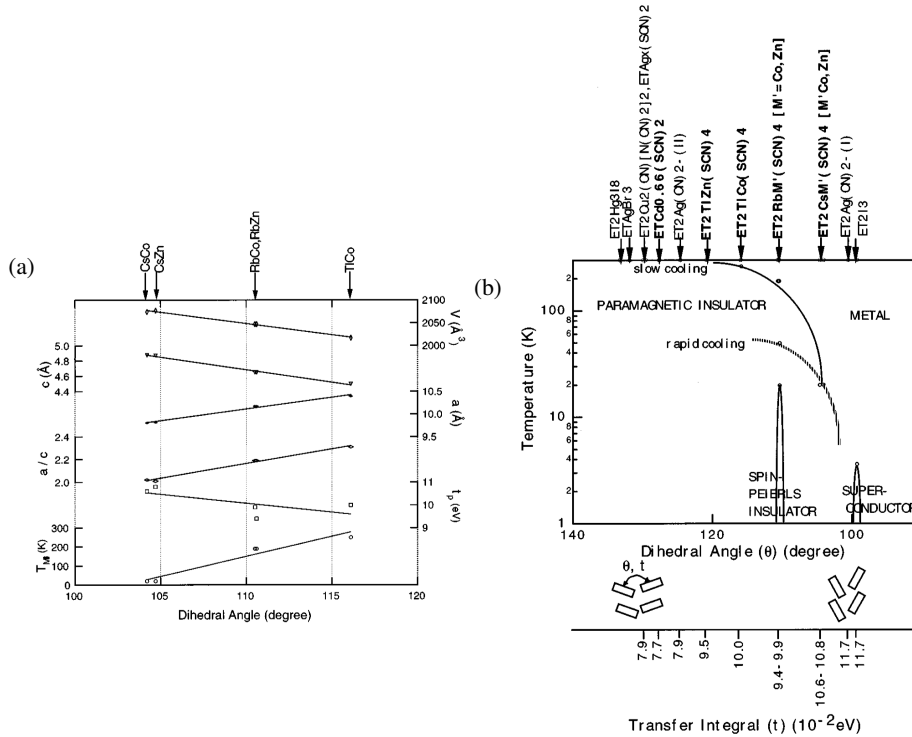


Figure 31. (a) Variation of structural parameters and MI transition temperature for several  $\theta$ -(ET)<sub>2</sub>XMM'(SCN)<sub>4</sub>. (b) Phase diagram. Here the horizontal axis is the dihedral angle between BEDT-TTF stacks (see text). Reprinted with permission from Ref. [408]. © 1998 The American Physical Society.

hydrostatic pressure [408, 409]. A complication in studying the insulating phases in the  $\theta$  CTS is that their properties depend strongly on cooling rate, with slow cooling required to obtain long-range order (LRO) [408].

CO coincides with  $T_{MI}$  in  $\theta$ -(ET)<sub>2</sub>X. The CO transition has been studied most intensely for two series of  $\theta$  CTS,  $\theta$ -(ET)<sub>2</sub>MM'(SCN)<sub>4</sub> with either (M,M')=(Rb, Zn) or (Rb, Co) and (Cs, Zn) or (Cs, Co) [406]. In the RbZn salt  $T_{MI} \sim 195$  K, and CO was confirmed by NMR (see Fig. 32(a)) [410, 412, 413], Raman and IR reflectance [414], X-rays [411, 415], and dielectric permittivity [416]. Here the MI/CO transition is first order, with a dimerization of the stacks occurring below  $T_{MI}$ . The pattern of CO is the horizontal stripe shown in Fig. 32(b), with charge disproportionation  $\Delta n = 0.6$  [412, 414, 415]. Above  $T_{MI}$  evidence for fluctuating charge order is seen in NMR line broadening [410, 417] (see Fig. 32) and in diffuse X-ray scattering [418]. The periodicity of the diffuse scattering above  $T_{MI}$  is however not the same as the periodicity in the CO state, suggesting that two different charge order patterns are competing [418]. In RbZn no change in the magnetic susceptibility is seen at  $T_{MI}$  [408]. However, in slowly cooled samples, a second transition occurs at  $T_{SG} \approx 20$  K into a non-magnetic state [408, 419]. Below  $T_{SG}$  a structural symmetry change occurs breaking the screw-axis symmetry existing along the horizontal charge order stripe (see Fig. 32) [419]. Within this symmetry breaking, the bonds  $p_4$  in Fig. 32 become inequivalent, consistent with a dimerization along the horizontal stripe direction giving a spin gap [419]. We discuss this further in Sections 6.2.2 and 6.2.3.

In comparison to RbM', in the CsM' salts are weakly metallic until low temperature, when a MI transition occurs at approximately 20 K [408]. Unlike the well-ordered insulating state in slowly cooled RbM' samples, experiments on CsM' suggest a phase separated state at low temperature [420]. The resistivity begins to rise slightly below  $\sim 100$  K, and then increase steeply below 20 K [408].  $T_{MI}$  here also increases with pressure [408]. X-rays show diffuse scattering at  $\mathbf{q}_1=(2/3, k, 1/3)$  as well as  $\mathbf{q}_2=(0, k, 1/2)$  in the 50 – 120 K range, with  $\mathbf{q}_2$  (the same periodicity as in RbZn) becoming stronger at low temperatures [421]. The  $\mathbf{q}_2$  modulation however remains short-range however in CsZn [421]. However, a finite jump in the specific heat is observed at 20 K in CsZn, confirming that a phase transition takes place (as also for RbZn) [422]. For CsM' the susceptibility increases at low temperature rather than entering a

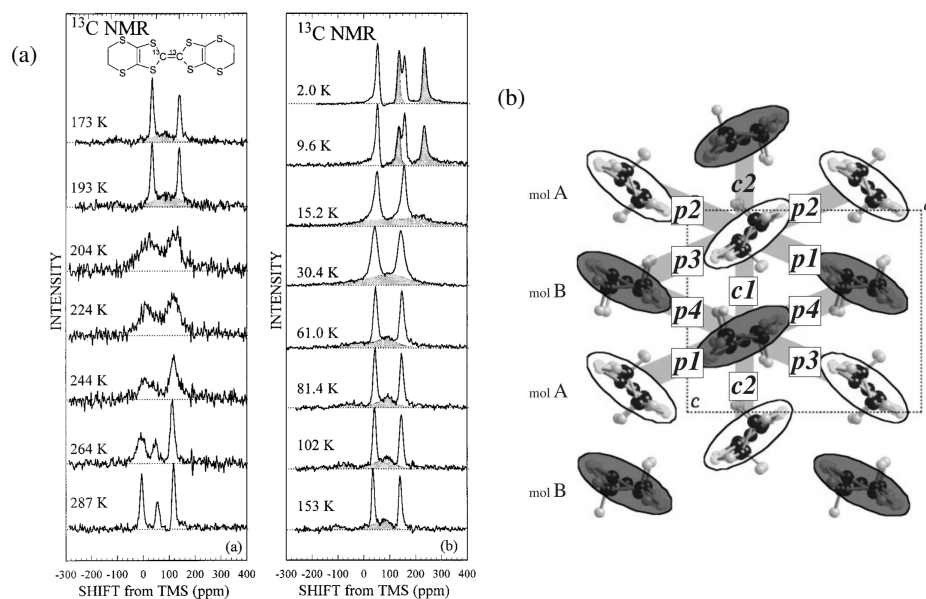


Figure 32. (a)  $^{13}\text{C}$  NMR spectra of  $\theta\text{-(ET)}_2\text{RbZn}'(\text{SCN})_4$  showing charge ordering at 195 K. Reprinted with permission from Ref. [410]. © 2000 The American Physical Society. (b) Horizontal stripe charge order found in  $\theta\text{-(ET)}_2\text{RbZn}'(\text{SCN})_4$  and other  $\theta$ -phase CTS. Here the dark and light ellipses denote charge-rich and charge-poor molecules, respectively. Note the charge occupancy pattern  $\cdots 1100\cdots$  along both the  $p$ -directions. Reprinted with permission from Ref. [411]. © 2004 The Physical Society of Japan.

spin-gapped state [408, 423]. Sample dependence was not noted in the low temperature susceptibility increase, ruling out Curie-tail impurities [423]. NMR and EPR results suggested three different temperature regimes: first, from 300 K to 140 K a region of charge fluctuations similar to those in RbZn above  $T_{\text{MI}}$ ; second, from 140 K to 50 K a slowing down of the charge fluctuations; and third, below 30 K a charge reorganization with the emergence of spin singlets *without* large charge disproportionation [423–425]. At low temperature some sites remain paramagnetic and cause the observed local magnetic moments [423–425]. Raman and IR investigation categorized  $\text{CsZn}$  as having short-range CO, with properties similar to those in RbZn which is rapidly cooled; under pressure long-range CO is stabilized [426].

Besides the  $\theta\text{-(ET)}_2\text{MM}'(\text{SCN})_4$  series, long-range horizontal stripe CO is seen in other  $\theta\text{-(ET)}_2\text{X}$ , for example in  $\text{X}=\text{Cu}_2\text{CN}[\text{N}(\text{CN})_2]_2$  below 220 K [427].

**Summary.** A metal-insulator transition to charge order is common in  $\theta\text{-(ET)}_2\text{X}$  and is often followed by a lower temperature transition to a nonmagnetic state with a spin gap. The pattern of the charge order at the lowest temperatures in most cases is the horizontal stripe (Fig. 32(b)), which is different from a simple Wigner crystal and has charge occupancies  $\cdots 1100\cdots$  along the two most strongly coupled directions. Superconductivity occurs in  $\theta\text{-(ET)}_2\text{I}_3$ .

#### 5.1.4. $\alpha$ CTS

The  $\alpha$  structure is nearly identical to the  $\theta$  structure (see Fig. 25), except the periodicity is doubled already in the room-temperature structure in the stacking direction by a weak dimerization.  $\alpha\text{-(ET)}_2\text{I}_3$  was discovered as a second crystal structure in the crystal growth of  $\beta\text{-(ET)}_2\text{I}_3$  [430]. This salt has been extensively studied because of its CO transition, unusual transport properties at low temperature, and superconductivity.  $\alpha\text{-(ET)}_2\text{I}_3$  undergoes a sharp MI transition at 135 K [430]. The susceptibility decreases with temperature until 135 K and then drops sharply at  $T_{\text{MI}}$ , indicating a nonmagnetic ground state [431]. The MI transition is suppressed by hydrostatic pressure, without however the appearance of SC. However, SC with  $T_c \sim 7$  K is found under conditions of  $\sim 0.2$  GPa uniaxial strain along the  $a$  axis (the  $a$  axis is the stacking direction, see Fig. 33) [432]. Unlike hydrostatic pressure,  $a$ -axis uniaxial strain does not change  $T_{\text{MI}}$  greatly, but instead greatly reduces the resistivity in the insulating state [432]. Strain along the other in-plane direction ( $b$  axis) reduced  $T_{\text{MI}}$  without the appearance of SC [432].

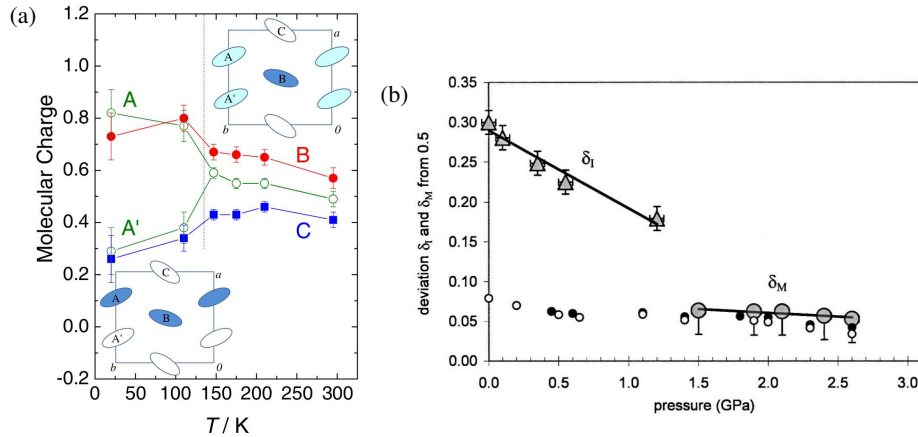


Figure 33. (a) Charge order transition in  $\alpha$ -(ET) $_2$ I $_3$  as measured by synchrotron X-ray scattering. Reprinted with permission from Ref. [428]. © 2007 The Physical Society of Japan. The insets show the crystal structure above and below the 135 K CO transition. A and A' are equivalent by inversion symmetry in the high-temperature phase. (b) Temperature and pressure dependence of the CO amplitude as determined by Raman spectroscopy. In the high-temperature phase the charge densities on sites A, A', B, and C are given by  $\rho_A = \rho_{A'} = \rho_B = 0.5 + \delta_M$  and  $\rho_C = 0.5 - 3\delta_M$ .  $\delta_I$  is defined in the CO phase as the average of the disproportionation of sites A and B,  $\delta_I = (\delta_A + \delta_B)/2$ . The CO phase vanishes under a hydrostatic pressure of approximately 1.5 GPa. Reprinted with permission from Ref. [429]. © 2003 The American Physical Society.

Charge order in  $\alpha$ -(ET) $_2$ I $_3$  has been confirmed by several experimental methods including optics [429, 433], X-rays [428, 434] and NMR [435, 436]. In this salt CO exists in both the high and low temperature phases (see Fig. 33). Above  $T_{MI}$ , alternate BEDT-TTF stacks are charge ordered in the pattern  $\cdots 1010 \cdots$  with a CO amplitude of  $\Delta n \sim 0.2$  [428, 429]. Below  $T_{MI}$  all stacks become charge ordered, with the CO pattern following a horizontal stripe as in  $\theta$ -(ET) $_2$ X. Unlike  $\theta$  where a spin gap only opens at lower temperatures, in  $\alpha$ -(ET) $_2$ I $_3$   $T_{SG}$  coincides with  $T_{MI}$ . Because of the lower symmetry of the  $\alpha$  structure compared to  $\theta$ , in the horizontal stripe CO in  $\alpha$  the bonds in the  $p$  direction (the bonds between molecules A and B in Fig. 33) become inequivalent at the MI transition. This is in contrast to the  $\theta$  CTS, where this inequivalence only occurs below the lower temperature magnetic transition [419].

The CO amplitude  $\Delta n$  is approximately 0.6 (see Fig. 33) [428, 429]. Like other CTS, evidence for relaxor ferroelectricity is found in measurements of the dielectric constant [437]. Measurements of the frequency dependence of the dielectric constant (with the electric field perpendicular to the BEDT-TTF layers) show two general effects [437]: first, for  $T \gtrsim 80$  K there is a gradual step-like decrease in the dielectric constant with decreasing temperature. The step feature shifts to larger temperatures at higher frequencies. Second, for low frequencies, a peak develops in the dielectric constant, which is located at 40–50 K for the lowest frequencies. Assuming the response corresponds to a relaxor ferroelectric, the extrapolated Curie-Weiss ordering temperature is 35 K [437]. It is unknown why these effects show up at temperatures that are much lower than  $T_{MI}=135$  K where the CO first occurs.

Hydrostatic pressure suppresses the CO, which vanishes at approximately 1.5 GPa [429]. The properties of  $\alpha$ -(ET) $_2$ I $_3$  under pressure are unusual.  $^{13}\text{C}$  NMR under a pressure of 2.3 GPa, where the CO is completely suppressed, show a vanishing of the spin susceptibility below approximately 50 K [438]. The transport properties under pressure are unusual and have been investigated by many authors. In the high-pressure state the resistivity becomes nearly constant in temperature [439, 440]. This was interpreted as a semiconductor in which as temperature decreases the mobility grows while the carrier density simultaneously falls [440]. Recently there has been great interest in the semi-metallic state of  $\alpha$ -(ET) $_2$ I $_3$  under pressure, which has been proposed as a candidate realization of a Dirac cone semi-metal [441, 442] (for a review see [443]). This is an intriguing possibility but beyond the scope of this review.

$\alpha$ -(ET) $_2$  MHg(SCN) $_4$  with  $M=\text{K, Rb, Tl, and NH}_4$  are another family of  $\alpha$ -phase conductors and superconductors [448–452]. The  $M=\text{NH}_4$  salt is an ambient pressure superconductor with  $T_c \sim 1$  K [450, 451]. For  $M=\text{K, Rb, and Tl}$  the resistivity drops with temperature, leveling off at around 10 K; below an anomaly about 8 K the resistance drops further [453, 454]. The resistivity decrease in some samples at low temperatures is suppressed by magnetic field below 100–300 mK, suggesting the appearance of a filamentary SC state [454, 455]. Hydrostatic pressure stabilizes the SC state, leading to the phase diagram shown in Fig. 34 [444, 456]. While  $T_c$  is low in this series at ambient or

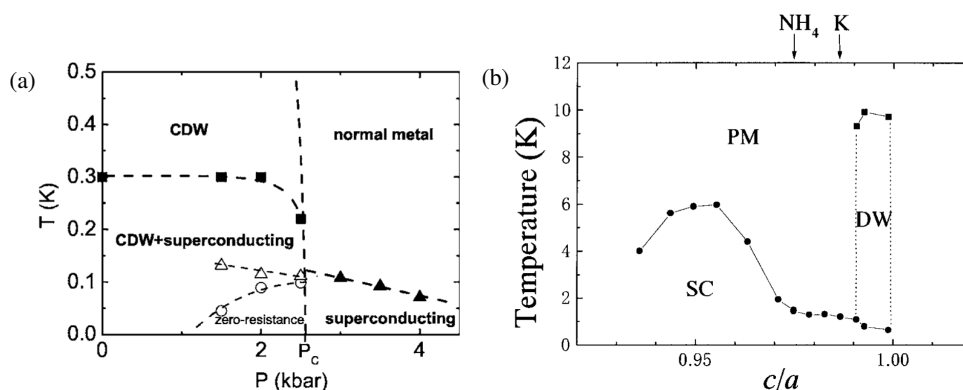


Figure 34. (a) Low temperature-pressure phase diagram of  $\alpha$ -(ET)<sub>2</sub>KHg(SCN)<sub>4</sub>. Reprinted with permission from Ref. [444]. © 2005 The American Physical Society. (b) Phase diagram of  $\alpha$ -(ET)<sub>2</sub>MHg(SCN)<sub>4</sub> determined from uniaxial strain experiments.  $c/a$  is the ratio of the in-plane lattice constants. The arrows indicate the approximate ambient-pressure locations of  $M$ =NH<sub>4</sub> and K. The  $a$  and  $c$  crystal axes in  $\alpha$ -(ET)<sub>2</sub>MHg(SCN)<sub>4</sub> are equivalent to the  $b$  and  $a$  axes, respectively, in  $\alpha$ -(ET)<sub>2</sub>I<sub>3</sub> (see Fig. 33). Reprinted with permission from Ref. [445]. © 2001 The American Physical Society.

under hydrostatic pressure, the application of uniaxial stress can increase  $T_c$  to  $\sim 5$  K [445]. Systematic studies of uniaxial stress applied to  $M$ =K and NH<sub>4</sub> suggest that SC occurs in this series for those salts with a smaller  $c/a$  ratio (see Fig. 34) [445].

The transition at 8–10 K has been considered “mysterious” as it has similarities with both charge- and spin-density wave systems [457]. A coexistence of metallic and magnetic ordering was also suggested [458]. Satellite X-ray reflections of an incommensurate wavevector are seen beginning at room temperature and increase sharply below 10 K in  $M$ =K; for  $M$ =Rb diffuse scattering at the same wavevectors is seen, reflecting short-range order [459, 460]. In this temperature range the resistivity decreases while the Hall resistance increases [457]. The spin susceptibility shows dependence on the field direction, being constant for fields perpendicular to the BEDT-TTF layers, and decreasing for fields within the layer [457]. Zero-field  $\mu$ SR experiments on  $M$ =K found two step-like increases in the relaxation rate at 12 K and 8 K [461]. These were interpreted as the onset of weak SDW order, first within the 2D planes at 12 K and then with 3D long range order at 8 K [461]. In the optical conductivity a significant dip centered around 200  $\text{cm}^{-1}$  develops below 200 K and was interpreted as a pseudogap [462]. From infrared and Raman studies on  $M$ =K, a breaking of the inversion symmetry between molecules A and A′ (see Fig. 33) was noted below about 200 K [463]. This would be consistent with short-ranged horizontal-stripe CO as found in  $\theta$ -(ET)<sub>2</sub>X [463].

Recent <sup>13</sup>C NMR experiments on RbHg(SCN)<sub>4</sub> have provided more information on the density-wave state [446, 447]. Below 300 K the NMR linewidth increases with decreasing temperature, as shown in Fig. 35 [446]. This is consistent with the development of incommensurate density waves as observed by X-rays [446, 459, 460]. The linewidth increase above the 8–10 K transition is principally in the A and A′ molecules (see Fig. 33) [446]. Fig. 35 shows the <sup>13</sup>C NMR spectra for  $M$ =Rb as a function of temperature [447]. Peak splitting is observed below 10 K: the splitting of peak A-B indicates that the A and A′ molecules become crystallographically inequivalent [447]. The splitting of peaks B and C indicates that the inversion symmetry between molecules B and C is also broken [447]. These features indicate that CO coexists with a lattice-based density wave in the low temperature state of  $\alpha$ -(ET)<sub>2</sub>MHg(SCN)<sub>4</sub>.

**Summary.** The  $\alpha$  structure has lower symmetry (inequivalent stacks) at room temperature than the  $\theta$  structure. Charge-ordering and spin-gap transitions occur at the same temperature in  $\alpha$ -(ET)<sub>2</sub>I<sub>3</sub>. In  $\alpha$ -(ET)<sub>2</sub>MHg(SCN)<sub>4</sub> there are likely coexisting charge- and spin-density waves. The dominant charge order pattern is the horizontal stripe.

## 5.2. Quasi-two dimensional anionic CTS

The materials in Sections 5.1.1–5.1.4 are all based on layers of cationic organic molecules that are  $\frac{3}{4}$ -filled with electrons, or  $\frac{1}{4}$ -filled in terms of holes. However, many organic conductors composed of anionic acceptor molecules are also known (see [26, 464] for reviews). Here we focus on one particular family composed of metal dithiolene

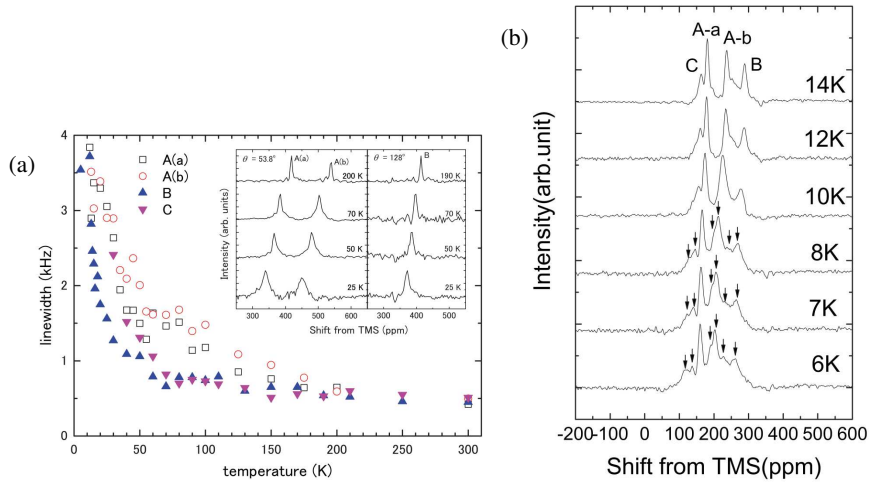


Figure 35. (a) Temperature dependence of the  $^{13}\text{C}$  NMR linewidth of  $\alpha\text{-(ET)}_2\text{RbHg(SCN)}_4$  [446]. Reprinted with permission from Ref. [444]. © 2005 The American Physical Society. Here the sites A(a) and A(b) correspond to A and A' in Fig. 33 respectively. (b)  $^{13}\text{C}$  NMR spectra of as a function of temperature. Peak splitting indicating CO is observed in the lines for the A, B, and C molecules below 10 K Reprinted with permission from Ref. [447]. © 2008 The American Physical Society.

Cation	$M$	$T_c$ (K)	$P_c$ (GPa)	$T_N$ (K)	Notes	references
$\text{Et}_2\text{Me}_2\text{N}$	Pd	4	0.2	—	single layer	[465]
$\beta\text{-Me}_4\text{N}$	Ni	5	0.7	—	solid crossing	[466]
$\beta\text{-Me}_4\text{N}$	Pd	6	0.7	12	solid crossing	[467, 468]
$\beta'\text{-Me}_4\text{P}$	Pd	—	—	42	solid crossing	[469, 470]
$\beta'\text{-Me}_4\text{P}$	Pt	—	—	—	solid crossing; $T_{\text{CO}}=218$ K	[469]
$\beta'\text{-Me}_4\text{Sb}$	Pt	3, 8*	1.0, 0.5*	18	solid crossing	[471, 472]
$\beta'\text{-Me}_4\text{As}$	Pt	4*	0.7*	35	solid crossing	[473, 474]
$\beta'\text{-Et}_2\text{Me}_2\text{P}$	Pd	4, 6*	0.7, 0.5*	18	solid crossing	[470, 475]
$\beta'\text{-Et}_2\text{Me}_2\text{As}$	Pd	5.5	0.8	18	solid crossing	[26, 468]
$\beta'\text{-Et}_2\text{Me}_2\text{Sb}$	Pd	—	—	—	solid crossing; $T_{\text{CO}}=70$ K	[475]
$\beta'\text{-EtMe}_3\text{As}$	Pd	4	0.7	23	solid crossing	[476]
$\beta'\text{-EtMe}_3\text{Sb}$	Pd	—	—	—	solid crossing, QSL	[477]
$m\text{-EtMe}_3\text{P}$	Pd	5	0.4	—	parallel column, $T_{\text{SG}}=25$ K	[476]
$t\text{-EtMe}_3\text{P}$	Pd	?	?	—	parallel column, $T_{\text{SG}}=50$ K	[478]

Table 5. Summary of the properties of the  $M(\text{dmit})_2$  salts discussed in this section.  $T_c$ 's and  $P_c$ 's marked with \* refer to uniaxial strain rather than hydrostatic pressure.

molecules,  $M(\text{dmit})_2$  ( $M=\text{Ni}, \text{Pd}, \text{Pt}$ ). Within this family a variety of quasi-2D superconductors are known, as well as insulating states with charge and spin order (see Table 5) [26, 215, 464]. In common with the cationic BEDT-TTF and related superconductors, SC in the  $M(\text{dmit})_2$  family also occurs when the carrier density is 0.5 per molecule.

$M(\text{dmit})_2$  salts have several important similarities and differences compared to BEDT-TTF salts. Compared to BEDT-TTF the HOMO-LUMO gap in the  $M(\text{dmit})_2$  molecule is smaller by a factor of about 3 [215]. In general the  $M(\text{dmit})_2$  salts for  $M=\text{Pd}$  are strongly dimerized, with more tightly coupled dimers than in  $\kappa\text{-(ET)}_2\text{X}$ . Structurally, within the  $M(\text{dmit})_2$  planes, the molecular packing is similar for all the materials in Table 5, with columnar packing of  $M(\text{dmit})_2$  molecules similar to the  $\beta$  and  $\beta'$  structures (Fig. 25). However, there are several different arrangements of the planes in the 3D crystal structures as shown in Figs. 36–38 (see [215]). These include single-layer structures (Fig. 36), the so-called “solid-crossing” layer structure, where molecules stack in different directions in alternate planes (Fig. 37), and a parallel column structure with two crystallographically distinct planes with stacking in the same direction (Fig. 38). Within the group of solid-crossing structures there are several types, including very similar  $\beta$  and  $\beta'$  structures [215]. An  $\alpha$ -type solid-crossing structure is also known (unrelated to the  $\alpha\text{-(ET)}_2\text{X}$  structure) [215].

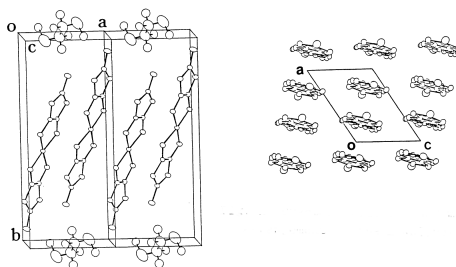


Figure 36. Crystal structure of  $\text{Et}_2\text{Me}_2\text{N}[\text{Pd}(\text{dmit})_2]_2$ . Reprinted with permission from Ref. [465]. © 1992 The Chemical Society of Japan.

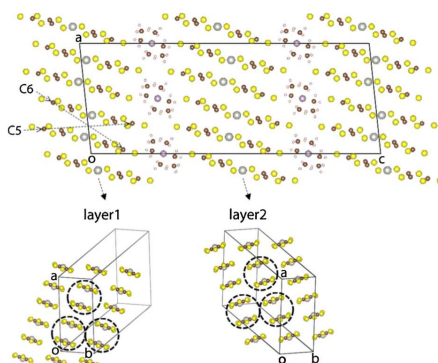


Figure 37. Crystal structure of  $\beta'$ - $\text{Et}_2\text{Me}_2\text{P}[\text{Pd}(\text{dmit})_2]_2$  with “solid-crossing” stacking in adjacent layers. Reprinted with permission from Ref. [479]. © 2014 The Physical Society of Japan. [479].

### 5.2.1. AFM, CO, and SC in $M(\text{dmit})_2$

SC was first observed in this class of CTS in  $\text{Me}_4\text{N}[\text{Ni}(\text{dmit})_2]_2$  with  $T_c = 5$  K [466, 480]. The resistivity undergoes a jump (with thermal hysteresis) at around 100 K, followed by a sharp rise in resistivity at 20 K. SC with  $T_c$  up to 5.0 K was observed, with however large sample dependence [466, 480].

Compared to  $\text{Ni}(\text{dmit})_2$  salts, in  $\text{Pd}(\text{dmit})_2$  salts the dimerization is typically very strong, with the ratio of the extended Huckel overlaps for intra- to inter-bonds within one stack of  $\text{Pd}(\text{dmit})_2$  molecules being of order 10:1 [468]. The strong dimerization suggests that an effectively  $\frac{1}{2}$ -filled band picture is appropriate, and AFM should be observed in many  $\text{Pd}(\text{dmit})_2$  salts provided the dimer lattice is not frustrated [26]. This is indeed seen, with many of the  $\text{Pd}(\text{dmit})_2$  materials having AFM transitions in the 10–40 K range (see Table 5).

SC is found under pressure in several of the  $\text{Pd}(\text{dmit})_2$  salts showing AFM under ambient pressure. It is, however, not clear that the transition to SC occurs from the AFM phase, or if there exist other intermediate phases. Fig. 39 shows the pressure-temperature phase diagrams determined by resistivity measurements for  $\text{Me}_4\text{N}$ . Under pressure, the AFM insulating phase in  $\text{Me}_4\text{N}$  is suppressed at about 0.4 GPa (see Fig. 39) [481]. After an anomaly in the resistivity at about 60 K a second metallic phase  $M_2$  is reached, followed by a different insulating phase  $I_3$  below 30 K [481]. It was noted that near onset the resistivity was very noisy, possibly due to a phase segregation of insulating and superconducting regions [481].

The phase diagram for  $\text{Et}_2\text{Me}_2\text{P}[\text{Pd}(\text{dmit})_2]_2$  is shown in Fig. 39(b) [475]. At ambient pressure the resistivity increases with decreasing temperature below 300 K [475]. Under pressure, metallic behavior is observed above 0.5 GPa [475]. At 0.69 GPa the resistivity reaches a minimum at about 30 K and then increases at lower temperature before the superconducting transition, becoming larger at low temperature than at room temperature [475]. An unusual feature of this salt is that at larger pressures, a second insulating phase is reached (see Fig. 39(b)). The salt  $\text{Et}_2\text{Me}_2\text{N}[\text{Pd}(\text{dmit})_2]_2$  also has a similar phase diagram with SC surrounded by two insulating phases, although it is not isostructural to  $\text{Et}_2\text{Me}_2\text{P}$  as it has a single-layer structure [481].  $\text{Et}_2\text{Me}_2\text{As}[\text{Pd}(\text{dmit})_2]_2$  is isostructural with  $\text{Et}_2\text{Me}_2\text{P}$  and is also superconducting under pressure [26].

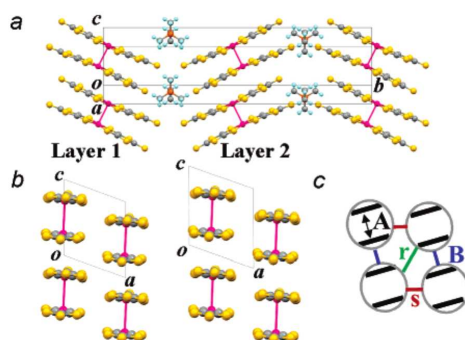


Figure 38. Crystal structure of  $\text{EtMe}_3\text{P}[\text{Pd}(\text{dmit})_2]_2$  with parallel stacking in adjacent layers. Reprinted with permission from [476]. © 2006 The American Chemical Society.

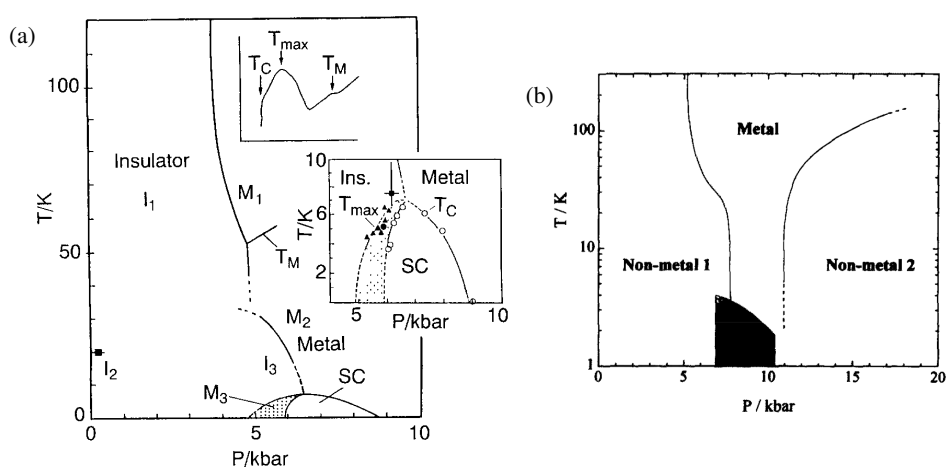


Figure 39. (a) Phase diagram of  $\beta\text{-Me}_4\text{N}[\text{Pd}(\text{dmit})_2]_2$ . Reprinted with permission from Ref. [481], © 1993 Elsevier.  $I_x$  and  $M_x$  indicate different insulating and metallic phases based on resistivity measurements. The AFM transition is indicated by  $I_2$  at ambient pressure. The shaded region indicates a drop in the resistivity without full SC. (b) Phase diagram of  $\beta'\text{-Et}_2\text{Me}_2\text{P}[\text{Pd}(\text{dmit})_2]_2$  based on resistivity measurements. Reprinted with permission from Ref. [475], © 1998 Elsevier.

Several of the  $\text{Pd}(\text{dmit})_2$  salts are superconducting only under the application of uniaxial strain, or reach higher  $T_c$ 's under the application of uniaxial strain (see Table 5) [472, 474]. The highest  $T_c$  reached is 8.4 K for  $\text{Me}_4\text{Sb}$  [472]. In all cases, the enhancement of SC occurs when the salts are compressed along the  $b$  axis, which is the inter-stack direction (see Fig. 37) [472, 474]. Application of pressure along the stacking ( $a$ ) direction resulted in enhanced non-metallic behavior in the low-pressure region [474].

As in the dimerized BEDT-TTF materials [310], the frequency dependence of the dielectric constant displays relaxor characteristics in many  $[\text{Pd}(\text{dmit})_2]_2$  CTS [482]. Extrapolated Curie-Weiss ordering temperatures are found in the range 10 ~ 30 K; in general a larger  $T_N$  appears to correlate with a smaller  $T_{\text{CW}}$  [482]. Assuming the relaxor behavior is due to fluctuating CO (with the same caveats as discussed in Section 5.1.1), a  $\Delta n \sim 0.1e$  was estimated, relatively independent of the cation [482]. Static CO has been confirmed for  $\text{EtMe}_3\text{P}$  as discussed in the following section.

### 5.2.2. $\text{EtMe}_3\text{P}[\text{Pd}(\text{dmit})_2]_2$

$\text{EtMe}_3\text{P}[\text{Pd}(\text{dmit})_2]_2$  is unique among this class of materials [476]. Instead of the solid crossing structure found in the  $\beta'$   $[\text{M}(\text{dmit})_2]$  CTS, stacks of  $[\text{Pd}(\text{dmit})_2]$  molecules in  $\text{EtMe}_3\text{P}[\text{Pd}(\text{dmit})_2]_2$  are parallel to those in other layers as shown in Fig. 38. Two different crystal structures of  $\text{EtMe}_3\text{P}$  are known, one with monoclinic structure ( $m\text{-EtMe}_3\text{P}$ ) [476] and one with triclinic structure ( $t\text{-EtMe}_3\text{P}$ ) [478]. Under ambient pressure both variants are semiconducting at

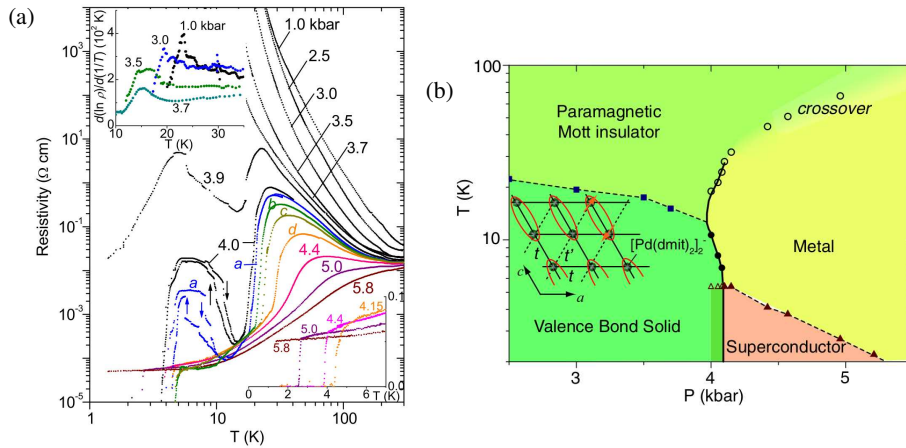


Figure 40. (a) Resistivity of  $\text{EtMe}_3\text{P}[\text{Pd}(\text{dmit})_2]_2$  as a function of temperature and pressure. (b) Phase diagram. Solid and dashed lines denote first and second order transitions, respectively. Reprinted with permission from Ref. [483], © 2007 The American Physical Society.

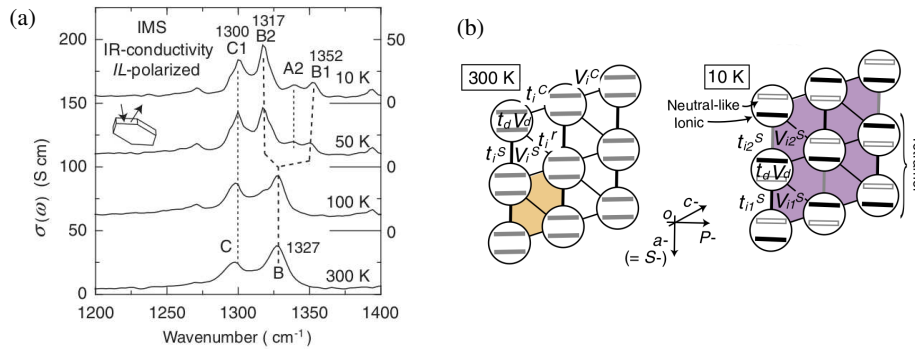


Figure 41. (a) Temperature dependence of the optical conductivity of  $t\text{-EtMe}_3\text{P}[\text{Pd}(\text{dmit})_2]_2$ . The peak splitting below 50 K indicates CO. (b) The pattern of CO is  $\cdots 1100 \cdots$  along the stack. Reprinted with permission from Ref. [478], © 2011 The Physical Society of Japan.

room temperature [476, 478]. Under pressure  $m\text{-EtMe}_3\text{P}$  is superconducting with  $T_c=5$  K at 0.4 GPa [476, 483]. The resistivity under pressure is shown in Fig. 40. At about 0.4 GPa, the resistivity drops by three orders of magnitude at around 20 K, but then increases further at lower temperatures. For pressures near the appearance of SC thermal hysteresis is observed, suggesting that the transition between the insulating state and the metallic state appears to be first order [483]. To our knowledge, experiments under pressure for ( $t\text{-EtMe}_3\text{P}$ ) have not been reported yet.

Under ambient pressure,  $\text{EtMe}_3\text{P}[\text{Pd}(\text{dmit})_2]_2$  undergoes a second-order phase transition to a non-magnetic ground state that breaks translational symmetry at 25 K (50 K) in the monoclinic (triclinic) forms [476, 478, 484–486]. The isotropic field dependence of the susceptibility rules out magnetic long-range order (i.e. AFM) for the ground state [484]. The spin gap for the monoclinic salt was estimated as  $\Delta \sim 40$  K [484]. This non-magnetic state was originally claimed to be a valence-bond solid (VBS) state, with formation of alternating spin-singlet inter-dimer bonds and with electron occupancy of 1 per dimer [484]. However, optical studies (see Fig. 41) have found that CO coexists with the bond ordering in the non-magnetic state [478, 486]. Again, considering the individual molecules and not dimers as units, the charge densities on the molecules have the pattern  $\cdots 0110 \cdots$  along the stacks. The individual molecules within each dimer are different, as shown in Fig. 41, indicating that the description as VBS is overly simplistic. Very recent careful optical studies [487] have clearly indicated the  $\frac{1}{4}$ -filled nature of this material. The same pattern is also found in the CO state of  $\beta\text{-}(meso\text{-DMBEDT-TTF})_2\text{X}$  [345] (see Fig. 27(a)). The amplitude of the CO is estimated as  $\delta\rho \sim 0.4 - 0.7$  in  $t\text{-EtMe}_3\text{P}$  and  $\sim 0.1$  in  $m\text{-EtMe}_3\text{P}$  [478, 486].

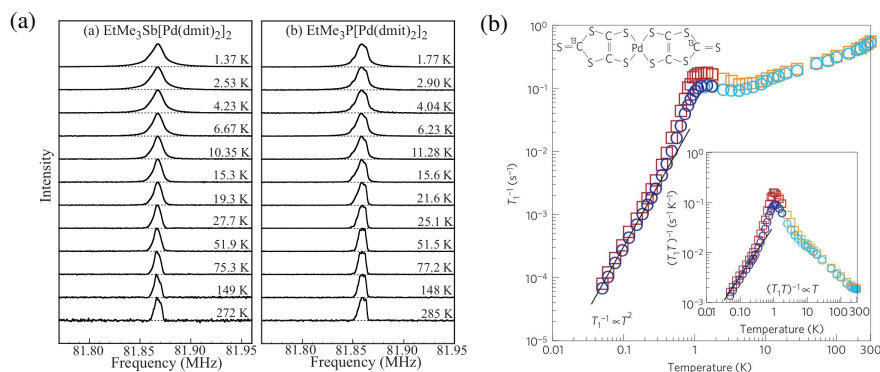


Figure 42. (a)  $^{13}\text{C}$  NMR spectra of  $\text{EtMe}_3\text{Sb}$  and  $m\text{-EtMe}_3\text{P}$ . Reprinted with permission from Ref. [477], © 2008 The American Physical Society. (b) relaxation time  $T_1^{-1}$  versus temperature. Reprinted with permission from Ref. [488], © 2010 MacMillan Publishers Ltd.

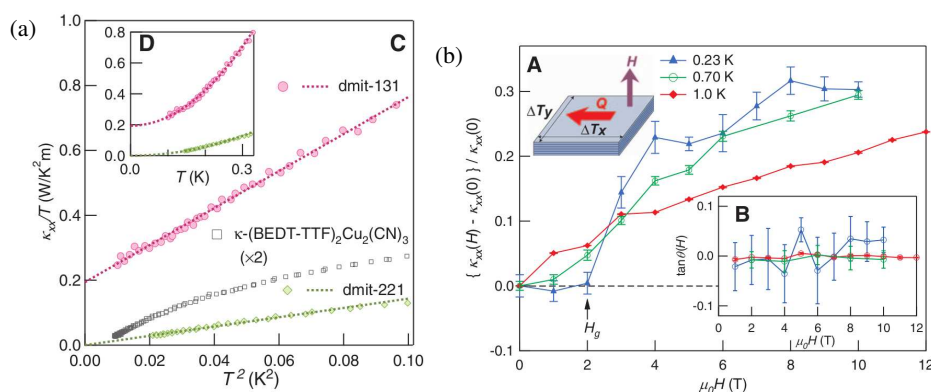


Figure 43. (a) Temperature dependence of the thermal conductivity of  $\text{EtMe}_3\text{Sb}$  (dmit-131),  $\text{Et}_2\text{Me}_2\text{Sb}$  (dmit-221), and  $\kappa\text{-(ET)}_2\text{Cu}_2(\text{CN})_3$  (b) Magnetic field dependence of the thermal conductivity, normalized to its zero-field value. Reprinted with permission from Ref. [490], © 2010 AAAS.

### 5.2.3. $\beta'\text{-EtMe}_3\text{Sb}[\text{Pd}(\text{dmit})_2]_2$

$\text{EtMe}_3\text{Sb}[\text{Pd}(\text{dmit})_2]_2$  has been the most studied CTS of this group because of the possibility that it is an experimental realization of a QSL [215]. As in  $\kappa\text{-(ET)}_2\text{Cu}_2(\text{CN})_3$ , in  $\text{EtMe}_3\text{Sb}$  the  $^{13}\text{C}$  NMR spectra hardly changes (see Fig. 42) down to  $\sim 1$  K, despite an estimated inter-dimer  $J$  of 220–250 [477]. As for  $\text{Cu}_2(\text{CN})_3$ , the NMR line in  $\text{EtMe}_3\text{Sb}$  also broadens at low temperature (broadening is also seen for  $m\text{-EtMe}_3\text{P}$  in the  $\delta\rho \sim 0.1$  CO state below 25 K, see Fig. 42). A kink is found in the  $^{13}\text{C}$  NMR relaxation time at  $\sim 1$  K indicating some kind of continuous phase transition [488]. While  $(T_1)^{-1}$  is consistent with gapless behavior above 1K, the rapid decrease below 1K indicates gap formation, although the power-law rather than exponential decrease suggests that the gap is nodal rather than complete [488].  $^{13}\text{C}$  NMR experiments using the inner instead of outer carbon atoms of the  $\text{Pd}(\text{dmit})$  molecule reached the same conclusion, suggesting that the results are not affected by the cation molecules [489].

Thermodynamic measurements are consistent with a mix of gapped and gapless behavior at low temperature [260, 490–493]. The magnetic susceptibility measured using a torque magnetometer, which cancels impurity Curie contributions, remains paramagnetic to very low temperatures (30 mK) [493]. The specific heat of  $\text{EtMe}_3\text{Sb}$  has a finite linear in temperature term as  $T \rightarrow 0$ , consistent with gapless excitations [491]. The thermal conductivity  $\kappa$  similarly extrapolates to a finite value for  $T \rightarrow 0$  (see Fig. 43) [490]. However, under a magnetic field gap-like behavior is seen, with a sudden increase in  $\kappa$  once the field exceeds a critical value (Fig. 43) [490].

**Summary.** A variety of crystal structures and normal state behavior (antiferromagnetism and charge ordering) are seen in the anionic CTS, in spite of much stronger dimerization than in the  $\kappa\text{-(ET)}_2\text{X}$ . A charge-order to superconductivity transition is seen most clearly in  $m\text{-EtMe}_3\text{P}[\text{Pd}(\text{dmit})_2]_2$ , where the pattern of the charge order is not that of a simple

valence bond solid, which requires equal charge densities on all the organic molecules. The charge pattern on the molecules is very clearly  $\cdots 0110\cdots$ , as expected in the  $\frac{1}{4}$ -filled band. Recent experiments in the spin liquid compound  $\beta'$ -EtMe<sub>3</sub>Sb indicate intradimer charge fluctuations and  $\frac{1}{4}$ -filled behavior [487].

### 5.3. Summary

Only in  $\kappa$ -(ET)<sub>2</sub>X is superconductivity (SC) found adjacent to antiferromagnetism. Antiferromagnetic order is found in very few  $\kappa$ -(ET)<sub>2</sub>X, specifically X= Cu[N(CN)<sub>2</sub>]Cl, Cu[N(CN)<sub>2</sub>]Br (deuterated), and X=CF<sub>3</sub>SO<sub>3</sub>. For X=CF<sub>3</sub>SO<sub>3</sub>, T<sub>N</sub> is lower than T<sub>c</sub>. There is evidence for intradimer charge fluctuations and pseudogap at temperatures greater than T<sub>c</sub> in  $\kappa$ -(ET)<sub>2</sub>X. In a greater number of 2D CTS, SC is reached upon applying pressure to a charge-ordered or density-wave state. Experimental phase diagrams of the anionic [M(dmit)<sub>2</sub>]<sub>2</sub> superconductors are similar in many ways to the ET and other cationic CTS. Here charge order is again found adjacent to SC, for example in EtMe<sub>3</sub>P[Pd(dmit)<sub>2</sub>]<sub>2</sub>. In all cases where a charge-order-to-SC transition occurs, and the charge order pattern is known, it does not correspond to a Wigner crystal; rather the charge order pattern  $\cdots 1100\cdots$  is common among these materials, and there occur spin gaps at low temperature. Finally, in general T<sub>c</sub> decreases with increasing pressure, inconsistent with the prediction of BCS theory. We return to the theoretical interpretation of these observations in the next Section.

## 6. Broken symmetries in quasi-two dimensional CTS, Theory

There is by now strong evidence that SC in the organic superconductors cannot be described by BCS theory and that any successful theory must incorporate the effect of e-e interactions from the beginning (see Reference [494] for a review of failures of the BCS model in the context of the CTS superconductors). In this Section we first review the most popular theories proposed to explain SC in the CTS. We review numerical results for 2D systems at  $\rho = 1$  and argue that understanding SC in the CTS requires going beyond concepts derived from the RVB theory or theories of spin-fluctuation mediated SC. We further present a VB theory of SC that is unique to  $\rho = \frac{1}{2}$ , that is inspired by the RVB theory but that is also substantially different (even as it has conceptual overlaps with VBS-to-SC theories). We present results of  $\rho$ -dependent numerical calculations of superconducting pair-pair correlations that strongly support our VB theory.

*Strongly correlated theories of SC in the CTS.* Correlated-electron theories of SC were largely born out of efforts to explain SC in the high T<sub>c</sub> cuprates. Broadly speaking, one can distinguish between two different classes of theory. The first class emphasizes site-diagonal density waves, AFM/SDW, and CDW, as the mechanism for pairing. Within these approaches, SC pairing is mediated by the coupling of charge carriers with *fluctuations* or excitations out of the density wave. Within the second class of theories, SC emerges out of a proximate *spin-singlet* semiconductor. In the context of the cuprates this second theory has been known as the RVB theory. Our theoretical approach belongs to this class and is based on VB theory but is yet substantially different from the RVB theory.

*Class I theories.* In the case of theories of AFM-driven SC the excitations exchanged between charge carriers are spin fluctuations or magnons. This approach has been widely used in the context of the cuprates, usually within the model of a weakly doped Mott-Hubbard semiconductor. In its application to the CTS, a pressure-induced increase in lattice frustration drives SC within the effectively  $\frac{1}{2}$ -filled band  $\kappa$ -phase CTS. The chief conceptual difficulty with spin-fluctuation mediated pairing is that unlike in BCS theory, where the phonons that lead to an attractive interaction between electrons are physically distinct particles from the electrons, the AFM fluctuations assumed to bind electrons into Cooper pairs are themselves generated by the same electrons. Most theoretical calculations in this class of theories are based on mean-field theory. It is however questionable as to whether the problem can be reduced to weak coupling by the separation of magnetic and charge degrees of freedom. From the perspective of experiments, it is not clear whether the pseudogap in either the cuprates or the organics (see Section 5.1.1) can be explained within this approach, although it is claimed that dynamical cluster approximation (DCA) results prove that there is a pseudogap within the Hubbard model [495–497]. Recent experimental work on the cuprates (see Section 6.3.4), in particular the finding of a CO phase within the pseudogap phase, are extremely difficult to explain within a weakly doped Mott-Hubbard semiconductor picture.

In the context of the 2D CTS, there are far more materials that exhibit a CO to SC transition than an AFM to SC transition (see Sections 5.1 and 5.2). In spite of this, the bulk of theories have emphasized the  $\frac{1}{2}$ -filled Hubbard model and the AFM state found there. It has also been proposed that charge rather than AFM fluctuations mediate SC in certain CTS superconductors, and that SC may be found adjacent to WC CO driven by the NN Coulomb interaction  $V$  in a  $\frac{1}{4}$ -filled model [498]. Here it is assumed that charge carriers couple to “charge fluctuations” of the WC [498], although unlike magnons there is no equivalent theory or experimental signature of the collective excitations out of a WC. In this theory, the application of a slave-boson transformation to Eq. 5 in the limit of large  $U$  replaces the electron creation operator  $c_{i,\sigma}^\dagger$  with the product of two operators  $f_{i,\sigma}^\dagger b_i$ , where  $f_{i,\sigma}^\dagger$  represents a fermion and  $b_i$  a boson associated with the electron charge [498]. The bosons introduced in this manner are coupled to the fermions, which is argued to produce SC. We will point out however in Section 6.2 that in the CTS that display a transition from CO to SC, the CO phase is in fact *not* a WC.

*Class II theories.* In this class of theories, SC is assumed to result from the destabilization of a spin-gapped or spin-liquid insulating state. Anderson proposed that a strongly correlated system could best be understood in a valence bond basis of spin-paired carriers [39, 499]. At large  $U$  and  $\rho = 1$  the Hubbard model reduces to the  $S = \frac{1}{2}$  Heisenberg spin Hamiltonian with exchange constant  $J \propto -t^2/U$ . Here the energy of a pair of spins in a singlet state is  $-\frac{3}{4}J$  while the classical energy of two anti-parallel spins is  $-\frac{1}{4}J$ . Thus, in a 1D  $\rho = 1$  system where each site has two nearest neighbors, the spin-paired SP state is lower in energy than an antiferromagnetically ordered state. A given spin can only be in a singlet bond with one neighbor, which limits the energy gain per site in the singlet valence bond state. Once the number of neighbors is large enough (for example the square lattice with four nearest neighbors), the AFM state becomes lower in energy than the valence bond singlet state. Anderson and Fazekas proposed a RVB wavefunction consisting of a superposition of valence bonds as a variational wavefunction for the Heisenberg model on the triangular lattice [39, 499]. The actual ground state however, turned out to not be a singlet, but rather the  $120^\circ$  AFM state [237–241]. The idea remained however, that the  $\rho = 1$  system with large  $U$  must be close to a spin-gapped RVB state.

Doping the  $\frac{1}{2}$ -filled band square lattice destroys the AFM. Anderson further proposed that in this case the RVB state would become the ground state, and that this would be a superconductor [40]. In theories of RVB SC applied to  $\kappa$ -(ET)<sub>2</sub>X, the assumption is made that the same or somewhat modified theory applies to a  $\frac{1}{2}$ -filled anisotropic triangular lattice of BEDT-TTF dimers, where the controlling parameter responsible for destroying AFM is lattice frustration rather than doping (see below). Such a theory in principle naturally explains preformed pairs in the pseudogap phase of the cuprates [500, 501] and probably also in the CTS. There are several problems however: first, no singlet state has been seen in calculations on the  $\frac{1}{2}$ -filled model. Second, we show below that numerical studies on frustrated lattices in general find no SC either in the  $\frac{1}{2}$ -filled band. The most difficult experimental observation to explain is how to extend the  $\rho = 1$  RVB theory to account for those CTS where a CO to SC transition is seen. This same problem has become relevant in the context of the cuprates since the discovery of CO phases [4]. Some authors have proposed the concept of a WC of Cooper pairs [43, 44, 502–504, 504–507]. The attractive feature of this idea is that it can explain both the presence of preformed pairs (giving the pseudogap) and an apparently competing phase (CO). The key problem however is that the precise nature of such an ordered state remains unknown.

The idea of SC emerging from a proximate spin-singlet has nevertheless remained popular. For instance, it has been proclaimed by multiple authors that SC emerges from a 2D SP state [508, 509]. The problem is that once again no such SP state in 2D is known. The only case where interactions give a  $\rho = 1$   $S = 0$  singlet state outside 1D are even-leg ladders. For doped two-leg ladders numerical studies using DMRG do find dominant superconducting correlations [510, 511]. Theories of ladders however cannot be extended to 2D. To the best of our knowledge there is no satisfactory theory of  $S = 0$  in 2D except ours that we present below.

*Our VB theory of SC.* The basis of our theory is the observation that a PEC is particularly stable in frustrated  $\rho = \frac{1}{2}$  systems. The frustration destroys the WC of single electrons, as well as the AFM that may occur in strongly dimerized  $\rho = \frac{1}{2}$ . The occurrence of the PEC in 2D uniquely at  $\rho = \frac{1}{2}$  can be understood physically. Only at the carrier density of  $\rho = \frac{1}{2}$  such a paired CO, in which singlet pairs are separated by pairs of vacancies, is commensurate, conferring it the exceptional stability that is necessary to dominate over both the metallic state as well as the WC of single electrons driven by the NN Coulomb interaction  $V$ . In other words, at this density there exists a range of parameters where there is a balance between the exchange energy gained from spin-singlet formation and the repulsive interaction between

the electrons. Alternatively, this state is the equivalent of a 2D SP state, with nearly decoupled 1D insulating stripes separated by stripes of vacancies (see Fig. 32(b) and below). We have called this paired WC the Paired Electron Crystal (PEC). In analogy with theories of VBS-to-SC transitions, we believe that the spin-singlet pairs of the PEC can behave as hard-core bosons, and the “melting” of the PEC, driven by further frustration or very weak doping, then gives SC (the key difference between our work and proposed VBS-to-SC transition theories is that we will demonstrate the transition to the PEC numerically). Note that the gain in kinetic energy from the crystal-to-fluid transition in such a lattice of hard core bosons is largest when the number of bosons is exactly half the number of effective sites. This is also  $\rho = \frac{1}{2}$  in terms of the electrons that constitute the spin-singlets. The chief advantage of our theory is that it has the potential of explaining SC in all CTS within a unified approach, irrespective of whether the broken symmetry in the insulating state is proximate to SC is AFM or CO.

In the next sections we present the results of precise numerical calculations to substantiate the above. We will begin with calculations for the  $\rho = 1$  Hubbard model, within which we show the absence of SC for any correlations or frustration. Following this, we present numerical results demonstrating the PEC and correlation-driven enhancement of superconducting pair-pair correlations uniquely for  $\rho = \frac{1}{2}$ .

### 6.1. Half-filled band

The simplest  $\rho = 1$  model in the context of the 2D CTS superconductors is the Hubbard model on the anisotropic triangular lattice with hopping integrals  $t$  and  $t'$  (see the inset, Fig. 44(a)). This lattice becomes equivalent to the simple square lattice when  $t' = 0$ . We have performed exact calculations for the  $4 \times 4$  periodic lattice, and Path Integral renormalization group (PIRG) calculations for periodic  $6 \times 6$  and  $8 \times 8$  lattices, for  $t'/t = 0.2, 0.5$ , and  $0.8$  [37, 38], whose results are discussed below. The PIRG method is an unbiased method free from the fermion sign problem which approximates the ground state wavefunction as a sum of Slater determinants [512]. Within each basis size PIRG is strictly variational and variance extrapolation is used to remove the basis size bias [512].

#### 6.1.1. Magnetic Phases

In the  $t' = 0$  limit AFM order is found in the ground state for all  $U > 0$  as shown in the phase diagram in Fig. 44(a) (for a comparison of different calculations of the phase diagrams see Fig. 16 of Reference [513]). As  $t'/t$  increases frustration reduces the region of the phase diagram over which AFM dominates, which occurs for  $U > U_c$  with finite  $U_c$  for  $t'/t > 0$ . At  $t'/t \approx 0.5$  a third phase enters, referred to as either a non-magnetic insulator (NMI) or QSL [515]. Compared to what is seen on finite size lattices, in the thermodynamic limit the NMI phase extends to a smaller  $U$  [38, 515]. The PIRG method has been used by several authors to study the phase diagram of this model [38, 512, 514–516]. These calculations find that the NMI phase extends for  $U$  as small as 4.0 at  $t'/t = 0.5$  [38]. PIRG calculations have further shown that in the NMI phase there is no dimerization, plaquette singlet state, staggered flux state, or charge order [516]. As shown in Fig. 44(b), the NMI phase also appears to be gapless. For these reasons the NMI phase was proposed to explain the QSL behavior seen in  $\kappa$ -(ET)<sub>2</sub>Cu<sub>2</sub>(CN)<sub>3</sub> [515].

In the isotropic limit ( $t'/t = 1$ ) three successive phases are found as  $U$  increases [517]. For  $U < U_{c1} \sim 7.4t$  the ground state is PM; for  $U_{c1} < U < U_{c2} \sim 9.2t$  the ground state is the NMI; and for  $U > U_{c2}$  the ground state is a  $120^\circ$  Néel ordered state [517]. Recent variational Monte Carlo (VMC) calculations find a similar value  $U_{c2} \sim 8$  [518]. As discussed in Section 5.1.1,  $120^\circ$  AFM ordering has not been observed experimentally in any CTS, despite the existence of a wide range of  $t'/t$  for different X (see Table 3 in Section 5.1.1). The range of  $t'/t$  experimentally investigated is further expanded by experiments under pressure. Assuming that the effective dimer model continues to be valid for  $\kappa$ -(ET)<sub>2</sub>X for large  $U$  and  $t'/t \approx 1$ , this implies that the effective dimer  $U$  must be less than about 9. The region of the phase diagram for  $U \sim U_{c2}$  close to  $t'/t = 1$  is difficult for numerical methods to access. Different methods give somewhat different ground states in this region, involving  $120^\circ$  AFM, QSL, and AFM states [518–521]. Given that the effective  $U$  here is likely larger than that in  $\kappa$ -(ET)<sub>2</sub>X, it is unlikely that this region of parameters is relevant for any 2D CTS.

#### 6.1.2. Superconductivity: suppression of superconducting pair-pair correlations

Numerous mean-field, cluster DMFT, and variational calculations have suggested that  $d$ -wave SC occurs within the  $\rho = 1$  Hubbard model on the anisotropic triangular lattice (or on the related lattice with two frustrating diagonals) usually near the boundary of the metallic and insulating phases [522–534]. In these works the mechanism of SC

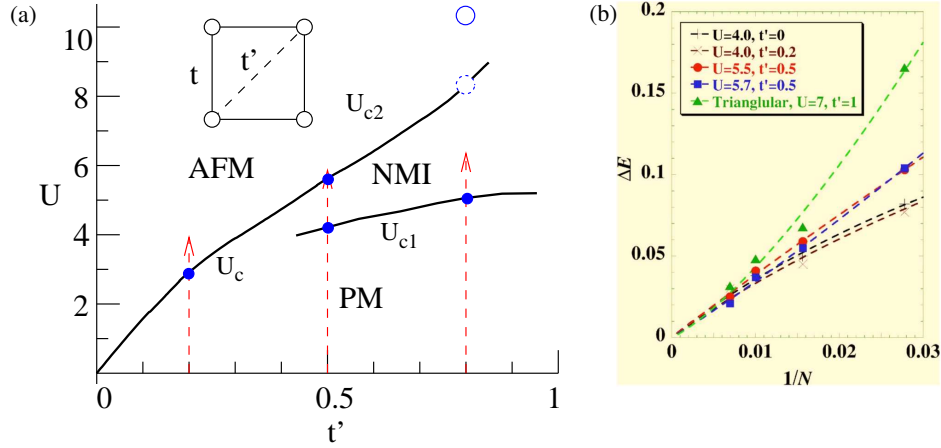


Figure 44. (color online) (a) Phase diagram of the  $\rho = 1$  Hubbard model on the anisotropic triangular lattice [38]. Filled circles are finite-size scaled values for the phase boundaries. At  $t' = 0.8$  the solid circle is an exact upper bound for the phase boundary, and the dashed circle shows the expected finite-size scaled value. The lines linking the points are schematic guides to the eye. The dashed lines with arrows show the parameters chosen for pair-pair correlation calculations (see Fig. 45). A  $120^\circ$  AFM phase not shown here exists for large  $U$  at  $t' = 1$  (see text). (b) Finite-size scaling of the singlet-triplet gap for  $N$  site lattices using the PIRG method [514]. Circles, squares, and triangles are for parameters within the NMI phase. Triangles are data for the the lattice with a single diagonal  $t'$  bond as in panel (a) and others are for the lattice with two  $t'$  bonds. The dashed lines are fits to the data. Reprinted with permission from Ref. [514], © 2006 The American Physical Society.

is assumed to be AFM spin fluctuations or RVB. A similar SC phase is also suggested for the related Hubbard-Heisenberg model (see below).

Superconducting pair-pair correlations calculated numerically from unbiased methods provide a way to investigate SC. We define singlet pair creation operators

$$\Delta_i^\dagger = \frac{1}{N_\nu} \sum_\nu g(\nu) \frac{1}{\sqrt{2}} (c_{i,\uparrow}^\dagger c_{i+\vec{r}_\nu,\downarrow}^\dagger - c_{i,\downarrow}^\dagger c_{i+\vec{r}_\nu,\uparrow}^\dagger), \quad (11)$$

where  $g(\nu)$  determines the pairing symmetry. For  $d_{x^2-y^2}$  symmetry,  $g(\nu) = \{1, -1, 1, -1\}$  for  $\vec{r}_\nu = \hat{x}, \hat{y}, -\hat{x}, -\hat{y}$ , respectively. For  $d_{xy}$  symmetry,  $g(\nu) = \{1, -1, 1, -1\}$  for  $\vec{r}_\nu = \hat{x} + \hat{y}, -\hat{x} + \hat{y}, -\hat{x} - \hat{y}, \hat{x} - \hat{y}$ , respectively.  $N_\nu$  is a normalization factor, with  $N_\nu = 2$  for a superposition of four singlets. The equal-time pair-pair correlation function is then defined as

$$P(r) \equiv P(|\vec{r}_i - \vec{r}_j|) = \langle \Delta_i^\dagger \Delta_j \rangle \quad (12)$$

Two criteria must be satisfied in the ground state for SC to exist: First, the pair-pair correlations must extrapolate to a finite value at long range ( $r \rightarrow \infty$ ). Using currently available unbiased methods it is unfortunately not possible to perform a full finite-size extrapolation of pair-pair correlations. Second, if the SC pairing is to be driven by e-e interactions, the pair-pair correlations must be enhanced over their  $U = 0$  value. This second criterion can be tested with precise calculations of pair-pair correlations. We show below the results of  $4 \times 4$  exact and up to  $8 \times 8$  PIRG calculations.

Exact diagonalization calculations on a  $4 \times 4$  lattice at  $\rho = 1$  show that the second criteria is not met for any value of  $U$  and  $t'$ , excluding very short-range correlations:  $P(r)$  decreases *monotonically* with  $U$  in all cases [37]. Early PIRG calculations suggested that at least for  $U < 4$  pair-pair correlations did not show long-range order [515]. Reference [38] calculated pair-pair correlations using an improved method, QP-PIRG, that includes space and spin symmetries that significantly improve the accuracy [535]. Fig. 45 shows results for  $t' = 0.5$  for up to  $8 \times 8$  lattices [38]. Fig. 45(a)-(b) show a discontinuous drop in the double occupancy and bond order along the diagonal bond direction, which indicates the transition from the PM to AFM state as  $U$  increases. Fig. 45(c) shows the long-range  $d_{x^2-y^2}$  pair-pair correlation versus  $U$ , which decreases monotonically with  $U$  with a further drop at the MI transition. Fig. 45(d) plots  $\Delta P_d(r, U) = P_u(r, U) - P_u(r, U = 0)$ . Except for the very short range region, the pair-pair correlation function is always smaller for nonzero  $U$  than at  $U = 0$ . Results for other values of  $t'$  are similar [38]. It is important to note

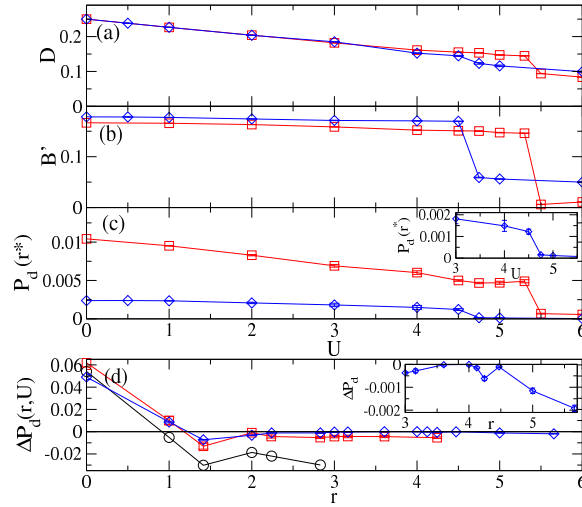


Figure 45. (color online) QP-PIRG results for the  $\rho = 1$  Hubbard model on the anisotropic triangular lattice with  $t'=0.5$  [38]. Circles, squares, and diamonds are for  $4\times 4$ ,  $6\times 6$ , and  $8\times 8$  lattices, respectively. (a) Double occupancy  $D$  (b)  $t'$  bond order  $B'$  (c)  $d_{x^2-y^2}$  pair-pair correlation  $P_d(r^*)$  for the next-to-furthest distance  $r^*$  on each lattice (d) enhancement of pair-pair correlations over the non-interacting system as a function of distance  $r$  for  $U = 4.5$ .

that the pair-pair correlations are trivially enhanced by  $U$  for the  $r = 0$  point, and for some parameters for  $r = 1$  (see Fig. 45(d)). At such short distances however, the pairs physically overlap. In particular, at  $r = 0$  the  $d_{x^2-y^2}$  pair-pair correlation function reduces to a linear combination of spin and charge correlations [536]. The increase of the anti-parallel spin correlation in the AFM state causes the  $r = 0$   $d_{x^2-y^2}$  correlation to increase [38, 536]. This short-range increase with  $U$  does not imply true SC but is perhaps the reason why mean-field or cluster DMFT methods find SC.

VMC calculations provide one way to investigate larger lattices. However, in VMC a specific form of the wavefunction must be assumed, and there is no way to assess the accuracy of the assumed functional form besides the comparison of the variational energies. Even with small differences in the variational energy there can be large differences in correlation functions. Some VMC calculations have claimed SC within the  $\rho = 1$  model [529, 530], but several more recent calculations have not found SC [518, 537]. It is of particular note that the authors of Reference [530] after improving their trial wavefunction found that SC was no longer favored [538]. Similarly, other groups using VMC also found that the tendency to SC went *down* after improving their wavefunctions [518, 537].

Due to lack of space we have not discussed the lightly doped half-filled model ( $\rho \lesssim 1$ ), where many of the same issues regarding SC exist. Recently several authors using the VMC [539–541] and DCA [496] methods have suggested that SC is present in the Hubbard model for  $\rho \sim 0.8$  only when  $U > U_c$ , with  $U_c \sim 4-6 t$ . While our PIRG calculations are limited to  $U \leq 6t$ , we remark that in exact diagonalization calculations for the  $\rho = 1$  Hubbard model on the anisotropic triangular lattice [37], there was no sign of any enhancement of SC at large  $U$ ; pairing correlations continued to decrease with  $U$  up to the largest values of  $U$  considered,  $U \sim 20t$ . Furthermore, we note that recent DMRG calculations for the Hubbard Hamiltonian with  $\rho = 0.875$  on cylinders of width 4 and 6 sites found that pairing correlations decay exponentially with distance even for  $U$  as large as  $8t$  [542].

### 6.1.3. $\rho = 1$ $U$ - $t$ - $J$ models

It has been claimed that the mean-field treatment of the simple Hubbard model does not correctly describe AFM (spin-spin) correlations, but a mean-field treatment of Hubbard-Heisenberg ( $U$ - $t$ - $J$ ) model does [543–547]. The  $U$ - $t$ - $J$  model includes an additional interaction between electron spins of the form  $J_{ij} \sum_{\langle ij \rangle} \vec{S}_i \cdot \vec{S}_j$ , with  $J_{ij}$  an independent interaction from the Hubbard  $U$ . Proponents of this model find SC within a wavefunction obtained by a Gutzwiller projection on a BCS wavefunction, which is a wavefunction of the RVB form [543, 544]. Other methods used to treat this model include slave-rotor theory, which finds a region of VBS order in addition to metal, QSL, and superconducting phases [548]. The authors proposed that the calculated VBS order explained the observed CO in  $\text{EtMe}_3\text{P}[\text{Pd}(\text{dmit})_2]_2$  (see Section 5.2.2).

Exact calculations within the  $U$ - $t$ - $J$  model again show no sign of enhancement of pair-pair correlations over the noninteracting results [549]. No tendency towards VBS order was found either [549]. The AFM region of the phase diagram of Fig. 44(a) gets broader for  $J \neq 0$  but no SC emerges. If VBS order is present in the  $U$ - $t$ - $J$  model, it would also be expected to be found *with greater tendencies* in the pure Heisenberg model on frustrated lattices. The most recent large-scale numerical results for the  $J_1$ - $J_2$  Heisenberg model do not find any evidence for a VBS phase [550, 551]. This strongly suggests that the “valence-bond” insulator phase in  $\text{EtMe}_3\text{P}[\text{Pd}(\text{dmit})_2]_2$  (see Section 5.2.2) requires a quarter-filled description in order to be understood. This last observation is in agreement with the latest work of Yamamoto *et al.*, who have concluded that this material should be considered a  $\frac{1}{4}$ -filled band system [487]. We consider the properties of  $\frac{1}{4}$ -filled band systems in the next Section.

## 6.2. Quarter-filled band

Since SC is found in the CTS at fixed carrier concentration  $\rho$ , and since in the previous subsection we have already seen that the effective  $\frac{1}{2}$ -filled model does not give enhanced superconducting correlations, the only choice is then to investigate the interacting  $\frac{1}{4}$ -filled band. We have already argued against the idea of charge fluctuation-induced SC [498], as such fluctuations out of the WC are simply not defined. Another approach taken by several authors is to argue that the basic principle of spin-fluctuation (Class I theories above) mediated SC in the  $\frac{1}{2}$ -filled band is correct, but that incorporating the actual bandfilling and crystal structure of the 2D CTS is necessary to reproduce details of the superconducting state, such as the pairing symmetry or location of nodes of the order parameter [218, 299, 552–554]. We do not see, given the failures of the spin-fluctuation approach we have pointed out above in the  $\frac{1}{2}$ -filled model, how any modification of this approach can lead to a successful theory of correlated electron SC. Going beyond the spin-fluctuation model leaves the idea of SC emerging from spin singlet VB states as the only option. In the rest of the section we show how such a state emerges in the interacting  $\frac{1}{4}$ -filled band.

### 6.2.1. Coupled spin-singlet and charge order at $\rho = \frac{1}{2}$

In Section 3 we showed the occurrence of the stable BCDW-I and II states in the interacting 1D  $\frac{1}{4}$ -filled band. These states are the natural  $2k_F$  states in 1D, but can also be thought to emerge because of the strong tendency to form spin singlets in the  $\frac{1}{4}$ -filled band, where the periodic arrangement of the spin singlets is stabilized because of the high order commensurability of BCDW. There is a natural tendency to have co-operative charge migration and spin-singlet formation in the  $\frac{1}{4}$ -filled band. In Fig. 46 we consider two coupled dimers with two electrons. The wavefunction for large  $U$  can be written as  $\frac{1}{2}|1010 + 1001 + 0110 + 0101\rangle$ . As the bond coupling the dimers (dashed line in Fig. 46(a)) is turned on, the energy of the configuration 0110 is lowered relative to the other three, via antiferromagnetic superexchange. We assume here that the relevant Hamiltonian is the EHM (Eq. 5) with  $V < V_c$  so that the Wigner crystal WC CO is of higher energy (for the triangular lattice with isotropic  $V$ , the classical energies of the PEC and WC of single electrons are equal, and upon taking into account the quantum effects due to electron hopping this statement is trivially true [122]). The stronger contribution by 0110 to the overall wavefunction, leads to charge disproportionation between the outer and inner sites in Fig. 46(a). The same effect also takes place between the coupled dimers in the lattice of Fig. 46(b). Fig. 46 shows the resulting  $\Delta n$  calculated for both 4-site systems for  $U = 4$  and  $V = 0$  as a function of  $t'$ , the bond coupling the two dimers. As  $t'$  becomes stronger  $\Delta n$  increases.

An extended system that shows a broken symmetry very similar to the 4-site square cluster of Fig. 46(b) is the zigzag ladder of Fig. 47 [34, 127]. This lattice has two different bonds with  $t_1$  along the rung (zigzag) direction of the lattice and  $t_2$  along the rail direction. The zigzag ladder is also of interest at  $\rho=1$ , since for  $t_2 \geq 0.25 t_1$  the ground state is a valence bond solid [555, 556]. We have shown that a coexisting CO-singlet occurs at  $\rho = \frac{1}{2}$  for  $t_2 < 1.707t_1$ . (see Fig. 47) [34, 127]. The energy dispersion in the noninteracting limit is

$$E(k) = -2t_1 \cos(q) - 2t_2 \cos(2q), \quad (13)$$

where  $q$  refers to a wavenumber defined along the  $t_1$  direction. The topology of the bandstructure for  $\rho = \frac{1}{2}$  changes when  $t_2/t_1 = (t_2/t_1)_c = (2 + \sqrt{2})/2 = 1.707$ . For  $t_2/t_1 < 1.707 \dots$  there are two points on the Fermi surface, while for  $t_2/t_1 > 1.707$  there are four. In the presence of e-p coupling a Peierls distorted state therefore occurs when  $t_2/t_1 < 1.707$ , and as in the pure 1D case this distorted state has  $\dots 1100 \dots$  CO.

The distorted state in the zigzag ladder is shown in Fig. 47(b). The bond pattern along the zigzag direction is the same as that of BCDW-II in the purely 1D case, with the strongest bond between the two large charges [34]. This

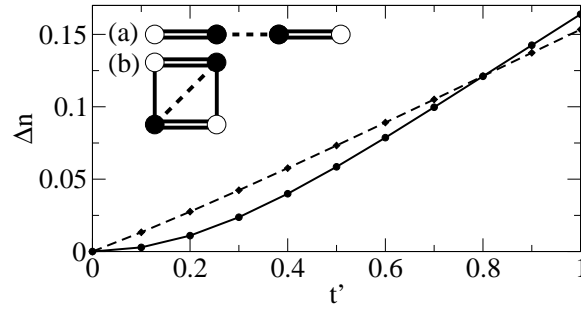


Figure 46. Charge difference  $\Delta n$  as a function of the hopping  $t'$  for 4-site clusters. The intradimer (double line) bonds have strength  $t_1 = 1.5$  and the single bonds in (b) are  $t_2=0.5$ . The dashed line has strength  $t'$ . Interaction parameters in 5 are  $U=4$  and  $V=0$ . Filled and empty circles are sites with charge densities  $0.5 + \frac{\Delta n}{2}$  and  $0.5 - \frac{\Delta n}{2}$ , respectively. Solid (dashed) curves are for clusters (a) (b)) [125].

distorted state continues to exist in the presence of e-e interactions, with the same bond and charge distortion pattern [34, 127]. As in the 1D BCDW-II, the amplitude of charge order can be quite large, accompanied by a large spin gap. Fig. 47(c) shows the finite-size scaled spin gap  $\Delta_\sigma$  as a function of the charge disproportionation  $\Delta n$  for the zigzag ladder, compared to a 1D chain with the same  $U$  and  $V$ . In the calculation of Fig. 47(c) the unit of energy is taken as the average hopping integral along the zigzag direction,  $\frac{t_1+t_2}{2}$ . In these calculations charge order was externally imposed by adding a term  $\sum_i \epsilon_i (n_{i,\uparrow} + n_{i,\downarrow})$  to Eq. 5, with the sign of  $\epsilon_i$  chosen to produce the CO pattern shown in Fig. 47(b). In the comparison 1D system the CO is  $\cdots 1100 \cdots$  and the bond pattern was BCDW-I. The resulting spin gap  $\Delta_\sigma$  is plotted as a function of the resulting  $\Delta n$ .  $\Delta_\sigma$  is found to be considerably larger in the ladder than in 1D for the same CO amplitude.

Importantly, the bond distortion in the ladder remains that of BCDW-II even for strong e-e interactions ( $U=6$  and  $V=1$  in Fig.47(c)), as compared to 1D where the pattern is BCDW-I (see Section 3.3.2). This is the reason the spin gap is large in the zigzag ladder. Large spin gaps can be expected in  $\rho = \frac{1}{2}$  CTS with zigzag ladder crystal structures. Similar to quasi-1D  $\rho = \frac{1}{2}$  CTS that show the BCDW-II distortion [130], a single coupled charge-bond-spin-gap transition would be expected in the zigzag ladder [34]. While not many CTS are known experimentally that have the zigzag structure, one example are the  $(\text{DTTF})_2M(\text{mnt})_2$  series [557], where large spin gaps are found experimentally:  $T_{\text{SG}} \sim 90$  K for  $M=\text{Cu}$  and  $\sim 70$  K for  $M=\text{Au}$ , respectively [558].

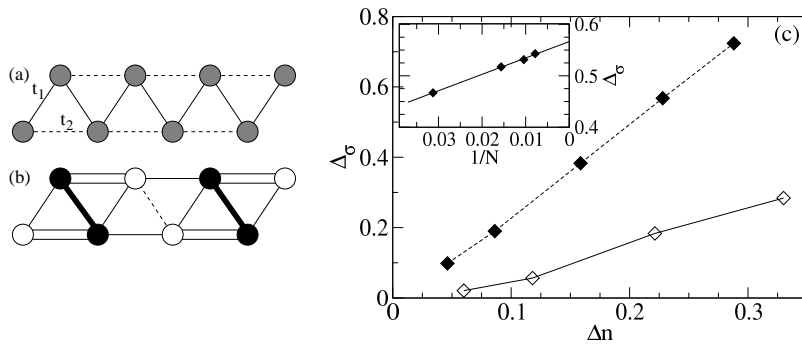


Figure 47. Zigzag ladder lattice with  $\rho = \frac{1}{2}$  (a) The ground state with  $t_2/t_1 > 1.707$  has uniform charges and bonds (b) For  $t_2/t_1 < 1.707$  the ground state is a PEC with bond order of the BCDW-II type along the zigzag direction. (c) Finite-size scaled spin gap  $\Delta_\sigma$  for  $t_2/t_1 = 1.43$ ,  $U = 6$ , and  $V = 1$  versus  $\Delta n$  for the zigzag ladder (filled symbols) and in a 1D chain with the same  $U$  and  $V$  (open symbols). The inset shows the finite-size scaling for the zigzag ladder with  $|\epsilon|=0.3$ . The unit of energy is taken as the average hopping integral along the zigzag direction (see text) [127].

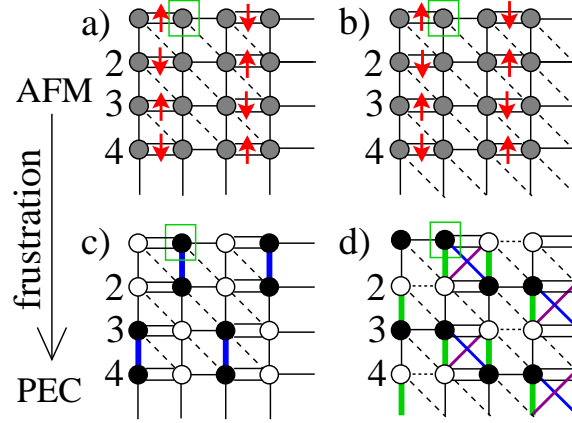


Figure 48. (color online) PEC formation in a  $4 \times 4$  lattice [124]. (a) OBC and (b) PBC lattices for  $t' < t'_c$ . Double bonds and thick lines indicate strong bonds; thin lines are weak bonds. Dashed lines indicate diagonal bonds whose strength is varied. Small, large, and uniform charge densities are indicated by white, black, and gray circles, respectively. (c) and (d) PEC state for  $t' > t'_c$ . Numbers correspond to the chain indices in Fig. 49. Boxes mark the site 2 of chain 1; spin-spin correlations between this site and other chains are shown in Fig. 49 [124].

### 6.2.2. Paired Electron Crystal in two dimensions

The absence of a spin-singlet phase in the phase diagram of Fig. 44, and the suppression of superconducting pair-pair correlations in the frustrated  $\frac{1}{2}$ -filled band Hubbard model are related. There is simply no evidence for either the proposed RVB state, or a VBS state that is driven by lattice frustration at  $\rho = 1$  (Given the tendency to form the  $120^\circ$  AFM at large  $t'$ , it may be argued that there is no physical reason why such a singlet state should form at all.) Yet the concept of mobile nearest neighbor singlets being the equivalents of Cooper pairs in configuration space remains attractive. Theoretical work on both rectangular [559] and zigzag [555, 556]  $\rho = 1$  ladders suggests that singlet formation, instead of being driven by lattice frustration, can be due to “effective one-dimensionalization” within a 2D lattice. The only way to have this in an extended lattice is to have  $\rho \neq 1$ , where the one-dimensionalization is due to formation of segregated stripes of sites occupied by charge carriers. This is a form of charge-ordering and will not occur at arbitrary  $\rho$ : for  $\rho \approx 1$  it is impossible for an “occupied” site to not have more than two neighbors, while for  $\rho$  very small the kinetic energy of individual carriers will overwhelm the gain in exchange energy that drives local singlet formation. The optimum concentration is exactly  $\rho = \frac{1}{2}$ , where one can visualize occupied and unoccupied stripes perfectly alternating, thereby conferring commensurability driven stability to the structure. Furthermore, we will show in this section that in the presence of geometric lattice frustration such a striped structure is simultaneously a PEC, in which pairs of singlet-bonded sites are separated by pairs of vacant sites. In the presence of e-p coupling the insulating striped structure undergoes lattice distortion that also resembles a 2D SP state, which we have already pointed out has in the past been thought to be behind correlated-electron SC [508, 509]. We have termed this charge-ordered state as the Paired Electron Crystal (PEC). It was shown that in the context of the interacting continuous electron gas, a PEC state has a variational energy that is *lower* than that of the WC [560, 561]. The PEC we describe below gains additional energy over the continuum case due to the lattice commensurability at  $\rho = \frac{1}{2}$ .

We first summarize the results of our calculations, after which we present further details. The Hamiltonian is

$$\begin{aligned}
 H = & - \sum_{\nu, \langle ij \rangle_\nu} t_\nu (1 + \alpha_\nu \Delta_{ij}) B_{ij} + \frac{1}{2} \sum_{\nu, \langle ij \rangle_\nu} K_\alpha^\nu \Delta_{ij}^2 \\
 & + g \sum_i v_i n_i + \frac{K_g}{2} \sum_i v_i^2 + U \sum_i n_{i\uparrow} n_{i\downarrow} + \frac{1}{2} \sum_{\langle ij \rangle} V_{ij} n_i n_j.
 \end{aligned} \tag{14}$$

In Eq. 14 the sums  $\nu$  run over three lattice directions in two dimensions,  $\hat{x}$ ,  $\hat{y}$ , and  $\hat{x} - \hat{y}$ .  $B_{ij} = \sum_\sigma (c_{i\sigma}^\dagger c_{j\sigma} + H.c.)$ ,  $\alpha_x$ ,  $\alpha_y$ , and  $\alpha_{x-y}$  are the intersite e-p couplings. Unless denoted otherwise we choose  $\alpha_x = \alpha_y \equiv \alpha$  and  $\alpha_{x-y} = 0$ .  $K_\alpha^x = K_\alpha^y = K_\alpha^{x-y} \equiv K_\alpha$  is the corresponding spring constant, and  $\Delta_{ij}$  is the distortion of the  $i$ - $j$  bond, to be determined

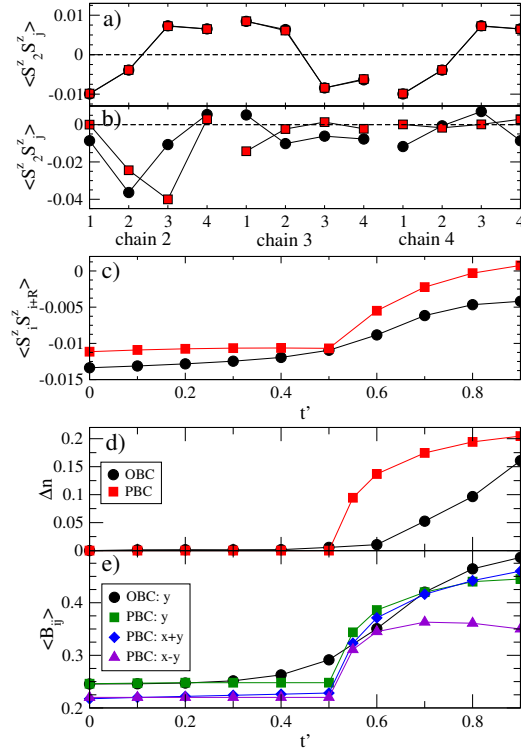


Figure 49. (color online) Correlation functions from exact  $4 \times 4$  lattice calculations corresponding to Fig. 48 [124]. Chain indexing is shown in Fig. 48. (a) Z-Z spin correlations between site 2 on chain 1 (marked with a box on Fig. 48) and sites on chains 2, 3, and 4, for  $t' = 0$  (b) same as (a) except  $t' = 0.7$ . (c) Spin-spin correlations between sites that are members of the most distant dimers (d) difference in charge density between charge-rich and charge-poor sites. (e) bond orders between nearest neighbor sites in the indicated directions. In all panels, circles and squares correspond to OBC and PBC calculations, respectively. In (e) bond orders for other directions in the PBC calculations are shown with additional symbols [124].

self-consistently;  $v_i$  is the intrasite phonon coordinate and  $g$  is the intrasite e-p coupling with the corresponding spring constant  $K_g$ . We assume the simplest form of frustration, with a bond strength  $t'$  in the  $\hat{x} - \hat{y}$  direction on a square lattice. However, we begin here with the simple, unfrustrated, square lattice ( $t' = 0$  and  $V_{x-y} = 0$ ) limit of Eq. 14. In this case two different semiconducting states are possible: in-phase dimerized AFM with all site charge densities equal (see Fig. 48(a) and (b)) and for sufficiently large  $V_x$  and  $V_y$ , the WC with checkerboard site occupancies. These two insulating phases are mutually exclusive. We choose parameters that give AFM in the weakly frustrated limit, as in 2D CTS with experimentally observed AFM lattices are universally dimerized. Fig. 48 shows schematically the results of exact ground state calculations on  $4 \times 4$  lattices with two different boundary conditions, open (OBC) and periodic (PBC). Both are periodic along  $x$  and  $y$  directions, but the OBC (PBC) is open (periodic) along  $x - y$  with 12 (16)  $t'$  bonds. For both boundary conditions we find a frustration-driven AFM-PEC transition as we increase the strength of the frustrating hopping  $t'$ . For the OBC we take  $\alpha_y = g = 0$  in Eq. 14; in order to have AFM order at  $t' = 0$  here we incorporate intrinsic dimerization  $t_x = t \pm \delta_t$  as indicated in Fig. 48(a). For the PBC lattice, lattice distortion is not assumed but results from the e-p interactions. Spin-spin correlations, charge densities and bond orders for the PBC are obtained self-consistently [124].

In Fig. 49 we show numerical results that prove the AFM-PEC transition indicated in Fig. 48. These results are for  $U = 4$ ,  $V_x = V_y = 1$ ,  $V_{x-y} = 0$  within Eq. 14, where the undistorted hopping integral in the  $x$  direction ( $t_\nu$  of Eq. 14 with  $\nu = x$ ) is taken as the unit of energy. For the OBC lattice  $\delta_t = 0.2$  and  $\alpha_y = g = 0$  as described above, and for the PBC  $\alpha_x = 1.3$ ,  $\alpha_y = 1.0$ ,  $\alpha_{x-y} = 0$ ,  $K_\alpha^x = K_\alpha^y = 2$ ,  $g = 0.1$ , and  $K_g = 2$ . In Fig. 49(a) we plot the z-z spin-spin correlation functions for  $t' = 0$  between a fixed site (marked with box on each lattice in Fig. 48) and sites  $j$ , labeled sequentially 1, 2, 3, 4 from the left, on neighboring chains labeled 2, 3, 4 in Fig. 48. In Fig. 49(a) only, the average

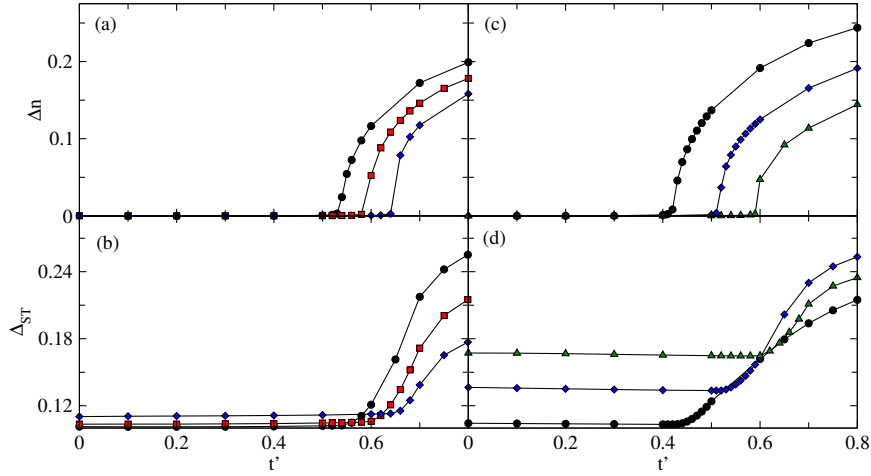


Figure 50. (color online) Charge order amplitude  $\Delta n$  ((a) and (c)) and singlet-triplet gap  $\Delta_{ST}$  ((b) and (d)) for the  $4 \times 4$  lattice as a function of  $t'$ . Circles, squares, diamonds, and triangles are for  $U=2, 3, 4,$  and  $6$ , respectively. For all  $\alpha = 1.1, g=0.1,$  and  $K_\alpha=K_g=2$ . In panels (a) and (b),  $V_x = V_y = V'=0$ , and in panels (c) and (d),  $V_x = V_y = 1$  and  $V'=0$ . The average (undistorted) hopping integral in the  $x$  direction is taken as the unit of energy [125].

spin-spin correlation with each chain has been shifted to zero (note dotted line for  $\langle S_2^z S_j^z \rangle = 0$  in Fig. 49(a)-(b)) in order to clearly show the AFM pattern, which is clearly  $\cdots - - + + \cdots$  and  $\cdots + + - - \cdots$ , indicating Néel ordering of the dimer spin moments in both lattices. The loss of this pattern in Fig. 49(b) for large  $t' = 0.7$  indicates loss of AFM order. In Fig. 49(c) we plot the spin-spin correlation between maximally separated dimers, which measures the strength of the AFM moment. This correlation is nearly constant until  $t'_c \sim 0.5$ , beyond which the AFM order is destroyed.

Fig. 49(d) shows  $\Delta n$  as a function of  $t'$ . There is a rapid increase in  $\Delta n$ , starting from zero, for  $t' > t'_c$  with both lattices. Simultaneously with CO, there is a jump in the bond orders  $\langle B_{ij} \rangle$  between the sites that form the localized spin-singlets. This is shown in Fig. 49(e). These bond orders are by far the strongest in both lattices for  $t' > t'_c$ . The spin-spin correlation between the same pairs of sites becomes strongly negative at the same  $t'$ , even as all other spin-spin correlations approach zero (Fig. 49(b)), indicating spin-singlet character of the strongest bonds. The simultaneous jumps in  $\langle S_i^z S_{i+R}^z \rangle$ ,  $\Delta n$ , and  $B_{ij}$  at this same  $t'$  give conclusive evidence for the AFM-PEC transition shown in Fig. 48.

Figs. 50(b) and (d) show the singlet-triplet gap  $\Delta_{ST}$  compared with  $\Delta n$ , for the  $4 \times 4$  lattice with periodic boundaries and  $V = 0$  ((a) and (b)) and  $V \neq 0$  ((c) and (d)). Although  $\Delta_{ST}$  is nonzero for all values of  $t'$  (as expected in a finite-size lattice), the spin gap increases sharply in the PEC state for  $t' > t'_c$ . The increase of  $\Delta_{ST}$  between the AFM and PEC states is also proportional to the amplitude of the distortion  $\Delta n$  as expected.

In the PEC the CO pattern is  $\cdots 1100 \cdots$  in two of three lattice directions,  $\hat{x}$  and  $(-\hat{x} + \hat{y})$  in Fig. 48(d), and  $\hat{y}$  and  $(\hat{x} + \hat{y})$  in Fig. 48(c). In the third direction the CO pattern is  $\cdots 1010 \cdots$ . The singlets that coexist with the CO are of the interdimer type as is found in BCDW-I in 1D, and the bond order pattern found here is the same SWSW' pattern (note that in Fig. 48 distortions of the dashed  $t'$  bonds are not indicated). The results here are for the ground state only. As in 1D (Sections 3.2.1 and 3.3) it is possible that the charge and bond distortion may occur at a higher temperature, with the SG only opening at a lower temperature. We discuss this further in relation to 2D CTS below.

Fig. 51 shows how e-e interactions  $U$  and  $V$  affect the PEC [125]. As shown in Fig. 51(a), increasing  $U$  moderately increases  $t'_c$ . The points not plotted for larger  $U$  indicate that a finite e-p coupling is required for the PEC state, which is expected due to the finite-size gap in this small lattice. Fig. 51 shows the effect of the NN Coulomb interaction  $V$ . Here the phase diagram depends critically on the form assumed for  $V_{ij}$ . With  $V_x = V_y = V$  but  $V' = 0$ , the WC is found for sufficiently strong  $V$ , along with a narrow region where it coexists with a SG (Fig. 51(b)). The very narrow width of the WC-SG phase in the figure indicates the small likelihood of the WC coexisting with SG in real materials. Equally importantly, most CTS lattices are partially triangular, and the assumption that  $V' = 0$  is not realistic. For  $V_x = V_y = V'$  the WC and the PEC have the same classical energies; as shown in Fig. 51(c) in this case the WC is completely replaced by the PEC.

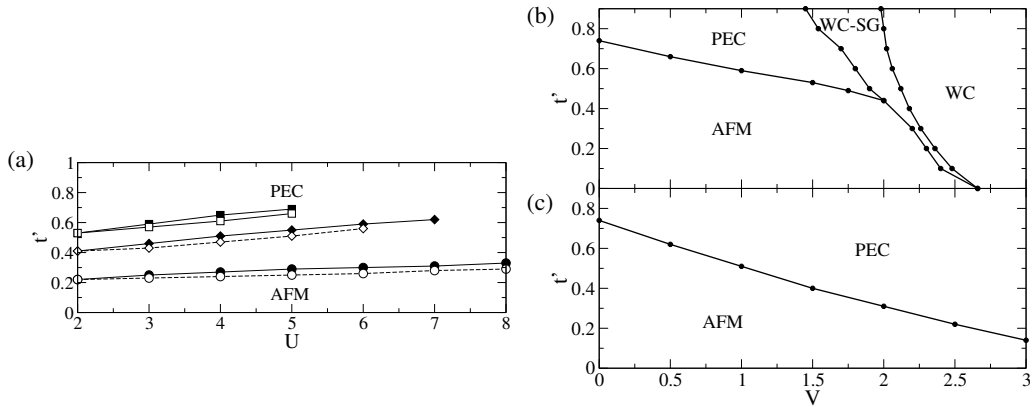


Figure 51. Ground state phase diagrams from self-consistent calculations of Eq. 14 on periodic  $4 \times 4$  lattice, showing AFM and PEC phases [125] For all plots  $g=0.1$  and  $K_\alpha = K_g = 2$ . (a) Phase diagram as a function of  $t'$  and  $U$ . Squares are the AFM-PEC phase boundary for  $\alpha = 1.1$  and  $V_x = V_y = V' = 0$ . Diamonds are for  $\alpha = 1.1$ ,  $V_x = V_y = 1$ , and  $V' = 0$ . Circles are for  $\alpha = 1.2$ ,  $V_x = V_y = 1$ , and  $V' = 0$ . Filled (open) points correspond to positive (negative)  $t'$ . For  $U$  values where no points are plotted, the lattice was undistorted. (b) Phase diagram for  $V_x = V_y = V$  and  $V' = 0$  with  $U = 6$  and  $\alpha = 1.1$ . WC and WC-SG are Wigner crystal of single electrons and the coexisting single electron Wigner crystal-spin-gap phases, respectively. (c) Same as (b), except  $V = V_x = V_y = V'$ .

### 6.2.3. Paired Electron Crystal in quasi-two dimensional CTS

Evidence for the PEC with CO, bond order, and spin gap, has been found experimentally in many 2D CTS. CO by itself does not necessarily imply that the PEC is present. As discussed in the previous section, the pattern of charge order in the PEC is *distinct* from that of the WC; in the PEC pattern there are NN charge-rich sites which are not present in the WC. The frustrated crystal lattice in all of the 2D CTS have significant inter-molecular hopping in three different lattice directions. Using the principle that in two lattice directions the CO pattern is  $\cdots 1100 \cdots$  while  $\cdots 1010 \cdots$  in one direction, the predicted pattern for different CTS lattices can be derived. However, even if the exact pattern of CO is not known, a period four lattice distortion occurring in a 2D crystal indicates PEC formation. This is because the competing CO state, the WC, does not coexist with a bond distortion. Similarly, a spin gap is a convincing signature of the PEC, even when accompanying CO has not been found. In contrast, only AFM can coexist with the WC [562] (the AFM pattern here is however different from that in Fig. 48).

$\beta$ ,  $\beta'$ , and  $\beta''$  CTS. The largest group of CTS where the PEC has been found are the  $\beta$ ,  $\beta'$ , and  $\beta''$  CTS. As discussed in Section 5.1.2, charge- and bond-ordered insulating states and spin gaps are frequently found adjacent to SC. In cases where the CO pattern has been determined, it matches the pattern of Fig. 48 exactly. For example,  $\beta$ -(*meso*-DMBEDT-TTF) $_2X$  is one well characterized example where the experimental CO and bond pattern is identical (compare Fig. 27(a) and Fig. 48). Here the bond pattern along the stacking direction goes  $\cdots SWSW' \cdots$ , exactly as in BCDW-I [345]. The ground state of  $\beta$ -(*meso*-DMBEDT-TTF) $_2X$  in the ambient pressure insulating phase is also spin gapped.

Although it is  $\frac{1}{4}$ -filled in terms of electrons rather than holes,  $\text{EtMe}_3\text{P}[\text{Pd}(\text{dmit})_2]_2$  is another example of the PEC with exactly the same CO and bond order pattern (see Section 5.2.2 and Fig. 41(b)). Again, under pressure,  $\text{EtMe}_3\text{P}[\text{Pd}(\text{dmit})_2]_2$  becomes superconducting. Kato et al. in their original work had referred to the CO in this system as a valence bond solid, as would be expected in a  $\frac{1}{2}$ -filled band [563]. In their recent work [487] the authors find that a  $\frac{1}{4}$ -filled description is more appropriate.

In  $\beta$ -( $\text{ET}$ ) $_2\text{ReO}_4$  (Fig. 26(a)) and  $\beta$ -(BDA-TTP) $_2X$  (Fig. 26(b)) the PEC is found adjacent to SC. In both of these CTS a period four lattice distortion and spin gap is found in the insulating state. Similarly, in the  $\beta''$  materials, strong evidence for a PEC ground state exists: here a  $\cdots 1100 \cdots$  CO pattern along the stacking direction has also been determined from optical experiments [399]. CO coexisting with spin gap has also recently been found in  $\beta''$ -( $\text{ET}$ ) $_2\text{Hg}(\text{SCN})_2\text{Cl}$  [564].

Less is known about  $\beta'$ -( $\text{ET}$ ) $_2\text{ICl}_2$  in its phase adjacent to SC due to the high pressure required to access this region of the phase diagram. It is clear however that the AFM state that exists at ambient pressure disappears under

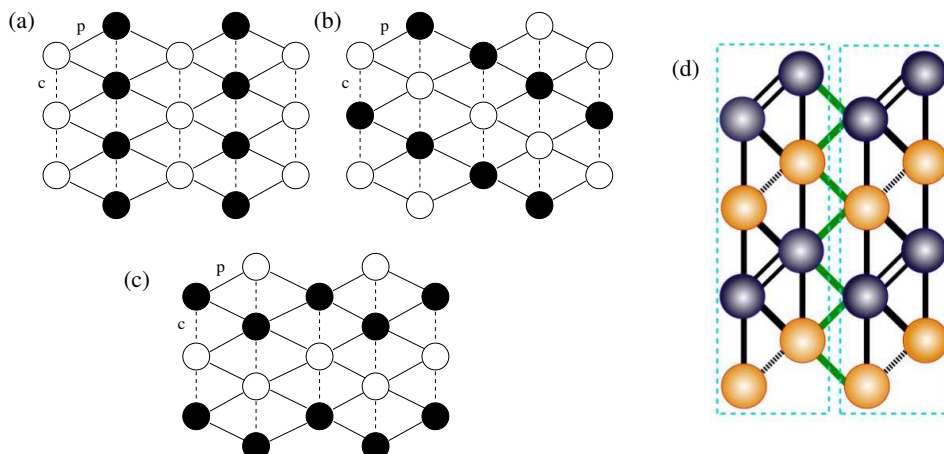


Figure 52. CO patterns and PEC in  $\theta$ -(ET)<sub>2</sub>X. (a) vertical stripe (b) diagonal stripe (c) horizontal stripe. The horizontal stripe has charge occupancy  $\cdots 1100 \cdots$  along the two  $p$ -directions with strong intermolecular coupling. (d) PEC within the horizontal stripe CO, which can be visualized as repeated zigzag ladders [565]. Note that the bond dimerization along the vertical bonds (crystal  $c$  direction) is not shown here.

high pressure before the superconducting state, and a different form of insulating state enters above around 6 GPa (see Fig. 28). Based on similarities with the  $\beta$ -phase CTS we predict that PEC-type CO and a spin gap will be found in the insulating state adjacent to SC here as well. The phase diagram of  $\beta$ -Me<sub>4</sub>NPd(dmit)<sub>2</sub> (Fig. 39) appears somewhat similar, as here again the ambient pressure AFM is suppressed by about 0.4 GPa, before the SC region is reached. Here and also in  $\beta'$ -Et<sub>2</sub>Me<sub>2</sub>P[Pd(dmit)<sub>2</sub>]<sub>2</sub> (see also Fig. 39) we suggest that the phase adjacent to SC is the PEC.

*$\theta$  and  $\alpha$  CTS.* In the  $\theta$  (Section 5.1.3) and  $\alpha$  (Section 5.1.4) CTS the most stable CO pattern is the horizontal stripe (see Fig. 52). In  $\theta$ -(ET)<sub>2</sub> MM'(SCN)<sub>4</sub> with MM' = RbZn, the horizontal stripe CO transition temperature is 195 K, but the PEC with spin gap only appears at  $\sim 20$  K within the horizontal stripe CO. The appearance of CO at a relatively high temperature without a spin gap suggests that NN Coulomb interactions ( $V_{ij}$ ) play an important role in determining the pattern of CO [107, 122]. All of the CO patterns shown in Fig. 52(a)-(c) have identical energies within the classical limit (assuming  $V_{ij}$  is identical in all three lattice directions). There is a key difference between the vertical and diagonal stripes (Fig. 52(a) and (b)) and the horizontal stripe (Fig. 52(c)) however: in both the vertical and diagonal stripes, the CO pattern is  $\cdots 1010 \cdots$  in *two* lattice directions, as is true for the checkerboard WC on the square lattice [122]. If mapped to a square lattice, both the vertical and diagonal CO patterns are identical to the usual WC. Because of this, mean field (Hartree or Hartree-Fock) calculations tend to predict the vertical or diagonal stripe patterns [107, 122]. In contrast, the horizontal stripe has CO patterns  $\cdots 1010 \cdots$  in the direction of weakest intermolecular hopping and  $\cdots 1100 \cdots$  along the two directions with strong intermolecular hopping. The horizontal stripe pattern thus gains additional stabilization energy because of the stronger tendency to spin-singlet formation. The horizontal stripe CO is only found as a solution in mean-field calculations provided the dimerization along the  $c$  axis (which only appears for  $T < T_{CO}$ ) is explicitly included [107]. This dimerization is a *consequence* rather than a cause of the CO [122].

In order for the horizontal stripe CO to have a spin gap, a further symmetry breaking accompanying NN singlet formation must take place along the direction of the stripe, as shown in Fig. 52(d). Within the horizontal stripe there are two possible locations for NN singlets; in Fig. 32 the NN singlet pair could be located at *either* of the two bonds labeled “p4” in the figure. This second symmetry breaking and the spin gap state occurs at  $\sim 20$  K in RbZn. The horizontal stripe PEC in this case can also be visualized as being composed of coupled zigzag ladders (see Fig. 52(d)) [565].

Compared to RbM', the CsM'  $\theta$  salts remain metallic to much lower temperature and have much more confusing low-temperature behavior with short-range rather than long-range charge order (see Section 5.1.3). Diffuse X-ray scattering is also found at several wavevectors in the CsM' salts indicating a competition between several CO patterns. This competition may be particularly important to understanding the unusual transport properties [566]. Several works

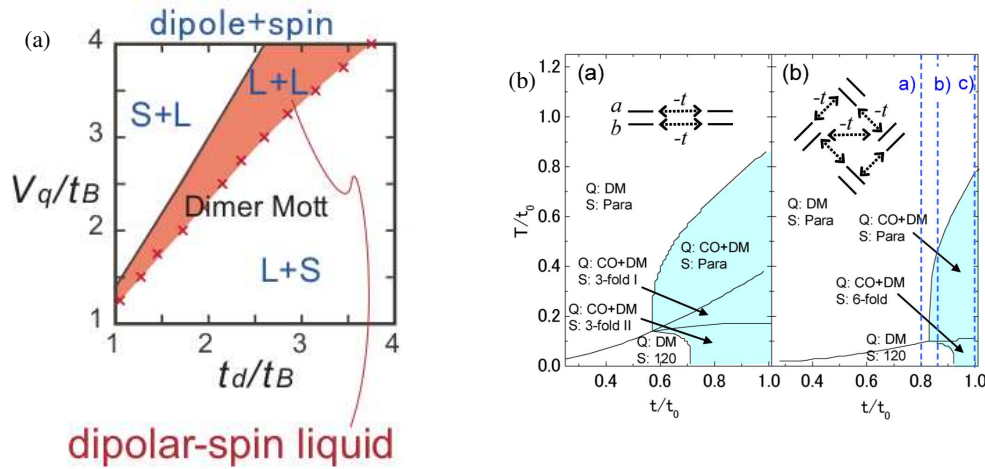


Figure 53. (a) Exact diagonalization ground state phase diagram for the effective strong-coupling Hamiltonian for  $\kappa$ -(ET)<sub>2</sub>X of Reference [571].  $t_B$ ,  $t_d$ , and  $V_q$  are the inter-dimer hopping integral  $t_{b2}$ , intra-dimer hopping integral, and n.n. Coulomb interaction, respectively (see Fig. 20). S+L denotes a charge ordered spin liquid phase, L+S a spin ordered charge liquid phase, and L+L a charge-spin liquid phase. Reprinted with permission from Ref. [571], © 2010 The American Physical Society. (b) Finite-temperature phase diagram calculated within mean-field theory [572, 573].  $t/t_0$  is the ratio of the inter- to intra-dimer hopping integral. Reprinted with permission from Ref. [572], © 2010 The Physical Society of Japan.

by Hotta and collaborators have explored the competition between different CO states as a function of  $V_{ij}$  [567–569]. A partially ordered “pinball liquid” phase was suggested to describe the unusual semi-metallic properties of  $\theta$ -(ET)<sub>2</sub>CsZn(SCN)<sub>4</sub> [568, 570]. Further work focused on the effect of thermal fluctuations [569].

The PEC is also found in  $\alpha$ -(ET)<sub>3</sub> (Fig. 33). Here the CO pattern is again the horizontal stripe with a coexisting SG. Unlike  $\theta$ -(ET)<sub>2</sub>X, the SG transition is at the same temperature as the CO (135 K). The presence of a single combined CO/SG PEC transition in  $\alpha$  as compared to  $\theta$  may be due to the lower symmetry of the  $\alpha$  crystal structure and the presence of partial CO already above 135 K (see Figs. 25 and 33).

$\kappa$  CTS. The stabilization energy the PEC gains from NN singlet formation will be less on the  $\kappa$  lattice due to the many nearly degenerate ways of connecting NN molecules with singlet bonds [124, 125]. Because dimers of BEDT-TTF molecules are nearly perpendicular to each other, any static insulating PEC state would be expected to be very weak [124]. Nevertheless, some experimental evidence for an insulating PEC state exists for two  $\kappa$  phase CTS. Recent experiments have shown that  $\kappa$ -(ET)<sub>2</sub>B(CN)<sub>4</sub>, which is more quasi-1D than most  $\kappa$  CTS, is spin-gapped below 5 K strongly suggesting a PEC ground state [222]. Raman scattering measurements were performed to 10 K, which is above the spin-gap transition [222], leaving open the possibility of CO below 5 K. CO is explicitly found in  $\kappa$ -(ET)<sub>2</sub>Hg(SCN)<sub>2</sub>Cl (see Section 5.1.1), although the pattern of CO has not been determined yet. The fairly low  $T_{CO}$ =30 K here suggests that the CO state has 1–0 charges within each dimer, rather than 1–1 and 0–0 dimer CO. So far a spin gap at low temperature has not been found however.

A PEC-like CO pattern was suggested to explain the relaxor-like dielectric response found in  $\kappa$ -(ET)<sub>2</sub>Cu<sub>2</sub>(CN)<sub>3</sub>, where CO within each dimer is the source of the dielectric polarization (see Fig. 5 of Reference [306]). Several theoretical works have proposed models based on a  $\frac{3}{4}$ -filled description with the goal of capturing the coupling between dimer charge dipoles and inter-dimer spin interactions [571–573]. In these models a strong-coupling limit is assumed, with only those states that have exactly one electron per dimer retained. While both groups found fluctuating charge ordered phases approximating the PEC CO pattern predicted in Reference [124], the possibility of spin-singlet formation was not considered. Fig. 53(a) shows the ground state phase diagram of an effective model where the effects of  $t_{ij}$  and  $V_{ij}$  between dimers are treated perturbatively [571]. The phase diagram is governed by a competition between  $V$  and the inter-dimer  $t_{ij}$  [571]. The “S+L” phase has ordered charge dipoles on each dimer, and has the same CO pattern as would be expected for a PEC state on the  $\kappa$  lattice (compare Fig. 1(d) of reference [571] with Fig. 4(c) of reference [124]). The “L+S” phase on the other hand has AFM order but no CO; this is the conventional dimer-Mott AFM state. A state with disordered charge and spin degrees of freedom is found at the boundary of these phases; this

was proposed to apply to  $\kappa$ -(ET)<sub>2</sub>Cu<sub>2</sub>(CN)<sub>3</sub>.

Naka and Ishihara [572] developed a similar effective model for a dimerized  $\frac{1}{4}$ -filled lattice, with four states per dimer and interactions between dimers treated perturbatively. The resulting model was studied under the mean-field approximation and using classical Monte Carlo. Fig. 53(b) shows the mean-field phase diagram for this model on a lattice appropriate for the  $\kappa$  CTS. As in Fig. 53(a), an increase of the ratio of inter- to intra- dimer hopping favors CO. Two different possible scenarios were proposed to describe  $\kappa$ -(ET)<sub>2</sub>Cu<sub>2</sub>(CN)<sub>3</sub> [572]. In the first, at high temperature the system has no CO (Q:DM phase in Fig. 53(b)). CO occurs at low temperature, followed by a spin ordered CO state at the lowest temperature. In the other suggested scenario, CO does not occur at low temperatures, with the system staying in the unshaded phases of Fig. 53(b) as  $T$  decreases. However, due to proximity to the CO phases some charge fluctuation features would be observed experimentally. The timescale of the dielectric constant experiments is much longer than the expected fluctuation time of a single BEDT-TTF dimer; this suggests that in any case rather than long-range PEC order, short ranged domains might exist in  $\kappa$ -(ET)<sub>2</sub>Cu<sub>2</sub>(CN)<sub>3</sub>, and it is these domains that fluctuate rather than single molecules. The question of whether CO exists within a single dimer, or if CO exists but is smaller than the limits ( $\Delta n = 0.01$ ) set by optical measurements still remains [312].

As discussed in Section 5.1.1, in  $\kappa$ -(ET)<sub>2</sub>X AFM and metallic/SC regions are phase segregated at low temperature. In Sections 6.2.4 and 6.2.5 below we will show that on the  $\frac{3}{4}$ -filled  $\kappa$  lattice superconducting pair-pair correlations are enhanced by Coulomb interactions ( $U$ ) in this metallic state. There we will propose that in the majority of  $\kappa$  phase CTS, the ground state when not AFM is a Paired Electron Liquid (PEL) of singlets, which is either a superconductor or a metallic state that is a precursor to SC.

#### 6.2.4. Selective enhancement of superconducting pair-pair correlations at $\rho = \frac{1}{2}$

The above results show that the PEC is a distinct phase in the correlated  $\rho = \frac{1}{2}$  systems and is actually observed in 2D CTS with CO. In analogy with the conjectures built around the concept of a density wave of Cooper pairs [43, 44, 502–504, 504–507], we have further proposed that SC will occur upon the destabilization of the PEC state [16, 124, 125, 565, 574]. Note that this idea also has overlaps with the idea of SC emerging from a 2D SP state (which we have emphasized does not exist at  $\rho = 1$ ), as the dimerized horizontal stripes of Figs. 52(c) and (d) can be thought of as weakly coupled SP stripes. In contrast to these other theories, we believe that the proposed density wave of Cooper pairs is unique to  $\rho = \frac{1}{2}$  in 1D and frustrated 2D systems. With further increase in frustration, there occurs a transition from the PEC to a Paired Electron Liquid, with mobile singlet pairs constituting the equivalent of Cooper pairs. We have therefore studied in detail the superconducting pair-pair correlations on multiple frustrated lattices, as a function of  $\rho$ ,  $0 < \rho < 1$ . In these calculations we do not explicitly include e-p interactions, with the result that the insulating PEC of Figs. 48 does not occur.

While many previous calculations have examined superconducting pair-pair correlations for  $\rho \sim 1$ , comparatively few calculations exist for  $\rho = \frac{1}{2}$  on strongly frustrated lattices. We consider again the anisotropic triangular lattice of Fig. 48, with  $t' \sim 0.8$  [565]. We performed calculations on up to  $10 \times 10$  lattices periodic in all three directions with four different numerical methods (exact diagonalization, QP-PIRG [535], Determinantal Quantum Monte Carlo (DQMC) [575], and Constrained Path Monte Carlo (CPMC) [576] [565]). These particular lattices were chosen using several criteria, including the requirement that the noninteracting system be nondegenerate at  $\rho = \frac{1}{2}$  [565]. Results from these calculations are shown in Fig. 54 and Fig. 55.

In order to compare different lattices and mitigate finite-size effects, we average the pair-pair correlations  $P(r)$  (see Eq. 12) over all pair separations with distances  $r > 2$  lattice spacings,

$$\bar{P} = N_p^{-1} \sum_{|\vec{r}| > 2} P(r), \quad (15)$$

where  $N_p$  is the number of terms in the sum. A similar averaged pair-pair correlation  $\bar{P}$  has been used in previous studies of pair-pair correlations near  $\rho = 1$  [529, 577]. In these calculations we found either  $d_{x^2-y^2}$  or  $d_{xy}$  pairing symmetries to dominate over  $s$ -wave pairing. Fig. 54 summarizes these calculations. Here  $\bar{P}$  is normalized by its  $U = 0$  value;  $\bar{P}(U)/\bar{P}(U = 0) > 1$  indicates enhancement. As seen in Fig. 54, for every lattice we find that pairing is enhanced *only* for  $\rho = \frac{1}{2}$  or one of two immediately adjacent available densities on that particular lattice. At all other densities, pair-pair correlations weaken continuously with increasing  $U$ . The suppression of pairing in the range  $0.75 < \rho < 1$  is consistent with previous PIRG [38] results, and consistent with many calculations using DQMC

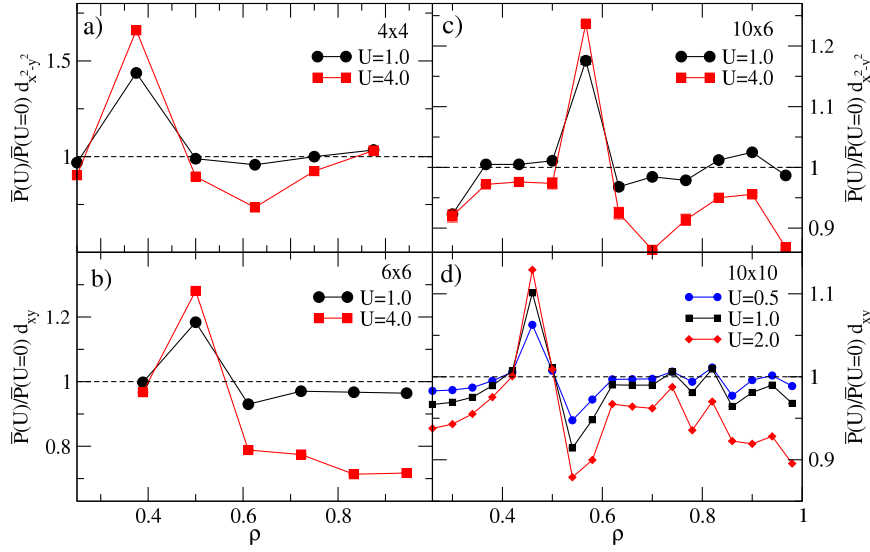


Figure 54. (color online) Average long-range pair-pair correlation  $\bar{P}(U)$  normalized by its noninteracting value versus  $\rho$  on the anisotropic triangular lattice with  $t_x = 1$ ,  $t_y = 0.9$ , and  $t' = 0.8$ . The lattices and methods used are (a)  $4 \times 4$  (exact), (b)  $6 \times 6$  (QP-PIRG), (c)  $10 \times 6$  (QP-PIRG), and (d)  $10 \times 10$  (CPMC).

[578], CPMC [579, 580], and DMRG [542] that find suppression of pairing by  $U$  in the unfrustrated model for the same density range. Ignoring the  $6 \times 6$  lattice where  $\bar{P}$  is enhanced at exactly  $\rho = \frac{1}{2}$ , for all other lattices the  $\rho$  where enhancement occurs becomes closer to  $\rho = \frac{1}{2}$  with increasing lattice size. On different lattices either  $d_{x^2-y^2}$  or  $d_{xy}$  pairing is enhanced by  $U$ ; it would be expected in this highly frustrated lattice ( $t' = 0.8$  in Fig. 54 and 55) that the optimum pair symmetry is a superposition of  $d_{x^2-y^2}$  and  $d_{xy}$ . The effect of nonzero  $V_{ij}$  was also investigated for the  $4 \times 4$  lattice [565]. With  $V_x = V_y = V' = V$  the magnitude of the pair-pair correlations decreases somewhat, but the unique enhancement at  $\rho \sim 0.5$  remains [565].

Fig. 55 shows the results of finite-temperature DQMC calculations. Here the sign problem becomes severe at large  $U$ , but low temperatures (an inverse temperature of  $\beta = 32$ ) can be reached for  $U = 2$ . As seen in Fig. 55(a)-(d), with decreasing temperature there is a progressive enhancement of  $\bar{P}(U)$  for  $\rho \sim \frac{1}{2}$  in the  $6 \times 6$  lattice. Fig. 55(e) and (f) show similar results for the  $4 \times 4$  and  $10 \times 6$  lattices. These results are in complete agreement with the PIRG results in Fig. 54: the  $\rho$  at which the enhancement occurs is identical.

To the best of our knowledge, the above results are the only demonstrations to date of enhancement of  $\bar{P}(U)$  by  $U$  for any lattice. The question remains as to whether the first criterion for SC given above is satisfied, e.g. do the pair-pair correlations show long-range order at  $\rho = \frac{1}{2}$ ? Unfortunately, the results of Figs. 54 and 55 are not sufficient to perform a finite-size scaling of  $\bar{P}(r)$ : the enhancement occurs at slightly different densities from  $\rho = \frac{1}{2}$  on different lattices, and in different pairing symmetries. It is possible that larger lattices and an optimized superposition of  $d_{xy}$  and  $d_{x^2-y^2}$  pair symmetries would resolve these difficulties. If superconducting long-range order (LRO) is present at finite  $U$ ,  $\bar{P}(U)$  would converge to a constant value as the system size increases while  $\bar{P}(U = 0)$  would continue to decrease. In this case  $\bar{P}(U)/\bar{P}(U = 0)$  would increase with increasing system size. Our finding that  $\bar{P}(U)/\bar{P}(U = 0)$  at its peak value instead decreases with increasing system size (compare the y-axis scales on Fig. 54(a)-(d)) on the other hand seems to suggest that long-range order is not present. The issue of the long range order is, however, complicated. We discuss this further in Section 7.

### 6.2.5. Superconducting pair-pair correlations in the $\kappa$ -(ET) $_2$ X lattice

The above results strongly suggest that SC is driven by e-e interactions uniquely at  $\rho = \frac{1}{2}$ . It is therefore important to see if they persist on other lattices, and in particular for  $\kappa$ -(ET) $_2$ X, whose monomer lattice (see Fig. 20(a)) is significantly different from the simple anisotropic triangular lattice of Fig. 54. The first question is what is an appropriate form for the pair wavefunction. In SC emerging from a charge ordered PEC state with strong e-e interactions,  $U$  for

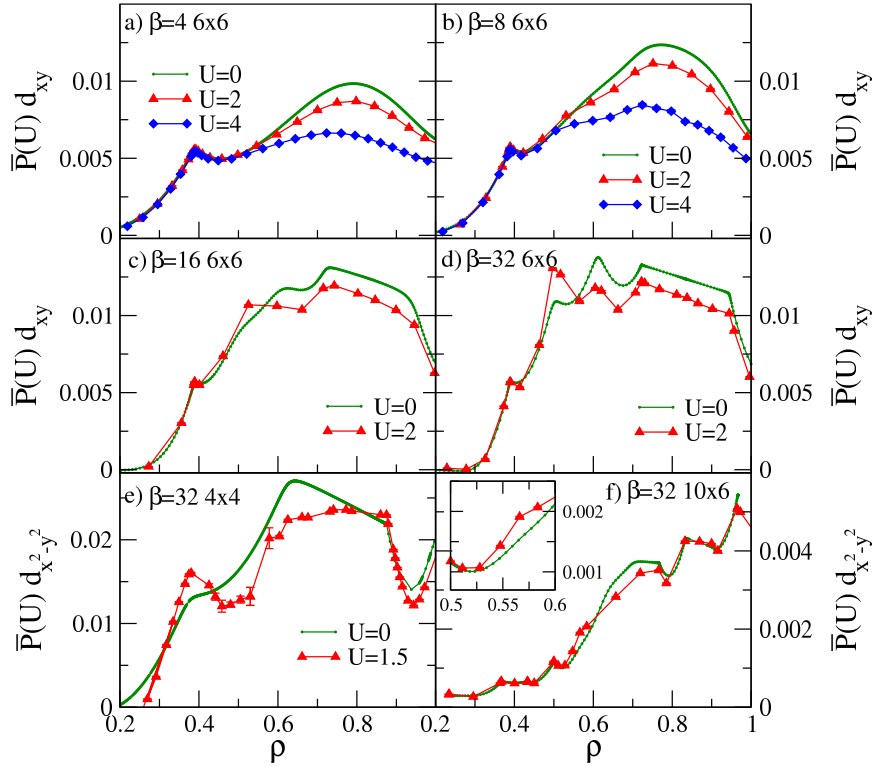


Figure 55. (color online) (a)-(d)  $\bar{P}(U)$  for  $d_{xy}$  pairing on the  $6 \times 6$  lattice as a function of  $\rho$  and inverse temperature  $\beta$ , calculated using DQMC.  $\bar{P}(U)$  for  $\rho \approx 0.5$  is enhanced by  $U$  at low temperatures, while it is suppressed at other  $\rho$ . (e)  $\bar{P}(U)$  for  $d_{x^2-y^2}$  pairing on the  $4 \times 4$  lattice, and (f)  $\bar{P}(U)$  for  $d_{x^2-y^2}$  pairing for the  $10 \times 6$  lattice [565]. The inset enlarges the density range near  $\rho \sim 0.5$ .

holes on a single *molecule* will be strong. The dominant configurations in the wavefunction will still have one hole per dimer, but while the charge densities are homogeneous in the configurations that give AFM, in the superconducting state, which is spin singlet, the intradimer charge densities in dominant wavefunction configurations are necessarily inhomogeneous, with singlet bonds between charge-rich sites on neighboring molecules (see Fig. 48). Fig. 56 shows possible  $d$ -wave (i.e. with four nodes) symmetries constructed using this constraint. Each ellipse in Fig. 56 corresponds to one term in the construction of  $\Delta_i^\dagger$  (Eq. 11) that creates a superconducting pair centered at dimer  $i$  [581]. The  $d_1$  symmetry consists of a superposition of four NN singlets, while the other symmetries ( $d_2$ ,  $d_3$ , and  $d_4$ ) are a superposition of 6 singlets. The nodes of these order parameters occur in different locations. For  $d_1$  they are aligned with the crystal axes, but for the other order parameters one or both of the nodal lines are at an angle to the crystal axes. The  $d_1$  symmetry is equivalent to the “ $d_{x^2-y^2}$ ” symmetry in the effective  $\frac{1}{2}$ -filled band model;  $d_2 \dots d_4$  correspond to mixed symmetries of  $s + d_{x^2-y^2}$  or  $s + d_{xy}$  form. We also investigated  $s$ -wave pair symmetries, but found no enhancement of  $s$ -wave pairing.

We performed calculations for the monomer  $\kappa$ -(ET) $_2$ X lattice as shown in Fig. 20(a) for two lattice sizes, 32 and 64 monomer sites. Calculations were done in the electron representation. As with the triangular lattice calculations (Fig. 54) we performed the  $\kappa$ -lattice calculations for a wide range of  $\rho$ , even as only  $\rho = 1.5$  corresponds to the carrier density in the CTS. Both lattices used periodic boundary conditions, chosen so that the corresponding effective dimer model would support Néel AFM order without frustration [581]. The 32 and 64 site lattices were arranged as  $4 \times 4$  and  $8 \times 4$  dimer lattices, respectively. The hopping parameters we used were taken from recent DFT calculations of Reference [221]. We investigated two different sets of parameters, for the crystal structures of  $\kappa$ -(ET) $_2$ X with  $X = \text{Cu}[\text{N}(\text{CN})_2]\text{Cl}$  and  $X = \text{Cu}_2(\text{CN})_3$ , in order to assess the importance of AFM order to SC in  $\kappa$ -(ET) $_2$ X. We calculated ground-state correlation functions with two different methods, QP-PIRG and CPMC. The CPMC was restricted to only closed-shell configurations where it is more accurate [576]. As in the results of Section 6.2.4 we calculated the

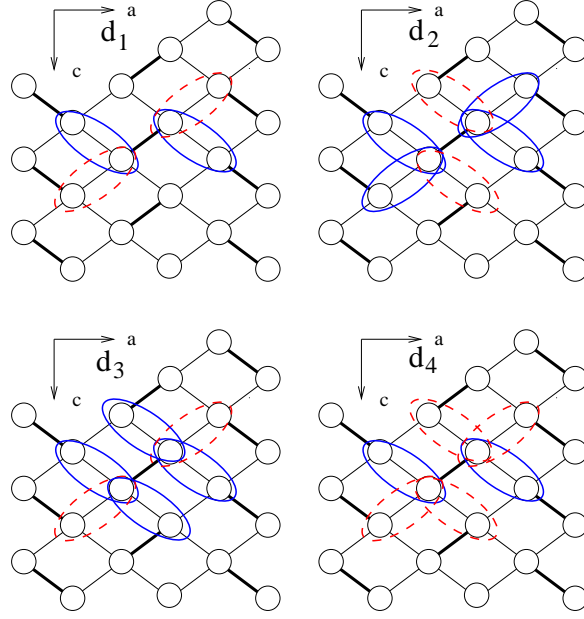


Figure 56. (color online) Pairing symmetries considered in Fig. 57. Here the thick lines correspond to BEDT-TTF dimers. Each ellipse surrounding two sites indicates a singlet in the superposition of the pair creation operator  $\Delta_i^\dagger$  centered at dimer  $i$ . Blue, solid (red, dashed) singlets have opposite signs [581].

average of long-range pair-pair correlations,  $\bar{P}$ . Because  $\Delta_i^\dagger$  creates a pair centered at dimer  $i$ , we define the pair-pair correlation function  $P(r)$  with the distance  $r$  measured in units of dimer-dimer spacing. The minimum distance cutoff in Eq. 15 is again two in units of the dimer-dimer distance.

Fig. 57 summarizes the results of these calculations. Instead of  $\bar{P}$  we plot  $\Theta_p = [\bar{P}(U)/\bar{P}(U=0)] - 1$ , which is positive only if e-e interactions enhance the pairing. The strongest enhancement for both lattices ( $\kappa$ -Cl and  $\kappa$ -CN) is found for  $\rho \approx 1.5$ . The results in Fig. 57 show that as in the anisotropic triangular lattice, pairing is enhanced by e-e interactions uniquely at or near quarter filling by holes, here at  $\rho = 1.5$  [581]. The enhancement is strongest for the  $d_2$  symmetry, which notably is the *only* pair symmetry that shows any significant enhancement for  $\kappa$ -CN. We note that a similar  $s + d_{x^2-y^2}$  order parameter was found in RPA spin-fluctuation calculations in a  $\frac{3}{4}$ -filled model [218, 299, 582] and in a subsequent VMC calculation [583]. The nodes of the order parameter in the  $d_2$  symmetry (Fig. 56) are located at an angle to the crystal axes [581].

Dimer-dimer AFM correlations can be measured by the dimer spin structure factor,

$$S(\mathbf{q}) = \frac{1}{N_d} \sum_{j,l} e^{i\mathbf{q}\cdot(\mathbf{r}_j - \mathbf{r}_l)} \langle S_j^z S_l^z \rangle,$$

where the sums run over all dimers in the system and  $N_d$  is the total number of dimers.  $S_j^z = n_{j_1,\uparrow} + n_{j_2,\uparrow} - n_{j_1,\downarrow} - n_{j_2,\downarrow}$  is the operator for the  $z$  component of the total spin on dimer  $j$  composed of molecules  $j_1$  and  $j_2$  and  $\mathbf{q}$  the wavevector defined in terms of dimer coordinates (the  $\hat{x}$  and  $\hat{y}$  axes of Fig. 20(a)). Results for  $S(\mathbf{q})$  are shown in Fig. 58. For  $\kappa$ -Cl (Fig. 58(a)), a clear peak at  $\mathbf{q}=(\pi, \pi)$  is seen indicating the tendency to Néel AFM order. For  $\kappa$ -CN (Fig. 58(b)) this peak is absent as expected due to the strong frustration in the effective dimer lattice. The lack of peaks in  $S(\mathbf{q})$  for  $\kappa$ -CN is consistent with the QSL behavior found in this salt. However, we find strong pairing enhancement in the  $d_2$  symmetry for both  $\kappa$ -Cl and  $\kappa$ -CN, which would not occur in a  $\rho = 1$  model of SC mediated by dimer-dimer AFM fluctuations.

Finally, we present preliminary results for calculations of SC pair-pair correlations on the lattice of  $\kappa$ -(ET)<sub>2</sub>CF<sub>3</sub>SO<sub>3</sub> ( $\kappa$ -SO<sub>3</sub>) [584].  $\kappa$ -SO<sub>3</sub> is unique among  $\kappa$ -(ET)<sub>2</sub>X superconductors for several reasons (see Section 5.1.1). First, this

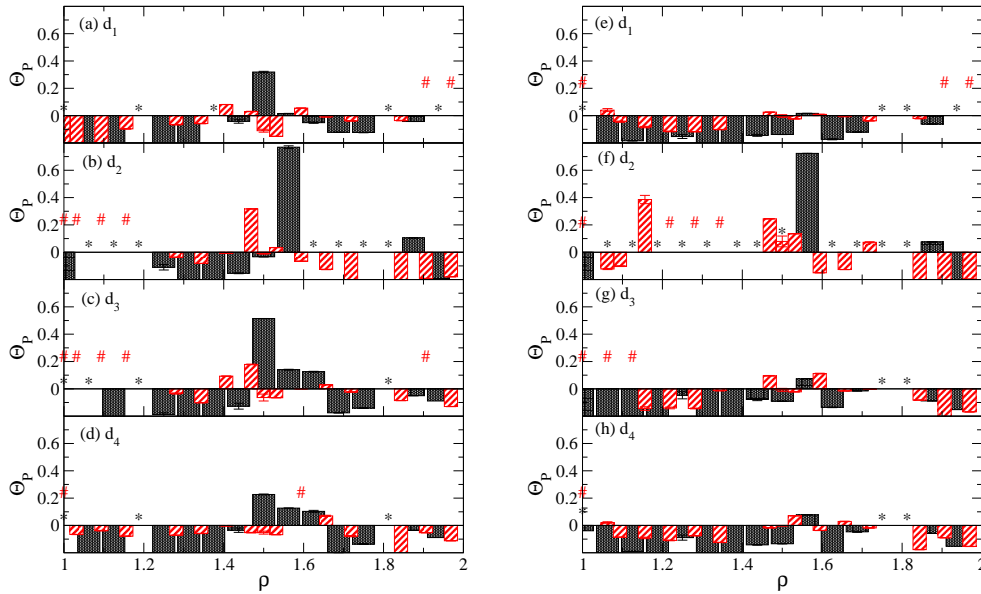


Figure 57. (color online) Enhancement factor  $\Theta_p$  (see text) versus electron density  $\rho$  for the long-range component of pair-pair correlations for a  $\frac{3}{4}$ -filled monomer model of  $\kappa$ -(ET) $_2$ X for four different pairing symmetries (see Fig. 56) [581]. Shaded (striped) bars are for 32 (64) site lattices using QP-PIRG for 32 sites and CPMC for 64 sites;  $U = 0.5$  eV for all results. Symbols “\*” and “#” indicate densities not shown, for 32 and 64 sites, respectively, due to strong finite-size effects at these  $\rho$  that result in  $\bar{P}(U = 0) \approx 0$ . Panels (a)-(d) are for  $X = \text{Cu}[\text{N}(\text{CN})_2]\text{Cl}$  and (e)-(h) are for  $X = \text{Cu}_2(\text{CN})_3$  [581]. We are ignoring the positive  $\Theta_p$  in panel (f) at  $\rho = 1.156$ . At this density, a discontinuous transition occurs for small  $U$ , suggesting that the apparent enhancement is a finite-size effect connected to the band structure [581].

material undergoes a structural transition at  $\sim 230$  K, below which it has a bilayer structure. Second, the superconducting critical temperature  $T_c$  under pressure ( $T_c = 4.8$  K) is *higher* than the ambient pressure Néel temperature  $T_N$  ( $T_N = 2.5$  K). This makes the applicability of any effective  $\frac{1}{2}$ -filled band theory, or spin-fluctuation mediated SC questionable. The lattice structure of  $\kappa$ -SO $_3$  is strongly anisotropic, with  $t'/t$  within the effective dimer lattice (see inset of Fig. 44) greater than one; it is the largest  $t'/t$  of all known  $\kappa$ -(ET) $_2$ X [235]. In the  $\rho = 1$  Hubbard model on the anisotropic triangular lattice,  $t'/t > 1$  gives AFM ordering with wavevector  $\mathbf{Q} = (\pi, 0)$  rather than  $\mathbf{Q} = (\pi, \pi)$  [37, 520]. Within  $\rho = 1$  models of spin-fluctuation induced SC on the anisotropic triangular lattice, large  $t'$  strongly reduces the  $T_c$  of  $d_{x^2-y^2}$  SC [522]. Other theoretical works suggest that the symmetry of the SC order parameter changes for  $t'/t > 1$ , from  $d_{x^2-y^2}$  to  $d_{xy} - s$  [546] or a  $d + id$  state [545]. It is however hard to reconcile the  $T_c > T_N$  within any theory of SC mediated by AFM fluctuations.

Because of the unusual properties of  $\kappa$ -SO $_3$  calculations within the full monomer lattice are desirable. We performed QP-PIRG and CPMC calculations on 32 and 64 site systems with the same methodology as detailed above for  $\kappa$ -Cl and  $\kappa$ -CN. We took hopping parameters from Reference [235]. The two distinct layers, labeled A and B here as in Reference [235], have slightly different hopping integrals.  $t'/t$  within the effective dimer model is 1.50 and 1.77 for layers A and B respectively [235]. Fig. 59 shows the results of preliminary calculations of ground-state superconducting pair-pair correlations both layers. As with the calculations for  $\kappa$ -Cl and  $\kappa$ -CN, the most striking feature of these results is that enhancement of SC by  $U$  is restricted to  $\rho = 1.5$ . For  $\kappa$ -SO $_3$  the greatest enhancement is again found for the  $d_2$  pair symmetry. Comparing the layers A and B, the enhancement is significantly larger for layer B: for monomer  $U = 0.4$  eV, the  $d_2$  enhancement factor  $\Theta_p$  is greater than 3 for layer B, while it is only  $\sim 0.4$  for layer A. A direct comparison of the amount of enhancement between  $\kappa$ -Cl,  $\kappa$ -CN, and  $\kappa$ -SO $_3$  is difficult with the lattice sizes we have access to, as the  $U = 0$  Fermi level degeneracies are different which leads to slightly different finite-size effects in each case. For  $\kappa$ -SO $_3$  both A and B layers *do* have similar Fermi level degeneracies however, so we believe that the finding of stronger pairing enhancement in layer B is significant.

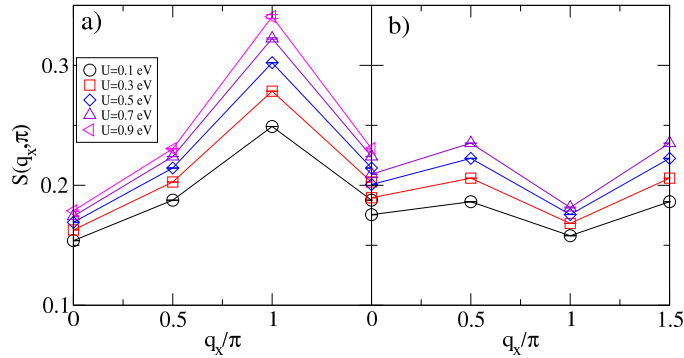


Figure 58. (color online) Dimer spin structure factor  $S(\mathbf{q})$  calculated by QP-PIRG for a 32 site monomer lattice of (a)  $\kappa$ -Cl and (b)  $\kappa$ -CN. Wavevectors are defined in terms of the effective dimer lattice (see text).

### 6.3. Summary

Direct many-body numerical calculations do not find superconductivity (SC) in  $\rho = 1$  models. The effective  $\rho = 1$  model for dimerized CTS also fails to correctly describe some of their insulating phases: while  $\rho = 1$  effective model can explain the presence of antiferromagnetic and metallic states in the CTS, a “valence-bond solid” (VBS) phase is not found in the effective  $\rho = 1$  model. The correct theoretical description of the VBS phase found in  $\text{EtMe}_3\text{P}[\text{Pd}(\text{dmit})_2]_2$  requires  $\rho = \frac{1}{2}$  [487]. The charge-ordered and spin-gapped state found here is the Paired Electron crystal (PEC). Our many-body calculations with monomer molecules as units reproduce the strong tendency to antiferromagnetism in  $\kappa$ -(ET)<sub>2</sub>Cu[N(CN)<sub>2</sub>]Cl and the absence of the same in  $\kappa$ -(ET)<sub>2</sub>Cu<sub>2</sub>(CN)<sub>3</sub>. SC in CTS is a consequence of the spin-singlets in the PEC becoming mobile to give a paired-electron liquid, driven by further increase in frustration. This feature is a unique characteristic of the correlated  $\frac{1}{4}$ -filled band (see also Appendix B), although it may be perhaps observed at other fillings depending on lattice geometry.

#### 6.3.1. Application of theory to CO-to-SC transitions.

As discussed extensively in Section 6.2.3 the pattern of the CO in CTS that exhibit CO-to-SC transition ( $\beta$ ,  $\beta'$ ,  $\beta''$ ,  $\theta$  and  $\alpha$  BEDT compounds, as well as in  $\text{EtMe}_3\text{P}[\text{Pd}(\text{dmit})_2]_2$ ) in every case corresponds to the PEC. This cannot be a coincidence. Note also that numerical calculations find that the PEC is favored over the WC of single electrons in the frustrated lattice (Fig. 51(c)). The VB theory of SC, and the calculations reported in Sections 6.2.2 and 6.2.4 apply most directly to these systems.

#### 6.3.2. Where is the PEC in the $\kappa$ -(ET)<sub>2</sub>X?

Considering  $\kappa$ -(ET)<sub>2</sub>X, the results shown in Figs. 57 and 59 show that the resulting picture of SC is quite different from that in the effective dimer model. Within the actual  $\rho = 1.5$  system in order to understand SC one must go beyond the effective dimer model, explicitly consider charge imbalance between the molecules within dimers, and the formation of interdimer spin-singlet pairs between the charge-rich sites of nearest-neighbor dimers. We emphasize that ours is a strong-correlation model very different from theories based on mean-field and random phase approximation. Such a model however raises the question: where is the PEC in these materials? The answer lies in the recognition that the frustration in the superconducting  $\kappa$ -(ET)<sub>2</sub>X, even when considering monomers and not dimers as the units, is significantly larger than in the other ET compounds, such that there are many equivalent and degenerate PEC configurations here [124]. Instead of crystallization to a single such configuration, there is thus transition to what we believe is a superposition of PEC-like configurations, which is however a spin-singlet state. It can also be thought of as a transition from an effective  $\frac{1}{2}$ -filled band to an effective  $\frac{3}{4}$ -filled band, as visualized in the schematic phase diagram of Fig. 28. This is perhaps the only scenario that can give consistent explanations of (i) the pseudogap in some compounds, whose spin-singlet nature should be obvious from Figs. 23–24, (ii) strong lattice effects including anomalies in the lattice expansivity in the same temperature region [279, 304]; and (iii) resistivity anomalies. Note also that the natures of the various broken symmetries below 6 K in  $\kappa$ -CN remain unresolved. It is not inconceivable

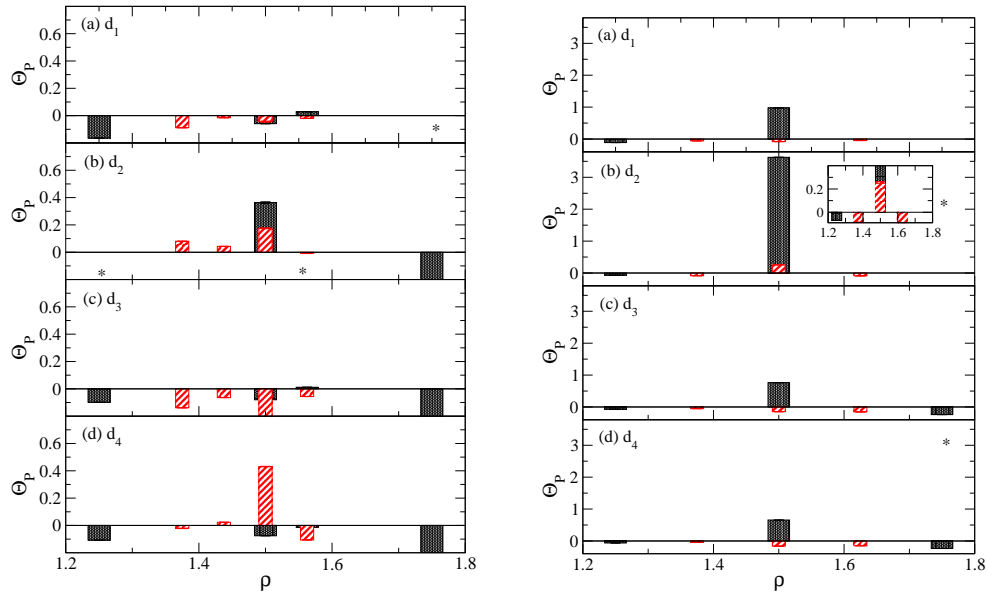


Figure 59. (color online) Preliminary results for the enhancement factor  $\Theta_P$  versus electron density  $\rho$  for the bilayer  $\kappa$ -(ET) $_2$ CF $_3$ SO $_3$  lattice. Panels (a)-(d) are for layer A and panels (e)-(h) for layer B (see text). Shaded (striped) bars are for 32 (64) site lattices using QP-PIRG for 32 sites and CPMC for 64 sites;  $U = 0.4$  eV for all results. 64 site results are restricted to the range  $1.35 < \rho < 1.65$ . As in Fig. 57, the symbols “\*” indicate 32 site points removed due to finite-size effects.

that in this highly frustrated system the same transition occurs at a much lower temperature. Finally, the occurrence of CO in  $X = \text{Hg}(\text{SCN})_2\text{Cl}$  and spin gap in  $X = \text{B}(\text{CN})_4$  give indirect evidence for the proximity of the PEC to SC.

### 6.3.3. Application to the quasi-1D superconductors.

Although we have not directly calculated superconducting pair-pair correlations for the quasi-1D (TMTSF) $_2$ X, we believe that our demonstration of the BCDW in (TMTTF) $_2$ X and the BCSDW in (TMTSF) $_2$ X (Section 4), taken together with our calculations for the  $t'/t > 1$  ET compound  $\kappa$ -SO $_3$  (Fig. 59) indicate very strongly that the mechanism of SC in the quasi-1D and quasi-2D CTS is the same. The only difference is that the superconducting wavefunction in the quasi-1D compounds must consist of predominantly intrastack spin-singlets with significantly smaller contribution from interdimer singlets. This will obviously change the gap symmetry.

### 6.3.4. Similarities with high- $T_c$ cuprates

The obvious similarities between SC in the cuprates and in the organic CTS are the layered natures of both families and the proximity of SC to AFM and QSL states in the  $\kappa$ -(ET) $_2$ X. The occurrence of a possible pseudogap phase in the  $\kappa$ -Br and  $\kappa$ -(NCS) $_2$  that has been ascribed to fluctuating SC [275, 280] is also reminiscent of the preformed pair-based explanations of the pseudogap behavior in the cuprates [282, 283, 500, 501]. These similarities have led to the effective  $\frac{1}{2}$ -filled band theories of SC in the CTS that we discussed in Section 6.1. Interestingly, the experimental literature on the cuprates itself has meanwhile seen some very dramatic turns, with the discovery of an ubiquitous CO phase *in between the AFM and superconducting phase* in the hole-doped cuprates [585–598]. Discovery of the CO phase in the electron-doped cuprates [595, 599] further indicates that the idea of the superconducting state evolving directly from the AFM state may be simplistic. Very interestingly, several groups have found that the CO in cuprates is *commensurate*, and has a periodicity of four Cu-O-Cu lattice spacings *independent of doping* [43, 44, 597, 598], which, as we have indicated throughout this review, is the CO periodicity in the quasi-1D and quasi-2D CTS at the lowest temperatures. It has been suggested that the CO and SC in the cuprates are isoenergetic, and perhaps there exists even a CO-SC duality in the cuprates [588]. Given the preponderance of CTS that show CO  $\rightarrow$  SC as well

as AFM  $\rightarrow$  SC transitions it is not inconceivable that the same mechanism of SC, or at least some variant of the same mechanism is also shared by the CTS. One of us has recently proposed a  $\text{Cu}^{2+} \rightarrow \text{Cu}^{1+}$  valence transition in the layered cuprates at the pseudogap phase transition, following which they the Cu-band becomes electronically inactive, and the CO and SC both emerge from the  $\frac{1}{4}$ -filled O-band [600]. This is discussed further in [Appendix B.7](#).

## 7. Conclusions

In this review we have focused on the large family of superconducting organic CTS. These unconventional superconductors feature a large diversity of crystal structures including quasi-1D as well as quasi-2D lattices, and both hole and electron charge carriers. We have argued that the most important unifying element of the organic CTS that exhibit SC is their unique carrier density,  $\rho = \frac{1}{2}$  per molecule (which includes both electron density of 1.5 per molecule in the hole carriers and 0.5 per molecule in the electron carriers). Deviations from this carrier density are both rare and tiny in real materials. From the perspective of the search for a theory of SC in strongly correlated-electron systems, CTS are attractive because of their relative simplicity: because no doping is required to achieve SC, a superconducting phase should be expected to emerge simply from changing the parameters of the same model Hamiltonian that describes the proximate insulating phases. The complex lattice structures and in particular presence of lattice frustration however make these challenging systems to study. The review therefore focused first on understanding the insulating phases found in those CTS that exhibit SC.

Examination of the normal state of the entire family of CTS, including the “old” TCNQ-based materials, as well as the  $\rho = \frac{1}{2}$  2D cationic and anionic CTS, indicates that there does exist a single theoretical model that explains the global behavior of the entire family. This is the EHM with significant Hubbard  $U$  and moderate Hubbard  $V$ . In addition to strong electronic correlations, e-p coupling is essential to understand the non-superconducting broken symmetry states. Coupling of the charge carriers with both intramolecular and intermolecular vibrations are relevant. At  $\rho = \frac{1}{2}$  these two e-p couplings act co-operatively, each enhancing the effect of the other. Equally importantly, although the CO broken symmetry is frequently taken to be a “classical” Coulomb effect driven by the Hubbard  $V$ , specifically at  $\rho = \frac{1}{2}$  there occurs also a CO *different from the classical WC* and that is driven by a *quantum effect*, the tendency of electrons to form spin-singlet pairs. We have presented numerical evidence for this Paired Electron Crystal (PEC), in 1D as well as in frustrated 2D lattices. The PEC competes with both AFM and WC. In 2D CTS, the manifestation of the PEC is the occurrence of charge periodicity  $\cdots 1100 \cdots$  in more than one direction, which in many cases leads to the formation of (dimerized) insulating stripes with spin gaps. We have pointed out (Section 6.2.3) that the pattern of the CO in all CTS that exhibit CO-to-SC transition corresponds to the PEC. It is unlikely that this is a coincidence.

The identification of the CO in superconducting CTS as the PEC implies that there exists a single unified theory of SC for the entire CTS family, in which SC emerges upon destabilization (“melting”) of the PEC, the spin-singlet pairs of which behave as hard core bosons. Existing theories of SC in the CTS have overwhelmingly (actually almost entirely) focused on the  $\kappa$ -(ET) $_2$ X, in which the superconducting state has been proclaimed to emerge from the AFM state. This in spite of the fact that few of the  $\kappa$ -(ET) $_2$ X are actually antiferromagnetic, at least two ( $\kappa$ -(ET) $_2$ Hg(SCN) $_2$ Cl and  $\kappa$ -(ET) $_2$ B(CN) $_4$ ) are likely PECs, and the critical temperature  $T_c$  in one ( $\kappa$ -(ET) $_2$ CF $_3$ SO $_3$ ) is larger than the Néel temperature  $T_N$ . Precise numerical calculations show that SC is absent in theoretical models of  $\kappa$ -(ET) $_2$ X that treat them within effective  $\rho = 1$  models. We have presented limited, but numerically precise calculations that show that within the standard Hubbard Hamiltonian, in both the triangular lattice and the  $\kappa$ -lattice, superconducting pair-pair correlations are enhanced by the Hubbard  $U$  only at  $\rho \simeq \frac{1}{2}$  and are suppressed at all other  $\rho$ , which supports our basic premise.

We reemphasize that our fundamental premise, viz., that correlated-electron SC emerges from a density wave of Cooper pairs has existed in the cuprate literature for some time now [502–506], and has also been suggested from very recent experimental observations [43, 44, 507]. The list of investigators who have expressed the opinion that SC emerges from the melting of a VBS (which in the context of cuprates is different from a PEC) is equally long or even longer. The reason for this is that this hypothesis resolves a key controversy concerning the pseudogap phase in the cuprates, viz., whether the pseudogap is due to pre-existing pairs or competing broken symmetry; the density wave of Cooper pairs satisfies both requirements simultaneously! Our work demonstrates explicitly that the PEC emerges naturally in 1D or frustrated 2D from the EHM at  $\rho = \frac{1}{2}$ . Beyond the conceptual overlap between the RVB theory and our VB theory of SC, there are also similarities between our picture and the original bipolaron theories

of metal-insulator transitions and SC [601–603]. The latter had hypothesized the formation of nearest neighbor spin-singlets, driven by e-p interactions that overscreened the nearest neighbor e-e repulsion. Our proposed mechanism of SC thus has overlaps with two very disparate theories, even as the actual mechanism behind the formation of the PEC is quite different from what had been proposed before. The driving force behind PEC formation in CTS and other  $\rho = \frac{1}{2}$  systems is a quantum effect - the tendency to form spin-singlets - that is strongly enhanced at this carrier concentration due to the commensurate nature of the PEC. Similarly, the kinetic energy gained from the motion of the effective hard core bosons is also largest when their effective density is  $\frac{1}{2}$ . It is interesting to note in this context that the original experimental materials that were considered to exhibit prototype bipolaron behavior were uniformly  $\rho = \frac{1}{2}$  (see Appendix B), even though this feature was not emphasized by the authors.

Our 2D numerical calculations of pairing correlations show an enhancement by e-e interactions selectively at  $\rho \approx \frac{1}{2}$  for multiple different lattice geometries and lattice sizes. To the best of our knowledge, there exists no other unbiased calculation that has shown correlation-induced enhancement of superconducting pairing correlations. Appendix B further indicates that the calculated enhancement is not a coincidence. Unfortunately, however, currently we are unable to present evidence for LRO in the calculated superconducting correlation functions, and it is even conceivable that true LRO is absent in our calculations. At the same time, we cannot rule LRO out completely within the present results, because of the approximation introduced by the free-electron trial wave function we used with the CPMC method in the  $10 \times 10$  lattice results of Fig. 54; in general we found that CPMC with the free-electron trial wavefunction slightly underestimated  $\bar{P}$  [565]. Recent improvements in the CPMC method may help to improve the accuracy of pairing calculations [604]. An alternate possibility is that the theory of the ground state as it exists now is incomplete, which itself can have two implications. First, even as the unique enhancement of SC pair correlations at  $\rho \approx \frac{1}{2}$  is meaningful, true SC may require additional interactions (e.g., e-p coupling) ignored in the purely electronic Hamiltonian. Because e-p coupling is required to realize the bond distorted PEC state, some role of e-p coupling in a PEC-to-SC transition might be expected. Second, even as the current calculations indicate the likelihood of pair formation, the question LRO has to be settled by calculations of a correlation function that is slightly different, because of the unconventional nature of the superconducting state. Note that the pair motion in the PEL has to be *correlated* (to minimize the repulsion between pairs). Thus the long range component of the order parameter for the correlated SC may very well be oscillating [605]. Elsewhere we have attempted to simulate the PEC-to-SC transition within an effective  $U < 0, V > 0$  model where the singlet bonds of  $\rho \approx \frac{1}{2}$  are replaced with double occupancies and the pairs of vacancies with single vacant sites [606]. Transition from a WC of double occupancies to a *s*-wave superconductor occurs as the frustrating hopping integral is slowly increased. Analysis of the exact wavefunctions shows however that the superconducting state at  $V > 0$  is substantially different from the well understood case of  $V = 0$ ; only a subset of the many-electron configurations that describe the superconducting state at  $V = 0$  dominate the  $V > 0$  wavefunction. This is because for  $V > 0$  pair motion has to occur within a background PEC. This last result gives partial support to the conjecture that the  $\rho = \frac{1}{2}$  PEL might be a true superconducting state, but more elaborate pairing correlations will be necessary to prove this. These and related topics are being investigated currently.

### Acknowledgments

Much of the early research on BCDW and BCSDW done in collaboration with D. K. Campbell. The authors also acknowledge collaborations with S. Dayal, W. Wasanthi De Silva, T. Dutta, N. Gomes, R. P. Hardikar, H. Li, S. Ramasesha, J.-P. Song, K.-C. Ung (deceased), and A. B. Ward. Over the many years that the research on organic charge-transfer solids was conducted the authors have benefited from numerous fruitful discussions with M. Abdel-Jawad, S. E. Brown, E. M. Conwell (deceased), N. Drichko, A. J. Epstein, M. Dressel, H. Fukuyama, A. Girlando, K. Kanoda, H. Mori, J. P. Pouget, R. Kato, S. Tomic, and T. Yamamoto. Parts of this work received financial support from U.S. National Science Foundation and Department of Energy.

**Appendix A. Molecule abbreviations**

abbreviation	molecule
BCPTTF	benzocyclopentyltetrathiafulvalene
BDA-TTF	2,5-Bis(1,3-dithian-2-ylidene)-1,3,4,6-tetrathiapentalene
BEDO-TTF	bis(ethylenedioxy)tetrathiafulvalene
BEDT-TSF	bis(ethylenedithio)tetraselenafulvalene
BEDT-TTF	bis(ethylenedithio)tetrathiafulvalene
DMEDO-TTF	dimethyl(ethylenedioxy)tetrathiafulvalene
DMET	dimethyl(ethylenedithio)diselenadithiafulvalene
M(dmit) <sub>2</sub>	bis(4,5-dimercapto-1,3-dithiole-2-thione)-M
DMTTF	3,4-dimethyl-tetrathiafulvalene
DODHT	(1,4-dioxan-2,3-diylidithio)dihydratetrathiafulvalene
EDO-TTF	ethylenedioxytetrathiafulvalene
EDT-TTF	ethylenedithiotetrathiafulvalene
HMTSF	hexamethylene-tetraselenafulvalene
HMTTF	hexamethylene-tetrathiafulvalene
MEM	N-methyl-N-ethyl-morpholinium
<i>meso</i> -DMBEDT-TTF	2-(5,6-dihydro-1,3-dithiolo[4,5-b][1,4]dithiin-2-ylidene) -5,6-dihydro-5,6-dimethyl-1,3-dithiolo[4,5-b][1,4]dithiin
NMP	N-methylphenazinium
TCNQ	tetracyanoquinodimethane
TMTSF	tetramethyltetraselenafulvalene
TMTTF	tetramethyltetrathiafulvalene
TSF	tetraselenafulvalene
TTF	tetrathiafulvalene

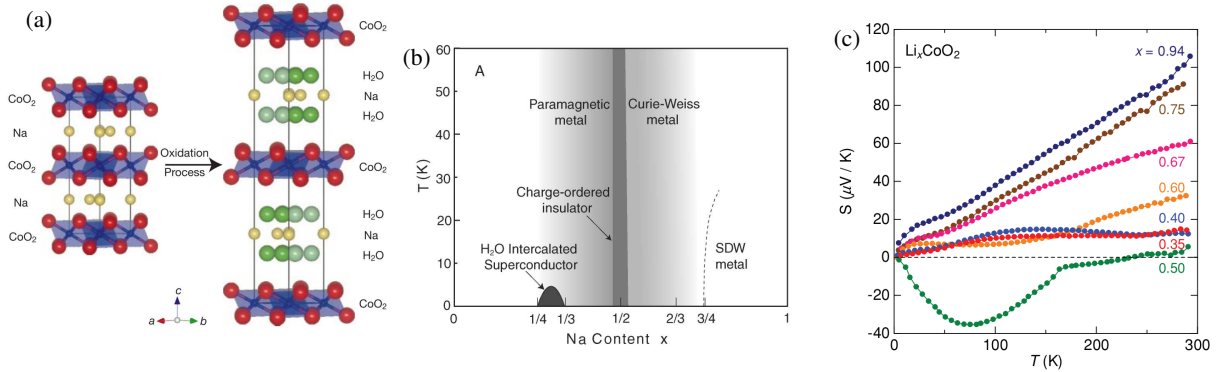


Figure B.60. (a) Structure of  $\text{Na}_x\text{CoO}_2$  and the hydrated superconductor Reprinted with permission from Ref. [607], © 2003 MacMillan Publishers Ltd. (b) phase diagram. Reprinted with permission from Ref. [608], © 2004 The American Physical Society. (c) Temperature dependence of the Seebeck coefficient of  $\text{Li}_x\text{CoO}_2$ . Reprinted with permission from Ref. [609], © 2011 The American Physical Society.

## Appendix B. Other $\rho = \frac{1}{2}$ superconductors

The principal thesis of the present work is that among strongly correlated materials the tendency to form spin-singlets, leading either to the PEC or the PEL, is strongest at  $\rho = \frac{1}{2}$  (or 1.5) in both 1D and 2D. It follows that there should be other  $\rho = \frac{1}{2}$  systems or families of materials where also correlated-electron SC is observed. We describe in this Appendix precisely such systems. Each material or family of materials has been of strong interest to the condensed matter physics community individually, but to date the common link between them, the same carrier density, has not been noted. In every case we discuss below, the following are true, (i) in structurally related materials with variable  $\rho$ , SC is limited to very narrow carrier concentration range about  $\rho = \frac{1}{2}$ , and (ii) in nearly all cases SC is proximate to a correlated CO state, and in those cases where the nature of the CO is understood there are reasons to believe that the CO is a PEC (either the periodicity is  $\cdots 0110 \cdots$ , or the CO coexists with a spin gap). The absence of any other carrier density where there exist so many systems with these common features gives credence to our VB theory of SC.

### Appendix B.1. Superconducting layered cobalt oxide hydrate

Layered cobaltates  $\text{M}_x\text{CoO}_2$  ( $\text{M} = \text{Li}, \text{Na}, \text{K}$ ) have attracted strong interest as strongly correlated-electron materials in which the carrier concentration can be varied over a wide range by varying the Na-concentration  $x$  [608, 610, 611].  $\text{Na}_x\text{CoO}_2$  is of particular interest as in the hydrated state it is an unconventional superconductor with  $T_c = 4.7$  K [607]. In the anhydrous materials the Co-ions in the  $\text{CoO}_2$  layers separated by the  $\text{Na}^+$ -ions occupy an isotropic triangular lattice as shown in Fig. B.60(a) and have charge ranging from  $3+$  (at  $x = 1$ ) to  $4+$  (at  $x = 0$ ). The corresponding electron configurations are  $t_{2g}^6$  with spin  $S = 0$ , and  $t_{2g}^5$  with  $S = \frac{1}{2}$ , respectively. Trigonal distortion splits the  $t_{2g}$  orbitals into degenerate low-lying  $e'_g$  levels and a higher  $a_{1g}$  level. Charge carriers are holes on the  $\text{Co}^{4+}$  sites [612], with hole density  $\rho = 1 - x$ . ARPES studies indicate that the  $e'_g$  levels are completely filled and therefore should be electronically inactive [612, 613], although this is somewhat controversial [614]. Band calculations find a larger Fermi surface due to  $a_{1g}$  levels, and a smaller Fermi surface due to the  $e'_g$  levels [615]. The physical behavior of anhydrous  $\text{Li}_x\text{CoO}_2$  and  $\text{Na}_x\text{CoO}_2$  are strongly  $x$ -dependent (see Fig. B.60(b)) [608]. The density  $\rho = \frac{1}{2}$  has unique properties here, as seen for example in its completely different thermoelectric properties as a function of temperature (see Fig. B.60(c)) [609]. The global feature of the  $x$ -dependence, with paramagnetic weakly correlated behavior at small  $x$  (large  $\rho$ ) and Curie-Weiss strongly correlated behavior at large  $x$  (small  $\rho$ ) was considered mysterious for a while. Since  $\rho = 1$  is a Mott-Hubbard semiconductor densities close to but not equal to  $\rho = 1$  would have been expected to be strongly correlated. Similarly, since  $\rho = 0$  is a band semiconductor, small  $\rho$  was expected to be weakly correlated. The observed behavior is exactly the opposite, see Fig. B.60(b)). The  $\rho$ -dependence was successfully explained by Li *et al.*, who showed that the observed behavior was exactly what would be expected within both one-band and two-band extended Hubbard models with realistic nearest neighbor Coulomb repulsion  $V$

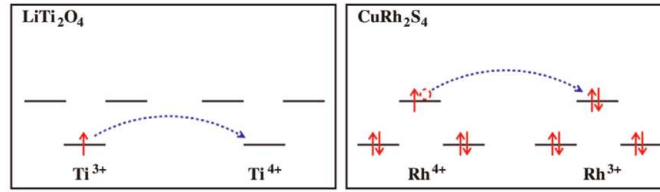


Figure B.61. Effective  $\frac{1}{4}$  ( $\frac{3}{4}$ )-filled bands of the spinel superconductors. The  $t_{2g}$  orbitals are split by Jahn-Teller distortion in (a) and by Jahn-Teller distortion or SOC in (b).

over and above the onsite Hubbard interaction  $U$  [611]. Identical  $\rho$ -dependent physical behavior are seen in the family of conducting organic charge-transfer solids [32]. Exactly as in the CTS (see discussions in Section 2.5) for fixed Hubbard  $U$ , Hubbard  $V$  enhances double occupancies at large  $\rho$  away from 1, and suppresses double occupancies at small  $\rho$  in the triangular Co-lattice (see Figs. 3 and 4 in reference [611]). Importantly, the fraction of holes occupying the  $e'_g$  levels is found to be  $\rho$ -dependent and is smaller for smaller  $\rho$  [611, 616]. The  $e'_g$ -occupancy is less than 10% at  $\rho \sim \frac{1}{2}$ .

SC in the hydrated  $\text{Na}_x\text{CoO}_2$  was found by Takada *et al.* [607]. The chemical composition was initially thought to be  $\text{Na}_x\text{CoO}_2 \cdot y\text{H}_2\text{O}$  ( $x \sim 0.35$ ,  $y \sim 1.3$ ), with the  $\text{H}_2\text{O}$  entering in between the  $\text{CoO}_2$  layers. Assuming that  $x$  alone determines the Co-ion valency as in the anhydrous material this gives  $\rho = 0.65$ . RVB theories of SC were proposed initially [617–620] even as this value of  $\rho$  is far from  $\rho = 1$  where the RVB state is supposed to occur [39]. It is now known that a significant proportion of the water in the hydrated material enters between the  $\text{CoO}_2$  layers as  $\text{H}_3\text{O}^+$  and the true superconducting composition [610] is  $\text{Na}_x(\text{H}_3\text{O})_z\text{CoO}_2 \cdot y\text{H}_2\text{O}$ , which would make Co-ion valency of 3.65+ an absolute lower limit (i.e.,  $\rho > 0.35$ ). Significant effort has gone into finding the true Co-ion valency in the bilayered hydrate that is superconducting. Several chemical studies [610, 621, 622] have found the valency to be very close to 3.5+. One ARPES study puts the Co valence at  $3.56 \pm 0.05$ , making  $\rho$  extremely close to 0.5. Spin fluctuation theories of SC based on RPA or FLEX calculations predict spin-triplet  $p$ - or  $f$ -wave SC [623, 624]. There is however no evidence experimentally for triplet pairing in these materials [610, 625]. These theories also require the presence of  $e'_g$  orbitals at the Fermi surface [624]. The observed limitation of SC to Co-ion valency  $\sim 3.5+$  and the evidence for strong e-e interaction [611] once again suggest that the mechanism of SC here too is related to our proposed mechanism, viz., correlated  $\text{Co}^{4+}$ – $\text{Co}^{4+}$  spin-singlet motion at  $\rho = \frac{1}{2}$ .

### Appendix B.2. Spinel superconductors

Spinel is an inorganic ternary compound  $\text{AB}_2\text{X}_4$ , with the B-cations as the active sites. The B sublattice in the spinels forms corner-sharing tetrahedra, giving rise to a geometrically frustrated pyrochlore lattice. Out of several hundred spinel compounds with transition metals as the B-cations only three undoped compounds are confirmed superconductors,  $\text{LiTi}_2\text{O}_4$  with  $T_c \simeq 12$  K [626],  $\text{CuRh}_2\text{S}_4$  ( $T_c = 4.8$  K [627] and up to 6.4 K under pressure [628]), and  $\text{CuRh}_2\text{Se}_4$  ( $T_c = 3.5$  K [627]). While early reports on powder samples indicated SC at  $\sim 4$  K in  $\text{CuV}_2\text{S}_4$ , later measurements on single crystals found no SC [629, 630]. The Cu-ion in the latter compounds are known to be monovalent [631]. Band calculations have shown that the transition metal's partially occupied  $t_{2g}$   $d$ -bands are well separated from the empty  $e_g$  bands by  $\sim 3$  eV, and also from the  $p$ -bands due to O and S by about the same amount [631–633]. The extreme selectivity of SC cannot be a coincidence, especially considering that (i) while  $\text{LiTi}_2\text{O}_4$  superconducts at 12 K, structurally related  $\text{LiV}_2\text{O}_4$  does not show SC down to 10 mK [634], (ii) SC in  $\text{Li}_{1+x}\text{Ti}_{2-x}\text{O}_4$  disappears for  $x$  as small as  $\sim 0.1$  [635], and (iii)  $\text{Ti}^{3.5+}$  in  $\text{LiTi}_2\text{O}_4$  has one  $d$ -electron per two Ti's, and  $\text{Rh}^{3.5+}$  in  $\text{CuRh}_2\text{S}_4$  and  $\text{CuRh}_2\text{Se}_4$  is in the low-spin state with one hole per two  $t_{2g}$  orbitals (see Fig. B.61). We give detailed discussions below why we believe that these materials should be considered correlated-electron  $\frac{1}{4}$  ( $\frac{3}{4}$ )-filled band superconductors just like the CTS.

As with the CTS, a hint to the mechanism of SC in the spinels is obtained by examining the metal-insulator transitions that occur in structurally related compounds. In  $\text{Ti}_4\text{O}_7$ , which also has Ti-valency of 3.5+, and which is structurally related to  $\text{LiTi}_2\text{O}_4$ , there occurs charge disproportionation into  $\text{Ti}^{3+}$  ( $d^1$ ) and  $\text{Ti}^{4+}$  ( $d^0$ ) and the formation

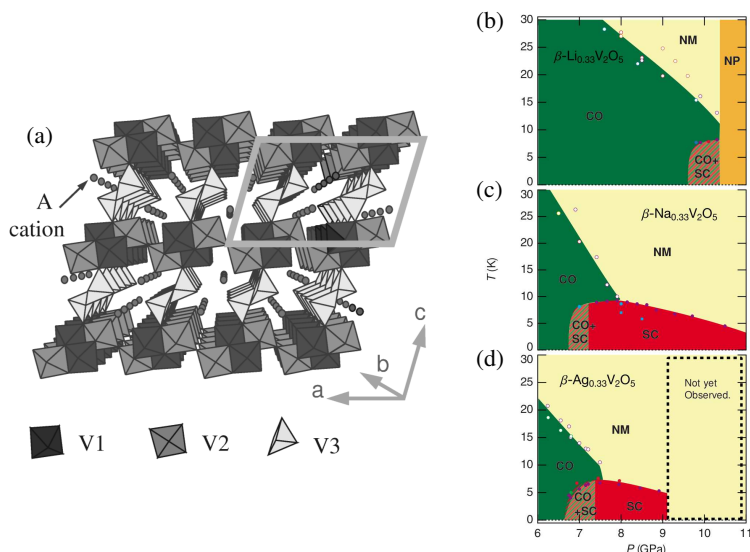


Figure B.62. (a) Crystal structure of  $\beta\text{-A}_{0.33}\text{V}_2\text{O}_5$ . Reprinted with permission from Ref. [654], © 2002 The American Physical Society. (b)-(d) Temperature-pressure phase diagrams for (b)  $\text{A}=\text{Li}$  (c)  $\text{A}=\text{Na}$  and (d)  $\text{A}=\text{Ag}$ . Here NM is a normal metal phase and NP is a high-pressure non-superconducting phase. Reprinted with permission from Ref. [655], © 2008 The American Physical Society.

of  $\text{Ti}^{3+}\text{-Ti}^{3+}$  *spin singlets* [636, 637]. The most likely explanation of this is orbitally-induced band Jahn-Teller distortion [638–641] that lifts the degeneracy of the  $t_{2g}$   $d$ -band, giving a  $\frac{1}{4}$ -filled nondegenerate  $d_{xy}$ -band (see Fig. B.61) [16, 574]. Importantly, the band Jahn-Teller distortion at this filling requires strong e-e interaction, which is the driver of singlet formation in  $\frac{1}{4}$ -filled band [642]. As shown in Fig. B.61 the occupancies of the  $t_{2g}$  orbitals on individual  $\text{Rh}^{3.5+}$  ions in  $\text{CuRh}_2\text{S}_4$  and  $\text{CuRh}_2\text{Se}_4$  fluctuate between  $t_{2g}^6$  with closed shell and  $t_{2g}^5$  with one hole. Metal-insulator transitions in isoelectronic  $\text{CuIr}_2\text{S}_4$  [638, 643] and  $\text{LiRh}_2\text{O}_4$  [644, 645] are accompanied by cubic-to-tetragonal structural transition *as well as PEC formation*, as evidenced by  $M^{4+} - M^{4+} - M^{3+} - M^{3+}$  ( $M = \text{Rh}, \text{Ir}$ ) charge and bond tetramerization and  $M^{4+} - M^{4+}$  spin-bonded dimers along specific directions. The charge ordering in  $\text{CuIr}_2\text{S}_4$  was originally also ascribed to orbitally-induced lifting of  $t_{2g}$  degeneracy that left filled degenerate  $d_{xz}$  and  $d_{yz}$  bands lowered in energy by band Jahn-Teller distortion, and a nondegenerate  $\rho = \frac{1}{2}$   $d_{xy}$  band, separated by an energy gap [638–641, 644]. More recent theoretical work has ascribed the degeneracy lifting in  $\text{Ir}^{4+}$  to spin-orbit coupling (SOC), with the splitting between  $J = \frac{3}{2}$  and  $J = \frac{1}{2}$  states [646–648]. For our purpose, *it is irrelevant whether the lifting of the degeneracy is due to band Jahn-Teller distortion or SOC*. More relevant is the effective  $\rho = \frac{1}{2}$  hole occupancy of the active orbital, and the implied proximity of SC to PEC.

We believe that the extreme selectivity of SC in the spinels, taken together with the PEC formation in isostructural isoelectronic compounds  $\text{CuIr}_2\text{S}_4$  and  $\text{LiRh}_2\text{O}_4$ , are strong indicators that the mechanism of SC in these materials is the same in these materials as in the CTS. Particularly in the context of  $\text{LiTi}_2\text{O}_4$ , there is ample evidence for strong e-e interactions among the  $3d$ -electrons [9, 649, 650], and that e-p interactions may not be the driver of SC (see Reference [651] for a review). A very recent experiment in  $\text{LiTi}_2\text{O}_4$  has found a transition from isotropic negative magnetoresistance to anisotropic positive magnetoresistance at 50 K [652], which is also the temperature where a Raman study has shown a strong anomaly in the  $T_{2g}$  e-p coupling [653]. The authors of both studies have suggested an orbital ordering transition at this temperature, which would give strong though indirect support to our proposed orbital ordering in Fig. B.61. We propose similar magnetoresistance and Raman measurements in  $\text{CuRh}_2\text{S}_4$  and  $\text{CuRh}_2\text{Se}_4$ . Within our theory SC is due to the correlated motion of n.n. singlets  $\text{Ti}^{3+}\text{-Ti}^{3+}$  and  $\text{Rh}^{4+}\text{-Rh}^{4+}$ .

### Appendix B.3. Superconducting vanadium bronzes

Yet another family of materials that are  $\frac{1}{4}$ -filled and exhibits pressure-induced CO-to-SC transition are the series of vanadium bronzes  $\beta\text{-A}_{0.33}\text{V}_2\text{O}_5$ ,  $\text{A} = \text{Li}, \text{Na}, \text{Ag}$  [654, 655]. Structurally, the materials consist of the  $\text{V}_2\text{O}_5$  framework

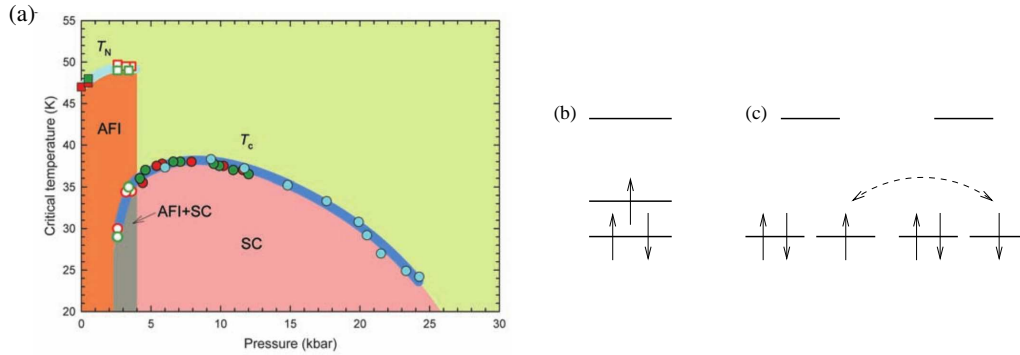


Figure B.63. (color online) (a) Phase diagram of A15  $\text{Cs}_3\text{C}_{60}$ . Reprinted with permission from Ref. [658], © 2009 AAAS. In the Mott insulator state (AFI region in (a)), two electrons occupy the lowest orbital, and one the second-lowest orbital on each  $\text{C}_{60}$  molecule. (b) The orbital occupation in the same Mott insulator state, but with finite  $U$ , resulting in a reduced gap between the lowest two orbitals. (c) The inclusion of off-diagonal terms between MOs equalizes populations between the lowest two MOs, resulting in a  $\frac{3}{4}$ -filled band (see text).

with three distinct V sites (referred to as V1, V2 and V3, respectively as shown in Fig. B.62(a)), with the V-ions forming quasi-1D chains along the b-axis of the crystal. The electronic configuration of the  $\text{V}^{5+}$ -ions in pure  $\text{V}_2\text{O}_5$  is  $3d^0$ . The metal ions occupy straight “tunnels” along the b-axis. Given that there are three different kinds of V-ions the compositions  $\beta\text{-A}_{0.33}\text{V}_2\text{O}_5$  are stoichiometric, even as other compounds with compositions that are slightly different are known.

The most interesting observations with this compounds are as follows. First, all vanadium bronzes show quasi-1D conduction at ambient pressure. It has, however, been proposed that there occurs a dimensional crossover to quasi-2D behavior under pressure [655]. Second, angle-resolved photoemission study of  $\beta\text{-Na}_{0.33}\text{V}_2\text{O}_5$  indicates that the perfectly stoichiometric compound consists of  $\frac{1}{4}$ -filled band 1D chains, with exactly equal populations of  $\text{V}^{5+}$  ( $3d^0$ ) and  $\text{V}^{4+}$  ( $3d^1$ ) [656]. Which of the three chains becomes  $\frac{1}{4}$ -filled on “doping” remains however unresolved. Third, both the CO phase and the SC phases are extremely sensitive to A-cation off stoichiometry, with smallest non-stoichiometry destroying SC, though not necessarily CO. Finally, even as the CO-to-SC transition is pressure-induced,  $T_{\text{SC}}$  decreases with pressure (see Figs. B.62(b)-(d)), in contrast to what is expected from a BCS-superconductor. All of these observations, in particular SC limited to commensurate  $\frac{1}{4}$ -filling and being destabilized by pressure, are reminiscent of the behavior of the CTS family and the other compounds listed above. It is relevant in this context to now point out that vanadium bronzes were among the first compounds in which nearest neighbor spin-paired bipolarons ( $\text{V}^{4+}\text{-V}^{4+}$ ) were hypothesized [601]. Similar nearest neighbor spin-pairings between  $\text{Ti}^3\text{-Ti}^{3+}$  had been proposed for  $\text{Ti}_4\text{O}_7$ , which is structurally related to  $\text{LiTi}_2\text{O}_4$  and also contains a  $\frac{1}{4}$ -filled Ti-band [636]. It was suggested that overscreening of e-e repulsion by e-p interactions drove the formation of the bipolarons [603, 637], but as has been shown in our work here,  $\frac{1}{4}$ -filling and moderate e-e interactions together can drive this transition to the PEC, which the earlier group of authors had referred to as the bipolaronic insulator. We also note that Hague *et al* [657] showed that *intersite* spin-singlets can have high mobility and small effective mass.

#### Appendix B.4. Superconducting fullerenes

One peculiarity of superconducting fullerenes is that SC is limited to trivalent  $\text{C}_{60}^{3-}$  [659]. Since there is nothing unique to this valence within purely e-p coupled models this should already be an indicator that e-e interactions may be relevant here. This has been further confirmed by the observation of AFM in  $\text{Cs}_3\text{C}_{60}$  with  $T_{\text{N}} \sim 46$  K [658], as well as of pressure-induced AFM-to-SC transition with  $T_{\text{C}} = 38$  K [658, 660, 661]. Careful experimental measurements have indicated that the AFM  $\text{Cs}_3\text{C}_{60}$  has a single unpaired electron per  $\text{C}_{60}^{3-}$  [661, 662]. This has a unique explanation, viz., the three-fold degeneracy of the antibonding  $t_{1u}$  MOs of  $\text{C}_{60}$  is lifted by Jahn-Teller instability in the trianion, with occupancies of 2, 1 and 0 electrons in the three nondegenerate MOs, in increasing order of energies (See Fig. B.63(a)) [662]. AFM is now due to spin-coupling between the unpaired electrons on neighboring ions. While it is true that given the low-spin nature of  $\text{Cs}_3\text{C}_{60}$  there is no alternative to the characterization of the insulating AFM state as a magnetic Mott-Jahn-Teller insulator [662], the nature of the so-called Jahn-Teller-metal that is reached under pressure

remains not understood. Existing theories of SC [15, 659, 663–666] explicitly or implicitly assume that the Jahn-Teller-metal has regained the degeneracy of the undoped state, and the SC is due to “on-ball pairing”, driven largely by the Jahn-Teller phonons, with the Mott-Hubbard  $U$  playing either a competing or co-operative role. Such a quasi-BCS mechanism would seem to be in disagreement with the observed decrease of  $T_c$  with pressure [660, 661]. Even more importantly, we believe that this picture fails to explain why  $T_c$  should be so sharply peaked at anionic charge of -3. The strong sensitivity of SC to commensurability is a characteristic feature of all the materials discussed in this review, and it should be clear by now that these cannot be merely shared coincidences.

We agree with the viewpoint that the orbital degeneracy of the so-called Jahn-Teller-metal is different from the Mott-Jahn-Teller insulator. We believe, however, that that the perfect nondegeneracy of the former is replaced with partial degeneracy in the latter, exactly as in the case of the spinels within a mechanism that is an analogue of the band Jahn-Teller instability. Recall first that the Hubbard  $U$  suppresses Jahn-Teller instability when the orbital occupancy is even, but not when the occupancy is odd [92]. Thus, unlike in Fig. B.63(a), where the gaps between the antibonding MOs of  $C_{60}$  are nearly identical (as they would be in the strictly  $U = 0$  case, where the energy gained upon distortion due to adding two electrons is exactly twice that gained when a single electron is added), for  $U \neq 0$  the gap between the lowest doubly occupied level and the singly occupied level is much smaller than that between the latter and the unoccupied level (see Fig. B.63(b)). Now as one includes intermolecular hopping of electrons, there will also be off-diagonal terms in the MO representation, hopping between MOs with different symmetry. Given the small intrinsic gap between the two lowest levels, this would equalize the populations of the two lowest MOs which are now degenerate, giving a population of 1.5 electrons per MO, with the unoccupied MO at a higher level. This equalization of populations of the two lower levels is further enhanced by e-e interactions [667]. Comparing Figs. B.63(c) and B.61, the similarity between superconducting spinels and a lattice of  $C_{60}^{3-}$  is readily observed. Note that within our proposed mechanism, pairing is “inter-ball”. The mechanism that we have proposed for the AFM-to-SC transition here is related to that proposed for  $\kappa$ -(ET) $_2$ X: in both cases the transition from the AFM insulator is driven by and accompanied with orbital (re)ordering that makes the “metallic” state effectively  $\frac{1}{4}$  ( $\frac{3}{4}$ )-filled.

#### Appendix B.5. $Li_{0.9}Mo_6O_{17}$

This is yet another low-dimensional superconductor where SC is proximate to an insulating state, with the active electrons belonging to the  $d$ -orbitals of a transition metal, and the bandfilling nearly  $\frac{1}{4}$ . The crystal structure is monoclinic [668, 669]. The conduction electrons are located mostly on two Mo-ions that occupy octahedral sites and form what has been described in the literature as double-zigzag chains or two-leg zigzag ladders along the b-axis, giving the system its strong one-dimensional behavior. The peculiarities of the system include a low temperature metal-insulator transition, as observed from resistivity studies at  $T_{MI} \sim 25$  K [670–673] that has remained poorly understood, and a superconducting transition below 2 K [671]. There is no signature of structural anomaly at  $T_{MI}$  from X-ray scattering and thermal expansion studies [674] or neutron scattering [669]. The high temperature behavior (above  $T_{MI}$ ) can be understood within a Luttinger liquid picture [675]. The absence of the structural anomaly at  $T_{MI}$  has led to suggestions that the transition is “purely electronic” or a dimensional crossover. The upper critical field for magnetic fields parallel to the conducting chains is five times larger than the Pauli paramagnetic para-magnetic limit [676], indicating that the SC is unconventional. Triplet pairing has been suggested [677], although this has not been confirmed experimentally yet. Note that large upper critical fields are also characteristic of CTS, where it is now known that SC is not due to triplet pairing [678, 679].

The strong 1D behavior at high temperatures can be understood from the crystal structure (see Fig. 2 in [669]). The unit cell contains six distinct Mo ions, of which two (labeled Mo3 and Mo6 in the literature) are on tetrahedral sites. Of the remaining four Mo-ions in octahedral sites Mo1 and Mo4 form highly 1D structures that have been described as double zigzag chains [669] or two-leg zigzag ladders [680]. Based on DFT calculations [681], Merino and McKenzie concluded that the chemical formula of  $LiMo_6O_{17}$  can be written as  $Li^{1+}(Mo^{4.5+})_2Mo_4^{6+}(O^{2-})_{17}$  where Mo but not Mo' constitute the coupled zigzag chains. Note that Mo-ion valence of 4.5+ implies electron configurations of  $4d^0$  and  $4d^1$ . Band structure calculations indicate that only the  $d_{xy}$  orbitals are the active bands, which are then exactly  $\frac{1}{4}$ -filled in  $LiMo_6O_{17}$  and slightly away from this in  $Li_{0.9}Mo_6O_{17}$ . We speculate that the transition at  $T_{MI}$  is *simultaneously* purely electronic as well as a dimensional crossover. As pointed out by Merino and McKenzie, the 3D electron-electron interactions and hoppings between the zigzag chains on different planes increase the frustration. Within our theory increased frustration leads to charge disproportionation in  $\rho = \frac{1}{2}$ , with spin-singlet formation between charge-rich sites that are NN on *different* chain pairs or ladders. The resultant electronic state that is no longer 1D can be

either a PEC or PEL. This viewpoint would be in agreement with the observation that the superconducting transition in  $\text{Li}_{0.9}\text{Mo}_6\text{O}_{17}$  is insulator-superconductor [675]. It is also tempting to assign the giant Nernst effect in  $\text{Li}_{0.9}\text{Mo}_6\text{O}_{17}$  [682] to preformed pairs [282]. Clearly further theoretical and experimental research are warranted here; what is however true is that  $\text{Li}_{0.9}\text{Mo}_6\text{O}_{17}$  exhibits the “generic” behavior of  $\rho = \frac{1}{2}$  superconductors.

#### Appendix B.6. Intercalated and doped $\text{IrTe}_2$

One other material of interest is  $\text{IrTe}_2$ , consisting of edge-sharing  $\text{IrTe}_6$  octahedra, with Ir layers sandwiched between Te layers [683]. The interlayer Te-Te distance is smaller than the intralayer distance. While  $\text{IrTe}_2$  itself does not exhibit SC, it undergoes a CDW-like transition at  $\sim 260$  K which remains poorly understood. There is broad agreement [684, 685] that at high temperatures the valence state of Ir is  $\text{Ir}^{3+}$ , which would make its electron configuration closed shell  $t_{2g}^6$ . Conversely, the ionic state of Te is  $\text{Te}^{1.5-}$ , which suggests equal populations of  $\text{Te}^{2-}$  and  $\text{Te}^{1-}$  and a hole concentration  $\rho = \frac{1}{2}$  on the Te sites. The transition at 260 K is accompanied by strong diamagnetism and structural anomaly [684, 685], and one way to understand the diamagnetism would be to assume spin-singlet formations between the open shell  $\text{Te}^{1-}$ , which would be in accordance with our theory of singlets in  $\rho = \frac{1}{2}$ , provided a DW with periodicity  $\text{Te}^{2-}-\text{Te}^{2-}-\text{Te}^{1-}-\text{Te}^{1-}$  was also found. There is, however, controversy as to whether the 260 K transition involves only the Te ions [685], or both Ir and Te; the latter would make the Ir ions mixed valence [683]. Pd intercalation into  $\text{IrTe}_2$ , giving  $\text{Pd}_x\text{IrTe}_2$ , or weak Ir-site doping, giving  $\text{Ir}_{1-y}\text{Pd}_y\text{Te}_2$ , give SC at  $\sim 3$  K for  $x$  and  $y$  as small as  $\sim 0.02$ , while beyond  $x = 0.1$  the SC vanishes [686]. Similar behavior is also seen with very weak Pt doping. Clearly whether or not the structural anomaly involves only Te, or both Ir and Te, is a very important question when it comes to ascertaining the mechanism of SC here. It is nevertheless interesting that the parent semiconductor is again  $\frac{1}{4}$ -filled at high temperature.

#### Appendix B.7. Superconducting hole- and electron-doped cuprates

Even after three decades of their discovery [1], high  $T_c$  superconductivity in the cuprates remains a formidable problem. There is little understanding of the pseudogap phase in the hole-doped materials, which is accompanied by a partial loss of density of states as seen in some experiments. The origin of the pseudogap in early studies had been assigned to preformed pairs and fluctuating SC, as would occur within RVB theories [282, 283, 500, 501]. More recent experiments have found a ubiquitous CO in all cuprates within the pseudogap phase [585–598], that coexists with broken rotational symmetry [687], which has been ascribed to inequivalent oxygens within the 2D unit  $\text{CuO}_2$  cell. The bulk of the theoretical work on the hole-doped cuprates has been within the weakly doped 2D Hubbard model. There is no satisfactory explanation of the various coexisting spatial broken symmetry phases within the pseudogap phase within these theories. To obviate the preformed pairs versus competing order conundrum some investigators have proposed that the CO is a density wave of Cooper pairs [43, 44, 502–504, 504–507]. This is reminiscent of our concept of the PEC.

The most difficult issues with the electron-doped cuprates involve, (i) robust AFM over a very broad doping range (up to dopant concentration  $\sim 0.14$  instead of the  $\sim 0.03$  in the hole-doped cuprates), and SC over a very narrow carrier concentration ( $\sim 0.15 - 0.17$ ) in the Ce-doped bulk  $\text{Nd}_2\text{CuO}_4$  and  $\text{Pr}_2\text{CuO}_4$  [33], and yet (ii) SC in the *undoped* specially prepared thin films [688], and (iii) holelike charge transport at optimal doping [689]. Understanding the similarities as well as differences between the hole- and electron-doped materials has not been possible within either the one-band or the so-called three-band weakly doped Mott-Hubbard models.

One of us has recently presented a valence transition model that attempts a unified explanation of all the difficult experiments in both hole- and electron-doped cuprates [600]. The theory is based on the concept of transition from positive to negative charge-transfer gap in strongly correlated charge-transfer insulators in which cation-anion hopping is much smaller than electron correlations. Such a transition has been documented over three decades in 1D mixed-stack donor-acceptor CTS, where it is known as the neutral-ionic transition [690]. The valence transition theory begins with the observation that the second ionization energy of the cuprate monoanion  $\text{Cu}^{1+}$  is unusually high because of its closed shell nature (higher than the monocations of Ni and Zn by  $\sim 2$  eV). Thus for small Cu-O  $d-p$  hopping it is only because of the large gain in Madelung energy in the undoped parent cuprates that the ionic charges  $\text{Cu}^{2+}$  and  $\text{O}^{2-}$  are obtained (the second electron affinity of oxygen,  $\text{O}^{1-} \rightarrow \text{O}^{2-}$  is actually positive because of the repulsion between the excess electrons). With doping, there is reduction in the Madelung energy and at a crystal structure-dependent ( $T$  vs

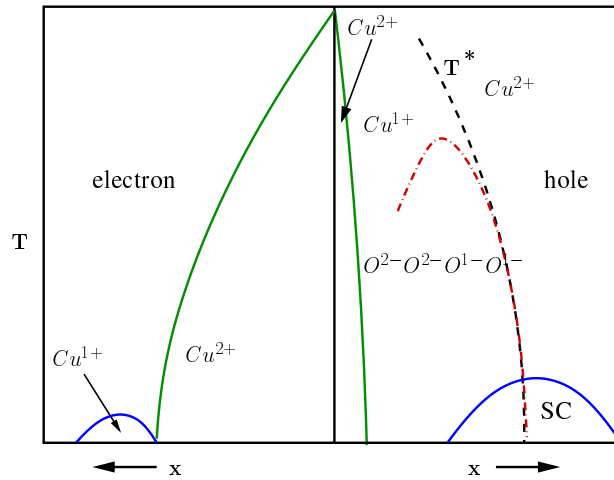


Figure B.64. Schematic phase diagram of the electron- and hole-doped superconducting cuprates within the valence transition model. The CO region has charge modulation  $O^{2-}-O^{2-}-O^{1-}-O^{1-}$  along any Cu-O bond direction. The precise quantum critical point at which  $T^*$  intersects the dopant axis in the hole-doped systems cannot be evaluated without detailed calculations, and is not relevant.

$T^*$ ) doping concentration there occurs a discrete jump in ionicity from  $Cu^{2+}$  to  $Cu^{1+}$  in both the hole- and electron-doped compounds. The hole in the erstwhile  $Cu^{2+}$  transfers to the oxygens in the  $CuO_2$  layer. In analogy with the neutral-ionic transition, the model envisages two distinct phases, even though the true Cu-charges are different from precisely 2+ and 1+. The essential point, however, is that in the undoped parent semiconductor the  $O^{2-}$  anions are closed shell and electronically inactive, and the Cu-band can be thought of as an effective  $\frac{1}{2}$ -filled band Mott-Hubbard semiconductor, a theoretical picture that we are all familiar with. The new conceptual development is that in the second phase the  $Cu^{1+}$  ions with  $3d^{10}$  electron configuration are similarly electronically inactive, and the effective model now corresponds to a  $\frac{1}{4}$ -filled O-band, with nearly half the O-ions as  $O^{1-}$ . The pseudogap transition in the hole-doped cuprates and the sudden transition from AFM semiconductor to superconductor in the electron-doped materials are both ascribed to this valence transition. Fig. B.64 shows a schematic of the phase diagram of both hole- and electron-doped cuprates within the model. The O-sublattice is a frustrated checkerboard lattice and therefore is susceptible to the transition to the PEC at  $\frac{1}{4}$ -filling. As discussed in the original reference [600], the experimentally observed period 4 CO [44, 593, 597, 598] is due to the nominally  $O^{2-}-O^{2-}-O^{1-}-O^{1-}$  charge distribution along both the Cu-O bonds, which also simultaneously destroys  $C_4$  symmetry [687]. Similarly, Hall coefficient measurements that indicate hole like transport in the optimally doped electron-doped cuprates [689] is expected since at this carrier concentration the charge carriers are the same holes on the  $O^{1-}$  as in the hole-doped materials. SC within the model is a consequence of the destabilization of the PEC on the  $\frac{1}{4}$ -filled O-sublattice, with  $O^{1-}-O^{1-}$  singlets being the equivalents of the Cooper pairs in configuration space. The theoretical work makes a large number of experimental predictions that can be found in the original paper [600].

## References

- [1] J. G. Bednorz, K. A. Müller, Possible high  $T_c$  superconductivity in the Ba-La-Cu-O system, *Z. Phys. B* 64 (1986) 189–193.
- [2] T. Timusk, B. Statt, The pseudogap in high-temperature superconductors: an experimental survey, *Rep. Prog. Phys.* 62 (1999) 61–122.
- [3] M. R. Norman, D. Pines, C. Kallin, The pseudogap: friend or foe of high  $T_c$ ?, *Adv. Phys.* 54 (2005) 714–733.
- [4] B. Keimer, S. A. Kivelson, M. R. Norman, S. Uchida, J. Zaanen, From quantum matter to high-temperature superconductivity in copper oxides, *Nature* 518 (2015) 179–186.
- [5] G. R. Stewart, Superconductivity in iron compounds, *Rev. Mod. Phys.* 83 (2011) 1589.
- [6] Q. Si, R. Yu, E. Abrahams, High-temperature superconductivity in iron pnictides and chalcogenides, *Nature Rev. Mater.* 1 (2016) 16017.
- [7] T. Kobayashi, *Study of Electronic Properties of 122 Iron Pnictide Through Structural, Carrier-Doping, and Impurity-Scattering Effects*, Springer, New York, 2017.
- [8] E. Dagotto, Open questions in CMR manganites, relevance of clustered states and analogies with other compounds including the cuprates, *New J. Phys.* 7 (2005) 67.
- [9] S. Mazumdar, A unified theoretical approach to superconductors with strong Coulomb correlations: the organics,  $\text{LiTi}_2\text{O}_4$ , electron- and hole-doped copper oxides and doped  $\text{BaBiO}_3$ , in: D. Baeriswyl, D. K. Campbell (Eds.), *Interacting Electrons in Reduced Dimensions. Proceedings of a NATO Advanced Research Workshop*, Plenum, New York, 1989, pp. 315–329.
- [10] Y. J. Uemura, L. P. Le, G. M. Luke, B. J. Sternlieb, W. D. Wu, J. H. Brewer, T. M. Riseman, C. L. Seaman, M. B. Maple, M. Ishikawa, D. G. Hinks, J. D. Jorgensen, G. Saito, H. Yamochi, Basic similarities among cuprate, bismuthate, organic, Chevrel-phase, and heavy-fermion superconductors shown by penetration-depth measurements, *Phys. Rev. Lett.* 66 (1991) 2665–2668.
- [11] H. Fukuyama, Y. Hasegawa, Superconductivity in organics and oxides: similarity and dissimilarity, *Physica B & C* 148B+C (1987) 204–211.
- [12] H. Fukuyama, On some organic conductors in the light of oxide superconductors, in: G. Saito, S. Kagoshima (Eds.), *Physics and Chemistry of Organic Superconductors. Proceedings of the ISSP International Symposium*, Springer-Verlag, Berlin, 1990, pp. 15–20.
- [13] R. H. McKenzie, Similarities between organic and cuprate superconductors, *Science* 278 (1997) 820.
- [14] Y. Iwasa, T. Takenobu, Superconductivity, Mott-Hubbard states, and molecular orbital order in intercalated fullerides, *J. Phys.: Condens. Matter* 15 (2003) R495.
- [15] M. Capone, M. Fabrizio, C. Castellani, E. Tosatti, Colloquium: Modeling the unconventional superconducting properties of expanded  $\text{A}_3\text{C}_{60}$  fullerides, *Rev. Mod. Phys.* 81 (2009) 943.
- [16] S. Mazumdar, R. T. Clay, Is there a common theme behind the correlated-electron superconductivity in organic charge-transfer solids, cobaltates, spinels and fullerides?, *Phys. Stat. Solidi* 249 (2012) 995–998.
- [17] G. Baskaran, RVB states in doped band insulators from Coulomb forces: theory and a case study of superconductivity in  $\text{BiS}_2$  layers, *Supercond. Sci. Technol.* 29 (2016) 124002.
- [18] D. Jérôme, A. Mazaud, M. Ribault, K. Bechgaard, Superconductivity in a synthetic organic conductor  $(\text{TMTSF})_2\text{PF}_6$ , *J. Phys. (Paris) Lett.* 41 (1980) L95–L98.
- [19] M. Ribault, J. P. Pouget, D. Jerome, K. Bechgaard, Superconductivity and absence of a Kohn anomaly in the quasi-one-dimensional organic conductor -  $(\text{TMTSF})_2\text{AsF}_6$ , *J. Phys. (Paris) Lett.* 41 (1980) L607–610.
- [20] S. S. P. Parkin, E. M. Engler, R. R. Schumaker, R. Lagier, V. Y. Lee, J. C. Scott, R. L. Greene, Superconductivity in a new family of organic conductors, *Phys. Rev. Lett.* 50 (1983) 270273.
- [21] A. M. Kini, U. Geiser, H. H. Wang, K. D. Carlson, J. M. Williams, W. K. Kwok, K. G. Vandervoort, J. E. Thompson, D. L. Stupka, New ambient-pressure organic superconductor,  $\kappa\text{-(ET)}_2\text{Cu}[\text{N}(\text{CN})_2]\text{Br}$ , with the highest transition temperature yet observed (inductive onset  $T_c = 11.6$  K, resistive onset = 12.5 K), *Inorg. Chem.* 29 (1990) 2555–2557.
- [22] T. Ishiguro, K. Yamaji, G. Saito, *Organic Superconductors*, Springer-Verlag, New York, 1998.
- [23] J. M. Williams, J. R. Ferraro, R. J. Thron, K. D. Carlson, U. Geiser, H. H. Wang, A. M. Kini, M. H. Whangbo, *Organic Superconductors (Including Fullerenes): Synthesis, Structure, Properties, and Theory*, Prentice-Hall, Englewood Cliffs, NJ, 1992.
- [24] G. Saito, Y. Yoshida, Development of conductive organic molecular assemblies: organic metals, superconductors, and exotic functional materials, *Bull. Chem. Soc. Jpn.* 80 (2007) 1137.
- [25] A. G. Lebed (Ed.), *The Physics of Organic Superconductors and Conductors*, Springer, Berlin, 2008.
- [26] R. Kato, Conducting metal dithiolenes complexes: Structural and electronic properties, *Chem. Rev.* 104 (2004) 5319–5346.
- [27] R. N. Lyubovskaya, E. A. Zhilyaeva, A. V. Zvarykina, V. N. Laukhin, R. B. Lyubovskii, S. I. Pesotskii, Is the organic metal  $(\text{ET})_4\text{Hg}_3\text{Br}_8$  a quasi-2D superconductor?, *JETP Lett.* 45 (1987) 530.
- [28] A. Naito, Y. Nakazawa, K. Saito, H. Taniguchi, K. Kanoda, M. Sorai, Anomalous enhancement of electronic heat capacity in the organic conductors  $\kappa\text{-(BEDT-TTF)}_4\text{Hg}_{3x}\text{X}_8$  ( $\text{X}=\text{Br}, \text{Cl}$ ), *Phys. Rev. B* 71 (2005) 054514.
- [29] H. Taniguchi, T. Okuhata, T. Nagai, K. Satoh, N. Mori, Y. Shimizu, M. Hedo, Y. Uwatoko, Anomalous pressure dependence of superconductivity in layered organic conductor,  $\kappa\text{-(BEDT-TTF)}_4\text{Hg}_{2.89}\text{Br}_8$ , *J. Phys. Soc. Jpn.* 76 (2007) 11370.
- [30] J. B. Torrance, Y. Tomkiewicz, B. D. Silverman, Enhancement of the magnetic susceptibility of TTF-TCNQ (tetrathiafulvalene-tetracyanoquinodimethane) by Coulomb correlations, *Phys. Rev. B* 15 (1977) 4738–4749.
- [31] J. B. Torrance, Spin waves, scattering at  $4k_F$ , and spin-Peierls fluctuations in an organic metal: tetrathiafulvalene-tetracyanoquinodimethane (TTF-TCNQ), *Phys. Rev. B* 17 (1978) 3099–3103.
- [32] S. Mazumdar, A. N. Bloch, Systematic trends in short-range Coulomb effects among nearly one-dimensional organic conductors, *Phys. Rev. Lett.* 50 (1983) 207–210.
- [33] N. P. Armitage, P. Fournier, R. L. Greene, Progress and perspectives on electron-doped cuprates, *Rev. Mod. Phys.* 82 (2010) 2421–2487, and references therein.
- [34] R. T. Clay, J. P. Song, S. Dayal, S. Mazumdar, Ground state and finite temperature behavior of 1/4-filled band zigzag ladders, *J. Phys. Soc. Jpn.* 81 (2012) 074707.
- [35] C. Bourbonnais, D. Jérôme, Interacting electrons in quasi-one-dimensional organic superconductors, in: A. G. Lebed (Ed.), *The Physics of Organic Superconductors and Conductors*, Springer, Berlin, 2008, pp. 357–412.

- [36] C. Bourbonnais, A. Sedeki, Superconductivity and antiferromagnetism as interfering orders in organic conductors, *Comptes Rendus Physique* 12 (2011) 532–541.
- [37] R. T. Clay, H. Li, S. Mazumdar, Absence of superconductivity in the half-filled band Hubbard model on the anisotropic triangular lattice, *Phys. Rev. Lett.* 101 (2008) 166403.
- [38] S. Dayal, R. T. Clay, S. Mazumdar, Absence of long-range superconducting correlations in the frustrated  $\frac{1}{2}$ -filled band Hubbard model, *Phys. Rev. B* 85 (2012) 165141.
- [39] P. W. Anderson, Resonating valence bonds: a new kind of insulator?, *Mater. Res. Bull.* 8 (1973) 153–160.
- [40] P. W. Anderson, The resonating valence bond state in  $\text{La}_2\text{CuO}_4$  and superconductivity, *Science* 235 (1987) 1196.
- [41] A. S. Alexandrov, N. F. Mott, *High Temperature Superconductors And Other Superfluids*, Taylor and Francis, London, 1994.
- [42] E. Fradkin, S. A. Kivelson, J. M. Tranquada, Colloquium: Theory of intertwined orders in high temperature superconductors, *Rev. Mod. Phys.* 87 (2015) 457–482.
- [43] P. Cai, W. Ruan, Y. Peng, C. Ye, X. Li, Z. Hao, X. Zhou, D.-H. Lee, Y. Wang, Visualizing the evolution from the Mott insulator to a charge-ordered insulator in lightly doped cuprates, *Proc. Natl. Acad. Sci.* 12 (2016) 1047–1052.
- [44] A. Mesaros, K. Fujita, S. D. Edkins, M. H. Hamidian, H. Eisaki, S. Uchida, J. C. S. Davis, M. J. Lawler, E.-A. Kim, Commensurate  $4a_0$  period charge density modulations throughout the  $\text{Bi}_2\text{Sr}_2\text{CaCu}_2\text{O}_{8+x}$  pseudogap regime, *Proc. Natl. Acad. Sci.* 113 (2016) 1266112666.
- [45] Z. G. Soos, Theory of  $\pi$ -molecular charge-transfer crystals, *Ann. Rev. Phys. Chem.* 25 (1974) 121–153.
- [46] Z. G. Soos, D. J. Klein, Charge-transfer in solid state complexes, in: R. Foster (Ed.), *Molecular Association*, Vol. 1, Academic, New York, 1975, p. 1.
- [47] J. B. Torrance, The difference between metallic and insulating salts of tetracyanoquinodimethane (TCNQ): How to design an organic metal, *Acc. Chem. Res.* 12 (1979) 7986.
- [48] J. B. Torrance, J. E. V. J. Mayerle, V. Y. Lee, Discovery of a neutral-to-ionic phase transition in organic materials, *Phys. Rev. Lett.* 46 (1981) 253257.
- [49] J. B. Torrance, A. Girlando, J. J. Mayerle, J. I. Crowley, V. Y. Lee, P. Batail, Anomalous nature of neutral-to-ionic phase transition in tetrathiafulvalene-chloranil, *Phys. Rev. Lett.* 47 (1981) 1747–1750.
- [50] S. Koshihara, Y. Tokura, T. Mitani, G. Saito, T. Koda, Photoinduced valence instability in the organic molecular compound tetrathiafulvalene-p-chloranil (TTF-CA), *Phys. Rev. B* 42 (1990) 68536856.
- [51] J. B. Torrance, B. A. Scott, F. B. Kaufman, Optical properties of charge-transfer salts of tetracyanoquinodimethane (TCNQ), *Solid St. Commun.* 17 (1975) 1369–1373.
- [52] M. Kumar, B. J. Topham, R. H. Yu, B. D. H. Quoc, Z. G. Soos, Magnetic susceptibility of alkali-tetracyanoquinodimethane salts and extended Hubbard models with bond order and charge density wave phases, *J. Chem. Phys.* 134 (2011) 234304.
- [53] A. Epstein, S. Etemad, A. Garito, A. Heeger, Metal-insulator transition in an organic solid: Experimental realization of the one-dimensional Hubbard model, *Solid St. Comm.* 9 (1971) 1803–1808.
- [54] A. Epstein, J. S. Miller, J. P. Pouget, R. Comes, X-ray observation of crossover of  $2k_F$  to  $4k_F$  scattering in (N-Methylphenazinium) $_x$ (Phenazine) $_{1-x}$  (Tetracyanoquinodimethane)[(NMP) $_x$ (Phen) $_{1-x}$ (TCNQ)],  $0.5 \leq x \leq 1.0$ , *Phys. Rev. Lett.* 47 (1981) 741–744.
- [55] J. P. Ferraris, D. O. Cowan, J. V. Wlatka, J. H. Perlstein, Electron transfer in a new highly conducting donor-acceptor complex, *J. Am. Chem. Soc.* 95 (1973) 948.
- [56] L. B. Coleman, M. J. Cohen, D. J. Sandman, F. G. Yamagishi, A. F. Garito, A. J. Heeger, Superconducting fluctuations and the Peierls instability in an organic solid, *Solid St. Comm.* 12 (1973) 1125.
- [57] H. J. Keller (Ed.), *Low-dimensional cooperative phenomena*, Springer, New York, 1975.
- [58] J. B. Torrance, J. J. Mayerle, K. Bechgaard, B. D. Silverman, Y. Tomkiewicz, Comparison of two isostructural organic compounds, one metallic and the other insulating, *Phys. Rev. B* 22 (1980) 4960–4965.
- [59] M. E. Hawley, T. O. Poehler, T. F. Carruthers, A. N. Bloch, D. O. Cowan, T. J. Kistenmacher, Magnetic and electrical behavior of a new organic charge-transfer salt, *Bull. Am. Phys. Soc.* 23 (1978) 424.
- [60] H. J. Keller (Ed.), *Chemistry and Physics of One Dimensional Metals*, Plenum, New York, 1977.
- [61] J. T. Devreese, R. P. Evrard, V. E. van Doren (Eds.), *Highly conducting one-dimensional solids*, Plenum, New York, 1979.
- [62] J. Bernasconi, M. J. Rice, W. R. Schneider, S. Strassler, Peierls transition in the strong-coupling Hubbard chain, *Phys. Rev. B* 12 (1975) 1090–1092.
- [63] D. J. Klein, W. A. Seitz, Partially filled linear Hubbard model near the atomic limit, *Phys. Rev. B* 10 (1974) 3217–3227.
- [64] J. W. Bray, H. R. H. Jr., L. V. Interrante, I. S. Jacobs, J. S. Kasper, G. D. Watkins, S. H. Wee, J. C. Bonner, Observation of a spin-Peierls transition in a Heisenberg antiferromagnetic linear-chain system, *Phys. Rev. Lett.* 35 (1975) 744–747.
- [65] J. W. Bray, L. V. Interrante, I. S. Jacobs, J. C. Bonner, The spin-Peierls transition, in: J. S. Miller (Ed.), *Extended linear chain compounds*, Vol. 3, Plenum, New York, 1983, Ch. 7, pp. 353–415.
- [66] M. C. Cross, D. S. Fisher, A new theory of the spin-Peierls transition with special relevance to the experiments on TTFcCuBDT, *Phys. Rev. B* 19 (1979) 402–419.
- [67] J. P. Pouget, S. K. Khanna, F. Denoyer, R. Comés, X ray observation of  $2k_F$  and  $4k_F$  scatterings in tetrathiafulvalene-tetracyanoquinodimethane (TTF-TCNQ), *Phys. Rev. Lett.* 37 (1976) 437–440.
- [68] R. Comés, X-ray and neutron scattering investigation of the charge density waves in TTF-TCNQ, in: H. J. Keller (Ed.), *Chemistry and Physics of One-Dimensional Conductors*, Plenum, New York, 1977, pp. 315–339.
- [69] S. Kagoshima, T. Ishiguro, H. Anzai, X-ray scattering study of phonon anomalies and superstructures in TTF-TCNQ, *J. Phys. Soc. Jpn.* 41 (1976) 2061.
- [70] H. A. Mook, J. C. R. Watson, Neutron inelastic scattering study of tetrathiafulvalene tetracyanoquinodimethane (TTF-TCNQ), *Phys. Rev. Lett.* 36 (1976) 801803.
- [71] G. Shirane, S. M. Shapiro, R. Comés, A. F. Garito, A. J. Heeger, Phonon dispersion and Kohn anomaly in tetrathiafulvalene-tetracyanoquinodimethane (TTF-TCNQ), *Phys. Rev. B* 14 (1976) 2325–2334.

- [72] A. Bosch, B. v. Bodegom, The crystal structure of the 1:2 complex of N-methyl-N-ethylmorpholinium and 7,7,8,8-tetracyanoquinodimethane, MEM(TCNQ)<sub>2</sub>, at -160° C, Acta Crystallogr. Sect. B 33 (1977) 3013.
- [73] S. Huizinga, J. Kommandeur, G. A. Sawatzky, B. T. Thole, K. Kopinga, W. J. M. de Jonge, J. Roos, Spin-Peierls transition in N-methyl-N-ethyl-morpholinium-ditetracyanoquinodimethanide [MEM-(TCNQ)<sub>2</sub>], Phys. Rev. B 19 (9) (1979) 4723–4732.
- [74] S. Huizinga, J. Kommandeur, H. T. Jonkman, C. Haas, Magnetic ( $2k_F$ ) and electronic ( $4k_F$ ) Peierls transitions from a Hubbard Hamiltonian extended with intersite-dependent transfer, Phys. Rev. B 25 (1982) 1717.
- [75] A. Epstein, J. W. Kaufer, H. Rommelmann, I. A. Howard, E. M. Conwell, J. S. Miller, J. P. Pouget, R. Comes, Evidence for solitons in conducting organic charge-transfer crystals, Phys. Rev. Lett. 49 (1982) 1037–1041.
- [76] E. M. Conwell, I. A. Howard, Solitons in quasi one-dimensional crystals, J. Phys. (Colloque) C3 (1983) 1487–1492.
- [77] M. J. Rice, E. J. Mele, Possibility of solitons with charge  $\pm e/2$  in highly correlated 1:2 salts of tetracyanoquinodimethane (TCNQ), Phys. Rev. B 25 (1982) 1339–1343.
- [78] J. E. Hirsch, D. J. Scalapino,  $2p_F$  and  $4p_F$  instabilities in the one-dimensional Hubbard model, Phys. Rev. B 29 (1984) 5554–5561.
- [79] A. N. Bloch, S. Mazumdar, Short-range Coulomb effects and the chemical systematics of conducting organic charge-transfer salts, J. Physique C-3 44 (1983) 1273–1279.
- [80] J. E. Hirsch, D. J. Scalapino,  $2p_F$  and  $4p_F$  instabilities in a one-quarter-filled-band Hubbard model, Phys. Rev. B 27 (1983) 7169.
- [81] F. Mila, X. Zotos, Phase diagram of the one-dimensional extended Hubbard model at quarter-filling, Europhys. Lett. 24 (1993) 133.
- [82] K. Penc, F. Mila, Phase diagram of the one-dimensional extended Hubbard model with attractive and/or repulsive interactions at quarter filling, Phys. Rev. B 49 (1994) 9670–9678.
- [83] R. T. Clay, S. Mazumdar, D. K. Campbell, The pattern of charge ordering in quasi-one dimensional organic charge-transfer solids, Phys. Rev. B 67 (2003) 115121.
- [84] R. J. J. Visser, S. Oostra, C. Vettier, J. Voiron, Determination of the spin-Peierls distortion in N-methyl-N-ethyl-morpholinium ditetracyanoquinodimethanide [MEM(TCNQ)<sub>2</sub>]: Neutron diffraction study at 6 K, Phys. Rev. B 28 (1983) 2074–2077.
- [85] W. P. Su, J. R. Schrieffer, A. J. Heeger, Solitons in polyacetylene, Phys. Rev. Lett. 42 (1979) 1698.
- [86] T. Holstein, Studies of polaron motion: Part I. the molecular-crystal model, Ann. Phys.(N.Y.) 8 (1959) 325.
- [87] M. J. Rice, C. B. Duke, N. O. Lipari, Intramolecular vibrational stabilization of the charge density wave state in organic metals, Solid St. Comm. 17 (1975) 1089–1093.
- [88] M. J. Rice, N. O. Lipari, Electronmolecular-vibration coupling in tetrathiafulvalene-tetracyanoquinodimethane (TTF-TCNQ), Phys. Rev. Lett. 38 (1977) 437–439.
- [89] E. M. Conwell, Introduction to highly conducting quasi-one-dimensional organic crystals, Semiconductors and Semimetals 27 (1988) 1–27.
- [90] S. Kivelson, Solitons with adjustable charge in a commensurate Peierls insulator, Phys. Rev. B 28 (1983) 2653.
- [91] W.-P. Su, Soliton excitations in a commensurability 2 mixed Peierls system, Solid St. Comm. 48 (1983) 479.
- [92] S. N. Dixit, S. Mazumdar, Electron-electron interaction effects on Peierls dimerization in a half-filled band, Phys. Rev. B 29 (1984) 1824–1839.
- [93] K.-C. Ung, S. Mazumdar, D. K. Campbell, Coexisting CDW and BOW in organic conductors with non-half-filled bands, Solid St. Comm. 85 (1993) 917–920.
- [94] M. Dressel, M. Dumm, T. Knoblauch, M. Masino, Comprehensive optical investigations of charge order in organic chain compounds (TMTTF)<sub>2</sub>X, Crystals 2 (2012) 528.
- [95] A. Girlando, Charge sensitive vibrations and electron-molecular vibration coupling in Bis(ethylenedithio)-tetrathiafulvalene (BEDT-TTF), J. Phys. Chem. C 115 (2011) 19371–19378.
- [96] Y. Tomkiewicz, B. Welber, P. E. Seiden, R. Schumaker, Electron-electron interactions in the fulvalene family of organic metals, Solid St. Commun. 23 (1977) 471.
- [97] S. Mazumdar, S. N. Dixit, Unified theory of segregated-stack organic charge-transfer solids: magnetic properties, Phys. Rev. B 34 (1986) 3683–3699.
- [98] A. W. Sandvik, A generalization of Handscomb’s quantum Monte Carlo scheme-application to the 1D Hubbard model, J. Phys. A 25 (1992) 3667–3682.
- [99] O. F. Syljuasen, A. W. Sandvik, Quantum Monte Carlo with directed loops, Phys. Rev. E 66 (2002) 046701.
- [100] D. Jérôme, The physics of organic superconductors, Science 252 (1991) 1509–1514.
- [101] B. Salameh, S. Yasin, M. Dumm, G. Untereiner, L. Montgomery, M. Dressel, Spin dynamics of the organic linear chain compounds (TMTTF)<sub>2</sub>X (X=SbF<sub>6</sub>, AsF<sub>6</sub>, BF<sub>4</sub>, ReO<sub>4</sub>, and SCN), Phys. Rev. B 83 (2011) 205126.
- [102] K. Yoshimi, H. Seo, S. Ishibashi, S. E. Brown, Tuning the magnetic dimensionality by charge ordering in the molecular TMTTF salts, Phys. Rev. Lett. 108 (2012) 096402.
- [103] A. B. Ward, R. Clay, S. Mazumdar, Comment on “Tuning the magnetic dimensionality by charge ordering in the molecular TMTTF salts”, Phys. Rev. Lett. 113 (2014) 029701.
- [104] H. Seo, S. Ishibashi, S. E. Brown, Seo *et al.* reply:, Phys. Rev. Lett. 113 (2014) 029702.
- [105] J. Hubbard, Generalized Wigner lattices in one dimension and some applications to tetracyanoquinodimethane (TCNQ) salts, Phys. Rev. B 17 (1978) 494–505.
- [106] H. Seo, H. Fukuyama, Antiferromagnetic phases of one-dimensional quarter-filled organic conductors, J. Phys. Soc. Jpn. 66 (1997) 1249–1252.
- [107] H. Seo, Charge ordering in organic ET compounds, J. Phys. Soc. Jpn. 69 (2000) 805–820.
- [108] Y. Shibata, S. Nishimoto, Y. Ohta, Charge ordering in the one-dimensional extended Hubbard model: Implication to the TMTTF family of organic conductors, Phys. Rev. B 64 (2001) 235107.
- [109] H. Seo, Y. Motome, T. Kato, Finite-temperature phase transitions in quasi-one-dimensional molecular conductors, J. Phys. Soc. Jpn. 76 (2007) 013707.
- [110] Y. Otsuka, H. Seo, Y. Motome, T. Kato, Finite-temperature phase diagram of quasi-one-dimensional molecular conductors: Quantum Monte Carlo study, J. Phys. Soc. Jpn. 77 (2008) 113705.

- [111] M. Tsuchiizu, H. Yoshioka, Y. Suzumura, Crossover from quarter-filling to half-filling in a one-dimensional electron system with a dimerized and quarter-filled band, *J. Phys. Soc. Jpn.* 70 (2001) 1460–1463.
- [112] M. Sugiura, M. Tsuchiizu, Y. Suzumura, Interplay of lattice dimerization and charge ordering in one-dimensional quarter-filled electron systems, *J. Phys. Soc. Jpn.* 73 (2004) 2487–2493.
- [113] M. Sugiura, M. Tsuchiizu, Y. Suzumura, Spin-Peierls transition temperature in quarter-filled organic conductors, *J. Phys. Soc. Jpn.* 74 (2005) 983–987.
- [114] H. Yoshioka, M. Tsuchiizu, H. Seo, Finite-temperature charge-ordering transition and fluctuation effects in quasi one-dimensional electron systems at quarter filling, *J. Phys. Soc. Jpn.* 75 (2006) 063706.
- [115] H. Yoshioka, M. Tsuchiizu, H. Seo, Charge-ordered state versus dimer-Mott insulator at finite temperatures, *J. Phys. Soc. Jpn.* 76 (2007) 103701.
- [116] H. Yoshioka, M. Tsuchiizu, Y. Otsuka, H. Seo, Finite-temperature properties across the charge ordering transition —combined bosonization, renormalization group, and numerical methods, *J. Phys. Soc. Jpn.* 79 (2014) 094714.
- [117] K. Sano, Y. Ono, Electronic structure of one-dimensional extended Hubbard model, *J. Phys. Soc. Jpn.* 63 (1994) 1250–1253.
- [118] K. C. Ung, S. Mazumdar, D. Toussaint, Metal-insulator and insulator-insulator transitions in the quarter-filled band organic conductors, *Phys. Rev. Lett.* 73 (1994) 2603–2606.
- [119] J. Riera, D. Poilblanc, Coexistence of charge-density waves, bond-order waves, and spin-density waves in quasi-one-dimensional charge-transfer salts, *Phys. Rev. B* 62 (2000) R16243–R16246.
- [120] M. Nakamura, Tricritical behavior in the extended Hubbard chains, *Phys. Rev. B* 61 (2000) 16377–16392.
- [121] J. Riera, D. Poilblanc, Influence of the anion potential on the charge ordering in quasi-one-dimensional charge-transfer salts, *Phys. Rev. B* 63 (2001) 241102.
- [122] R. T. Clay, S. Mazumdar, D. K. Campbell, Charge ordering in  $\theta$ -(BEDT-TTF)<sub>2</sub>X materials, *J. Phys. Soc. Jpn.* 71 (2002) 1816–1819.
- [123] K. Sano, Y. Ono, Critical behavior near the metal-insulator transition in the one-dimensional extended Hubbard model at quarter filling, *Phys. Rev. B* 70 (2004) 155102.
- [124] H. Li, R. T. Clay, S. Mazumdar, The paired-electron crystal in the two-dimensional frustrated quarter-filled band, *J. Phys.: Condens. Matter* 22 (2010) 272201.
- [125] S. Dayal, R. T. Clay, H. Li, S. Mazumdar, Paired electron crystal: Order from frustration in the quarter-filled band, *Phys. Rev. B* 83 (2011) 245106.
- [126] R. T. Clay, S. Mazumdar, D. K. Campbell, Re-integerization of fractional charges in the correlated quarter-filled band, *Phys. Rev. Lett.* 86 (2001) 4084–4087.
- [127] R. T. Clay, S. Mazumdar, Co-operative bond-charge density wave and giant spin gap in the quarter-filled zigzag electron ladder, *Phys. Rev. Lett.* 94 (2005) 207206.
- [128] S. Mazumdar, R. T. Clay, D. K. Campbell, Bond-order and charge-density waves in the isotropic interacting two-dimensional quarter-filled band and the insulating state proximate to organic superconductivity, *Phys. Rev. B* 62 (2000) 13400–13425.
- [129] R. T. Clay, R. P. Hardikar, S. Mazumdar, Temperature-driven transition from the Wigner crystal to the bond-charge-density wave in the quasi-one-dimensional quarter-filled band, *Phys. Rev. B* 76 (2007) 205118.
- [130] R. T. Clay, A. B. Ward, N. Gomes, S. Mazumdar, Bond patterns and charge order amplitude in  $\frac{1}{4}$ -filled charge-transfer solids, *Phys. Rev. B* 95 (2017) 125114.
- [131] S. Nishimoto, M. Takahashi, Y. Ohta, Charge gap of the quasi-one-dimensional organic conductors: a density-matrix renormalization-group study, *J. Phys. Soc. Jpn.* 69 (2000) 1594–1597.
- [132] M. Kuwabara, H. Seo, M. Ogata, Coexistence of charge order and spin-Peierls lattice distortion in one-dimensional organic conductors, *J. Phys. Soc. Jpn.* 72 (2003) 225.
- [133] S. Ejima, F. Gebhard, S. Nishimoto, Tomonaga-Luttinger parameters for doped Mott insulators, *Eur. Phys. Lett.* 70 (2005) 492–498.
- [134] S. Ejima, F. Gebhard, S. Nishimoto, Tomonaga-Luttinger parameters and spin excitations in the dimerized extended Hubbard model, *Phys. Rev. B* 74 (2006) 245110.
- [135] H. Benthien, E. Jeckelmann, Optical conductivity of the one-dimensional dimerized Hubbard model at quarter filling, *Eur. Phys. J. B* 44 (2005) 287–297.
- [136] T. Shirakawa, E. Jeckelmann, Charge and spin Drude weight of the one-dimensional extended Hubbard model at quarter filling, *Phys. Rev. B* 79 (2009) 195121.
- [137] D. Baeriswyl, D. K. Campbell, S. Mazumdar, *Conjugated Conducting Polymers*, Kiess, H., Ed.; Springer: Berlin, 1992.
- [138] S. Mazumdar, S. N. Dixit, Coulomb effects on one-dimensional Peierls instability: the Peierls-Hubbard model, *Phys. Rev. Lett.* 51 (1983) 292–295.
- [139] J. E. Hirsch, Effect of Coulomb interactions on the Peierls instability, *Phys. Rev. Lett.* 51 (1983) 296–299.
- [140] Z. G. Soos, S. Ramasesha, Valence-bond theory of linear Hubbard and Pariser-Parr-Pople models, *Phys. Rev. B* 29 (1984) 5410–5422.
- [141] S. Mazumdar, D. K. Campbell, Broken symmetries in a one-dimensional half-filled band with arbitrarily long-range Coulomb interactions, *Phys. Rev. Lett.* 55 (1985) 2067–2070.
- [142] S. Mazumdar, Valence-bond approach to two-dimensional broken symmetries: Application to La<sub>2</sub>CuO<sub>4</sub>, *Phys. Rev. B* 36 (1987) 7190–7193.
- [143] N. Kobayashi, M. Ogata, K. Yonemitsu, Coexistence of SDW and purely-electronic CDW in quarter-filled organic conductors, *J. Phys. Soc. Jpn.* 67 (1998) 1098–1101.
- [144] F. D. M. Haldane, General relation of correlation exponents and spectral properties of one-dimensional Fermi systems: application to the anisotropic  $S = \frac{1}{2}$  Heisenberg chain, *Phys. Rev. Lett.* 45 (1980) 1358–1362.
- [145] F. D. M. Haldane, 'Luttinger liquid theory' of one-dimensional quantum fluids: I. properties of the Luttinger model and their extension to the general 1D interacting spinless Fermi gas, *J. Phys. C* 14 (1981) 2585–2609.
- [146] J. Voit, One-dimensional Fermi liquids, *Rep. Prog. Phys.* 58 (1995) 977.
- [147] H. Seo, M. Kuwabara, M. Ogata, Co-existence of charge order and spin Peierls lattice distortion in one-dimensional organic compounds, *J. Phys. IV France* 12 (2002) Pr9–205.

- [148] E. H. Lieb, D. Mattis, Ordering energy levels of interacting spin systems, *J. Math. Phys. (NY)* 3 (1962) 749.
- [149] S. Mazumdar, S. Ramasesha, R. T. Clay, D. K. Campbell, Theory of coexisting charge- and spin-density waves in  $(\text{TMTTF})_2\text{Br}$ ,  $(\text{TMTSF})_2\text{PF}_6$ , and  $\alpha$ - $(\text{BEDT-TTF})_2\text{MHg}(\text{SCN})_4$ , *Phys. Rev. Lett.* 82 (1999) 1522–1525.
- [150] A. Ota, H. Yamochi, G. Saito, A novel metal-insulator phase transition observed in  $(\text{EDO-TTF})_2\text{PF}_6$ , *J. Mater. Chem.* 12 (2002) 2600–2602.
- [151] K. Furukawa, K. Sugiura, F. Iwase, T. Nakamura, Structural investigation of the spin-singlet phase in  $(\text{TMTTF})_2\text{I}$ , *Phys. Rev. B* 83 (2011) 184419.
- [152] L. Ducasse, C. Coulon, D. Chasseau, R. Yagbasan, J. M. Fabre, A. K. Gousamia, Structural, electronic and physical properties of  $(\text{BCPTTF})_2\text{MF}_6$  ( $M = \text{P}, \text{As}$ ), occurrence of a spin-Peierls transition ( $T_{\text{SP}} \approx 30\text{K}$ ), *Synth. Metals* 27 (1988) B543–B548.
- [153] Q. Liu, S. Ravy, J. P. Pouget, C. Coulon, Structural fluctuations and spin-Peierls transitions revisited, *Synth. Metals* 55–57 (1993) 1840–1845.
- [154] P. Foury-Leylekian, P. Auban-Senzier, C. Coulon, O. Jeannin, M. Fourmigué, C. Pasquier, J.-P. Pouget, Phase diagram of the correlated quarter-filled-band organic salt series  $(\text{o-DMTTF})_2\text{X}$  ( $X = \text{Cl}, \text{Br}, \text{I}$ ), *Phys. Rev. B* 84 (2011) 195134.
- [155] P. Auban-Senzier, C. R. Pasquier, D. Jérôme, S. Suh, S. E. Brown, C. Meziere, J. P. Pouget, Phase diagram of quarter-filled band organic salts  $[\text{EDT-TTF-CONMe}_2]_2\text{X}$ ,  $x = \text{AsF}_6$  and  $\text{Br}$ , *Phys. Rev. Lett.* 102 (2009) 257001.
- [156] S. Hirose, A. Kawamoto, N. Matsunaga, K. Nomura, K. Yamamoto, K. Yakushi, Reexamination of  $^{13}\text{C}$ -NMR in  $(\text{TMTTF})_2\text{AsF}_6$ : Comparison with infrared spectroscopy, *Phys. Rev. B* 81 (2010) 205107.
- [157] S. Fujiyama, T. Nakamura, Redistribution of electronic charges in spin-Peierls state in  $(\text{TMTTF})_2\text{AsF}_6$  observed by  $^{13}\text{C}$  NMR, *J. Phys. Soc. Jpn.* 75 (2006) 014705.
- [158] T. Nakamura, K. Furukawa, T. Hara, Redistribution of charge in the proximity of the spin-Peierls transition:  $^{13}\text{C}$  NMR investigation of  $(\text{TMTTF})_2\text{PF}_6$ , *J. Phys. Soc. Jpn.* 76 (2007) 064715.
- [159] F. Iwase, K. Sugiura, K. Furukawa, T. Nakamura,  $^{13}\text{C}$  NMR study of the magnetic properties of the quasi-one-dimensional conductor  $(\text{TMTTF})_2\text{SbF}_6$ , *Phys. Rev. B* 84 (2011) 115140.
- [160] F. Iwase, K. Sugiura, K. Furukawa, T. Nakamura, Electronic properties of a TMTTF-family salt,  $(\text{TMTTF})_2\text{TaF}_6$ : New member located on the modified generalized phase-diagram, *J. Phys. Soc. Jpn.* 78 (10) (2009) 104717.
- [161] H. H. S. Javadi, R. Laversanne, A. J. Epstein, Microwave conductivity and dielectric constant of tetramethyltetrathiafulvalene salts  $[(\text{TMTTF})_2\text{X}, X = \text{SCN}, \text{ReO}_4, \text{SbF}_6]$ , *Phys. Rev. B* 37 (1988) 4280–4283.
- [162] M. Itoi, C. Araki, M. Hedo, Y. Uwatoko, T. Nakamura, Anomalous wide superconducting phase of one-dimensional organic conductor  $(\text{TMTTF})_2\text{SbF}_6$ , *J. Phys. Soc. Jpn.* 77 (2008) 023701.
- [163] C. Coulon, S. S. P. Parkin, R. Laversanne, Structureless transition and strong localization effects in bis-tetramethyltetrathiafulvalenium salts  $[(\text{TMTTF})_2\text{X}]$ , *Phys. Rev. B* 31 (1985) 3583.
- [164] P. Monceau, Electronic crystals: an experimental overview, *Adv. Phys.* 61 (2012) 325.
- [165] W. Yu, F. Zhang, F. Zamborszky, B. Alavi, A. Baur, C. A. Merlic, S. E. Brown, Electron-lattice coupling and broken symmetries of the molecular salt  $(\text{TMTTF})_2\text{SbF}_6$ , *Phys. Rev. B* 70 (2004) 121101.
- [166] D. S. Chow, F. Zamborszky, B. Alavi, D. J. Tantillo, A. Baur, C. A. Merlic, S. E. Brown, Charge ordering in the TMTTF family of molecular conductors, *Phys. Rev. Lett.* 85 (2000) 1698–1701.
- [167] F. Zamborszky, W. Yu, W. Raas, S. E. Brown, B. Alavi, C. A. Merlic, A. Baur, Competition and coexistence of bond and charge orders in  $(\text{TMTTF})_2\text{AsF}_6$ , *Phys. Rev. B* 66 (2002) 081103.
- [168] T. Nakamura, T. Nobutoki, Y. Kobayashi, T. Takahashi, G. Saito,  $^1\text{H}$ -NMR investigation of the SDW wave-number in  $(\text{TMTTF})_2\text{Br}$ , *Synth. Metals* 70 (1995) 1293–1294.
- [169] J. P. Pouget, S. Ravy, X-ray evidence of charge density wave modulations in the magnetic phases of  $(\text{TMTSF})_2\text{PF}_6$  and  $(\text{TMTTF})_2\text{Br}$ , *Synth. Metals* 85 (1997) 1523.
- [170] C. Coulon, A. Maaroufi, J. Amiell, E. Dupart, S. Flandrois, P. Delhaes, R. Moret, J. P. Pouget, J. P. Morand, Antiferromagnetic and structural instabilities in tetramethyltetrathiafulvalene thiocyanate  $[(\text{TMTTF})_2\text{SCN}]$ , *Phys. Rev. B* 26 (1982) 6322–6325.
- [171] M. Peo, J. C. Scott, E. M. Engler, Proton NMR linewidth and relaxation-rate study of an organic conductor with an antiferromagnetic ground state, *Phys. Rev. B* 30 (1984) 3639–3643.
- [172] F. Nad, P. Monceau, Dielectric response of the charge ordered state in quasi-one-dimensional organic conductors, *J. Phys. Soc. Jpn.* 75 (2006) 051005.
- [173] B. Köhler, E. Rose, M. Dumm, G. Untereiner, M. Dressel, Comprehensive transport study of anisotropy and ordering phenomena in quasi-one-dimensional  $(\text{TMTTF})_2\text{X}$  salts ( $X = \text{PF}_6, \text{AsF}_6, \text{SbF}_6, \text{BF}_4, \text{ClO}_4, \text{ReO}_4$ ), *Phys. Rev. B* 84 (2011) 035124.
- [174] M. de Souza, P. Foury-Leylekian, A. Moradpour, J.-P. Pouget, M. Lang, Evidence for lattice effects at the charge-ordering transition in  $(\text{TMTTF})_2\text{X}$ , *Phys. Rev. Lett.* 101 (2008) 216403.
- [175] P. Monceau, F. Y. Nad, S. Brazovskii, Ferroelectric Mott-Hubbard phase of organic  $(\text{TMTTF})_2\text{X}$  conductors, *Phys. Rev. Lett.* 86 (2001) 4080.
- [176] F. Nad, P. Monceau, T. Nakamura, K. Furukawa, The effect of deuteration on the transition into a charge ordered state of  $(\text{TMTTF})_2\text{X}$  salts, *J. Phys.: Condens. Matter* 17 (2005) L399–L406.
- [177] K. Furukawa, T. Hara, T. Nakamura, Deuteration effect and possible origin of the charge-ordering transition of  $(\text{TMTTF})_2\text{X}$ , *J. Phys. Soc. Jpn.* 74 (2005) 3288–3294.
- [178] P. Foury-Leylekian, D. L. Bolloc'h, B. Hennion, S. Ravy, A. Moradpour, J.-P. Pouget, Neutron-scattering evidence for a spin-Peierls ground state in  $(\text{TMTTF})_2\text{PF}_6$ , *Phys. Rev. B* 70 (18) (2004) 180405.
- [179] I. Voloshenko, M. Herter, R. Breyer, A. Pustogow, M. Dressel, Pressure-dependent optical investigations of Fabre salts in the charge-ordered state, *J. Phys.: Condens. Matter* 29 (2017) 115601.
- [180] R. Świetlik, B. Barszcz, A. Pustogow, M. Dressel, Raman spectroscopy evidence of domain walls in the organic ferroelectrics  $(\text{TMTTF})_2\text{X}$  ( $X = \text{SbF}_6, \text{AsF}_6, \text{PF}_6$ ), *Phys. Rev. B* 95 (2017) 085205.
- [181] F. Nad, P. Monceau, J. M. Fabre, Low frequency dielectric permittivity of quasi-one-dimensional conductor  $(\text{TMTTF})_2\text{Br}$ , *Eur. Phys. J. B* 3 (1998) 301–306.
- [182] E. Barthel, G. Quirion, P. Wzietek, D. Jérôme, J. B. Christensen, M. Jorgensen, K. Bechgaard, NMR in commensurate and incommensurate

- spin density waves, *Eur. Phys. Lett.* 21 (1993) 87.
- [183] J. P. Pouget, S. Ravy, Structural aspects of the Bechgaard salts and related compounds, *J. Physique I* 6 (1996) 1501.
- [184] M. Dumm, A. Loidl, B. W. Fravel, K. P. Starkey, L. K. Montgomery, M. Dressel, Electron spin resonance studies on the organic linear-chain compounds  $(\text{TMTCF})_2\text{X}$  (C=S, Se; X=PF<sub>6</sub>, AsF<sub>6</sub>, ClO<sub>4</sub>, Br), *Phys. Rev. B* 61 (2000) 511.
- [185] A. Zorko, D. Arčon, K. Biljaković, C. Carcel, J. M. Fabre, J. Dolinšek, Spin-Peierls fluctuations in  $(\text{TMTTF})_2\text{Br}$  studied by pulsed electron spin resonance spin-lattice relaxation, *Phys. Rev. B* 64 (2001) 172404.
- [186] D. Jérôme, H. J. Schulz, Organic conductors and superconductors, *Adv. Physics* 31 (1982) 299.
- [187] T. Takahashi, Y. Maniwa, H. Kawamura, G. Saito, Determination of SDW characteristics in  $(\text{TMTSF})_2\text{PF}_6$  by <sup>1</sup>H-NMR analysis, *J. Phys. Soc. Jpn.* 55 (1986) 1364–1373.
- [188] J. Pouget, R. Moret, R. Comés, K. Bechgaard, J. Fabre, L. Giral, X-ray diffuse scattering study of some  $(\text{TMTSF})_2\text{X}$  and  $(\text{TMTTF})_2\text{X}$  salts, *Mol. Cryst. Liq. Cryst.* 79 (1982) 485–499.
- [189] G. Grüner, The dynamics of spin-density waves, *Rev. Mod. Phys.* 66 (1994) 1–24.
- [190] S. E. Brown, B. Alavi, G. Gruner, K. Bartholomew, Softening of Young's modulus and collective spin-density-wave transport in  $(\text{TMTSF})_2\text{PF}_6$  (where TMTSF is tetramethyltetraselenafulvalene), *Phys. Rev. B* 46 (1992) 10483–10486.
- [191] J. Odín, J. C. Lasjaunias, K. Biljakovic, P. Monceau, K. Bechgaard, Low temperature specific heat of the spin-density-wave compound  $(\text{TMTSF})_2\text{PF}_6$ , *Solid St. Comm.* 91 (1994) 523–527.
- [192] H. Yang, J. C. Lasjaunias, P. Monceau, Specific heat measurements of the lattice contribution and spin-density-wave transition in  $(\text{TMTSF})_2\text{X}$  (x = PF<sub>6</sub> and AsF<sub>6</sub>) and  $(\text{TMTTF})_2\text{Br}$  salts, *J. Phys.:Condens. Matter* 11 (1999) 5083.
- [193] S. Kagoshima, Y. Saso, M. Maesato, R. Kondo, Low-temperature diffuse X-ray studies of charge-density waves coexisting with spin-density waves in the organic conductors  $(\text{TMTSF})_2\text{PF}_6$  and  $(\text{TMTSF})_2\text{AsF}_6$ , *Solid St. Comm.* 110 (1999) 479–483.
- [194] S. Kagoshima, Y. Saso, M. Maesato, R. Kondo, T. Yamaguchi, V. A. Bondarenko, T. Hasegawa, Electronic states in the spin-density wave phase of organic conductors: roles of the coexisting  $2k_F$  and  $4k_F$  charge-density waves, *Synth. Metals* 117 (2001) 39–43.
- [195] S. Valfells, P. Kuhns, A. Kleinhammes, J. S. Brooks, W. Moulton, S. Takasaki, J. Yamada, H. Anzai, Spin-density-wave state in  $(\text{TMTSF})_2\text{PF}_6$ : A <sup>77</sup>Se NMR study at high magnetic fields, *Phys. Rev. B* 56 (1997) 2585–2593.
- [196] K. Nomura, N. Keitoku, T. Shimizu, T. Sanbongi, M. Tokumoto, N. Kinoshita, H. Anzai, NMR in spin-density wave phase of  $(\text{TMTSF})_2\text{ClO}_4$ , *J. de Phys. IV* 3 (1993) C2–C21.
- [197] A. Hoshikawa, K. Nomura, S. Takasaki, J. Yamada, S. Nakatsuji, H. Anzai, M. Tokumoto, N. Kinoshita, Collective mode of spin-density-wave in  $(\text{TMTSF})_2\text{ClO}_4$ , *J. Phys. Soc. Jpn.* 69 (2000) 1457–1461.
- [198] J. C. Lasjaunias, K. Biljaković, F. Nad', P. Monceau, K. Bechgaard, Glass transition in the spin-density wave phase of  $(\text{TMTSF})_2\text{PF}_6$ , *Phys. Rev. Lett.* 72 (1994) 1283–1286.
- [199] S. Nagata, M. Misawa, Y. Ihara, A. Kawamoto, Commensurability of the spin-density-wave state of  $(\text{TMTSF})_2\text{PF}_6$  observed by <sup>13</sup>C-NMR, *Phys. Rev. Lett.* 110 (2013) 167001.
- [200] J. L. Galigne, S. Peytavin, B. Litautard, G. Brun, Tetramethyltrathiofulvalene iodide,  $(\text{C}_{10}\text{H}_{12}\text{S}_4)_2\text{I}$ , *Cryst. Struct. Commun.* 9 (1980) 61–63.
- [201] D. Jankowski, R. Swietlik, E. W. Reinheimer, M. Fourmigué, Involvement of weak C—H...X hydrogen bonds in metal-to-semiconductor regime change in one-dimensional organic conductors  $(\text{o-DMTTF})_2\text{X}$  (X= Cl, Br, and I): combined IR and Raman studies, *J. Raman Spectros.* 42 (2011) 1518.
- [202] L. Zorina, S. Simonov, C. Meziere, E. Canadell, S. Suh, S. E. Brown, P. Foury-Leylekan, P. Fertey, J.-P. Pouget, P. Batail, Charge ordering, symmetry and electronic structure issues and Wigner crystal structure of the quarter-filled band Mott insulators and high pressure metals  $\delta$ -(EDT-TTF-CONMe<sub>2</sub>)<sub>2</sub>X, X = Br and AsF<sub>6</sub>, *J. Mater. Chem.* 19 (2009) 6980.
- [203] K. Heuzé, M. Fourmigué, P. Batail, C. Coulon, R. Cl'eric, E. Canadell, P. Auban-Senzier, S. Ravy, D. Jérôme, A genuine quarter-filled band Mott insulator,  $(\text{EDT-TTF-CONMe}_2)_2\text{AsF}_6$ : Where the chemistry and physics of weak intermolecular interactions act in unison, *Adv. Mater.* 15 (2003) 1251.
- [204] J. P. Song, R. Clay, Monte Carlo simulations of two-dimensional fermion systems with string-bond states, *Phys. Rev. B* 89 (2014) 075101.
- [205] H. Yamochi, S. Koshihara, Organic metal  $(\text{EDO-TTF})_2\text{PF}_6$  with multi-instability, *Sci. Technol. Adv. Mater* 10 (2009) 024305.
- [206] M. Chollet, L. Guerin, N. Uchida, S. Fukaya, H. Shimoda, T. Ishikawa, K. Matsuda, T. Hasegawa, A. Ota, H. Yamochi, G. Saito, R. Tazaki, S. Adachi, S. Koshihara, Gigantic photoresponse in  $\frac{1}{4}$ -filled-band organic salt  $(\text{EDO-TTF})_2\text{PF}_6$ , *Science* 307 (2005) 86–89.
- [207] O. Drozdova, K. Yakushi, K. Yamamoto, A. Ota, H. Hideki, Y. Yamochi, G. Saito, H. Tashiro, D. B. Tanner, Optical characterization of  $2k_F$  bond-charge-density wave in quasi-one-dimensional  $\frac{3}{4}$ -filled  $(\text{EDO-TTF})_2\text{X}$  (X = PF<sub>6</sub> and AsF<sub>6</sub>), *Phys. Rev. B* 70 (2004) 075107.
- [208] S. Aoyagi, K. Kato, A. Ota, H. Yamochi, G. Saito, H. Suematsu, M. Sakata, M. Takata, Direct observation of bonding and charge ordering in  $(\text{EDO-TTF})_2\text{PF}_6$ , *Angew. Chem. Int. Ed.* 116 (2004) 3756.
- [209] K. Iwano, Y. Shimoi, Large electric-potential bias in an EDO-TTF tetramer as a major mechanism of charge ordering observed in its PF<sub>6</sub> salt: A density functional theory study, *Phys. Rev. B* 77 (2008) 075120.
- [210] K. Onda, S. Ogihara, K. Yonemitsu, N. Maeshima, T. Ishikawa, Y. Okimoto, X. Shao, Y. Nakano, H. Yamochi, G. Saito, S. Koshihara, Photoinduced change in the charge order pattern in the quarter-filled organic conductor  $(\text{EDOTTF})_2\text{PF}_6$  with a strong electron-phonon interaction, *Phys. Rev. Lett.* 101 (2008) 067403.
- [211] N. Fukazawa, M. Shimizu, T. Ishikawa, Y. Okimoto, S. Koshihara, T. Hiramatsu, Y. Nakano, H. Yamochi, G. Saito, K. Onda, Charge and structural dynamics in photoinduced phase transition of  $(\text{EDO-TTF})_2\text{PF}_6$  examined by picosecond time-resolved vibrational spectroscopy, *J. Phys. Chem. C* 116 (2012) 58925899.
- [212] K. Iwano, Y. Shimoi, Revealing the photorelaxation mechanism in a molecular solid using density-functional theory, *Phys. Rev. Lett.* 110 (2013) 116401.
- [213] K. Yonemitsu, K. Nasu, Theory of photoinduced phase transitions in itinerant electron systems, *Phys. Reports* 465 (2008) 1–60.
- [214] H. Taniguchi, M. Miyashita, K. Uchiyama, K. Satoh, N. Mori, H. Okamoto, K. Miyagawa, K. Kanoda, M. Hedo, Y. Uwatoko, Superconductivity at 14.2 K in layered organics under extreme pressure, *J. Phys. Soc. Jpn.* 72 (2003) 469–471.
- [215] K. Kanoda, R. Kato, Mott physics in organic conductors with triangular lattices, *Annu. Rev. Condens. Matter Phys.* 2 (2011) 167–188.

- [216] H. C. Kandpal, I. Opahle, Y.-Z. Zhang, H. O. Jeschke, R. Valentí, Revision of model parameters for  $\kappa$ -type charge-transfer solids: An *ab initio* study, *Phys. Rev. Lett.* 103 (2009) 067004.
- [217] K. Nakamura, Y. Yoshimoto, T. Kosugi, R. Arita, M. Imada, *Ab initio* derivation of low-energy model for  $\kappa$ -ET type organic conductors, *J. Phys. Soc. Jpn.* 78 (2009) 083710.
- [218] D. Guterding, M. Altmeyer, H. O. Jeschke, R. Valentí, Near-degeneracy of extended  $s+d_{x^2-y^2}$  and  $d_{xy}$  order parameters in quasi-two-dimensional organic superconductors, *Phys. Rev. B* 94 (2016) 024515.
- [219] A. Kobayashi, R. Kato, H. Kobayashi, S. Moriyama, Y. Nishio, K. Kajita, W. Sasaki, Crystal and electronic structures of a new molecular superconductor,  $\kappa$ -(BEDT-TTF)<sub>2</sub>I<sub>3</sub>, *Chem. Lett.* 16 (1987) 459–462.
- [220] T. Hiramatsu, Y. Yoshida, G. Saito, A. Otsuka, H. Yamochi, M. Maesato, Y. Shimizu, H. Ito, H. Kishida, Quantum spin liquid: design of a quantum spin liquid next to a superconducting state based on a dimer-type ET Mott insulator, *J. Mater. Chem. C* 2015 (2015) 1378.
- [221] T. Koretsune, C. Hotta, Evaluating model parameters of the  $\kappa$  and  $\beta'$ -type Mott insulating organic solids, *Phys. Rev. B* 89 (2014) 045102.
- [222] Y. Yoshida, H. Ito, M. Maesato, Y. Shimizu, H. Hayama, T. Hiramatsu, Y. Nakamura, H. Kishida, T. Koretsune, C. Hotta, G. Saito, Spin-disordered quantum phases in a quasi-one-dimensional triangular lattice, *Nat. Phys.* 11 (2015) 679–684.
- [223] K. Miyagawa, A. Kawamoto, K. Kanoda, Proximity of pseudogapped superconductor and commensurate antiferromagnet in a quasi-two-dimensional organic system, *Phys. Rev. Lett.* 89 (2002) 017003.
- [224] H. H. Wang, K. D. Carlson, U. Geiser, A. M. Kini, A. J. Schultz, J. M. Williams, L. K. Montgomery, W. K. Kwok, U. Welp, K. G. Vandervoort, S. J. Boryschuk, A. V. S. Crouch, J. M. Kommers, D. M. Watkins, New  $\kappa$ -phase materials,  $\kappa$ -(ET)<sub>2</sub>Cu[N(CN)<sub>2</sub>]X, X=Cl, Br, and I. The synthesis, structure and superconductivity above 11 K in the Cl ( $T_c=12.8$  K, 0.3 kbar) and Br ( $T_c=11.6$  K) salts, *Synth. Metals* 41–43 (1991) 1983–1990.
- [225] N. D. Kushch, M. A. Tanatar, E. B. Yagubskii, T. Ishiguro, Superconductivity of  $\kappa$ -(BEDT-TTF)<sub>2</sub>Cu[N(CN)<sub>2</sub>]I under pressure, *JETP Lett.* 73 (2001) 429.
- [226] H. Mori, I. Hirabayashi, S. Tanaka, T. Mori, H. Inokuchi, A new ambient-pressure organic superconductor,  $\kappa$ -(BEDT-TTF)<sub>2</sub>Ag(CN)<sub>2</sub>H<sub>2</sub>O ( $T_c=5.0$ K), *Solid St. Comm.* 76 (1990) 35–37.
- [227] T. Mori, H. Mori, S. Tanaka, Structural genealogy of BEDT-TTF-based organic conductors II. Inclined:  $\theta$ ,  $\alpha$ ,  $\kappa$  phases, *Bull. Chem. Soc. Jpn.* 72 (1999) 179–197.
- [228] T. Komatsu, T. Nakamura, N. Matsukawa, H. Yamochi, G. Saito, H. Ito, T. Ishiguro, M. Kusunoki, K. Sakaguchi, New ambient-pressure organic superconductors based on BEDT-TTF, Cu, N(CN)<sub>2</sub>, and CN with  $T_c=10.7$ K and 3.8K, *Solid St. Comm.* 80 (1991) 843.
- [229] S. Yasin, E. Rose, M. Dumm, N. Drichko, M. Dressel, J. A. Schlueter, E. I. Zhilyaeva, S. Torunova, R. N. Lyubovskaya, Electronic and magnetic studies of  $\kappa$ -(BEDT-TTF)<sub>2</sub>Hg(SCN)<sub>2</sub>Cl, *Physica B* 407 (2012) 1689.
- [230] N. Drichko, R. Beyer, E. Rose, M. Dressel, J. A. Schlueter, S. A. Turunova, E. I. Zhilyaeva, R. N. Lyubovskaya, Metallic state and charge-order metal-insulator transition in the quasi-two-dimensional conductor  $\kappa$ -(BEDT-TTF)<sub>2</sub>Hg(SCN)<sub>2</sub>Cl, *Phys. Rev. B* 89 (2014) 075133.
- [231] A. Löhle, E. Rose, S. Singh, R. Beyer, E. Tafra, E. I. Zhilyaeva, R. N. Lyubovskaya, M. Dressel, Pressure dependence of the metal-insulator transition in  $\kappa$ -(BEDT-TTF)<sub>2</sub>Hg(SCN)<sub>2</sub>Cl: optical and transport studies, *J. Phys.: Condens. Matter* 29 (2017) 055601.
- [232] Y. Shimizu, T. Hiramatsu, M. Maesato, A. Otsuka, H. Yamochi, A. Ono, M. Itoh, M. Yoshida, M. Takigawa, Y. Yoshida, G. Saito, Pressure-tuned exchange coupling of a quantum spin liquid in the molecular triangular lattice  $\kappa$ -(ET)<sub>2</sub>Ag<sub>2</sub>(CN)<sub>3</sub>, *Phys. Rev. Lett.* 117 (2016) 107203.
- [233] Y. Shimizu, M. Maesato, G. Saito, Uniaxial strain effects on Mott and superconducting transitions in  $\kappa$ -(ET)<sub>2</sub>Cu<sub>2</sub>(CN)<sub>3</sub>, *J. Phys. Soc. Jpn.* 80 (2011) 074702.
- [234] M. Fettouhi, L. Ouahab, C. Gomez-Garcia, L. Ducasse, P. Delhaes, Structural and physical properties of  $\kappa$ -(BEDT-TTF)<sub>2</sub>(CF<sub>3</sub>SO<sub>3</sub>), *Synth. Metals* 70 (1995) 1131–1132.
- [235] H. Ito, T. Asai, Y. Shimizu, H. Hayama, Y. Yoshida, G. Saito, Pressure-induced superconductivity in the antiferromagnet  $\kappa$ -(ET)<sub>2</sub>CF<sub>2</sub>(SO<sub>3</sub>), *Phys. Rev. B* 94 (2016) 020503.
- [236] K. Miyagawa, A. Kawamoto, Y. Nakazawa, K. Kanoda, Antiferromagnetic ordering and spin structure in the organic conductor,  $\kappa$ -(BEDT-TTF)<sub>2</sub>Cu[N(CN)<sub>2</sub>]Cl, *Phys. Rev. Lett.* 75 (1995) 1174–1177.
- [237] D. A. Huse, V. Elser, Simple variational wave functions for two-dimensional Heisenberg  $\frac{1}{2}$  antiferromagnets, *Phys. Rev. Lett.* 60 (24) (1988) 2531–2534.
- [238] S. J. Miyake, Spin-wave results for the staggered magnetization of triangular Heisenberg antiferromagnet, *J. Phys. Soc. Jpn.* 61 (1992) 983–988.
- [239] B. Bernu, C. Lhuillier, L. Pierre, Signature of Néel order in exact spectra of quantum antiferromagnets on finite lattices, *Phys. Rev. Lett.* 69 (1992) 2590.
- [240] N. Elstner, R. R. P. Singh, A. P. Young, Finite temperature properties of the spin- $\frac{1}{2}$  Heisenberg antiferromagnet on the triangular lattice, *Phys. Rev. Lett.* 71 (1993) 1629–1623.
- [241] L. Capriotti, A. E. Trumper, A. Sorella, Long-range Néel order in the triangular Heisenberg model, *Phys. Rev. Lett.* 82 (1999) 3899.
- [242] H. Ito, T. Ishiguro, M. Kobota, G. Saito, Metal-nonmetal transition and superconductivity localization in the two-dimensional conductor  $\kappa$ -(BEDT-TTF)<sub>2</sub>Cu[N(CN)<sub>2</sub>]Cl under pressure, *J. Phys. Soc. Jpn.* 65 (1996) 2987–2993.
- [243] U. Welp, S. Fleshler, W. Kwok, G. W. Crabtree, K. D. Carlson, H. H. Wang, U. Geiser, J. M. Williams, V. M. Hitsman, Weak ferromagnetism in  $\kappa$ -(ET)<sub>2</sub>Cu[N(CN)<sub>2</sub>]Cl, where (ET) is bis(ethylenedithio)tetrathiafulvalene, *Phys. Rev. Lett.* 69 (1992) 840–843.
- [244] J. M. Williams, A. M. Kini, H. H. Wang, K. D. Carlson, U. Geiser, L. K. Montgomery, G. J. Pyrka, D. M. Watkins, J. M. Kommers, From semiconductor-semiconductor transition (42 K) to the highest- $T_c$  organic superconductor,  $\kappa$ -(ET)<sub>2</sub>Cu[N(CN)<sub>2</sub>]Cl ( $T_c = 12.5$  K), *Inorg. Chem.* 29 (1990) 3272–3274.
- [245] H. Kobayashi, K. Bun, A. Miyamoto, T. Naito, R. Kato, A. Kobayashi, J. M. Williams, Superconducting transition of a grease-coated crystal of  $\kappa$ -(BEDT-TTF)<sub>2</sub>Cu[N(CN)<sub>2</sub>]Cl, *Chem. Lett.* 20 (1991) 1997–2000.
- [246] M. Dressel, G. Gruner, K. D. Carlson, H. H. Wang, Studies of the microwave resistivity of  $\kappa$ -(BEDT-TTF)<sub>2</sub>Cu[N(CN)<sub>2</sub>]Cl, *Synth. Metals* 70 (1995) 927–928.
- [247] Y. V. Sushko, H. Ito, T. Ishiguro, S. Horiuchi, G. Saito, Reentrant superconductivity in  $\kappa$ -(BEDT-TTF)<sub>2</sub>Cu[N(CN)<sub>2</sub>]Cl and its pressure phase diagram, *Solid St. Comm.* 87 (1993) 997–1000.

- [248] S. Lefebvre, P. Wzietek, S. Brown, C. Bourbonnais, D. Jérôme, C. Mèzière, M. Fourmigué, P. Batail, Mott transition, antiferromagnetism, and unconventional superconductivity in layered organic superconductors, *Phys. Rev. Lett.* 85 (2000) 5420–5423.
- [249] M. A. Tanatar, S. Kagoshima, T. Ishiguro, H. Ito, V. S. Yefanov, V. A. Bondarenko, N. D. Kushch, E. B. Yagubskii, Electronic transport properties and structural transformations of  $\kappa$ -(BEDT-TTF)<sub>2</sub>Cu[N(CN)<sub>2</sub>]I, *Phys. Rev. B* 62 (2000) 15561–15568.
- [250] M. A. Tanatar, T. Ishiguro, S. Kagoshima, N. D. Kushch, E. B. Yagubskii, Pressure-temperature phase diagram of the organic superconductor  $\kappa$ -(BEDT-TTF)<sub>2</sub>Cu[N(CN)<sub>2</sub>]I, *Phys. Rev. B* 65 (2002) 064516.
- [251] A. Kawamoto, K. Miyagawa, K. Kanoda, Deuterated  $\kappa$ -(BEDT-TTF)<sub>2</sub>Cu[N(CN)<sub>2</sub>]Br: a system on the border of the superconductor-magnetic-insulator transition, *Phys. Rev. B* 55 (1997) 14140–14143.
- [252] H. Taniguchi, A. Kawamoto, K. Kanoda, Superconductor-insulator phase transformation of partially deuterated  $\kappa$ -(BEDT-TTF)<sub>2</sub>Cu[N(CN)<sub>2</sub>]Br by control of the cooling rate, *Phys. Rev. B* 59 (1999) 8424–8427.
- [253] Y. Nakazawa, H. Taniguchi, A. Kawamoto, K. Kanoda, Electronic specific heat at the boundary region of the metal-insulator transition in the two-dimensional electronic system of  $\kappa$ -(BEDT-TTF)<sub>2</sub>Cu[N(CN)<sub>2</sub>]Br, *Phys. Rev. B* 61 (2000) R16295.
- [254] N. Yoneyama, T. Sasaki, N. Kobayashi, Substitution effect by deuterated donors on superconductivity in  $\kappa$ -(BEDT-TTF)<sub>2</sub>Cu[N(CM)<sub>2</sub>]Br, *J. Phys. Soc. Jpn.* 73 (2004) 1434–1437.
- [255] T. Sasaki, N. Yoneyama, A. Suzuki, N. Kobayashi, Y. Ikemoto, H. Kimura, Real space imaging of the metal-insulator phase separation in the band width controlled organic Mott system  $\kappa$ -(BEDT-TTF)<sub>2</sub>Cu[N(CN)<sub>2</sub>]Br, *J. Phys. Soc. Jpn.* 74 (2005) 2351–2360.
- [256] Y. Kurosaki, Y. Shimizu, K. Miyagawa, K. Kanoda, G. Saito, Mott transition from a spin liquid to a Fermi liquid in the spin-frustrated organic conductor  $\kappa$ -(ET)<sub>2</sub>Cu<sub>2</sub>(CN)<sub>3</sub>, *Phys. Rev. Lett.* 95 (2005) 177001.
- [257] D. Fournier, M. Poirier, K. D. Truong, Competition between magnetism and superconductivity in the organic metal  $\kappa$ -(BEDT-TTF)<sub>2</sub>Cu[N(CN)<sub>2</sub>]Br, *Phys. Rev. B* 76 (2007) 054509.
- [258] T. Sasaki, N. Yoneyama, A. Suzuki, N. Kobayashi, Y. Ikemoto, H. Kimura, Imaging phase separation near the Mott boundary of the correlated organic superconductors  $\kappa$ -(BEDT-TTF)<sub>2</sub>X, *Phys. Rev. Lett.* 92 (2004) 227001.
- [259] J. Gezo, T.-K. Lui, B. Wolin, C. P. Slichter, R. Giannetta, Stretched exponential spin relaxation in organic superconductors, *Phys. Rev. B* 88 (2013) 140504(R).
- [260] Y. Nakazawa, S. Yamashita, Thermodynamics of a liquid-like spin state in molecule-based magnets with geometric frustrations, *Chem. Lett.* 42 (2013) 1446–1454.
- [261] Y. Shimizu, Y. Kurosaki, K. Miyagawa, K. Kanoda, M. Maesato, G. Saito, NMR study of the spin-liquid state and Mott transition in the spin-frustrated organic system  $\kappa$ -(ET)<sub>2</sub>Cu<sub>2</sub>(CN)<sub>3</sub>, *Synth. Metals* 152 (2005) 393–396.
- [262] Y. Shimizu, K. Miyagawa, K. Kanoda, M. Maesato, G. Saito, Spin liquid state in an organic Mott insulator with a triangular lattice, *Phys. Rev. Lett.* 91 (2003) 107001.
- [263] U. Geiser, H. H. Wang, K. D. Carlson, J. M. Williams, H. A. Charlier, J. E. Heindl, G. A. Yaconi, B. J. Love, M. W. Lathrop, Superconductivity at 2.8 K and 1.5 kbar in  $\kappa$ -(BEDT-TTF)<sub>2</sub>Cu<sub>2</sub>(CN)<sub>3</sub>: the first organic superconductor containing a polymeric copper cyanide anion, *Inorg. Chem.* 30 (1991) 2586–2588.
- [264] T. Komatsu, N. Matsukawa, T. Inoue, G. Saito, Realization of superconductivity at ambient pressure by band-filling control in  $\kappa$ -(BEDT-TTF)<sub>2</sub>Cu<sub>2</sub>(CN)<sub>3</sub>, *J. Phys. Soc. Jpn.* 65 (1996) 1340–1354.
- [265] K. Miyagawa, K. Kanoda, A. Kawamoto, NMR studies on two-dimensional molecular conductors and superconductors: Mott transition in  $\kappa$ -(BEDT-TTF)<sub>2</sub>X, *Chem. Rev.* 104 (2004) 5635–5654.
- [266] A. Kawamoto, Y. Honma, K. Kumagai, Electron localization in the strongly correlated organic system  $\kappa$ -(BEDT-TTF)<sub>2</sub>X probed with nuclear magnetic resonance <sup>13</sup>C-NMR, *Phys. Rev. B* 70 (2004) 060510R.
- [267] Y. Shimizu, K. Miyagawa, K. Kanoda, M. Maesato, G. Saito, Emergence of inhomogeneous moments from spin liquid in the triangular-lattice Mott insulator  $\kappa$ -(ET)<sub>2</sub>Cu<sub>2</sub>(CN)<sub>3</sub>, *Phys. Rev. B* 73 (2006) 140407.
- [268] A. Kawamoto, Y. Honma, K. Kumagai, N. Matsunaga, K. Nomura, Suppression of inhomogeneous electron localization in  $\kappa$ -(BEDT-TTF)<sub>2</sub>Cu<sub>2</sub>(CN)<sub>3</sub> under pressure, *Phys. Rev. B* 74 (2006) 212508.
- [269] S. Ohira, Y. Shimizu, K. Kanoda, G. Saito, Spin liquid state in  $\kappa$ -(BEDT-TTF)<sub>2</sub>Cu<sub>2</sub>(CN)<sub>3</sub> studied by muon spin relaxation method, *J. Low Temp. Phys.* 142 (2006) 153.
- [270] F. L. Pratt, P. J. Baker, S. J. Blundell, T. Lancaster, S. Ohira-Kawamura, C. Baines, Y. Shimizu, K. Kanoda, I. Watanabe, G. Saito, Magnetic and non-magnetic phases of a quantum spin liquid, *Nature* 471 (2011) 612.
- [271] S. Nakajima, T. Suzuki, K. Ohishi, I. Watanabe, T. Goto, A. Oosawa, N. Yoneyama, N. Kobayashi, F. L. Pratt, T. Sasaki, Microscopic phase separation in triangular-lattice quantum spin magnet  $\kappa$ -(BEDT-TTF)<sub>2</sub>Cu<sub>2</sub>(CN)<sub>3</sub> probed by muon spin relaxation, *J. Phys. Soc. Jpn.* 81 (2012) 063706.
- [272] S. Yamashita, Y. Nakazawa, M. Oguni, Y. Oshima, H. Nohji, Y. Shimizu, K. Miyagawa, K. Kanoda, Thermodynamic properties of a spin-1/2 spin-liquid state in a  $\kappa$ -type organic salt, *Nature Phys.* 4 (2008) 459–462.
- [273] M. Yamashita, N. Nakata, Y. Kasahara, T. Sasaki, N. Yoneyama, N. Kobayashi, S. Fujimoto, T. Shibauchi, Y. Matsuda, Thermal-transport measurements in a quantum spin-liquid state of the frustrated triangular magnet  $\kappa$ -(BEDT-TTF)<sub>2</sub>Cu<sub>2</sub>(CN)<sub>3</sub>, *Nature Phys.* 5 (2009) 44–47.
- [274] A. Kawamoto, K. Miyagawa, Y. Nakazawa, K. Kanoda, Electron correlation in the  $\kappa$ -phase family of BEDT-TTF compounds studied by <sup>13</sup>C NMR where BEDT-TTF is bis(ethylenedithio)tetrafulvalene, *Phys. Rev. B* 52 (1995) 15522.
- [275] V. Kataev, G. Winkel, D. Khomskii, S. Wohlleben, W. Crump, K. F. Tebbe, J. Hahn, ESR of single crystals of  $\kappa$ -(BEDT-TTF)<sub>2</sub>Cu[N(CN)<sub>2</sub>]X (X=Br and I), *Solid St. Comm.* 83 (1992) 435–439.
- [276] T. Kobayashi, Y. Ihara, Y. Saito, A. Kawamoto, Microscopic observation of superconducting fluctuations in  $\kappa$ -(BEDT-TTF)<sub>2</sub>Cu[N(CN)<sub>2</sub>]Br by <sup>13</sup>C NMR spectroscopy, *Phys. Rev. B* 89 (2014) 165141.
- [277] S. Gärtner, E. Gogu, I. Heinen, H. J. Keller, T. Klutz, D. Schweitzer, Superconductivity at 10 K and ambient pressure in the organic metal (BEDT-TTF)<sub>2</sub>Cu(SCN)<sub>2</sub>, *Solid St. Comm.* 65 (1988) 1531–1534.
- [278] Y. V. Sushko, V. A. Bondarenko, R. A. Petrosov, N. D. Kushch, E. Yagubskii, Hydrostatic pressure effect on T<sub>c</sub> and resistance anomaly in normal state of  $\kappa$ -(BEDT-TTF)<sub>2</sub>CuN(CN)<sub>2</sub>Br, *J. de Physique I* 1 (1991) 1375–1379.
- [279] J. Müller, M. Lang, F. Steglich, J. A. Schlueter, A. M. Kini, T. Sasaki, Evidence for structural and electronic instabilities at intermediate

- temperatures in  $\kappa$ -(BEDT-TTF)<sub>2</sub>X for X = Cu[N(CN)<sub>2</sub>]Cl, Cu[N(CN)<sub>2</sub>]Br and Cu(NCS)<sub>2</sub>: Implications for the phase diagram of these quasi-two-dimensional organic superconductors, Phys. Rev. B 65 (2002) 144521.
- [280] A. Kawamoto, K. Miyagawa, Y. Nakazawa, K. Kanoda, <sup>13</sup>C NMR study of layered organic superconductors based on BEDT-TTF molecules, Phys. Rev. Lett. 74 (1995) 3455.
- [281] Y. Shimizu, H. Kasahara, T. Furuta, K. Miyagawa, K. Kanoda, M. Maesato, G. Saito, Pressure-induced superconductivity and Mott transition in spin-liquid  $\kappa$ -(ET)<sub>2</sub>Cu<sub>2</sub>(CN)<sub>3</sub> probed by <sup>13</sup>C NMR, Phys. Rev. B 81 (22) (2010) 224508.
- [282] Y. Wang, L. Li, N. P. Ong, Nernst effect in high-T<sub>c</sub> superconductors, Phys. Rev. B 73 (2006) 024510.
- [283] L. Li, Y. Wang, S. Komiya, Y. A. Abd G. D. Gu, N. P. Ong, Diamagnetism and Cooper pairing above T<sub>c</sub> in cuprates, Phys. Rev. B 81 (2010) 054510.
- [284] O. Cyr-Choiniere, R. Daou, F. Laliberté, D. LeBoeuf, N. Doiron-Leyraud, J. Chang, J.-Q. Yan, J.-G. Cheng, J.-S. Zhou, J. B. Goodenough, S. Pyon, T. Takayama, H. Takagi, Y. Tanaka, L. Taillefer, Enhancement of the Nernst effect by stripe order in a high-T<sub>c</sub> superconductor, Nature 458 (2009) 743–745.
- [285] M.-S. Nam, A. Ardavan, S. J. Blundell, J. A. Schlueter, Fluctuating superconductivity in organic molecular metals close to the Mott transition, Nature 449 (2007) 584–587.
- [286] M.-S. Nam, C. Mézière, P. Batail, L. Zorina, S. Simonov, A. Ardavan, Superconducting fluctuations in organic molecular metals enhanced by Mott criticality, Scientific Reports 3 (2013) 3390.
- [287] S. Tsuchiya, J. Yamada, S. Tanda, K. Ichimura, T. Terashima, N. Kurita, K. Kodama, S. Uji, Fluctuating superconductivity in the strongly correlated two-dimensional organic superconductor  $\kappa$ -(BEDT-TTF)<sub>2</sub>Cu(NCS)<sub>2</sub> in an in-plane magnetic field, Phys. Rev. B 85 (2012) 220506(R).
- [288] S. M. D. Soto, C. P. Slichter, A. M. Kini, H. H. Wang, U. Geiser, J. M. Williams, <sup>13</sup>C NMR studies of the normal and superconducting states of the organic superconductor  $\kappa$ -(BEDT-TTF)<sub>2</sub>Cu[N(CN)<sub>2</sub>]Br, Phys. Rev. B 52 (1995) 10364.
- [289] O. J. Taylor, A. Carrington, J. A. Schlueter, Specific-heat measurements of the gap structure of the organic superconductors  $\kappa$ -(ET)<sub>2</sub>Cu[N(CN)<sub>2</sub>]Br and  $\kappa$ -(ET)<sub>2</sub>Cu(NCS)<sub>2</sub>, Phys. Rev. Lett. 99 (2007) 057001.
- [290] M. Pinterić, S. Tomić, M. Prester, D. Drobac, K. Maki, Influence of internal disorder on the superconducting state in the organic layered superconductor  $\kappa$ -(BEDT-TTF)<sub>2</sub>Cu[N(CN)<sub>2</sub>]Br, Phys. Rev. B 66 (2002) 174521.
- [291] S. Milbradt, A. A. Bardin, C. J. S. Truncik, W. A. Huttema, A. C. Jacko, P. L. Burn, S.-C. Lo, B. J. Powell, D. M. Broun, In-plane superfluid density and microwave conductivity of the organic superconductor  $\kappa$ -(BEDT-TTF)<sub>2</sub>Cu[N(CN)<sub>2</sub>]Br: Evidence for d-wave pairing and resilient quasiparticles, Phys. Rev. B 88 (2013) 064501.
- [292] N. V. Perunov, A. F. Shevchun, N. D. Kushch, M. R. Trunin, Surface impedance of  $\kappa$ -(BEDT-TTF)<sub>2</sub>Cu[N(CN)<sub>2</sub>]Br crystals, JETP Letters 96 (2012) 184.
- [293] T. Arai, K. Ichimura, K. Nomura, S. Takasaki, J. Yamada, S. Nakatsuji, H. Anzai, Tunneling spectroscopy on the organic superconductor  $\kappa$ -(BEDT-TTF)<sub>2</sub>Cu(NCS)<sub>2</sub> using STM, Phys. Rev. B 63 (2001) 104518.
- [294] K. Ichimura, M. Takami, K. Nomura, Direct observation of d-wave superconducting gap in  $\kappa$ -(BEDT-TTF)<sub>2</sub>Cu[N(CN)<sub>2</sub>]Br with scanning tunneling microscopy, Journal of the Physical Society of Japan 77 (11) (2008) 114707.
- [295] Y. Oka, H. Nobukane, N. Matsunaga, K. Nomura, K. Katono, K. Ichimura, A. Kawamoto, Tunneling spectroscopy in organic superconductor  $\kappa$ -(BEDT-TTF-d[3,3])<sub>2</sub>Cu[N(CN)<sub>2</sub>]Br, J. Phys. Soc. Jpn. 84 (2015) 064713.
- [296] J. M. Schrama, E. Rzepniewski, R. S. Edwards, J. Singleton, A. Ardavan, M. Kurmoo, P. Day, Millimeter-wave magneto-optical determination of the anisotropy of the superconducting order parameter in the molecular superconductor  $\kappa$ -(BEDT-TTF)<sub>2</sub>Cu(NCS)<sub>2</sub>, Phys. Rev. Lett. 83 (1999) 3041–3044.
- [297] L. Malone, O. J. Taylor, J. A. Schlueter, A. Carrington, Location of gap nodes in the organic superconductors  $\kappa$ -(ET)<sub>2</sub>Cu(NCS)<sub>2</sub> and  $\kappa$ -(ET)<sub>2</sub>Cu[N(CN)<sub>2</sub>]Br determined by magnetocalorimetry, Phys. Rev. B 82 (2010) 014522.
- [298] K. Izawa, H. Yamaguchi, T. Sasaki, Y. Matsuda, Superconducting gap structure of  $\kappa$ -(BEDT-TTF)<sub>2</sub>Cu(NCS)<sub>2</sub> probed by thermal conductivity tensor, Phys. Rev. Lett. 88 (2001) 027002.
- [299] D. Guterding, S. Diehl, M. Altmeyer, T. Methfessel, U. Tutsch, H. Schubert, M. Lang, J. Müller, M. Huth, H. O. Jeschke, R. Valentí, M. Jourdan, H.-J. Elmers, Evidence for eight-node mixed-symmetry superconductivity in a correlated organic metal, Phys. Rev. Lett. 116 (2016) 237001.
- [300] S. Kühlmorgen, R. Schönemann, E. L. Greene, J. Müller, J. Wosnitza, Investigation of the superconducting gap structure in  $\kappa$ -(BEDT-TTF)<sub>2</sub>Cu(NCS)<sub>2</sub> and  $\kappa$ -(BEDT-TTF)<sub>2</sub>Cu[N(CN)<sub>2</sub>]Br by means of thermal-conductivity measurements, J. Phys.: Condens. Matter 29 (2017) 405604.
- [301] H. Elsinger, J. Wosnitza, S. Wanka, J. Hagel, D. Schweitzer, W. Strunz,  $\kappa$ -(BEDT-TTF)<sub>2</sub>Cu[N(CN)<sub>2</sub>]Br: A fully gapped strong-coupling superconductor, Phys. Rev. Lett. 84 (2000) 6098–6101.
- [302] J. Müller, M. Lang, R. Helfrich, F. Steglich, T. Sasaki, High-resolution ac-calorimetry studies of the quasi-two-dimensional organic superconductor  $\kappa$ -(BEDT-TTF)<sub>2</sub>Cu(NCS)<sub>2</sub>, Phys. Rev. B 65 (2002) 140509.
- [303] D. Fournier, M. Poirier, M. Castonguay, K. D. Truong, Mott transition, compressibility divergence, and the P-T phase diagram of layered organic superconductors: an ultrasonic investigation, Phys. Rev. Lett. 90 (2003) 127002.
- [304] M. de Souza, L. Bartosch, Probing the Mott physics in  $\kappa$ -(BEDT-TTF)<sub>2</sub>X salts via thermal expansion, J. Phys.: Condens. Matter 27 (2015) 053203.
- [305] R. S. Manna, M. de Souza, A. Bruhl, J. A. Schlueter, M. Lang, Lattice effects and entropy release at the low-temperature phase transition in the spin-liquid candidate  $\kappa$ -(BEDT-TTF)<sub>2</sub>Cu<sub>2</sub>(CN)<sub>3</sub>, Phys. Rev. Lett. 104 (2010) 016403.
- [306] M. Abdel-Jawad, I. Terasaki, T. Sasaki, N. Yoneyama, N. Kobayashi, Y. Uesu, C. Hotta, Anomalous dielectric response in the dimer Mott insulator  $\kappa$ -(BEDT-TTF)<sub>2</sub>Cu<sub>2</sub>(CN)<sub>3</sub>, Phys. Rev. B 82 (2010) 125119.
- [307] M. Pinterić, M. Čulo, M. Basletić, B. Korin-Hamzić, E. Tafra, A. Hamzić, T. Ivek, T. Peterseim, K. Miyagawa, K. Kanoda, J. A. Schlueter, M. Dressel, S. Tomić, Anisotropic charge dynamics in the quantum spin-liquid candidate  $\kappa$ -(BEDT-TTF)<sub>2</sub>Cu<sub>2</sub>(CN)<sub>3</sub>, Phys. Rev. B 90 (2014) 195139.
- [308] P. Lunkenheimer, J. Müller, S. Krohns, F. Schrettle, A. Loidl, B. Hartmann, R. Rommel, M. de Souza, C. Hotta, J. Schlueter, M. Lang,

- Multiferroicity in an organic charge-transfer salt: Electric-dipole-driven magnetism, *Nat. Mater.* 11 (2012) 755–758.
- [309] M. Lang, P. Lunkenheimer, J. Müller, A. Loidl, B. Hartmann, N. H. Hoang, E. Gati, H. Schubert, J. A. Schlueter, Multiferroicity in the Mott insulating charge-transfer salt  $\kappa$ -(BEDT-TTF)<sub>2</sub>Cu[N(CN)<sub>2</sub>]Cl, *IEEE Trans. Magnetics* 50 (2014) 2700107.
- [310] P. Lunkenheimer, A. Loidl, Dielectric spectroscopy on organic charge-transfer salts, *J. Phys.: Condens. Matter* 27 (2015) 373001 (21 pages).
- [311] M. Poirier, S. Parent, A. Cote, K. Miyagawa, K. Kanoda, Y. Shimizu, Magnetodielectric effects and spin-charge coupling in the spin-liquid candidate  $\kappa$ -(BEDT-TTF)<sub>2</sub>Cu<sub>2</sub>(CN)<sub>3</sub>, *Phys. Rev. B* 85 (2012) 134444.
- [312] K. Sedlmeier, S. Elsässer, D. Neubauer, R. Beyer, D. Wu, T. Ivek, S. Tomic, J. A. Schlueter, M. Dressel, Absence of charge order in the dimerized  $\kappa$ -phase BEDT-TTF salts, *Phys. Rev. B* 86 (2012) 245103.
- [313] K. Yakushi, K. Yamamoto, T. Yamamoto, Y. Saito, A. Kawamoto, Raman spectroscopy study of charge fluctuation in the spin-liquid  $\kappa$ -(BEDT-TTF)<sub>2</sub>Cu<sub>2</sub>(CN)<sub>3</sub>, *J. Phys. Soc. Jpn.* 84 (2015) 084711.
- [314] K. Itoh, H. Itoh, M. Naka, S. Saito, I. Hosako, N. Yoneyama, S. Ishihara, T. Sasaki, S. Iwai, Collective excitation of and electric dipole on a molecular dimer in an organic dimer-Mott insulator, *Phys. Rev. Lett.* 110 (2013) 106401.
- [315] T. Ivek, B. Korin-Hamzić, O. Milat, S. Tomic, C. Clauss, N. Drichko, D. Schweitzer, M. Dressel, Collective excitations in the charge-ordered phase of  $\alpha$ -(BEDT-TTF)<sub>2</sub>I<sub>3</sub>, *Phys. Rev. Lett.* 104 (2010) 206406.
- [316] T. Ivek, B. Korin-Hamzić, O. Milat, S. Tomic, C. Clauss, N. Drichko, D. Schweitzer, M. Dressel, Electrodynamic response of the charge ordering phase: Dielectric and optical studies of  $\alpha$ -(BEDT-TTF)<sub>2</sub>I<sub>3</sub>, *Phys. Rev. B* 83 (2011) 165128.
- [317] S. Tomicić, M. Pinterić, T. Ivek, K. Sedlmeier, R. Beyer, D. Wu, J. A. Schlueter, D. Schweitzer, M. Dressel, Magnetic ordering and charge dynamics in  $\kappa$ -(BEDT-TTF)<sub>2</sub>Cu[N(CN)<sub>2</sub>]Cl, *J. Phys.: Condens. Matter* 25 (2013) 436004 (7 pages).
- [318] O. Drozdova, G. Saito, H. Yamochi, K. Ookubo, K. Yakushi, M. Uruichi, L. Ouahab, Composition and structure of the anion layer in the organic superconductor  $\kappa'$ -(ET)<sub>2</sub>Cu<sub>2</sub>(CN)<sub>3</sub>: optical study, *Inorg. Chem.* 40 (2001) 3265–3266.
- [319] M. Pinterić, P. Lazić, A. Pustogow, T. Ivek, M. Kuveždić, O. Milat, B. Gumhalter, M. Basletić, M. Čulo, B. Korin-Hamzić, A. Löhle, R. Hübner, M. Sanz Alonso, T. Hiramatsu, Y. Yoshida, G. Saito, M. Dressel, S. Tomic, Anion effects on electronic structure and electrodynamic properties of the Mott insulator  $\kappa$ -(BEDT-TTF)<sub>2</sub>Ag<sub>2</sub>(CN)<sub>3</sub>, *Phys. Rev. B* 94 (2016) 161105.
- [320] S. Iguchi, S. Sasaki, N. Yoneyama, H. Taniguchi, T. Nishizaki, T. Sasaki, Relaxor ferroelectricity induced by electron correlations in a molecular dimer Mott insulator, *Phys. Rev. B* 87 (2013) 075107.
- [321] S. Niizeki, F. Yoshikane, K. Kohno, K. Takahashi, H. Mori, Y. Bando, T. Kawamoto, T. Mori, Dielectric response and electric-field-induced metastable state in an organic conductor  $\beta$ -(*meso*-DMBEDT-TTF)<sub>2</sub>PF<sub>6</sub>, *J. Phys. Soc. Jpn.* 77 (2008) 073710.
- [322] M. Z. Aldoshina, R. N. Lyubovskaya, S. V. Konovalikhin, O. A. Dyachenko, G. V. Shilov, M. K. Makova, R. B. Lyubovskii, A new series of ET-based organic metals: synthesis, crystal structure and properties, *Synth. Metals* 55–57 (1993) 1905–1909.
- [323] E. I. Yudanova, S. K. Hoffmann, A. Graja, S. V. Konovalikhin, O. A. Dyachenko, R. B. Lyubovskii, R. N. Lyubovskaya, Crystal structure, ESR and conductivity studies of bis(ethylenedithio)tetrafulvalene (ET) organic conductor (H<sub>8</sub>ET)<sub>2</sub>[Hg(SCN)<sub>2</sub>Br] and its deuterated analogue (D<sub>8</sub>ET)<sub>2</sub>[Hg(SCN)<sub>2</sub>Br], *Synth. Metals* 73 (1995) 227.
- [324] E. I. Yudanova, L. M. Makarova, S. V. Konovalikhin, O. A. Dyachenko, R. B. Lyubovskii, R. N. Lyubovskaya, The new salt  $\kappa$ -ET<sub>2</sub>[Hg(SCN)<sub>2</sub>]: crystal structure and physical properties, *Synth. Metals* 79 (1996) 201.
- [325] A. Ota, L. Ouahab, S. Golhen, Y. Yoshida, M. Maesato, G. Saito, R. Swietlik, Phase transition from Mott insulating phase into the charge ordering phase with molecular deformation in charge-transfer salts  $\kappa$ -(ET)<sub>4</sub>[M(CN)<sub>6</sub>][N(C<sub>2</sub>H<sub>5</sub>)<sub>4</sub>]·2H<sub>2</sub>O (M = Co<sup>III</sup> and Fe<sup>III</sup>), *Chemistry of Materials* 19 (2007) 2455–2462.
- [326] A. Lapinski, R. Swietlik, L. Ouahab, S. Golhen, Spectroscopic studies of the phase transition from the Mott insulator state to the charge-ordering state of  $\kappa$ -(ET)<sub>4</sub>[M(CN)<sub>6</sub>][N(C<sub>2</sub>H<sub>5</sub>)<sub>4</sub>]·2H<sub>2</sub>O (M = Co<sup>III</sup> and Fe<sup>III</sup>) salts, *J. Phys. Chem. A* 117 (2013) 5241–5250.
- [327] P. L. Maguerès, L. Ouahab, N. Corian, C. J. Gomez-Garcia, P. Delhaes, Phase transitions in new BEDT-TTF  $\kappa$ -phase salts with hexacyanometalate anions [M(CN)<sub>6</sub>]<sup>3-</sup> M=Co<sup>III</sup> and Fe<sup>III</sup>, *Solid St. Comm.* 97 (1996) 27–32.
- [328] P. L. Maguerès, L. Ouahab, P. Briard, J. Even, M. Bertault, L. Touper, J. Ramos, C. J. Gomez-Garcia, P. Delhaes, T. Mallah, Phase transitions  $[\kappa$ -(ET)<sub>4</sub>N]ET<sub>4</sub>M(CN)<sub>6</sub>·3H<sub>2</sub>O; M=Fe<sup>III</sup>, Co<sup>III</sup>, Cr<sup>III</sup>, *Synth. Metals* 86 (1997) 1859–1860.
- [329] R. Swietlik, M. Polomska, L. Ouahab, J. Guillevic, Infrared and Raman studies of  $\kappa$ -phase charge-transfer salts formed by BEDT-TTF and magnetic anions M(CN)<sub>6</sub><sup>3-</sup> (where M=Co<sup>III</sup>, Fe<sup>III</sup>, Cr<sup>III</sup>), *J. Mater. Chem.* 11 (2001) 1313–1318.
- [330] R. Swietlik, A. Lapinski, M. Polomska, L. Ouahab, J. Guillevic, Spectroscopic evidence of the charge ordering in  $\kappa$ -[Et<sub>4</sub>N](BEDT-TTF)<sub>4</sub>M(CN)<sub>6</sub>·3H<sub>2</sub>O (M = Co<sup>III</sup>, Fe<sup>III</sup>, Cr<sup>III</sup>), *Synth. Metals* 133 (2003) 273–275.
- [331] R. Swietlik, L. Ouahab, J. Guillevic, K. Yakushi, Infrared and Raman studies of the charge ordering in the organic semiconductor  $\kappa$ -[Et<sub>4</sub>N][Co(CN)<sub>6</sub>(ET)<sub>4</sub>]·3H<sub>2</sub>O, *Macromol. Symp.* 212 (2004) 219–224.
- [332] R. Swietlik, A. Lapinski, M. Polomska, L. Ouahab, A. Ota, Infrared and Raman investigations of the charge ordering phenomena in the monoclinic salts  $\kappa$ -(ET)<sub>4</sub>[M(CN)<sub>6</sub>][N(C<sub>2</sub>H<sub>5</sub>)<sub>4</sub>]·2H<sub>2</sub>O (M = Co<sup>III</sup> and Fe<sup>III</sup>), *J. Low Temp. Phys.* 142 (2006) 653–656.
- [333] E. B. Yagubskii, I. F. Shchegolev, V. N. Laukhin, P. A. Konovich, M. V. Karatsovnik, A. V. Zvarykina, L. I. Buravov, Normal-pressure superconductivity in an organic metal (BEDT-TTF)<sub>2</sub>I<sub>3</sub> [bis (ethylene dithiolo) tetrathiofulvalene triiodide], *JETP Lett.* 39 (1984) 12–15.
- [334] K. Murata, M. Tokumoto, H. Anzai, H. Bando, G. Saito, K. Kajimura, T. Ishiguro, Superconductivity with the onset at 8 K in the organic conductor  $\beta$ -(BEDT-TTF)<sub>2</sub>I<sub>3</sub> under pressure, *J. Phys. Soc. Jpn.* 54 (1985) 1236.
- [335] J. M. Williams, H. H. Wang, M. A. Beno, T. J. Emge, L. M. Sowa, P. T. Copps, F. Behroozi, L. N. Hall, K. D. Carlson, G. W. Crabtree, Ambient-pressure superconductivity at 2.7 K and higher temperatures in derivatives of (BEDT-TTF)<sub>2</sub>IBr<sub>2</sub>: synthesis, structure, and detection of superconductivity, *Inorg. Chem.* 23 (1983) 3839–3841.
- [336] T. J. Emge, H. H. Wang, M. A. Beno, P. C. W. Leung, M. A. Firestone, H. C. Jenkins, J. D. Cook, J. M. Williams, E. L. Venturini, A test of superconductivity vs. molecular disorder in (BEDT-TTF)<sub>2</sub>X synthetic metals: synthesis, structure (298, 120 K), and microwave/ESR conductivity of (BEDT-TTF)<sub>2</sub>2I<sub>2</sub>Br, *Inorg. Chem.* 24 (1985) 1736–1738.
- [337] H. H. Wang, M. A. Beno, U. Geiser, M. A. Firestone, K. S. Webb, L. Nunez, G. W. Crabtree, K. D. Carlson, J. M. Williams, Ambient-pressure superconductivity at the highest temperature (5 K) observed in an organic system:  $\beta$ -(BEDT-TTF)<sub>2</sub>Au<sub>2</sub>, *Inorg. Chem.* 24 (1985) 2465–2466.
- [338] J. Yamada, M. Watanabe, H. Akutsu, S. Nakatsuji, H. Nishikawa, I. Ikemoto, K. Kikuchi, New organic superconductors  $\beta$ -(BDA-TTF)<sub>2</sub>X

- [BDA-TTP = 2,5-Bis(1,3-dithian-2-ylidene)-1,3,4,6-tetrathiapentalene;  $X^- = \text{SbF}_6^-$ ,  $\text{AsF}_6^-$ , and  $\text{PF}_6^-$ ], J. Am. Chem. Soc. 123 (2001) 4174–4180.
- [339] J. Yamada, T. Toita, H. Akutsu, S. Nakatsuji, H. Nishikawa, I. Ikemoto, K. Kikuchi, The crystal structure and physical properties of  $\beta$ -(BDA-TTP)<sub>2</sub>FeCl<sub>4</sub> [BDA-TTP = 2,5-bis(1,3-dithian-2-ylidene)-1,3,4,6-tetrathiapentalene], Chem. Commun. 2001 (2001) 2538–2539.
- [340] E. S. Choi, D. Graf, J. S. Brooks, J. Yamada, H. Akutsu, K. Kikuchi, M. Tokumoto, Pressure-dependent ground states and fermiology in  $\beta$ -(BDA-TTP)<sub>2</sub>MCl<sub>4</sub> ( $M = \text{Fe, Ga}$ ), Phys. Rev. B 70 (2004) 024517.
- [341] J. Yamada, T. Toita, H. Akutsu, S. Nakatsuji, H. Nishikawa, I. Ikemoto, K. Kikuchi, E. S. Choi, D. Graf, J. S. Brooks, A new organic superconductor,  $\beta$ -(BDA-TTP)<sub>2</sub>GaCl<sub>4</sub> [BDA-TTP = 2,5-(1,3-dithian-2-ylidene)-1,3,4,6-tetrathiapentalene], Chem. Commun. 2003 (2003) 2230–2231.
- [342] J. Yamada, K. Fujimoto, H. Akutsu, S. Nakatsuji, A. Miyazaki, M. Aimatsu, S. Kudo, T. Enoki, K. Kikuchi, Pressure effect on the electrical conductivity and superconductivity of  $\beta$ -(BDA-TTP)<sub>2</sub>I<sub>3</sub>, Chem. Commun. 2006 (2006) 1331–1333.
- [343] S. Kimura, T. Maejima, H. Suzuki, R. Chiba, H. Mori, T. Kawamoto, T. Mori, H. Moriyama, Y. Nishio, K. Kajita, A new organic superconductor  $\beta$ -(*meso*-DMBEDT-TTF)<sub>2</sub>PF<sub>6</sub>, Chem. Commun. 2004 (2004) 2454.
- [344] N. Morinaka, K. Takahashi, R. Chiba, F. Yoshikane, S. Niizeki, M. Tanaka, K. Yakushi, M. Koeda, M. Hedo, T. Fujiwara, Y. Uwatoko, Y. Nishio, K. Kajita, H. Mori, Superconductivity competitive with checkerboard-type charge ordering in the organic conductor  $\beta$ -(*meso*-DMBEDT-TTF)<sub>2</sub>PF<sub>6</sub>, Phys. Rev. B 80 (2009) 092508.
- [345] T. Shikama, T. Shimokawa, S. Lee, T. Isono, A. Ueda, K. Takahashi, A. Nakao, R. Kumai, H. Nakao, K. Kobayashi, Y. Murakami, M. Kimata, H. Tajima, K. Matsubayashi, Y. Uwatoko, Y. Nishio, K. Kajita, H. Mori, Magnetism and pressure-induced superconductivity of checkerboard-type charge-ordered molecular conductor  $\beta$ -(*meso*-DMBEDT-TTF)<sub>2</sub>X ( $X = \text{PF}_6$  and  $\text{AsF}_6$ ), Crystals 2 (2012) 1502–1513.
- [346] H. Anzai, M. Tokumoto, T. Ishiguro, G. Saito, H. Kobayashi, R. Kato, A. Kobayashi, Crystal growth of BEDT-TTF trihalides, Synth. Metals 19 (1987) 611–616.
- [347] T. Mori, H. Inokuchi, Crystal structures of AuCl<sub>2</sub> salts of bis(ethylenedithio)-tetrathiafulvalene BEDT-TTF. Existence of divalent gold, Au(II), Solid St. Comm. 62 (1987) 525–529.
- [348] H. Taniguchi, M. Miyashita, K. Uchiyama, R. Sato, Y. Ishi, K. Satoh, N. Mori, M. Hedo, Y. Uwatoko, High-pressure study up to 9.9 GPa of organic Mott insulator,  $\beta'$ -(BEDT-TTF)<sub>2</sub>AuCl<sub>2</sub>, J. Phys. Soc. Jpn. 74 (2005) 1370–1373.
- [349] B. H. Ward, J. A. Schlueter, U. Geiser, H. Wang, E. Morales, J. P. Parakka, S. Thomas, J. Williams, P. Nixon, R. W. Winter, G. L. Gard, H. J. Koo, M. H. Whangbo, Comparison of the crystal and electronic structures of three 2:1 salts of the organic donor molecule BEDT-TTF with pentafluorothiometylsulfonate anions SF<sub>5</sub>CH<sub>2</sub>SO<sub>3</sub><sup>-</sup>, SF<sub>5</sub>CHF<sub>2</sub>SO<sub>3</sub><sup>-</sup>, and SF<sub>5</sub>CF<sub>2</sub>SO<sub>3</sub><sup>-</sup>, Chem. Mater. 2000 (2000) 343–351.
- [350] A. Graja, I. Olejniczak, B. Barszcz, J. A. Schlueter, Vibrational spectra of two BEDT-TTF-based organic conductors: charge order, Cent. Eur. J. Phys. 7 (2009) 663–667.
- [351] T. Mori, F. Sakai, G. Saito, H. Inokuchi, Crystal and band structures of an organic conductor  $\beta''$ -(BEDT-TTF)<sub>2</sub>AuBr<sub>2</sub>, Chem. Lett. 15 (1986) 1037–1040.
- [352] R. Kondo, M. Higa, S. Kagoshima, N. Hanasaki, Y. Nogami, H. Nishikawa, Interplay of charge-density waves and superconductivity in the organic conductor  $\beta''$ -(BEDT-TTF)<sub>2</sub>AuBr<sub>2</sub>, Phys. Rev. B 81 (2010) 024519.
- [353] U. Geiser, J. A. Schlueter, H. H. Wang, A. M. Kini, J. M. Williams, P. P. Sche, H. I. Zakowicz, M. L. VanZile, J. D. Dudek, P. G. Nixon, R. W. Winter, G. L. Gard, J. Ren, M. H. Whangbo, Superconductivity at 5.2 K in an electron donor radical salt of bis(ethylenedithio)tetrathiafulvalene (BEDT-TTF) with the novel polyfluorinated organic anion SF<sub>5</sub>CH<sub>2</sub>CF<sub>2</sub>SO<sub>3</sub><sup>-</sup>, J. Am. Chem. Soc. 118 (1996) 9996–9997.
- [354] J. A. Schlueter, B. H. Ward, U. Geiser, H. H. Wang, A. M. Kini, J. Parakka, E. Morales, H.-J. Koo, M.-H. Whangbo, R. W. Winter, J. Mohtasham, G. L. Gard, Crystal structure, physical properties and electronic structure of a new organic conductor (BEDT-TTF)<sub>2</sub>SF<sub>5</sub>CHF<sub>2</sub>SO<sub>3</sub>, J. Chem. Mater. 11 (2001) 2008–2013.
- [355] J. A. Schlueter, B. H. Ward, U. Geiser, A. M. Kini, H. H. Wang, A. N. Hata, J. Mohtasham, R. W. Winter, G. L. Gard, Chemical modification of the superconducting  $\beta''$ -(ET)<sub>2</sub>SF<sub>5</sub>CH<sub>2</sub>CF<sub>2</sub>SO<sub>3</sub> structure through use of CF<sub>3</sub>CR<sub>2</sub>SO<sub>3</sub><sup>-</sup> anions, Mol. Cryst. Liq. Cryst. 380 (2002) 129.
- [356] I. Olejniczak, B. Barszcz, A. Szutarska, A. Graja, R. Wojciechowski, J. A. Schlueter, A. N. Hata, B. H. Ward, and Raman spectra of  $\beta''$ -(BEDT-TTF)<sub>2</sub>RCH<sub>2</sub>SO<sub>3</sub> ( $R = \text{SF}_5, \text{CF}_3$ ): dimerization related to hydrogen bonding, Phys. Chem. Chem. Phys. 11 (2009) 3910–3920.
- [357] H. Nishikawa, T. Morimoto, T. Kodama, I. Ikemoto, K. Kikuchi, J. Yamada, H. Yoshino, K. Murata, New organic superconductors consisting of an unprecedented  $\pi$ -electron donor, J. Am. Chem. Soc. 124 (5) (2002) 730.
- [358] H. Nishikawa, Y. Sato, K. Kikuchi, T. Kodama, I. Ikemoto, J. Yamada, H. Oshio, R. Kondo, S. Kagoshima, Charge ordering and pressure-induced superconductivity in  $\beta''$ -(DODHT)<sub>2</sub>PF<sub>6</sub>, Phys. Rev. B 72 (2005) 052510.
- [359] H. Akutsu, A. Akutsu-Sato, S. S. Turner, D. L. Pevelen, P. Day, A.-K. Klehe, J. Singleton, D. A. Tocher, M. R. Probert, J. A. K. Howard, Effect of included guest molecules on the normal state conductivity and superconductivity of  $\beta''$ -(ET)<sub>4</sub>[(H<sub>3</sub>O)Ga(C<sub>2</sub>O<sub>4</sub>)<sub>3</sub>]-G (G=Pyridine, Nitrobenzene), J. Am. Chem. Soc. 124 (2002) 12430–12431.
- [360] H. Mori, I. Hirabayashi, S. Tanaka, T. Mori, Y. Maruyama, H. Inokuchi, Superconductivity in (BEDT-TTF)<sub>4</sub>Pt(CN)<sub>4</sub>H<sub>2</sub>O, Solid St. Comm. 80 (1991) 411–415.
- [361] T. Mori, K. Karo, Y. Maruyama, H. Inokuchi, H. Mori, I. Hirabayashi, S. Tanaka, Structural and physical properties of a new organic superconductor, (BEDT-TTF)<sub>4</sub>Pd(CN)<sub>4</sub>H<sub>2</sub>O, Solid St. Comm. 82 (1992) 177.
- [362] T. Mori, M. Inokuchi, Superconductivity in (BEDT-TTF)<sub>3</sub>Cl<sub>2</sub>H<sub>2</sub>O, Solid St. Comm. 64 (1987) 335–337.
- [363] W. Lubczynski, S. V. Demishev, J. Singleton, J. M. Caulfield, L. d. C. de Jongh, C. J. Kepert, S. J. Blundell, W. Hayes, M. Kurmoo, P. Day, A study of the magnetoresistance of the charge-transfer salt (BEDT-TTF)<sub>3</sub>Cl<sub>2</sub>·2H<sub>2</sub>O at hydrostatic pressures of up to 20 kbar: evidence for a charge-density-wave ground state and the observation of pressure-induced superconductivity, J. Phys.: Condens. Matter 8 (1996) 6005.
- [364] T. Mori, Structural genealogy of BEDT-TTF-based organic conductors I. Parallel molecules:  $\beta$  and  $\beta''$  phases, Bull. Chem. Soc. Jpn. 71 (1998) 2509–2526.
- [365] H. Mori, Materials viewpoint of organic superconductors, J. Phys. Soc. Jpn. 75 (2006) 051003.
- [366] A. Ugawa, K. Yakushi, H. Kuroda, A. Kawamoto, J. Tanaka, Crystal structure and reflectance spectrum of  $\beta''$ -(BEDT-TTF)<sub>2</sub>IAuBr, Chem. Lett. 15 (1986) 1875–1878.

- [367] A. J. Schulz, T. J. Emge, P. C. W. Leung, M. A. Beno, H. H. Wang, J. M. Williams, A neutron diffraction study of the extent of disorder in the low temperature (20 K) structure of  $\beta$ -(BEDT-TTF)<sub>2</sub>I<sub>2</sub>Br, *Physica B+C* 143 (1986) 351–353.
- [368] S. Ravy, R. Moret, J. P. Pouget, R. Comes, S. S. P. Parkin, Competition between organic superconductivity and a displacive structural modulation in bis(ethylenedithio) tetrathiafulvalene perchlorate, (BEDT-TTF)<sub>2</sub>ReO<sub>4</sub>, *Phys. Rev. B* 33 (1986) 2049.
- [369] K. Carneiro, J. C. Scott, E. M. Engler, Comparative ESR study of three (BEDT-TTF):ReO<sub>4</sub> salts: an organic superconductor, a Peierls metal and a semiconductor, *Solid St. Comm.* 50 (1984) 477–481.
- [370] S. M. Baker, J. Dong, G. Li, Z. Zhu, J. L. Musfeldt, J. A. Schlueter, M. E. Kelly, R. G. Daugherty, J. M. Williams, Infrared studies of low-temperature symmetry breaking in the perchlorate family of ET-based organic molecular conductors, *Phys. Rev. B* 60 (1999) 931.
- [371] S. Kimura, H. Suzuki, T. Maejima, H. Mori, J. Yamaura, T. Kakiuchi, H. Sawa, H. Moriyama, Checkerboard-type charge-ordered state of a pressure-induced superconductor,  $\beta$ -(meso-DMBEDT-TTF)<sub>2</sub>PF<sub>6</sub>, *J. Am. Chem. Soc.* 128 (2006) 1456.
- [372] J. Yamada, New approach to achievement of organic superconductivity, *J. Mater. Chem.* 14 (2004) 2951–2953.
- [373] J. Yamada, H. Akutsu, H. Nishikawa, K. Kikuchi, New trends in the synthesis of  $\pi$ -electron donors for molecular conductors and superconductors, *Chem. Rev.* 104 (2004) 5057–5083.
- [374] T. Tokumoto, J. S. Brooks, Y. Oshima, E. S. Choi, L. C. Brunel, H. Akutsu, T. Kaihatsu, J. Yamada, J. can Tol, Antiferromagnetic *d*-electron exchange via a spin-singlet  $\pi$ -electron ground state in an organic conductor, *Phys. Rev. Lett.* 100 (2008) 147602.
- [375] K. Sasamori, K. Takahashi, T. Kodama, W. Fujita, K. Kikuchi, J. Yamada, Structural variations in  $\beta$ -(BDA-TTP)<sub>2</sub>FeCl<sub>4</sub> at low temperature and under pressure: charge-ordered state with a two-fold crystal structure, *J. Phys. Soc. Jpn.* 82 (2013) 054705.
- [376] M. Tanaka, K. Yamamoto, M. Uruichi, T. Yamamoto, K. Yakushi, S. Kimura, H. Mori, Infrared and Raman study of the charge-ordered state in the vicinity of the superconducting state in the organic conductor  $\beta$ -(meso-DMBEDT-TTF)<sub>2</sub>PF<sub>6</sub>, *J. Phys. Soc. Jpn.* 77 (2008) 024714.
- [377] R. Okazaki, Y. Ikemoto, T. Moriwaki, T. Shikama, K. Takahashi, H. Mori, H. Nakaya, T. Sasaki, Y. Yasui, I. Terasaki, Optical conductivity measurement of a dimer Mott-insulator to charge-order phase transition in a two-dimensional quarter-filled organic salt compound, *Phys. Rev. Lett.* 111 (2013) 217801.
- [378] M. Tokumoto, H. Anzai, T. Ishiguro, G. Saito, H. Kobayashi, R. Kato, A. Kobayashi, Electrical and magnetic properties of organic semiconductors, (BEDT-TTF)<sub>2</sub>X (X=IBr<sub>2</sub>, IBrCl, and ICl<sub>2</sub>), *Synth. Metals* 19 (1987) 215–220.
- [379] Y. Eto, A. Kawamoto, Antiferromagnetic phase in  $\beta'$ -(BEDT-TTF)<sub>2</sub>ICl<sub>2</sub> under pressure as seen via <sup>13</sup>C NMR, *Phys. Rev. B* 81 (2010) 020512(R).
- [380] K. Satoh, H. Taniguchi, A. Kawamoto, W. Higemoto,  $\mu$ SR study of an antiferromagnetic Mott insulator  $\beta'$ -(BEDT-TTF)<sub>2</sub>ICl<sub>2</sub>, *Physica B* 374–375 (2006) 99–101.
- [381] K. Satoh, K. Sato, T. Yoshida, H. Taniguchi, T. Goko, T. U. Ito, K. Ohishi, W. Higemoto,  $\mu$ SR study of organic antiferromagnet  $\beta'$ -(BEDT-TTF)<sub>2</sub>ICl<sub>2</sub> under high pressure, *Physica B* 404 (2009) 600–602.
- [382] K. Hashimoto, R. Kobayashi, H. Okamura, H. Taniguchi, Y. Ikemoto, T. Moriwaki, S. Iguchi, M. Naka, S. Ishihara, T. Sasaki, Emergence of charge degrees of freedom under high pressure in the organic dimer-Mott insulator  $\beta'$ -(BEDT-TTF)<sub>2</sub>ICl<sub>2</sub>, *Phys. Rev. B* 92 (2015) 085149.
- [383] Y. Hattori, S. Iguchi, T. Sasaki, S. Iwai, H. Taniguchi, H. Kishida, Electric-field-induced intradimer charge disproportionation in the dimer-Mott insulator  $\beta'$ -(BEDT-TTF)<sub>2</sub>ICl<sub>2</sub>, *Phys. Rev. B* 95 (2017) 085149.
- [384] M. Kurmoo, D. R. Talham, P. Day, I. D. Parker, R. H. Friend, A. M. Stringer, J. Howard, Structure and properties of a new conducting organic charge-transfer salt  $\beta$ -(BEDT-TTF)<sub>2</sub>AuBr<sub>2</sub>, *Solid St. Comm.* 61 (1987) 459–464.
- [385] A. Ugawa, D. B. Tanner, K. Yakushi, Far-infrared reflectance of  $\beta'$ -(BEDT-TTF)<sub>2</sub>AuBr<sub>2</sub>: co-existence of free carriers and a single-particle gap at  $2\Delta=130\text{cm}^{-1}$ , *Synth. Metals* 70 (1995) 979–980.
- [386] A. Girlando, M. Masino, J. A. Schlueter, N. Drichko, S. Kaiser, M. Dressel, Charge-order fluctuations and superconductivity in two-dimensional organic metals, *Phys. Rev. B* 89 (2014) 174503.
- [387] U. Geiser, J. A. Schlueter, A. M. Kini, H. H. Wang, B. H. Ward, M. A. Whited, J. Mohtasham, G. L. Gard, BEDT-TTF salts with fluorinated sulfonate anions, *Synth. Metals* 133–134 (2003) 401–403.
- [388] S. Kaiser, M. Dressel, Y. Sun, A. Greco, J. A. Schlueter, G. L. Gard, N. Drichko, Bandwidth tuning triggers interplay of charge order and superconductivity in two-dimensional organic materials, *Phys. Rev. Lett.* 105 (2010) 206402.
- [389] R. Kubo, A stochastic theory of line shape, in: K. E. Shuler (Ed.), *Stochastic processes in chemical physics*, Vol. 15 of *Advances in Chemical Physics*, Wiley, New York, 1969, pp. 101–128.
- [390] A. Girlando, M. Masino, S. Kaiser, Y. Sun, N. Drichko, M. Dressel, H. Mori, Spectroscopic characterization of charge order fluctuations in BEDT-TTF metals and superconductors, *Phys. Status Solidi B* 249 (2012) 953–956.
- [391] H. Nishikawa, A. Machida, T. Morimoto, K. Kikuchi, T. Kodama, I. Ikemoto, J. Yamada, H. Yoshino, K. Murata, A new organic superconductor, (DODHT)<sub>2</sub>BF<sub>4</sub>·H<sub>2</sub>O, *Chem. Commun.* 2003 (2003) 494–495.
- [392] H. Nishikawa, Y. Sato, T. Kodama, K. Kikuchi, I. Ikemoto, J. Yamada, H. Oshio, R. Kondo, S. Kagoshima, Charge ordered insulating state in DODHT salts, *J. Low Temp. Phys.* 142 (2006) 633–636.
- [393] H. Nishikawa, H. Oshio, M. Higa, R. Kondo, S. Kagoshima, A. Nakao, H. Sawa, S. Yasuzuka, K. Murata, Charge ordered insulating phases of DODHT salts with octahedral anions and a new radical salt,  $\beta''$ -(DODHT)<sub>2</sub>TaF<sub>6</sub>, *Journal of Physics: Conf. Series* 132 (2008) –12–23.
- [394] M. Higa, R. Kondo, S. Kagoshima, H. Nishikawa, Structural studies of pressure-induced organic superconductor  $\beta''$ -(DODHT)<sub>2</sub>PF<sub>6</sub> having charge-ordered phase at ambient pressure, *J. Phys. Soc. Jpn.* 76 (2007) 034709.
- [395] A. F. Bangura, A. I. Coldea, J. Singleton, A. Ardavan, A. Akutsu-Sato, H. Akutsu, S. S. Turner, P. Day, T. Yamamoto, K. Yakushi, Robust superconducting state in the low-quasiparticle-density organic metals  $\beta''$ -(BEDT-TTF)<sub>4</sub>[(H<sub>3</sub>O)M(C<sub>2</sub>O<sub>4</sub>)<sub>3</sub>]-Y : Superconductivity due to proximity to a charge-ordered state, *Phys. Rev. B* 72 (2005) 014543.
- [396] A. I. Coldea, A. F. Bangura, J. Singleton, A. Ardavan, A. Akutsu-Sato, H. Akutsu, S. S. Turner, P. Day, Fermi-surface topology and the effects of intrinsic disorder in a class of charge-transfer salts containing magnetic ion:  $\beta''$ -(BEDT-TTF)<sub>4</sub>[(H<sub>3</sub>O)M(C<sub>2</sub>O<sub>4</sub>)<sub>3</sub>]Y ( $M=\text{Ga, Cr, Fe; } Y=\text{C}_5\text{H}_5\text{N}$ ), *Phys. Rev. B* 69 (2004) 085112.
- [397] M. Kurmoo, A. W. Graham, P. Day, S. J. Coles, M. B. Hursthouse, J. L. Caulfield, J. Singleton, F. L. Pratt, W. Hayes, Superconducting and semiconducting magnetic charge transfer salts: (BEDT-TTF)<sub>4</sub>AFe(C<sub>2</sub>O<sub>4</sub>)<sub>3</sub>-C<sub>6</sub>H<sub>5</sub>CN ( $A = \text{H}_2\text{O, K, NH}_4$ ), *J. Am. Chem. Soc.* 117 (1995) 12209–12217.

- [398] S. Rashid, S. S. Turner, P. Day, J. A. K. Howard, P. Guionneau, E. J. L. McInnes, F. E. Mabbs, J. H. Clark, S. Firth, T. Biggs, New superconducting charge-transfer salts (BEDT-TTF)<sub>4</sub>[A·M(C<sub>2</sub>O<sub>4</sub>)<sub>3</sub>]<sub>3</sub>·C<sub>6</sub>H<sub>5</sub>NO<sub>2</sub> (A=H<sub>3</sub>O or NH<sub>4</sub>, M=Cr or Fe, BEDT-TTF=bis(ethylenedithio)tetrathiafulvalene), *J. Mater. Chem.* 2001 (2001) 2095–2101.
- [399] T. Yamamoto, H. M. Yamamoto, R. Kato, M. Uruichi, K. Yakushi, H. Akutsu, A. Sato-Akutsu, A. Kawamoto, S. S. Turner, P. Day, Inhomogeneous site charges at the boundary between insulating, superconducting, and metallic phases of β''-type bis-ethylenedithio-tetrathiafulvalene molecular charge-transfer salts, *Phys. Rev. B* 77 (2008) 205120.
- [400] T. Mori, H. Inokuchi, Structural and electrical properties of (BEDT-TTF)<sub>3</sub>Cl<sub>2</sub>(H<sub>2</sub>O)<sub>2</sub>, *Chem. Lett.* 16 (1987) 1657.
- [401] J. Gaultier, S. Hébrard-Bracchetti, P. Guionneau, C. J. Kepert, D. Chasseau, L. Ducasse, Y. Barrans, M. Kurmoo, P. Day, Structural properties of the superconducting salt (BEDT-TTF)<sub>3</sub>Cl<sub>3</sub>·(H<sub>2</sub>O)<sub>2</sub> at low temperatures, *J. Solid State Chem.* 145 (1999) 496–502.
- [402] S. Nagata, T. Ogura, A. Kawamoto, H. Taniguchi, <sup>13</sup>C-NMR studies of the paramagnetic and charge-ordered states of the organic superconductor β''-(BEDT-TTF)<sub>3</sub>Cl<sub>2</sub>·2H<sub>2</sub>O under pressure, *Phys. Rev. B* 84 (2011) 035105.
- [403] H. Kobayashi, R. Kato, A. Kobayashi, Y. Nishio, K. Kajita, W. Sasaki, A new molecular superconductor, (BEDT-TTF)<sub>2</sub>(I<sub>3</sub>)<sub>1-x</sub>(AuI<sub>2</sub>)<sub>x</sub> (x < 0.02), *Chem. Lett.* 15 (5) (1986) 789–792.
- [404] M. Tamura, K. Yakushi, H. Kuroda, A. Kobayashi, R. Kato, H. Kobayashi, Temperature dependence of the polarized reflectance spectra of the θ-type of bis(ethylenedithio)tetrathiafulvalenium triiodide θ-(BEDT-TTF)<sub>2</sub>I<sub>3</sub>: estimation of band parameters, *J. Phys. Soc. Jpn.* 57 (1988) 3239–3247.
- [405] K. Takenaka, M. Tamura, N. Tajima, H. Takagi, Collapse of coherent quasiparticle states in θ-(BEDT-TTF)<sub>2</sub>I<sub>3</sub> observed by optical spectroscopy, *Phys. Rev. Lett.* 95 (2005) 227801.
- [406] H. Mori, I. Hirabayashi, S. Tanaka, T. Mori, Y. Maruyama, Crystal structures and electrical resistivities of three-component organic conductors: (BEDT-TTF)<sub>2</sub>MM'(SCN)<sub>4</sub> [M = K, Rb, Cs; M' = Co, Zn, Cd], *Bull. Chem. Soc. Jpn.* 68 (1995) 1136.
- [407] H. Mori, S. Tanaka, T. Mori, A. Fuse, Crystal structure and physical properties of α-(BEDT-TTF)<sub>2</sub> MM'(SCN)<sub>4</sub> [M=Rb, Cs, M'=Co, Zn], *Synth. Metals* 86 (1997) 1789.
- [408] H. Mori, S. Tanaka, T. Mori, Systematic study of the electronic state in θ-type BEDT-TTF organic conductors by changing the electronic correlation, *Phys. Rev. B* 57 (1998) 12023–12029.
- [409] M. Watanabe, Y. Noda, Y. Nogami, H. Mori, Structural phase transition of θ-(BEDT-TTF)<sub>2</sub>RbZn(SCN)<sub>4</sub> under high pressure, *J. Phys. Soc. Jpn.* 73 (2004) 921–925.
- [410] K. Miyagawa, A. Kawamoto, K. Kanoda, Charge ordering in a quasi-two-dimensional organic conductor, *Phys. Rev. B* 62 (2000) R7679–R7682.
- [411] M. Watanabe, Y. Noda, Y. Nogami, H. Mori, Transfer integrals and the spatial pattern of charge ordering in θ-(BEDT-TTF)<sub>2</sub>RbZn(SCN)<sub>4</sub> at 90 K, *J. Phys. Soc. Jpn.* 73 (2004) 116–122.
- [412] R. Chiba, H. M. Yamamoto, K. Hiraki, T. Nakamura, Charge ordering in θ-(BEDT-TTF)<sub>2</sub>RbZn(SCN)<sub>4</sub>, *Synth. Metals* 120 (2001) 919–920.
- [413] R. Chiba, H. Yamamoto, K. Hiraki, T. Takahashi, Charge disproportionation in (BEDT-TTF)<sub>2</sub>RbZn(SCN)<sub>4</sub>, *J. Phys. Chem. Solids* 62 (2001) 389–391.
- [414] K. Yamamoto, K. Yakushi, K. Miyagawa, K. Kanoda, A. Kawamoto, Charge ordering in θ-(BEDT-TTF)<sub>2</sub>RbZn(SCN)<sub>4</sub> studied by vibrational spectroscopy, *Phys. Rev. B* 65 (2002) 085110.
- [415] M. Watanabe, Y. Noda, Y. Nogami, H. Mori, S. Tanaka, Structural phase transition in θ-(BEDT-TTF)<sub>2</sub>RbM'(SCN)<sub>4</sub> (M'=Zn,Co), *Synth. Metals* 133–134 (2003) 283–285.
- [416] F. Nad, P. Monceau, H. M. Yamamoto, Dielectric response in the charge-ordered θ-(BEDT-TTF)<sub>2</sub>RbZn(SCN)<sub>4</sub> organic compound, *J. Phys.: Condens. Matter* 18 (2006) L509–L514.
- [417] R. Chiba, K. Hiraki, T. Takahashi, H. M. Yamamoto, T. Nakamura, Extremely slow charge fluctuations in the metallic state of the two-dimensional molecular conductor θ-(BEDT-TTF)<sub>2</sub>RbZn(SCN)<sub>4</sub>, *Phys. Rev. Lett.* 93 (2004) 216405.
- [418] M. Watanabe, Y. Noda, Y. Nogami, H. Mori, Investigation of X-ray diffuse scattering in θ-(BEDT-TTF)<sub>2</sub>RbM'(SCN)<sub>4</sub>, *Synth. Metals* 135–136 (2003) 665–666.
- [419] M. Watanabe, Y. Noda, Y. Nogami, H. Mori, Spin-Peierls transition in the charge-ordered organic conductor θ-BEDT-TTF<sub>2</sub>RbZn(SCN)<sub>4</sub>, *J. Phys. Soc. Jpn.* 76 (2007) 124602.
- [420] F. Nad, P. Monceau, H. M. Yamamoto, A possible glass-like state in θ-(BEDT-TTF)<sub>2</sub>CsZn(SCN)<sub>4</sub> at low temperature, *J. Phys.: Condens. Matter* 20 (2008) 485211.
- [421] Y. Nogami, J. P. Pouget, M. Watanabe, K. Oshima, Structural modulation in θ-(BEDT-TTF)<sub>2</sub>CsM'(SCN)<sub>4</sub> [M' = Co, Zn], *Synth. Metals* 103 (1999) 1911.
- [422] Y. Nishio, Y. Nihei, M. Tamura, K. Kajita, T. Nakamura, T. Takahashi, Specific heat and metal-insulator transition of (BEDT-TTF)<sub>2</sub>MZn(SCN)<sub>4</sub>, *Synth. Metals* 103 (1999) 1907–1908.
- [423] T. Nakamura, W. Minagawa, R. Kinami, T. Takahashi, Possible charge disproportionation and new type charge localization in θ-(BEDT-TTF)<sub>2</sub>CsZn(SCN)<sub>4</sub>, *J. Phys. Soc. Jpn.* 69 (2000) 504–509.
- [424] R. Chiba, K. Hiraki, T. Takahashi, H. M. Yamamoto, T. Nakamura, Charge ordering in θ-(BEDT-TTF)<sub>2</sub>MZn(SCN)<sub>4</sub> [M=Rb, Cs], *Synth. Metals* 133–134 (2003) 305–306.
- [425] R. Chiba, K. Hiraki, T. Takahashi, H. M. Yamamoto, T. Nakamura, Charge disproportionation and dynamics in θ-(BEDT-TTF)<sub>2</sub>CsZn(SCN)<sub>4</sub>, *Phys. Rev. B* 77 (2008) 115113.
- [426] K. Suzuki, K. Yamamoto, K. Yakushi, A. Kawamoto, Infrared and Raman studies of θ-(BEDT-TTF)<sub>2</sub>CsZn(SCN)<sub>4</sub>: comparison with the frozen state of θ-(BEDT-TTF)<sub>2</sub>RbZn(SCN)<sub>4</sub>, *J. Phys. Soc. Jpn.* 74 (2005) 2631–2639.
- [427] K. Yamamoto, K. Yakushi, Y. Shimizu, G. Saito, Infrared and Raman study of the charge-ordered state of θ-(ET)<sub>2</sub>Cu<sub>2</sub>CN[N(CN)<sub>2</sub>]<sub>2</sub>, *J. Phys. Soc. Jpn.* 73 (2004) 2326–2332.
- [428] T. Kakiuchi, Y. Wakabayashi, H. Sawa, T. Takahashi, T. Nakamura, Charge ordering in α-(BEDT-TTF)<sub>2</sub>I<sub>3</sub> by synchrotron X-ray diffraction, *J. Phys. Soc. Jpn.* 76 (2007) 113702.
- [429] R. Wojciechowski, K. Yamamoto, K. Yakushi, M. Inokuchi, A. Kawamoto, High-pressure Raman study of the charge ordering in α-(BEDT-TTF)<sub>2</sub>I<sub>3</sub>, *Phys. Rev. B* 67 (2003) 224105.

- [430] V. F. Kaminskii, T. G. Prokhorova, R. P. Shibaeva, E. B. Yagubskii, Crystal structure of the organic superconductor (BEDT-TTF)<sub>2</sub>I<sub>3</sub>, JETP Lett. 39 (1983) 17–20.
- [431] B. Rothaemel, L. Forró, J. Cooper, J. Schilling, M. Weger, P. Bele, H. Brunner, D. Schweitzer, H. Keller, Magnetic susceptibility of  $\alpha$  and  $\beta$  phases of di[bis(ethylenedithiolo)tetrathiafulvalene] tri-iodide [(BEDT-TTF)<sub>2</sub>I<sub>3</sub>] under pressure, Phys. Rev. B 34 (2) (1986) 704–712.
- [432] N. Tajima, A. Ebina-Tajima, M. Tamura, Y. Nishio, K. Kajita, Effects of uniaxial strain on transport properties of organic conductor  $\alpha$ -(BEDT-TTF)<sub>2</sub>I<sub>3</sub> and discovery of superconductivity, J. Phys. Soc. Jpn. 71 (2002) 1832–1835.
- [433] J. Moldenhauer, C. Horn, K. I. Pokodnia, D. Schweitzer, I. Heinen, H. J. Keller, FT-IR absorption spectroscopy of BEDT-TTF radical salts: charge transfer and donor-anion interaction, Synth. Metals 60 (1993) 31–38.
- [434] C.-P. Heidmann, A. Barnsteiner, F. Groß-Alltag, B. S. Chandrasekhar, E. Hess, Anisotropic thermal expansion of the organic conductor  $\alpha$ -(BEDT-TTF)<sub>2</sub>I<sub>3</sub>: new aspects of the metal-insulator transition, Solid St. Comm. 84 (1992) 711–716.
- [435] Y. Takano, K. Hiraki, H. M. Yamamoto, T. Nakamura, T. Takahashi, Charge disproportionation in the organic conductor,  $\alpha$ -(BEDT-TTF)<sub>2</sub>I<sub>3</sub>, J. Phys. Chem. Solids 62 (2001) 393.
- [436] T. Kawai, A. Kawamoto, <sup>13</sup>C-NMR study of charge ordering state in the organic conductor,  $\alpha$ -(BEDT-TTF)<sub>2</sub>I<sub>3</sub>, J. Phys. Soc. Jpn. 78 (2009) 074711.
- [437] P. Lunkenheimer, B. Hartmann, M. Lang, J. Müller, D. Schweitzer, S. Krohns, A. Loidl, Ferroelectric properties of charge-ordered  $\alpha$ -(BEDT-TTF)<sub>2</sub>I<sub>3</sub>, Phys. Rev. B 91 (2015) 245132.
- [438] M. Hirata, K. Ishikawa, K. Miyagawa, M. Tamura, C. Berthier, D. Basko, A. Kobayashi, G. Matsuno, K. Kanoda, Observation of an anisotropic Dirac cone reshaping and ferrimagnetic spin polarization in an organic conductor, Nature Commun. 7 (2015) 12666.
- [439] T. Mishima, T. Ojio, Y. Nishio, Y. Iye, Temperature independent conductivity of  $\alpha$ -(BEDT-TTF)<sub>2</sub>I<sub>3</sub> -compensation of the change in the carrier density and the mobility-, Synth. Metals 70 (1995) 771–774.
- [440] N. Tajima, M. Tamura, Y. Nishio, K. Kajita, Y. Iye, Transport property of an organic conductor  $\alpha$ -(BEDT-TTF)<sub>2</sub>I<sub>3</sub> under high pressure –Discovery of a novel type of conductor–, J. Phys. Soc. Jpn. 69 (2000) 543–551.
- [441] S. Katayama, A. Kobayashi, Y. Suzumura, Pressure-induced zero-gap semiconducting state in organic conductor  $\alpha$ -(BEDT-TTF)<sub>2</sub>I<sub>3</sub> salt, J. Phys. Soc. Jpn. 75 (2006) 054705.
- [442] A. Kobayashi, S. Katayama, Y. Suzumura, H. Fukuyama, Massless Fermions in organic conductor, J. Phys. Soc. Jpn. 76 (2007) 034711.
- [443] K. Kajita, Y. Nishio, N. Tajima, Y. Suzumura, A. Kobayashi, Molecular Dirac Fermion systems – theoretical and experimental approaches –, J. Phys. Soc. Jpn. 83 (2014) 072002.
- [444] D. Andres, M. V. Kartsovnik, W. Biberacher, K. Neumaier, E. Schuberth, H. Müller, Superconductivity in the charge-density-wave state of the organic metal  $\alpha$ -(BEDT-TTF)<sub>2</sub>KHg(SCN)<sub>4</sub>, Phys. Rev. B 72 (2005) 174513.
- [445] M. Maesato, Y. Kaga, R. Kondo, S. Kagoshima, Control of electronic properties of  $\alpha$ -(BEDT-TTF)<sub>2</sub>MHg(SCN)<sub>4</sub> (M=K, NH<sub>4</sub>) by the uniaxial strain method, Phys. Rev. B 64 (2001) 155104.
- [446] K. Noda, Y. Ihara, A. Kawamoto, Charge disproportionation with lattice distortion of  $\alpha$ -(BEDT-TTF)<sub>2</sub>RbHg(SCN)<sub>4</sub> observed by <sup>13</sup>C-NMR, Phys. Rev. B 87 (2013) 085105.
- [447] T. Kawai, A. Kawamoto, Charge disproportionation and inversion symmetry breaking in organic conductor  $\alpha$ -(BEDT-TTF)<sub>2</sub>RbHg(SCN)<sub>4</sub>, Phys. Rev. B 78 (2008) 165119.
- [448] M. Oshima, H. Mori, G. Saito, K. Oshima, Crystal structures and electrical properties of BEDT-TTF salts of mercury(II) and thiocyanate with and without K ion, Chem. Lett. 18 (1989) 1159–1162.
- [449] H. Mori, S. Tanaka, M. Oshima, G. Saito, T. Mori, Y. Maruyama, H. Inokuchi, Crystal and electronic structures of (BEDT-TTF)<sub>2</sub>[MHg(SCN)<sub>4</sub>] (M=K and NH<sub>4</sub>), Bull. Chem. Soc. Jpn. 63 (1990) 2183–2190.
- [450] H. Mori, S. Tanaka, K. Oshima, M. Oshima, G. Saito, T. Mori, Y. Maruyama, H. Inokuchi, Electrical properties and crystal structures of mercury(II) and thiocyanate salts based upon BEDT-TTF with Li<sup>+</sup>, K<sup>+</sup>, NH<sub>4</sub><sup>+</sup>, Rb<sup>+</sup>, and Cs<sup>+</sup>, Solid St. Comm. 74 (1990) 1261–1264.
- [451] H. H. Wang, K. D. Carlson, U. Geiser, W. K. Kwok, M. D. Vashon, J. E. Thompson, N. F. Larsen, G. D. McCabe, R. S. Hulscher, J. M. Williams, A new ambient-pressure organic superconductor: (BEDT-TTF)<sub>2</sub>(NH<sub>4</sub>)Hg(SCN)<sub>4</sub>, Physica C 166 (1990) 57–61.
- [452] N. D. Kushch, L. I. Buravov, M. V. Kartsovnik, V. N. Laukhin, S. I. Pesotskii, R. P. Shibaeva, L. P. Rozenberg, E. B. Yagubskii, A. V. Zvarikina, Resistance and magnetoresistance anomaly in a new stable organic metal (ET)<sub>2</sub>TlHg(SCN)<sub>4</sub>, Synth. Metals 46 (1992) 271–276.
- [453] T. Sasaki, N. Toyota, M. Tokumoto, N. Kinoshita, H. Anzai, Transport properties of organic conductor (BEDT-TTF)<sub>2</sub>KHg(SCN)<sub>4</sub>: I. Resistance and magnetoresistance anomaly, Solid St. Comm. 75 (1990) 93–96.
- [454] H. Ito, M. V. Kartsovnik, H. Ishimoto, K. Kono, H. Mori, N. D. Kushch, G. Saito, T. Ishiguro, S. Tanaka, Superconductivity in  $\alpha$ -(BEDT-TTF)<sub>2</sub>MHg(SCN)<sub>4</sub> (M=K, Rb, Tl, NH<sub>4</sub>), Synth. Metals 70 (1995) 899–902.
- [455] H. Ito, H. Kaneko, T. Ishiguro, H. Ishimoto, K. Kono, S. Horiuchi, T. Komatsu, G. Saito, On superconductivity of the organic conductor  $\alpha$ -(BEDT-TTF)<sub>2</sub>KHg(SCN)<sub>4</sub>, Solid St. Comm. 85 (1993) 1005–1009.
- [456] M. V. Kartsovnik, D. Andres, W. Biberacher, Hierarchy of the density-wave states and superconductivity in the organic conductor  $\alpha$ -(BEDT-TTF)<sub>2</sub>KHg(SCN)<sub>4</sub>, C. R. Chimie 10 (2007) 6–14.
- [457] T. Sasaki, N. Toyota, Mysterious ground states in the organic conductor  $\alpha$ -(BEDT-TTF)<sub>2</sub>KHg(SCN)<sub>4</sub>: Mixed SDW and CDW?, Synth. Metals 70 (1995) 849–852.
- [458] N. Kinoshita, M. Tokumoto, H. Anzai, Electron spin resonance and electric resistance anomaly of (BEDT-TTF)<sub>2</sub>RbHg(SCN)<sub>4</sub>, J. Phys. Soc. Jpn. 60 (1991) 2131–2134.
- [459] P. Foury-Leylekan, S. Ravy, J.-P. Pouget, H. Müller, X-ray study of the density wave instability of  $\alpha$ -(BEDT-TTF)<sub>2</sub>MHg(SCN)<sub>4</sub> with M=K and Rb, Synth. Metals 137 (2003) 1271–1272.
- [460] P. Foury-Leylekan, J.-P. Pouget, Y.-J. Lee, R. M. Nieminen, P. Ordejón, E. Canadell, Density-wave instability in  $\alpha$ -(BEDT-TTF)<sub>2</sub>KHg(SCN)<sub>4</sub> studied by x-ray diffuse scattering and by first-principles calculations, Phys. Rev. B 82 (2010) 134116.
- [461] F. L. Pratt, T. Sasaki, N. Toyota, K. Nagamine, Zero field muon spin relaxation study of the low temperature state in  $\alpha$ -(BEDT-TTF)<sub>2</sub>KHg(SCN)<sub>4</sub>, Phys. Rev. Lett. 74 (1995) 3892.
- [462] M. Dressel, N. Drichko, J. Schlueter, J. Merino, Proximity of the layered organic conductors  $\alpha$ -(BEDT-TTF)<sub>2</sub>MHg(SCN)<sub>4</sub> (M=K, protectNH<sub>4</sub>) to a charge-ordering transition, Phys. Rev. Lett. 90.

- [463] T. Hiejima, S. Yamada, M. Uruichi, K. Yakushi, Infrared and Raman studies of  $\alpha$ -(BEDT-TTF)<sub>2</sub>MHg(SCN)<sub>4</sub> with M=NH<sub>4</sub> and K at low temperature: breaking of inversion symmetry due to charge-ordering fluctuation, *Physica B* 405 (2010) S153–S156.
- [464] R. Kato, Development of  $\pi$ -electron systems based on [M(dmit)<sub>2</sub>] (M=Ni and Pd; dmit: 1,3-dithiole-2-thione-4,5-dithiolate) anion radicals, *Bull. Chem. Soc. Jpn.* 87 (2014) 335–374.
- [465] H. Kobayashi, K. Bun, T. Naito, R. Kato, A. Kobayashi, New molecular superconductor, [Me<sub>2</sub>Et<sub>2</sub>N][Pd(dmit)<sub>2</sub>]<sub>2</sub>, *Chem. Lett.* 21 (1992) 1909–1912.
- [466] A. Kobayashi, H. Kim, Y. Sasaki, R. Kato, H. Kobayashi, S. Moriyama, Y. Nishio, K. Kajita, W. Sasaki, The first molecular superconductor based on  $\pi$ -acceptor molecules and closed-shell cations, [(CH<sub>3</sub>)<sub>4</sub>N][Ni(dmit)<sub>2</sub>]<sub>2</sub>, low-temperature X-ray studies and superconducting transition, *Chem. Lett.* 16 (1987) 1819–1822.
- [467] A. Kobayashi, H. Kobayashi, A. Miyamoto, R. Kato, R. A. Clark, A. E. Underhill, New molecular superconductor,  $\beta$ -[(CH<sub>3</sub>)<sub>4</sub>N][Pd(dmit)<sub>2</sub>]<sub>2</sub>, *Chem. Lett.* 20 (1991) 2163–2166.
- [468] T. Nakamura, T. Takahashi, S. Aonuma, R. Kato, EPR investigation of the electronic states in  $\beta'$ -type [Pd(dmit)<sub>2</sub>]<sub>2</sub> compounds (where dmit is 2-thioxo-1,3-dithiole-4,5-dithiolate), *J. Mater. Chem.* 11 (2001) 2159–2162.
- [469] R. Kato, Y.-L. Liu, Y. Hosokoshi, S. Aonuma, H. Sawa, Se-substitution and cation effects on the high-pressure molecular superconductor,  $\beta$ -Me<sub>4</sub>N[Pd(dmit)<sub>2</sub>]<sub>2</sub> – A unique two-band system, *Molec. Cryst. and Liq. Cryst. Science and Technology, Sect. A* 296 (1997) 217–244.
- [470] T. Nakamura, H. Tsukada, T. Takahashi, S. Aonuma, R. Kato, Low temperature electronic states of  $\beta'$ -type Pd(dmit)<sub>2</sub> compounds, *Molec. Cryst. Liq. Cryst.* 343 (2006) 187–192.
- [471] S. Rouzière, J.-I. Yamaura, R. Kato, Low-temperature structural studies of  $\beta$ -Pd(dmit)<sub>2</sub> conductors, *Phys. Rev. B* 60 (1999) 3113.
- [472] A. Tajima, A. Nakao, R. Kato, Uniaxial strain effects in the conducting Pd(dmit)<sub>2</sub> system (dmit = 1,2-dithiol-2-thione-4,5-dithiolate), *J. Phys. Soc. Jpn.* 74 (2005) 412–416.
- [473] A. Kobayashi, H. Kim, Y. Sasaki, K. Murata, R. Kato, H. Kobayashi, Crystal and electronic structures of new molecular conductors tetramethylammonium and tetramethylarsonium complexes of Pd(dmit)<sub>2</sub>, *J. Chem. Soc., Faraday Trans.* 86 (1990) 361.
- [474] R. Kato, N. Tajima, M. Tamura, J.-I. Yamaura, Uniaxial strain effect in a strongly correlated two-dimensional system  $\beta'$ -(CH<sub>3</sub>)<sub>4</sub>As[P(dmit)<sub>2</sub>]<sub>2</sub>, *Phys. Rev. B* 66 (2002) 020508(R).
- [475] R. Kato, Y. Kashimura, S. Aonuma, N. Hanasaki, H. Tajima, A new molecular superconductor  $\beta'$ -Et<sub>2</sub>Me<sub>2</sub>P[Pd(dmit)<sub>2</sub>]<sub>2</sub> (dmit=2-thioxo-1,3-dithiole-4,5-dithiolate), *Solid St. Comm.* 105 (1998) 561–565.
- [476] R. Kato, A. Tajima, A. Nakao, M. Tamura, Two pressure-induced superconducting anion radical salts exhibiting different spin states at ambient pressure, *J. Am. Chem. Soc.* 128 (2006) 10016–10017.
- [477] T. Itou, A. Oyamada, S. Maegawa, M. Tamura, R. Kato, Quantum spin liquid in the spin-1/2 triangular antiferromagnet EtMe<sub>3</sub>Sb[Pd(dmit)<sub>2</sub>]<sub>2</sub>, *Phys. Rev. B* 77 (2008) 104413.
- [478] T. Yamamoto, Y. Nakazawa, M. Tamura, A. Nakao, Y. Ikemoto, T. Moriwaki, A. Fukaya, R. Kato, K. Yakushi, Intradimer charge disproportionation in *Triclinic*-EtMe<sub>3</sub>P[Pd(dmit)<sub>2</sub>]<sub>2</sub> (dmit: 1,3-dithiole-2-thione-4,5-dithiolate), *J. Phys. Soc. Jpn.* 80 (2011) 123709.
- [479] K. Otsuka, H. Iikubo, T. Kogure, Y. Takano, K. Hiraki, T. Takahashi, H. Cui, R. Kato, Antiferromagnetic ordering in quasi-triangular localized spin system  $\beta'$ -Et<sub>2</sub>Me<sub>2</sub>P[Pd(dmit)<sub>2</sub>]<sub>2</sub>, studied by <sup>13</sup>C NMR, *J. Phys. Soc. Jpn.* 83 (2014) 054712.
- [480] A. Kobayashi, H. Kim, Y. Sasaki, S. Moriyama, Y. Nishio, K. Kajita, W. Sasaki, R. Kato, H. Kobayashi, The first molecular superconductor bases on the  $\pi$ -acceptor molecule and the closed shell cation, [(CH<sub>3</sub>)<sub>4</sub>N][Ni(dmit)<sub>2</sub>]<sub>2</sub>, *Synth. Metals* 27 (1988) 339.
- [481] A. Kobayashi, R. Kato, R. A. Clark, A. E. Underhill, A. Miyamoto, K. Bun, T. Naito, H. Kobayashi, New molecular superconductors,  $\beta$ -[(CH<sub>3</sub>)<sub>4</sub>N][Pd(dmit)<sub>2</sub>]<sub>2</sub> and [(CH<sub>3</sub>)<sub>2</sub>(C<sub>2</sub>H<sub>5</sub>)<sub>2</sub>N][Pd(dmit)<sub>2</sub>]<sub>2</sub>, *Synth. Metals* 55-57 (1993) 2927–2932.
- [482] M. Abdel-Jawad, N. Tajima, R. Kato, I. Terasaki, Disordered conduction in single-crystalline dimer Mott compounds, *Phys. Rev. B* 88 (2013) 075139.
- [483] Y. Shimizu, H. Akimoto, H. Tsujii, A. Tajima, R. Kato, Mott transition in a valence-bond solid insulator with a triangular lattice, *Phys. Rev. Lett.* 99 (2007) 256403.
- [484] M. Tamura, A. Nakao, R. Kato, Frustration-induced valence-bond ordering in a new quantum triangular antiferromagnet based on [Pd(dmit)<sub>2</sub>]<sub>2</sub>, *J. Phys. Soc. Jpn.* 75 (2006) 093701.
- [485] Y. Ishii, M. Tamura, R. Kato, Magnetic study of pressure-induced superconductivity in the [Pd(dmit)<sub>2</sub>]<sub>2</sub> salt with spin-gapped ground state, *J. Phys. Soc. Jpn.* 76 (2007) 033704.
- [486] T. Yamamoto, Y. Nakazawa, M. Tamura, A. Nakao, A. Fukaya, R. Kato, K. Yakushi, Property of the valence-bond ordering in molecular superconductor with a quasi-triangular lattice, *J. Phys. Soc. Jpn.* 83 (2014) 053703.
- [487] T. Yamamoto, T. Fujimoto, T. Naito, Y. Nakazawa, M. Tamura, K. Yakushi, Y. Ikemoto, T. Moriwaki, R. Kato, Charge and lattice fluctuations in molecule-based spin liquids, *Scientific Reports* 7 (2017) 12930.
- [488] T. Itou, A. Oyamada, S. Maegawa, R. Kato, Instability in a quantum spin liquid in an organic triangular-lattice antiferromagnet, *Nat. Phys.* 6 (2010) 673–676.
- [489] T. Itou, K. Yamashita, M. Nishiyama, A. Oyamada, S. Maegawa, K. Kubo, R. Kato, Nuclear magnetic resonance of the inequivalent carbon atoms in the organic spin-liquid material EtMe<sub>3</sub>Sb[Pd(dmit)<sub>2</sub>]<sub>2</sub>, *Phys. Rev. B* 84 (2011) 094405.
- [490] M. Yamashita, N. Nakata, Y. Senshu, M. Nagata, H. M. Yamamoto, R. Kato, T. Shibauchi, Y. Matsuda, Highly mobile gapless excitations in a two-dimensional candidate quantum spin liquid, *Science* 328 (2010) 1246–1248.
- [491] S. Yamashita, T. Yamamoto, Y. Nakazawa, M. Tamura, R. Kato, Gapless spin liquid of an organic triangular compound evidenced by thermodynamic measurements, *Nature Commun.* 2 (2011) 275.
- [492] M. Yamashita, T. Shibauchi, Y. Matsuda, Thermal-transport studies on two-dimensional quantum spin liquids, *Chem. Phys. Chem.* 13 (2012) 74–78.
- [493] D. Watanabe, M. Yamashita, S. Tonegawa, Y. Oshima, H. M. Yamamoto, R. Kato, I. Sheikin, K. Behnia, T. Terashima, S. Uji, T. Shibauchi, Y. Matsuda, Novel Pauli-paramagnetic quantum phase in a Mott insulator, *Nature Commun.* 3 (2012) 1090.
- [494] B. J. Powell, R. H. McKenzie, Strong electronic correlations in superconducting organic charge transfer salts, *J. Phys: Condens. Matter* 18 (2006) R827–R866.
- [495] T. Maier, M. Jarrell, T. Pruschke, J. Keller, d-wave superconductivity in the Hubbard model, *Phys. Rev. Lett.* 85 (2000) 1524–1527.

- [496] E. Gull, O. Parcollet, A. J. Millis, Superconductivity and the pseudogap in the two-dimensional Hubbard model, *Phys. Rev. Lett.* 110 (2013) 216405.
- [497] J. Merino, O. Gunnarsson, Pseudogap and singlet formation in organic and cuprate superconductors, *Phys. Rev. B* 89 (2014) 245130.
- [498] J. Merino, R. H. McKenzie, Superconductivity mediated by charge fluctuations in layered molecular crystals, *Phys. Rev. Lett.* 87 (2001) 237002.
- [499] P. Fazekas, P. W. Anderson, Ground state properties of anisotropic triangular antiferromagnet, *Phil. Mag.* 30 (1974) 423–440.
- [500] U. Chatterjee, D. Ai, J. Zhao, S. Rosenkranz, A. Kaminski, H. Raffy, Z. Li, K. Kadowaki, M. Randeria, M. R. Norman, J. C. Compuzano, Electronic phase diagram of high temperature copper oxide superconductors, *Proc. Natl. Acad. Sci.* 108 (2011) 9346–9349.
- [501] V. Mishra, U. Chatterjee, J. C. Campuzano, M. R. Norman, Effect of the pseudogap on the transition temperature in the cuprates and the implications for its origin, *Nature Physics* 10 (2014) 357–360.
- [502] P. W. Anderson, A suggested 4×4 structure in underdoped cuprate superconductors: a Wigner supersolid, [arXiv:cond-mat/0406038](https://arxiv.org/abs/cond-mat/0406038) (2004).
- [503] M. Franz, Crystalline electron pairs, *Science* 305 (2004) 1410–1411.
- [504] A. Tesanovic, Charge modulation, spin response, and dual Hofstadter butterfly in high- $T_c$  cuprates, *Phys. Rev. Lett.* 93 (2004) 217004.
- [505] H.-D. Chen, O. Vafek, A. Yazdani, S.-C. Zhang, Pair density wave in the pseudogap state of high temperature superconductors, *Phys. Rev. Lett.* 93 (2004) 187002.
- [506] M. Vojta, O. Rösch, Superconducting d-wave stripes in cuprates: Valence bond order coexisting with nodal quasiparticles, *Phys. Rev. B* 77 (2008) 094504.
- [507] M. H. Hamidian, S. D. Edkins, S. H. Joo, A. Kostin, H. Eisaki, S. Uchida, M. J. Lawler, E.-A. Kim, A. P. Mackenzie, K. Fujita, J. Lee, J. C. Séamus Davis, Detection of a Cooper-pair density wave in  $\text{Bi}_2\text{Sr}_2\text{CaCu}_2\text{O}_{8+x}$ , *Nature* 532 (2016) 343–347.
- [508] J. E. Hirsch, Antiferromagnetic singlet pairs, high-frequency phonons, and superconductivity, *Phys. Rev. B* 35 (1987) 8726–8729.
- [509] M. Imada, Spin dimer state model and spin-phonon coupling model of superconductivity, *J. Phys. Soc. Jpn.* 60 (1991) 1877–1880.
- [510] R. M. Noack, N. Bulut, D. J. Scalapino, M. G. Zacher, Enhanced  $d_{x^2-y^2}$  pairing correlations in the two-leg Hubbard ladder, *Phys. Rev. B* 56 (1997) 7162.
- [511] M. Dolfi, B. Bauer, S. Keller, M. Troyer, Pair correlations in doped Hubbard ladders, *Phys. Rev. B* 92 (2015) 195139.
- [512] T. Kashima, M. Imada, Path-integral renormalization group method for numerical study on ground states of strongly correlated electronic systems, *J. Phys. Soc. Jpn.* 70 (2001) 2287–2299.
- [513] C. Hotta, Theories on frustrated electrons in two-dimensional organic solids, *Crystals* 2012 (2012) 1155–1200.
- [514] T. Mizusaki, M. Imada, Gapless quantum spin liquid, stripe, and antiferromagnetic phases in frustrated Hubbard models in two dimensions, *Phys. Rev. B* 74 (2006) 014421.
- [515] H. Morita, S. Watanabe, M. Imada, Nonmagnetic insulating states near the Mott transitions on lattices with geometrical frustration and implications for  $\kappa$ -( $\text{ET}$ ) $_2\text{Cu}_2(\text{CN})_3$ , *J. Phys. Soc. Jpn.* 71 (2002) 2109–2112.
- [516] S. Watanabe, Absence of unit-cell doubling in nonmagnetic insulator phase on two-dimensional lattice with geometrical frustration, *J. Phys. Soc. Jpn.* 72 (2003) 2042–2045.
- [517] T. Yoshioka, A. Koga, N. Kawakami, Quantum phase transitions in the Hubbard model on a triangular lattice, *Phys. Rev. Lett.* 103 (2009) 036401.
- [518] L. F. Tocchio, C. Gros, R. Valentí, F. Becca, One-dimensional spin liquid, collinear, and spiral phases from uncoupled chains to the triangular lattice, *Phys. Rev. B* 89 (2014) 235107.
- [519] M. Laubach, R. Thomale, C. Platt, W. Hanke, G. Li, Phase diagram of the Hubbard model on the anisotropic triangular lattice, *Phys. Rev. B* 91 (2015) 245125.
- [520] S. Acheche, A. Reymbaut, M. Charlebois, D. Sénéchal, A.-M. S. Tremblay, Mott transition and magnetism on the anisotropic triangular lattice, *Phys. Rev. B* 94 (2016) 245133.
- [521] S. Goto, S. Kurihara, D. Yamamoto, Incommensurate spiral magnetic order on anisotropic triangular lattice: Dynamical mean-field study in a spin-rotating frame, *Phys. Rev. B* 94 (2016) 245145.
- [522] H. Kino, H. Kontani, Phase diagram of superconductivity on the anisotropic triangular lattice Hubbard model: An effective model of  $\kappa$ -(BEDT-TTF) salts, *J. Phys. Soc. Jpn.* 67 (1998) 3691.
- [523] J. Schmalian, Pairing due to spin fluctuations in layered organic superconductors, *Phys. Rev. Lett.* 81 (1998) 4232–4235.
- [524] H. Kondo, T. Moriya, Spin fluctuation-induced superconductivity in organic compounds, *J. Phys. Soc. Jpn.* 67 (1998) 3695–3698.
- [525] M. Vojta, E. Dagotto, Indications of unconventional superconductivity in doped and undoped triangular antiferromagnets, *Phys. Rev. B* 59 (1999) R713–716.
- [526] G. Baskaran, Mott insulator to high  $T_c$  superconductor via pressure: Resonating valence bond theory and prediction of new systems, *Phys. Rev. Lett.* 90 (2003) 197007.
- [527] J. Liu, J. Schmalian, N. Trivedi, Pairing and superconductivity driven by strong quasiparticle renormalization in two-dimensional organic charge transfer salts, *Phys. Rev. Lett.* 94 (2005) 127003.
- [528] B. Kyung, A. M. S. Tremblay, Mott transition, antiferromagnetism, and d-wave superconductivity in two-dimensional organic conductors, *Phys. Rev. Lett.* 97 (2006) 046402.
- [529] H. Yokoyama, M. Ogata, Y. Tanaka, Mott transitions and d-wave superconductivity in half-filled-band Hubbard model on square lattice with geometric frustration, *J. Phys. Soc. Jpn.* 75 (11) (2006) 114706.
- [530] T. Watanabe, H. Yokoyama, Y. Tanaka, J. Inoue, Superconductivity and a Mott transition in a Hubbard model on an anisotropic triangular lattice, *J. Phys. Soc. Jpn.* 75 (2006) 074707.
- [531] P. Sahebsara, D. Sénéchal, Antiferromagnetism and superconductivity in layered organic conductors: Variational cluster approach, *Phys. Rev. Lett.* 97 (2006) 257004.
- [532] A. H. Nevidomskyy, C. Scheiber, D. Sénéchal, A.-M. S. Tremblay, Magnetism and d-wave superconductivity on the half-filled square lattice with frustration, *Phys. Rev. B* 77 (2008) 064427.
- [533] M. Sentef, P. Werner, E. Gull, A. Kampf, Superconducting phase and pairing fluctuations in the half-filled two-dimensional Hubbard model, *Phys. Rev. Lett.* 107 (2001) 126401.

- [534] C. D. Hebert, P. Semon, A. M. S. Tremblay, Superconducting dome in doped quasi-two-dimensional organic Mott insulators: A paradigm for strongly correlated superconductivity, *Phys. Rev. B* 92 (2015) 195112.
- [535] T. Mizusaki, M. Imada, Quantum-number projection in the path-integral renormalization group method, *Phys. Rev. B* 69 (2004) 125110.
- [536] T. Aimi, M. Imada, Does simple two-dimensional Hubbard model account for high- $T_c$  superconductivity in copper oxides?, *J. Phys. Soc. Jpn.* 76 (2007) 113708.
- [537] L. F. Tocchio, A. Parola, C. Gros, F. Becca, Spin-liquid and magnetic phases in the anisotropic triangular lattice: The case of  $\kappa$ -(ET) $_2$ X, *Phys. Rev. B* 80 (2009) 064419.
- [538] T. Watanabe, H. Yokoyama, Y. Tanaka, J. Inoue, Predominant magnetic states in the Hubbard model on anisotropic triangular lattices, *Phys. Rev. B* 77 (2008) 214505.
- [539] H. Yokoyama, M. Ogata, Y. Tanaka, K. Kobayashi, H. Tsuchiura, Crossover between BCS superconductor and doped Mott insulator of  $d$ -wave pairing state in two-dimensional Hubbard model, *J. Phys. Soc. Jpn.* 82 (2013) 014707.
- [540] T. Yanagisawa, Crossover from weakly to strongly correlated regions in the two-dimensional Hubbard model—off-diagonal wavefunction Monte Carlo studies of Hubbard model II—, *J. Phys. Soc. Jpn.* 85 (2016) 114707.
- [541] L. F. Tocchio, F. Becca, S. Sorella, Hidden Mott transition and large- $U$  superconductivity in the two-dimensional Hubbard model, *Phys. Rev. B* 94 (2016) 195126.
- [542] G. Ehlers, S. R. White, R. M. Noack, Hybrid-space density matrix renormalization group study of the doped two-dimensional Hubbard model, *Phys. Rev. B* 95 (2017) 125125.
- [543] J. Y. Gan, Y. Chen, Z. B. Su, F. C. Zhang, Gossamer superconductivity near antiferromagnetic Mott insulator in layered organic conductors, *Phys. Rev. Lett.* 94 (2005) 067005.
- [544] B. J. Powell, R. H. McKenzie, Half-filled layered organic superconductors and the resonating-valence-bond theory of the Hubbard-Heisenberg model, *Phys. Rev. Lett.* 94 (2005) 047004.
- [545] J. Y. Gan, Y. Chen, F. C. Zhang, Superconducting pairing symmetries in anisotropic triangular quantum antiferromagnets, *Phys. Rev. B* 74 (2006) 094515.
- [546] B. J. Powell, R. H. McKenzie, Symmetry of the superconducting order parameter in frustrated systems determined by the spatial anisotropy of spin correlations, *Phys. Rev. Lett.* 98 (2007) 027005.
- [547] S. Guertler, Q. H. Wang, F. C. Zhang, Variational Monte Carlo studies of gossamer superconductivity, *Phys. Rev. B* 79 (2009) 144526.
- [548] J. G. Rau, H.-Y. Kee, Emergence of superconductivity, valence bond order, and Mott insulators in Pd[(dmit) $_2$ ] based organic salts, *Phys. Rev. Lett.* 106 (2011) 056405.
- [549] N. Gomes, R. T. Clay, S. Mazumdar, Absence of superconductivity and valence bond order in the Hubbard-Heisenberg model for organic charge-transfer solids, *J. Phys. Condens. Matter* 25 (2013) 385603.
- [550] H.-C. Jiang, H. Yao, L. Balents, Spin liquid ground state of the spin- $\frac{1}{2}$  square  $J_1$ - $J_2$  Heisenberg model, *Phys. Rev. B* 86 (2012) 024424.
- [551] W.-J. Hu, F. Becca, A. Parola, S. Sorella, Direct evidence for a gapless  $Z_2$  spin liquid by frustrating Néel antiferromagnetism, *Phys. Rev. B* 88 (2013) 060402(R).
- [552] H. Kondo, T. Moriya, Essential importance of dimerization for the superconductivity in organic compounds (ET) $_2$ X, *J. Phys. Soc. Jpn.* 70 (2001) 2800–2801.
- [553] K. Kuroki, Pairing symmetry competition in organic superconductors, *J. Phys. Soc. Jpn.* 75 (2006) 051013.
- [554] A. Sekine, J. Nasu, S. Ishihara, Polar charge fluctuation and superconductivity in organic conductors, *Phys. Rev. B* 87 (2013) 085133.
- [555] R. Chitra, S. Pati, H. R. Krishnamurthy, D. Sen, S. Ramasesha, Density-matrix renormalization-group studies of the spin-1/2 Heisenberg system with dimerization and frustration, *Phys. Rev. B* 52 (1995) 6581–6587.
- [556] S. R. White, I. Affleck, Dimerization and incommensurate spiral spin correlations in the zigzag spin chain: analogies to the Kondo lattice, *Phys. Rev. B* 54 (1996) 9862–9869.
- [557] C. Rovira, Molecular spin ladders, *Chem. Eur. J.* 6 (2000) 1723–1729.
- [558] X. Ribas, M. Mas-Torrent, A. Prez-Bentez, J. C. Dias, H. Alves, E. B. Lopes, R. T. Henriques, E. Molins, I. C. Santos, K. Wurst, P. Fourty-Leylekian, M. Almeida, J. Veciana, C. Rovira, Organic spin ladders from tetrathiafulvalene (TTF) derivatives, *Adv. Functional Materials* 15 (6) (2005) 1023–1035.
- [559] E. Dagotto, Experiments on ladders reveal a complex interplay between a spin-gapped normal state and superconductivity, *Rep. Prog. Phys.* 62 (1999) 1525.
- [560] K. Mouloupoulos, N. W. Ashcroft, New low density phase of interacting electrons: The paired electron crystal, *Phys. Rev. Lett.* 69 (1992) 2555.
- [561] K. Mouloupoulos, N. W. Ashcroft, Many-body theory of paired electron crystals, *Phys. Rev. B* 48 (1993) 11646–11665.
- [562] R. H. McKenzie, J. Merino, J. B. Marston, O. P. Sushkov, Charge ordering and antiferromagnetic exchange in layered molecular crystals of the theta type, *Phys. Rev. B* 64 (2001) 085109.
- [563] M. Tamura, R. Kato, Variety of valence bond states formed of frustrated spins on triangular lattices based on a two-level system Pd(dmit) $_2$ , *Sci. Technol. Adv. Mater.* 10 (2009) 024304.
- [564] W. Li, E. Rose, M. V. Tran, R. Hübner, A. Lapinski, R. Swietlik, S. A. Torunova, E. I. Zhilyaeva, R. N. Lyubovskaya, M. Dressel, The metal-insulator transition in the organic conductor  $\beta'$ -(BEDT-TTF) $_2$ Hg(SCN) $_2$ Cl, *J. Chem. Phys.* 147 (2017) 064503.
- [565] N. Gomes, W. W. De Silva, T. Dutta, R. T. Clay, S. Mazumdar, Coulomb enhanced superconducting pair correlations in the frustrated quarter-filled band, *Phys. Rev. B* 93 (2016) 165110.
- [566] K. Inagaki, I. Terasaki, H. Mori, T. Mori, Large dielectric constant and giant nonlinear conduction in the organic conductor  $\theta$ -(BEDT-TTF) $_2$ CsZn(SCN) $_4$ , *J. Phys. Soc. Jpn.* 73 (2004) 3364–3369.
- [567] C. Hotta, N. Furukawa, Strong coupling theory of the spinless charges on triangular lattice: possible formation of a gapless charge-ordered liquid, *Phys. Rev. B* 74 (2006) 193107.
- [568] S. Nishimoto, C. Hotta, Density-matrix renormalization study of frustrated fermions on a triangular lattice, *Phys. Rev. B* 79 (2009) 195124.
- [569] T. Yoshida, C. Hotta, Frustrated electrons on a spatially anisotropic triangular lattice: Emergent competition of charge orders and exotic disorders due to thermal fluctuations, *Phys. Rev. B* 90 (2014) 245115.

- [570] T. Hotta, Orbital ordering phenomena in d- and f-electron systems, *Rep. Prog. Phys.* 69 (2006) 2061–2155.
- [571] C. Hotta, Quantum electric dipoles in spin-liquid dimer Mott insulator  $\kappa$ -(ET)<sub>2</sub>Cu<sub>2</sub>(CN)<sub>3</sub>, *Phys. Rev. B* 82 (2010) 241104.
- [572] M. Naka, S. Ishihara, Electronic ferroelectricity in a dimer Mott insulator, *J. Phys. Soc. Jpn.* 79 (2010) 063707.
- [573] S. Ishihara, Electronic ferroelectricity in molecular organic crystals, *J. Phys.: Condens. Matter* 26 (2014) 493201.
- [574] S. Mazumdar, R. T. Clay, The chemical physics of unconventional superconductivity, *Int. J. Quant. Chem.* 2014 (2014) 1053.
- [575] R. Blankenbecler, D. J. Scalapino, R. L. Sugar, Monte Carlo calculations of coupled boson-fermion systems. I, *Phys. Rev. D* 24 (1981) 2278.
- [576] S. Zhang, J. Carlson, J. E. Gubernatis, Constrained path Monte Carlo method for fermion ground states, *Phys. Rev. B* 55 (1997) 7464–7477.
- [577] Z. B. Huang, H. Q. Lin, J. E. Gubernatis, Quantum Monte Carlo study of spin, charge, and pairing correlations in the t-t'-U Hubbard model, *Phys. Rev. B* 64 (2001) 205101.
- [578] S. R. White, D. J. Scalapino, R. L. Sugar, N. E. Bickers, R. T. Scalettar, Attractive and repulsive pairing interaction vertices for the two-dimensional Hubbard model, *Phys. Rev. B* 39 (1989) R839–R842.
- [579] S. Zhang, J. Carlson, J. E. Gubernatis, Pairing correlations in the two-dimensional Hubbard model, *Phys. Rev. Lett.* 78 (1997) 4486.
- [580] M. Guerrero, G. Ortiz, J. E. Gubernatis, Correlated wave functions and the absence of long-range order in numerical studies of the Hubbard model, *Phys. Rev. B* 59 (3) (1999) 1706–1711.
- [581] W. W. De Silva, N. Gomes, S. Mazumdar, R. T. Clay, Coulomb enhancement of superconducting pair-pair correlations in a  $\frac{3}{4}$ -filled model for  $\kappa$ -(BEDT-TTF)<sub>2</sub>X, *Phys. Rev. B* 93 (2016) 205111.
- [582] K. Zantout, M. Altmeyer, S. Backes, R. Valentí, Superconductivity in correlated BEDT-TTF molecular conductors: critical temperatures and gap symmetries, *Phys. Rev. B* 97 (2018) 014530.
- [583] H. Watanabe, H. Seo, S. Yunoki, Phase competition and superconductivity in  $\kappa$ -(BEDT-TTF)<sub>2</sub>X: importance of intermolecular Coulomb interactions, *J. Phys. Soc. Jpn.* 86 (2017) 033703.
- [584] N. Gomes, Superconductivity in strongly correlated quarter filled systems, Ph.D. thesis, University of Arizona (2017).
- [585] J. Chang, E. Blackburn, A. T. Holmes, N. B. Christensen, J. Larsen, J. Mesot, R. Liang, D. A. Bonn, W. N. Hardy, A. Watenphul, M. v. Zimmermann, E. M. Forgan, S. M. Hayden, Direct observation of competition between superconductivity and charge density wave order in YBa<sub>2</sub>Cu<sub>3</sub>O<sub>6.67</sub>, *Nature Physics* 8 (2012) 871–876.
- [586] G. Ghiringhelli, M. L. Tacon, M. Minola, S. Blanco-Canosa, C. Mazzoli, N. B. Brookes, G. M. D. Luca, A. Frano, D. G. Hawthorn, F. He, T. Loew, M. M. Sala, D. C. Peets, M. Salluzzo, E. Schierle, R. Sutarto, G. A. Sawatzky, E. Weschke, B. Keimer, L. Braicovich, Long-range incommensurate charge fluctuations in (Y,Nd)Ba<sub>2</sub>Cu<sub>3</sub>O<sub>6+x</sub>, *Science* 337 (2012) 821–825.
- [587] T. Wu, H. Mayaffre, S. Krämer, M. Horvatić, C. Berthier, W. N. Hardy, R. Liang, D. A. Bonn, M.-H. Julien, Magnetic-field-induced charge-stripe order in the high-temperature superconductor YBa<sub>2</sub>Cu<sub>3</sub>O<sub>y</sub>, *Nature* 477 (2011) 191.
- [588] T. Wu, H. Mayaffre, S. Krämer, M. Horvatić, C. Berthier, P. L. Kuhns, A. P. Reyes, R. Liang, W. N. Hardy, D. A. Bonn, M. H. Julien, Emergence of charge order from the vortex state of a high-temperature superconductor, *Nature Communications* 4 (2013) 2113.
- [589] T. Wu, H. Mayaffre, S. Krämer, M. Horvatić, C. Berthier, W. N. Hardy, R. Liang, D. Bonn, M.-H. Julien, Incipient charge order observed by NMR in the normal state of YBa<sub>2</sub>Cu<sub>3</sub>O<sub>y</sub>, *Nature Communications* 6 (2015) 6438.
- [590] S. Blanco-Canosa, A. Frano, E. Schierle, J. Porras, T. Loew, M. Minola, M. Bluschke, E. Weschke, B. Keimer, M. Le Tacon, Momentum-dependent charge correlations in YBa<sub>2</sub>Cu<sub>3</sub>O<sub>6+δ</sub> superconductors probed by resonant x-ray scattering: Evidence for three competing phases, *Phys. Rev. Lett.* 110 (2013) 187001.
- [591] S. Blanco-Canosa, A. Frano, E. Schierle, J. Porras, T. Loew, M. Minola, M. Bluschke, E. Weschke, B. Keimer, M. L. Tacon, Resonant x-ray scattering of charge-density wave correlations in YBa<sub>2</sub>Cu<sub>3</sub>O<sub>6+x</sub>, *Phys. Rev. B* 90 (2014) 054513.
- [592] M. Hücker, N. B. Christensen, A. T. Holmes, E. Blackburn, E. M. Forgan, R. Liang, D. A. Bonn, W. N. Hardy, O. Gutowski, M. v. Zimmermann, S. M. Hayden, J. Chang, Competing charge, spin, and superconducting orders in underdoped YBa<sub>2</sub>Cu<sub>3</sub>O<sub>y</sub>, *Phys. Rev. B* 90 (2014) 054514.
- [593] R. Comin, A. Frano, M. M. Yee, Y. Yoshida, H. Eisaki, E. Schierle, E. Weschke, R. Sutarto, F. He, A. Soumyanarayanan, Y. He, M. L. Tacon, I. S. Elfimov, J. E. Hoffman, G. A. Sawatzky, B. Keimer, A. Damascelli, Charge order driven by Fermi-arc instability in Bi<sub>2</sub>Sr<sub>2-x</sub>La<sub>x</sub>CuO<sub>6+δ</sub>, *Science* 343 (2014) 390–392.
- [594] E. H. D. S. Neto, P. Aynajian, A. Frano, R. Comin, E. Schierle, E. Weschke, A. Gyenis, J. Wen, J. Schneeloch, Z. Xu, S. Ono, G. Gu, M. L. Tacon, A. Yazdani, Ubiquitous interplay between charge ordering and high-temperature superconductivity in cuprates, *Science* 343 (2014) 393–396.
- [595] E. H. D. S. Neto, R. Comin, F. He, R. Sutaro, Y. Jiang, R. L. Greene, G. A. Sawatzky, A. Damascelli, Charge ordering in the electron-doped Nd<sub>2-x</sub>Ce<sub>x</sub>CuO<sub>4</sub>, *Science* 347 (2015) 282–285.
- [596] R. Comin, R. Sutarto, F. He, E. H. da Silva Neto, L. Chauviere, A. Frano, R. Liang, W. N. Hardy, D. A. Bonn, Y. Yoshida, H. Eisaki, A. J. Achkar, D. G. Hawthorn, B. Keimer, G. A. Sawatzky, A. Damascelli, Symmetry of charge order in cuprates, *Nature Materials* 14 (2015) 796–800.
- [597] T. Hanaguri, C. Lupien, Y. Kohsaka, D.-H. Lee, M. Azuma, M. Takano, H. Takagi, J. C. Davis, A 'checkerboard' electronic crystal state in lightly hole-doped Ca<sub>2-x</sub>Na<sub>x</sub>CuO<sub>2</sub>Cl<sub>2</sub>, *Nature* 430 (2004) 1001–1005.
- [598] K. M. Shen, F. Ronning, D. H. Lu, F. Baumberger, N. J. C. Ingle, W. S. Lee, W. Meevasana, Y. Kohsaka, M. Azuma, M. Takano, H. Takagi, Z.-X. Shen, Nodal quasiparticles and antinodal charge ordering in Ca<sub>2-x</sub>Na<sub>x</sub>CuO<sub>2</sub>Cl<sub>2</sub>, *Science* 307 (2005) 901–904.
- [599] E. H. D. S. Neto, B. Yu, M. Minola, R. Sutarto, E. Schierle, F. Boschini, M. Zonno, M. Bluschke, J. Higgins, Y. Li, G. Yu, E. Weschke, F. He, M. L. Tacon, R. L. Greene, M. Greven, G. A. Sawatzky, B. Keimer, A. Damascelli, Doping-dependent charge order correlations in electron-doped cuprates, *Sci. Adv* 2 (2016) e1600782.
- [600] The valence transition model of pseudogap, charge-order and superconductivity in electron- and hole-doped copper oxides, preprint, [arXiv:1807.00872](https://arxiv.org/abs/1807.00872) (2018).
- [601] B. K. Chakraverty, M. J. Sienko, J. Bonnerot, Low-temperature specific heat and magnetic susceptibility of nonmetallic vanadium bronzes, *Phys. Rev. B* 17 (1978) 3781.
- [602] B. K. Chakraverty, Possibility of insulator to superconductor phase transition, *J. Phys. (Paris)* 40 (1979) L–99.
- [603] B. K. Chakraverty, Insulating ground states and nonmetal-metal transitions, *Nature* 287 (1980) 393–396.

- [604] H. Shi, C. A. Jimenez-Hoyos, R. Rodriguez-Guzman, G. E. Scuseria, S. Zhang, Symmetry-projected wave functions in quantum Monte Carlo calculations, *Phys. Rev. B* 89 (21014) 125129.
- [605] E. Berg, E. Fradkin, S. A. Kivelson, Pair-density-wave correlations in the Kondo-Heisenberg model, *Phys. Rev. Lett.* 105 (2010) 146403.
- [606] S. Mazumdar, R. T. Clay, Quantum critical transition from charge-ordered to superconducting state in the negative-U extended Hubbard model on a triangular lattice, *Phys. Rev. B* 77 (2008) 180515(R).
- [607] K. Takada, H. Sakurai, E. Takayama-Muromachi, F. Izumi, R. A. Dilanian, T. Sasaki, Superconductivity in two-dimensional CoO<sub>2</sub> layers, *Nature* 422 (2003) 53–55.
- [608] M. L. Foo, Y. Wang, S. Watauchi, H. W. Zandbergen, T. He, R. J. Cava, N. P. Ong, Charge ordering, commensurability, and metallicity in the phase diagram of the layered Na<sub>x</sub>CoO<sub>2</sub>, *Phys. Rev. Lett.* 92 (2004) 247001.
- [609] T. Motohashi, Y. Sugimoto, Y. Masubuchi, T. Sasagawa, W. Koshibae, T. Tohyama, H. Yamauchi, S. Kikkawa, Impact of lithium composition on the thermoelectric properties of the layered cobalt oxide system Li<sub>x</sub>CoO<sub>2</sub>, *Phys. Rev. B* 83 (2011) 195128.
- [610] H. Sakurai, Y. Ihara, K. Takada, Superconductivity of cobalt hydrate, Na<sub>x</sub>(H<sub>3</sub>O)<sub>z</sub>CoO<sub>2</sub>·yH<sub>2</sub>O, *Physica C* 514 (2015) 378–387.
- [611] H. Li, R. T. Clay, S. Mazumdar, Theory of carrier concentration-dependent electronic behavior in layered cobaltates, *Phys. Rev. Lett.* 106 (2011) 216401.
- [612] M. Z. Hasan, Y.-D. Chuang, D. Qian, Y. W. Li, Y. Kong, A. Kuprin, A. V. Fedorov, R. Kimmerling, E. Rotenberg, K. Kossnagel, Z. Hussain, H. Koh, N. S. Rogado, M. L. Foo, R. J. Cava, Fermi surface and quasiparticle dynamics of Na<sub>0.7</sub>CoO<sub>2</sub> investigated by angle-resolved photoemission spectroscopy, *Phys. Rev. Lett.* 92 (2004) 246402.
- [613] T. Shimojima, K. Ishizaka, S. Tsuda, T. Kiss, T. Yokoya, A. Chainani, S. Shin, P. Badica, K. Yamada, K. Togano, Angle-resolved photoemission study of the cobalt oxide superconductor Na<sub>x</sub>CoO<sub>2</sub>·yH<sub>2</sub>O: Observation of the Fermi surface, *Phys. Rev. Lett.* 97 (2006) 267003.
- [614] J. Laverock, S. B. Dugdale, J. A. Duffy, J. Wooldridge, G. Balakrishnan, M. R. Lees, G. q. Zheng, C. T. Lin, A. Andrejczuk, M. Ito, Y. Sakurai, Elliptical hole pockets in the Fermi surfaces of unhydrated and hydrated sodium cobalt oxides, *Phys. Rev. B* 76 (2007) 052509.
- [615] D. J. Singh, Electronic structure of NaCo<sub>2</sub>O<sub>4</sub>, *Phys. Rev. B* 61 (2000) 13397–13402.
- [616] K.-W. Lee, W. E. Pickett, Na<sub>x</sub>CoO<sub>2</sub> in the  $x \rightarrow 0$  regime: Coupling of structure and correlation effects, *Phys. Rev. B* 72 (11) (2005) 115110.
- [617] G. Baskaran, Electronic model for CoO<sub>2</sub> layer based systems: Chiral resonating valence bond metal and superconductivity, *Phys. Rev. Lett.* 91 (2003) 097003.
- [618] B. Kumar, B. S. Shastry, Superconductivity in CoO<sub>2</sub> layers and the resonating valence bond mean-field theory of the triangular lattice  $t$ - $J$  model, *Phys. Rev. B* 68 (2003) 104508.
- [619] M. Ogata, Superconducting states in frustrating  $t - J$  model: a model connecting high- $T_c$  cuprates, organic conductors and Na<sub>x</sub>CoO<sub>2</sub>, *J. Phys. Soc. Jpn.* 72 (2003) 1839–1842.
- [620] Q.-H. Wang, D.-H. Lee, P. A. Lee, Doped  $t - J$  model on a triangular lattice: possible application to Na<sub>x</sub>CoO<sub>2</sub>·H<sub>2</sub>O and Na<sub>1-x</sub>TiO<sub>2</sub>, *Phys. Rev. B* 69 (2004) 092504.
- [621] H. Sakurai, N. Tsujii, O. Suzuki, H. Kitazawa, G. Kido, K. Takada, T. Sasaki, E. Takayama-Muromachi, Valence and Na content dependences of superconductivity in Na<sub>x</sub>CoO<sub>2</sub>·yH<sub>2</sub>O, *Phys. Rev. B* 74 (2006) 092502.
- [622] M. Banobre-Lopez, F. Rivadulla, M. A. López-Quintela, J. Rivas, Competing magnetism and superconductivity in Na<sub>x</sub>CoO<sub>2</sub> at half doping, *J. Am. Chem. Soc.* 131 (2009) 9632.
- [623] K. Kuroki, Y. Tanaka, R. Arita, Possible spin-triplet  $f$ -wave pairing due to disconnected Fermi surfaces in Na<sub>x</sub>CoO<sub>2</sub>·H<sub>2</sub>O, *Phys. Rev. Lett.* 93 (2004) 077001.
- [624] M. Ogata, A new triangular system: Na<sub>x</sub>CoO<sub>2</sub>, *J. Phys. Condens. Matt.* 19 (2007) 145282.
- [625] M. Sato, Y. Kobayashi, T. Moyoshi, Studies on the superconducting state of Na<sub>x</sub>CoO<sub>2</sub>·yH<sub>2</sub>O – overview, *Physica C* 470 (2010) S673–S677.
- [626] D. C. Johnston, H. Prakash, W. H. Zachariah, R. Viswanathan, High temperature superconductivity in the Li-Ti-O ternary system, *Mater. Res. Bull.* 8 (1973) 77.
- [627] T. Hagino, Y. Seki, N. Wada, S. Tsuji, T. Shirane, K. Kumagai, S. Nagata, Superconductivity in spinel-type compounds CuRh<sub>2</sub>S<sub>4</sub> and CuRh<sub>2</sub>Se<sub>4</sub>, *Phys. Rev. B* 51 (1995) 12673–12684.
- [628] M. Ito, J. Hori, H. Kurisaki, H. Okada, A. J. P. Kuroki, N. Ogata, M. Udagawa, H. Fujii, F. Nakamura, T. Fujita, T. Suzuki, Pressure-induced superconductor-insulator transition in the spinel compound CuRh<sub>2</sub>S<sub>4</sub>, *Phys. Rev. Lett.* 91 (2003) 077001.
- [629] Y. Seki, T. Hagino, S. Takayanagi, S. Nagata, Electrical and thermal properties in thiospinel CuV<sub>2</sub>S<sub>4</sub>, *J. Phys. Soc. Jpn.* 61 (1992) 2597–2598.
- [630] T. Hagino, Y. Seki, S. Takayanagi, N. Wada, S. Nagata, Electrical-resistivity and low-temperature specific-heat measurements of single crystals of thiospinel CuV<sub>2</sub>S<sub>4</sub>, *Phys. Rev. B* 49 (1994) 6822–6829.
- [631] G. L. W. Hart, W. E. Pickett, E. Z. Kurmaev, D. Hartmann, N. Neumann, A. Moewes, D. L. Ederer, R. Endoh, K. Taniguchi, S. Nagata, Electronic structure of Cu<sub>1-x</sub>Ni<sub>x</sub>Rh<sub>2</sub>S<sub>4</sub> and CuRh<sub>2</sub>Se<sub>4</sub>: band-structure calculations, x-ray photoemission, and fluorescence measurements, *Phys. Rev. B* 61 (2000) 4230.
- [632] S. Satpathy, R. M. Martin, Electronic structure of the superconducting oxide spinel LiTi<sub>2</sub>O<sub>4</sub>, *Phys. Rev. B* 36 (1987) R7269.
- [633] S. Massidda, J. Yu, A. J. Freeman, Electronic structure and properties of superconducting LiTi<sub>2</sub>O<sub>4</sub>, *Phys. Rev. B* 38 (1988) 11352–11357.
- [634] S. Kondo, D. C. Johnston, C. A. Swenson, F. Borsa, A. V. Mahajan, L. L. Miller, T. Gu, A. I. Goldman, M. B. Maple, D. A. Gajski, E. J. Freeman, N. R. Dilley, R. P. Dickey, J. Merrin, K. Kojima, G. M. Luke, Y. J. Uemura, O. Chmaissem, J. D. Jorgensen, LiV<sub>2</sub>O<sub>4</sub>: A heavy Fermion transition metal oxide, *Phys. Rev. Lett.* 78 (1997) 3729–3732.
- [635] R. W. McCallum, D. C. Johnston, C. A. Luengo, M. B. Maple, Superconducting and normal state properties of Li<sub>1+x</sub>Ti<sub>2x</sub>O<sub>4</sub> spinel compounds. II. Low-temperature heat capacity, *J. Low Temp. Phys.* 25 (1976) 177–193.
- [636] S. Lakkis, C. Schlenker, B. K. Chakraverty, R. Buder, M. Marezio, Metal-insulator transitions in Ti<sub>4</sub>O<sub>7</sub> single crystals: Crystal characterization, specific heat, and electron paramagnetic resonance, *Phys. Rev. B* 14 (1976) 1429.
- [637] B. K. Chakraverty, Charge ordering in Fe<sub>3</sub>O<sub>4</sub>, Ti<sub>4</sub>O<sub>7</sub> and bipolarons, *Phil. Mag.* B 42 (1980) 473–478.
- [638] D. I. Khomskii, T. Mizokawa, Orbital induced Peierls state in spinels, *Phys. Rev. Lett.* 94 (2005) 156402.
- [639] D. I. Khomskii, Role of orbitals in the physics of correlated electron systems, *Physica Scripta* 72 (2005) CC8–14.

- [640] P. G. Radaelli, Orbital ordering in transition-metal spinels, *New J. Phys.* 7 (2005) 53.
- [641] M. Croft, V. Kiryukhin, Y. Horibe, S.-W. Cheong, Universality in one-dimensional orbital wave ordering in spinel and related compounds: an experimental perspective, *New J. Phys.* 9 (2007) 86.
- [642] R. T. Clay, H. Li, S. Sarkar, S. Mazumdar, T. Saha-Dasgupta, Cooperative orbital ordering and Peierls instability in the checkerboard lattice with doubly degenerate orbitals, *Phys. Rev. B* 82 (2010) 035108.
- [643] P. G. Radaelli, Y. Horibe, M. J. Gutmann, H. Ishibashi, C. H. Chen, R. M. Ibberson, Y. Koyama, Y.-S. Hor, V. Kiryukhin, S.-W. Cheong, Formation of isomorphous  $\text{Ir}^{3+}$  and  $\text{Ir}^{4+}$  octamers and spin dimerization in the spinel  $\text{CuIr}_2\text{S}_4$ , *Nature* 416 (2002) 155–158.
- [644] Y. Okamoto, S. Niitaka, M. Uchida, T. Waki, M. Takigawa, Y. Nakatsu, A. Sekiyama, S. Suga, R. Arita, H. Takagi, Band Jahn-Teller instability and formation of valence bond solid in a mixed-valent spinel oxide  $\text{LiRh}_2\text{O}_4$ , *Phys. Rev. Lett.* 101 (2008) 086404.
- [645] K. R. Knox, A. M. M. Abeykoon, H. Zheng, W.-G. Yin, A. M. Tselik, J. F. Mitchell, S. J. L. Billinge, E. S. Bozin, Local structural evidence for strong electronic correlations in spinel  $\text{LiRh}_2\text{O}_4$ , *Phys. Rev. B* 88 (2013) 174114.
- [646] J. G. Rau, E. K.-H. Lee, H.-Y. Kee, Spin-orbit physics giving rise to novel phases in correlated systems: iridates and related materials, *Ann. Rev. Cond. Matter Phys.* 7 (2016) 195–221.
- [647] B. J. Kim, H. Jin, S. J. Moon, J.-Y. Kim, B.-G. Park, C. S. Leem, J. Yu, T. W. Noh, C. Kim, S.-J. Oh, J. H. Park, V. Durairaj, G. Cao, E. Rotenberg, Novel  $J_{\text{eff}}=1/2$  Mott state induced by relativistic spin-orbit coupling in  $\text{Sr}_2\text{IrO}_4$ , *Phys. Rev. Lett.* 101 (2008) 076402.
- [648] W. Witczak-Krempa, G. Chen, Y. B. Kim, L. Balents, Correlated quantum phenomena in the strong spin-orbit regime, *Ann. Rev. Cond. Matter Phys.* 5 (2014) 57–82.
- [649] W. D. Wu, A. Keren, L. P. Le, G. M. Luke, B. J. Sternlieb, Y. J. Uemura, Magnetic penetration depth in  $\text{V}_3\text{Si}$  and  $\text{LiTi}_2\text{O}_4$  measured by  $\mu\text{SR}$ , *Hyperfine Interactions* 86 (1994) 615–621.
- [650] F. Fazileh, R. J. Gooding, W. A. Atkinson, D. C. Johnston, Role of strong electronic correlations in the metal-to-insulator transition in disordered  $\text{LiAl}_y\text{Ti}_{2-y}\text{O}_4$ , *Phys. Rev. Lett.* 96 (2006) 046410.
- [651] E. G. Moshopoulou, Superconductivity in the spinel compound  $\text{LiTi}_2\text{O}_4$ , *J. Am. Ceram. Soc.* 82 (1999) 3317–3320.
- [652] K. Jin, G. He, X. Zhang, S. Maruyama, S. Yasui, R. Suchoski, J. Shin, Y. Jiang, H. S. Yu, J. Yuan, L. Shan, F. V. Kusmartsev, R. L. Greene, I. Takeuchi, Anomalous magnetoresistance in the spinel superconductor  $\text{LiTi}_2\text{O}_4$ , *Nat. Commun.* 6 (2015) 7183–7191.
- [653] D. Chen, Y.-L. Jia, T.-T. Zhang, Z. Fang, K. Jin, P. Richard, H. Ding, Raman study of electron-phonon coupling in thin films of the spinel oxide superconductor  $\text{LiTi}_2\text{O}_4$ , *Phys. Rev. B* 96 (2017) 094501.
- [654] T. Yamauchi, Y. Ueda, N. Mori, Pressure-induced superconductivity in  $\beta\text{-Na}_{0.33}\text{V}_2\text{O}_5$  beyond charge ordering, *Phys. Rev. Lett.* 89 (2002) 057002.
- [655] T. Yamauchi, Y. Ueda, Superconducting  $\beta(\beta')$ -vanadium bronzes under pressure, *Phys. Rev. B* 77 (2008) 104529.
- [656] K. Okazaki, A. Fujimori, T. Yamauchi, Y. Ueda, Angle-resolved photoemission study of the quasi-one-dimensional superconductor  $\beta\text{-Na}_{0.33}\text{V}_2\text{O}_5$ , *Phys. Rev. B* 69 (2004) 140506.
- [657] J. P. Hague, P. E. Kornilovitch, J. H. Samson, A. S. Alexandrov, Superlight small bipolarons in the presence of a strong Coulomb repulsion, *Phys. Rev. Lett.* 98 (2007) 037002.
- [658] Y. Takabayashi, A. Y. Ganin, P. Jeglič, D. Arčon, T. Takano, Y. Iwasa, Y. Ohishi, M. Takata, N. Takeshita, K. Prassides, M. J. Rosseinsky, The disorder-free non-BCS superconductor  $\text{Cs}_3\text{C}_{60}$  emerges from an antiferromagnetic insulator parent state, *Science* 323 (2009) 1585–1590.
- [659] O. Gunnarsson, Superconductivity in fullerenes, *Rev. Mod. Phys.* 69 (1997) 575–606.
- [660] A. Y. Ganin, Y. Takabayashi, Y. Z. Khimyak, S. Margadonna, A. Tamai, M. J. Rosseinsky, K. Prassides, Bulk superconductivity at 38 K in a molecular system, *Nat. Mater.* 7 (5) (2008) 367–371.
- [661] A. Y. Ganin, Y. Takabayashi, P. Jeglič, D. Arčon, A. Potočnik, P. J. Baker, Y. Ohishi, M. T. McDonald, M. D. Tzirakis, A. McLennan, G. R. Darling, M. Takata, M. J. Rosseinsky, K. Prassides, Polymorphism control of superconductivity and magnetism in  $\text{Cs}_3\text{C}_{60}$  close to the Mott transition, *Nature* 466 (2010) 221–225.
- [662] G. Klupp, P. Matus, K. Kamařas, A. Y. Ganin, A. McLennan, M. J. Rosseinsky, Y. Takabayashi, M. T. McDonald, K. Prassides, Dynamic Jahn-Teller effect in the parent insulating state of the molecular superconductor  $\text{Cs}_3\text{C}_{60}$ , *Nature Commun.* 3 (2012) 912.
- [663] S. Chakravarty, M. Gelfand, S. Kivelson, Electronic correlation effects and superconductivity in doped fullerenes, *Science* 254 (1991) 970–974.
- [664] C. M. Varma, J. Zaanen, K. Raghavachari, Superconductivity in the fullerenes, *Science* 254 (1991) 989–992.
- [665] M. Schluter, M. Lannoo, M. Needels, G. A. Baraff, D. Tománek, Electron-phonon coupling and superconductivity in alkali-intercalated  $\text{C}_{60}$  solid, *Phys. Rev. Lett.* 68 (1992) 526.
- [666] S. R. White, S. Chakravarty, M. P. Gelfand, S. A. Kivelson, Pair binding in small Hubbard-model molecules, *Phys. Rev. B* 45 (1992) 5062–5065.
- [667] T. Dutta, S. Mazumdar, Theory of metal-intercalated phenacenes: Why molecular valence 3 is special, *Phys. Rev. B* 89 (2014) 245129.
- [668] M. Onoda, K. Toriumi, Y. Matsuda, M. Sato, Crystal-structure of lithium molybdenum purple bronze  $\text{Li}_{0.9}\text{Mo}_6\text{O}_{17}$ , *J. Solid St. Chem.* 66 (1987) 163–170.
- [669] M. S. da Luz, J. J. Neumeier, C. A. M. dos Santos, B. D. White, H. J. I. Filho, J. B. Leao, Q. Huang, Neutron diffraction study of quasi-one-dimensional lithium purple bronze: Possible mechanism for dimensional crossover, *Phys. Rev. B* 84 (2011) 014108.
- [670] M. Greenblatt, Molybdenum oxide bronzes with quasi-low-dimensional properties, *Chem. Rev.* 88 (1988) 31–53.
- [671] C. Schlenker, H. Schwenk, C. Escribe-Filippini, J. Marcus, Superconducting properties of the low dimensional purple bronze  $\text{Li}_{0.9}\text{Mo}_6\text{O}_{17}$ , *Physica B+C* 135 (1985) 511.
- [672] M. Sato, Y. Matsuda, H. Fukuyama, Localization and superconductivity in  $\text{Li}_{0.9}\text{Mo}_6\text{O}_{17}$ , *J. Phys. C* 20 (1987) L137–L142.
- [673] J. Choi, J. L. Musfeldt, J. He, R. Jin, J. R. Thompson, D. Mandrus, X. N. Lin, V. A. Bondarenko, J. W. Brill, Probing localization effects in  $\text{Li}_{0.9}\text{Mo}_6\text{O}_{17}$  purple bronze: An optical-properties investigation, *Phys. Rev. B* 69 (2004) 085120.
- [674] C. A. M. dos Santos, B. D. White, Y.-K. Yu, J. J. Neumeier, J. A. Souza, Dimensional crossover in the purple bronze  $\text{Li}_{0.9}\text{Mo}_6\text{O}_{17}$ , *Phys. Rev. Lett.* 98 (2007) 266405.
- [675] C. A. M. dos Santos, M. S. da Luz, Y.-K. Yu, J. J. Neumeier, J. Moreno, B. D. White, Electrical transport in single-crystalline  $\text{Li}_{0.9}\text{Mo}_6\text{O}_{17}$ : A two-band Luttinger liquid exhibiting Bose metal behavior, *Phys. Rev. B* 77 (2008) 193106.

- [676] J. F. Mercure, A. F. Bangura, X. F. Xu, N. Wakeham, A. Carrington, P. Walmsley, M. Greenblatt, N. E. Hussey, Upper critical magnetic field far above the paramagnetic pair-breaking limit of superconducting one-dimensional  $\text{Li}_{0.9}\text{Mo}_6\text{O}_{17}$  single crystals, *Phys. Rev. Lett.* 108 (2012) 187003.
- [677] A. G. Lebed, O. Sepper, Possible triplet superconductivity in the quasi-one-dimensional conductor  $\text{Li}_{0.9}\text{Mo}_6\text{O}_{17}$ , *Phys. Rev. B* 87 (2013) 100511(R).
- [678] F. Zuo, J. S. Brooks, R. H. McKenzie, J. A. Schlueter, J. M. Williams, Paramagnetic limiting of the upper critical field of the layered organic superconductor  $\kappa\text{-(BEDT-TTF)}_2\text{Cu(SCN)}_2$ , *Phys. Rev. B* 61 (2000) 750–755.
- [679] J. Shinagawa, Y. Kurosaki, F. Zhang, C. Parker, S. E. Brown, D. Jérôme, J. B. Christensen, K. Bechgaard, Superconducting state of the organic conductor  $(\text{TMTSF})_2\text{ClO}_4$ , *Phys. Rev. Lett.* 98 (2007) 147002.
- [680] H. Merino, R. H. McKenzie, Effective Hamiltonian for the electronic properties of the quasi-one-dimensional material  $\text{Li}_{0.9}\text{Mo}_6\text{O}_{17}$ , *Phys. Rev. B* 85 (2012) 235128.
- [681] Z. S. Popovic, S. Satpathy, Density-functional study of the Luttinger liquid behavior of the lithium molybdenum purple  $\text{Li}_{0.9}\text{Mo}_6\text{O}_{17}$ , *Phys. Rev. B* 74 (2006) 045117.
- [682] J. Cohn, B. D. White, C. A. M. dos Santos, J. J. Neumeier, Giant Nernst effect and bipolarity in the quasi-one-dimensional metal  $\text{Li}_{0.9}\text{Mo}_6\text{O}_{17}$ , *Phys. Rev. Lett.* 108 (2012) 056604.
- [683] K.-T. Ko, H.-H. Lee, D.-H. Kim, J.-J. Yang, S.-W. Cheong, M. Eom, J. Kim, R. Gammag, K.-S. Kim, H.-S. Kim, T.-H. Kim, H.-W. Yeom, T.-Y. Koo, H.-D. Kim, J.-H. Park, Charge-ordering cascade with spinorbit Mott dimer states in metallic iridium ditelluride, *Nat. Commun.* 6 (2015) 7342.
- [684] Y. S. Oh, J. J. Yang, Y. Horibe, S.-W. Cheong, Anionic depolymerization transition in  $\text{IrTe}_2$ , *Phys. Rev. Lett.* 110 (2013) 127209.
- [685] A. F. Fang, G. Xu, T. Dong, P. Zheng, N. L. Wang, Structural phase transition in  $\text{IrTe}_2$ : a combined study of optical spectroscopy and band structure calculations, *Sci. Rep.* 3 (2013) 1153.
- [686] J. J. Yang, Y. J. Choi, Y. S. Oh, A. Hogan, Y. Horibe, K. Kim, B. I. Min, S.-W. Cheong, Charge-orbital density wave and superconductivity in the strong spin-orbit coupled  $\text{IrTe}_2\text{:Pd}$ , *Phys. Rev. Lett.* 108 (2012) 116402.
- [687] Y. Kohsaka, T. Hanaguri, M. Azuma, M. Takano, J. C. Davis, H. Takagi, Visualization of the emergence of the pseudogap state and the evolution to superconductivity in a lightly hole-doped Mott insulator, *Nat. Phys.* 8 (2012) 534–538.
- [688] M. Naito, Y. Krockenberger, A. Ikeda, H. Yamamoto, Reassessment of the electronic state, magnetism, and superconductivity in high- $T_c$  cuprates with the  $\text{Nd}_2\text{CuO}_4$  structure, *Physica C* 523 (2016) 28–54.
- [689] Y. Dagan, R. L. Greene, Hole superconductivity in the electron-doped superconductor  $\text{Pr}_{2-x}\text{Ce}_x\text{CuO}_4$ , *Phys. Rev. Lett.* 94 (2007) 187003.
- [690] M. Masino, N. Castagnetti, A. Girlando, Phenomenology of the neutral-ionic valence instability in mixed stack charge-transfer crystals, *Crystals* 7 (2017) 108, and references therein.